

UNIVERSITY OF NOTTINGHAM
School of Chemical, Environmental and
Mining Engineering

**THE INTERFACIAL CHARACTERISTICS
OF FALLING FILM REACTORS**

by

Wayne William Philip Clark M.Eng. (Hons.)

Thesis submitted to the University of Nottingham
for the degree of Doctor of Philosophy, December 2000

ABSTRACT

Falling film reactors are a very effective geometry in which to carry out fast exothermic gas-liquid reactions, because they allow easy removal of the heat produced. To optimise and improve falling film reactors, soundly based physical models are required. Existing models assume a flat liquid film combined with empirically-determined mass transfer coefficients, but there is growing evidence that this is unsatisfactory, since the interface is dominated by ripples and larger disturbance waves which have a significant effect on the mass and heat transfer rates through and into the film.

The main objective of this study was the better understanding through experimental study of the interfacial characteristics of liquid falling films in the presence of a co-current down flow of air, with emphasis on the physical and hydrodynamic conditions encountered in current falling film reactor technology, so that the information obtained can be implemented in the enhancement of falling film reactor modelling. The liquids chosen were water, for validation of the measurement techniques through comparison with the literature, and two common falling film sulphonation reactor feedstocks; dodecylbenzene and ethoxylated alcohol.

The experimental study consisted of film thickness and disturbance wave celerity measurements in a purpose built flow facility with a flat plate flow surface. A novel spatial film thickness measurement technique, the Light Absorption Imaging Technique (LAIT), was developed to give unparalleled spatial information on the interfacial characteristics of liquid films. A computer algorithm-based technique has been developed for categorisation of the spatial film data obtained by LAIT into substrate and disturbance wave regions, from which globally averaged characteristics of the interfacial structure have been obtained. Disturbance wave celerity measurements were obtained utilising the cross-correlated output signal from two light sources and a manual time-of-flight measurement technique using the images from a high-speed video camera.

The study has provided a comprehensive set of data on the hydrodynamic structure of the interface, with and without the influence of a co-current downflow of air, for both water and actual sulphonation feed stocks as the liquid phase. The dramatic influence of

ABSTRACT

both flow conditions and physical properties on interfacial characteristics has been demonstrated. In particular, a transition has been observed of the disturbance wave structures in falling films due to the influence of a co-current airflow. Differences in the disturbance wave structure have been identified between the organic and water films after this transition.

ACKNOWLEDGEMENTS

I would like to take this opportunity to express my gratitude to the following:

My supervisors, Prof. B.J. Azzopardi and Dr J.H. Hills, for their constant help, support and patience.

The technical staff of the School of Chemical, Environmental, and Mining Engineering for their invaluable expertise, patience and hard work throughout this study.

Dr. F. Talens for his considerable advice on all aspects of falling film reactor modelling.

EPSRC for their primary funding of this work under research grant number GR/K77044.

Unilever Plc. (and in particular Mr. P. Chadwick and Dr. D. Roberts) for their insight into the industrial application of falling film reactors, and for supplying the organic liquids utilised in this study.

My colleagues, past and present, in the postgraduate office that helped make this “adventure” a pleasurable experience.

My family and friends outside of university for their interest and restricting their “Is it finished?” questions to a minimum.

And finally, I would like to dedicate this work to my wife “Samantha” and son “Conor” for their unfailing love, sacrifice and support

CONTENTS

ABSTRACT	i
ACKNOWLEDGEMENTS	iii
CONTENTS	iv
LIST OF FIGURES	xi
LIST OF TABLES	xix
Chapter 1: INTRODUCTION	1
1.1 MOTIVATION BEHIND STUDY	1
1.2 STUDY OBJECTIVES	3
1.3 THESIS STRUCTURE	4
Chapter 2: EXPERIMENTAL FLOW FACILITY	7
2.1 INTRODUCTION	7
2.2 OVERVIEW OF THE FLOW FACILITY	7
2.3. FLOW FACILITY COMPONENTS	10
2.3.1 Rectangular Test Section	10
2.3.2. Liquid Feed Arrangement	11
2.3.3 Air Feed Arrangement	13
2.3.4 Air Distribution Section	15
2.3.5 Liquid Distribution Section	16
2.3.6 Air/Liquid Separation System	20
2.4 LIQUIDS UNDER STUDY	22
2.5 OPERATING PROCEDURE	23
2.5.1 Start-Up	23
2.5.2 Shut-down	25
2.6 MAINTAINANCE	25
2.6.1 Test Section Cleaning	25
2.6.2 Changeover of Liquid Inventories	26

LIQUID FILM THICKNESS MEASUREMENTS

Chapter 3:	REVIEW OF THE LITERATURE	28
3.1	INTRODUCTION	28
3.2	FILM AVERAGE TECHNIQUES	32
3.2.1	Hold-up Measurements	32
3.2.2	Film Conductance Method	34
3.2.3	Weighing Method	35
3.3	LOCALISED TECHNIQUES	36
3.3.1	Capacitance Probes	36
3.3.2	Conductance probes	41
3.3.2.1	Flush-mounted	42
3.3.2.2	Parallel-wire	47
3.3.2.3	Flush-wire	49
3.3.2.4	Electronic Circuitry	51
3.3.2.5	Calibration	53
3.3.3	Radioactive Absorption Techniques	61
3.3.3.1	X-Ray Absorption Technique	61
3.3.3.2	Beta Ray Attenuation Method	62
3.3.3.3	Microwave Techniques	63
3.3.4	Radioactive Emission Techniques	65
3.3.5	Acoustic Method	67
3.3.6	Ultrasonic Pulse-Echo Method	68
3.4	POINT METHODS	70
3.4.1	Needle Contact Probe	70
3.4.2	Hot-wire Method	73
3.4.3	Shadow Method	75
3.4.4	Fiber-Optic Techniques	76
3.4.5	Light Absorption Techniques	78
3.4.6	Fluorescence Technique	83
3.4.7	Laser Scattering Method	88
3.4.8	Interferometric Methods	91
3.5	SPATIAL METHODS	93
3.5.1	Light Absorption	93
3.5.2	Multiple Electrode Probes	96
3.5.3	Multi-Conductance Probe	99
3.5.4	Pigment Luminance Method	101
3.5.5	Fluorescent Imaging	103
3.5.6	Ultrasonic Transmission	104
3.6	SUMMARY	107

Chapter 4:	THE LIGHT ABSORPTION IMAGING TECHNIQUE	108
4.1	INTRODUCTION	108
4.2	EVOLUTION	108
4.3	METHODOLOGY	114
4.3.1	Theory	114
4.3.2	Experimental Arrangement	115
4.3.2.1	Overview	115
4.3.2.2	Test Section Geometry	115
4.3.2.3	Photographic Arrangement	115
4.3.2.4	Uniform Lighting	116
4.3.2.5	Dyes Used	118
4.3.2.6	Calibration Cell	120
4.3.3	Measurement Procedure	122
4.3.4	Image Analysis	124
Chapter 5:	ANALYSIS OF THE SPATIAL FILM	128
5.1	INTRODUCTION	128
5.2	ANALYSIS OF THE SPATIAL FILM DATA	129
5.2.1	Edge Effects	129
5.2.2	Correction of Rogue Points Caused by Total Light Exclusion	129
5.2.3	Generation of a Histogram of the Spatial Film	132
5.2.4	Categorisation of the Film Data	133
5.2.5	Generation of Histograms for the Disturbance Wave and Substrate Regions of the Film	136
5.2.6	Collation and Analysis of Disturbance Wave and Substrate Film Data Packets	138
5.2.7	Determination of Area and Volume Relationships for the Disturbance Wave and Substrate Film Regions	139
5.2.8	Final Output	139

LIQUID FILM VELOCITY MEASUREMENT

Chapter 6: REVIEW OF THE LITERATURE	141
6.1 INTRODUCTION	141
6.2 VELOCITY PROFILE MEASUREMENT	143
6.2.1 Receiving Vessel Method	143
6.2.2 Ultra Microscope Technique	144
6.2.3 Pneumometric Method	144
6.2.4 Hot-Wire Anemometry	144
6.2.5 Hydrogen Bubble Technique	146
6.2.6 Stereoscopic Photography	147
6.2.7 Mirrored Wall Stroboscopic Particle Visualisation	149
6.2.8 Photochromic Dye Activation Technique	151
6.2.9 Laser Doppler Anemometry	154
6.3 DISTURBANCE WAVE CELERITY MEASUREMENT	157
6.3.1 Fast Stopwatch Method	157
6.3.2 Direct Photographic Measurement	158
6.3.3 Paired Film Thickness Probe Output (Cross-Correlation)	159
6.4 SUMMARY	161
Chapter 7: DISTURBANCE WAVE CELERITY	163
7.1 INTRODUCTION	163
7.2 DIRECT PHOTOGRAPHIC MEASUREMENT	163
7.3 LIGHT ABSORPTION BASED CROSS CORRELATION METHOD	166
7.4 COMPARISON OF THE TWO TECHNIQUES	175

RESULTS

Chapter 8:	AIR-WATER: COMPARISON WITH THE LITERATURE	177
8.1	INTRODUCTION	177
8.2	WATER	178
8.2.1	Experimental Flow Conditions	178
8.2.2	Flow Visualisation	179
8.2.3	Mean Film Thickness	187
8.2.3.1	Free Falling Films	187
8.2.3.2	Falling Water Films with a Co-current Airflow	190
8.2.4	Maximum & Minimum Film Thickness	192
8.2.5	Disturbance Wave Characteristics	196
8.2.5.1	Maximum Disturbance Wave Height	196
8.2.5.2	Disturbance Wave Celerity	197
8.2.5.3	Characteristic Length of Disturbance Waves	199
8.2.6	Base Substrate Film Characteristics	201
8.2.6.1	Mean Substrate Thickness	201
8.2.6.2	Ratio of Mean Substrate Height to Maximum Disturbance Height	202
Chapter 9:	AIR-ORGANICS: THE STUDY OF HYDRODYNAMIC CONDITIONS IN FALLING FILM REACTORS	205
9.1	INTRODUCTION	205
9.2	DODECYLBENZENE	206
9.2.1	Experimental Flow Conditions	206
9.2.2	Flow Visualisation	211
9.2.3	Mean Film Thickness	215
9.2.3.1	Free Falling Films	215
9.2.3.2	Falling Films with a Co-current Airflow	216
9.2.4	Disturbance Wave Characteristics	217
9.2.4.1	Mean Disturbance Wave Amplitude	217
9.2.4.2	Mean Characteristic Length of Disturbance Waves	219
9.2.4.3	Disturbance Wave Celerity	220
9.2.4.4	Fraction of Interface Covered by Disturbance Waves	221
9.2.4.5	Liquid Hold-up Fraction Contained in Disturbance Waves	222

9.2.5	Base Substrate Film Characteristics	223
9.2.5.1	Mean Substrate Height	224
9.2.5.2	Ratio of Mean Substrate Height and Maximum Disturbance Height	224
9.3	ETHOXYLATED ALCOHOL	226
9.3.1	Experimental Flow Conditions	226
9.3.2	Flow Visualisation	231
9.3.3	Mean Film Thickness	235
9.3.3.1	Free Falling Films	235
9.3.3.2	Falling Films with a Co-current Airflow	236
9.3.4	Disturbance Wave Characteristics	237
9.3.4.1	Mean Disturbance Wave Amplitude	237
9.3.4.2	Mean Characteristic Length of Disturbance Waves	238
9.3.4.3	Disturbance Wave Celerity	239
9.3.4.4	Fraction of Interface Covered by Disturbance Waves	240
9.3.4.5	Liquid Hold-up Fraction Contained in Disturbance Waves	242
9.3.5	Base Substrate Film Characteristics	243
9.3.5.1	Mean Substrate Height	243
9.3.5.2	Ratio of Mean Substrate Height and Maximum Disturbance Height	244
9.4	HYDRODYNAMIC EFFECTS OF PHYSICAL PROPERTIES ON INTERFACIAL STRUCTURE	245
9.4.1	Mean Film Thickness	246
9.4.2	Disturbance Wave Characteristics	247
9.4.2.1	Mean Disturbance Wave Height	247
9.4.2.2	Mean Characteristic Length of Disturbance Waves	248
9.4.2.3	Mean Disturbance Wave Celerity	249
9.4.2.4	Fraction of Interface Covered by Disturbance Waves	251
9.4.2.5	Liquid Hold-up Fraction Contained in Disturbance Waves	252
9.4.3	Base Substrate Film Characteristics	253
9.4.3.1	Mean Substrate Height	253
9.4.3.2	Ratio of Mean Substrate Height and Maximum Disturbance Height	254

Chapter 10: CONCLUSIONS AND RECOMMENDATIONS	256
10.1 INTRODUCTION	256
10.2 CONCLUSIONS	256
10.3 RECOMMENDATIONS FOR FUTURE WORK	258
BIBLIOGRAPHY	262
Appendix A: DETERMINATION OF LIQUID PHYSICAL PROPERTIES	277
A.1 DENSITY	277
A.2 VISCOSITY	277
A.3 SURFACE TENSION	278
Appendix B: OPTICAL EFFECTS	280
B.1 INTRODUCTION	280
B.2 LIGHT EXCLUSION FROM THE IMAGE	280
B.3 FILM THICKNESS MEASUREMENT ERROR	284
Appendix C: SUMMARY OF MEASUREMENT DATA	289
C.1 INTRODUCTION	289
C.2 WATER	290
C.2.1 Data from Spatial Film Thickness Measurements	290
C.2.2 Disturbance Wave Celerity Data	294
C.3 DODECYLBENZENE	296
C.3.1 Data from Spatial Film Thickness Measurements	296
C.3.2 Disturbance Wave Celerity Data	302
C.4 ETHOXYLATED ALCOHOL	303
C.4.1 Data from Spatial Film Thickness Measurements	303
C.4.2 Disturbance Wave Celerity Data	306

LIST OF FIGURES

Figure 1.1:	Sulphonation Multi-tube Film Reactor.	2
Figure 2.1:	Schematic of Flow Facility.	8
Figure 2.2:	Photograph of Flow Facility.	9
Figure 2.3:	Photograph of rectangular test section.	10
Figure 2.4:	Photograph of liquid feed arrangement.	12
Figure 2.5:	Photograph of air feed arrangement.	14
Figure 2.6:	Schematic of air distribution section.	15
Figure 2.7:	Schematic of liquid distribution section.	18
Figure 2.8:	Photograph of demister box.	22
Figure 3.1:	Linked valve arrangements for hold-up measurements.	33
Figure 3.2:	Schematic of film conductance measurement components.	34
Figure 3.3:	Schematic diagram of weighing method apparatus.	36
Figure 3.4:	Variants on capacitive thickness sensors.	37
Figure 3.5:	Schematic diagram of differing conductance probe types.	42
Figure 3.6:	Schematic of two-pin electrodes.	43
Figure 3.7:	Schematic of parallel-strip electrodes.	44
Figure 3.8:	Schematic of segmented parallel-strip electrodes.	45
Figure 3.9:	Schematic of concentric electrode.	46
Figure 3.10:	Schematic of ring/rod combination probe.	47
Figure 3.11:	Parallel-Wire Conductance Probe installed on a vertical cylindrical column.	48
Figure 3.12:	Flush wire film thickness measurement circuit.	50
Figure 3.13:	Example of electronic circuitry used in conductance probe application.	51
Figure 3.14:	Inserts calibration device.	57
Figure 3.15:	Static calibration equipment	58
Figure 3.16:	Concept of the calibration method using probabilities.	59
Figure 3.17:	Example of dynamic calibration procedure.	60
Figure 3.18:	X-ray absorption measurement technique.	62
Figure 3.19:	Microwave Waveguide Measurement Section.	64
Figure 3.20:	Microstrip resonating structure used in film thickness measurement.	65
Figure 3.21:	Schematic of column construction for film thickness measurement utilising radioactive emissions.	66
Figure 3.22:	Block diagram of the unit for measuring the thickness of a liquid film by the acoustic method.	67
Figure 3.23:	Ultrasonic liquid-film thickness measurement system and test section geometries.	69
Figure 3.24:	Typical needle contact device used for film thickness measurements.	71
Figure 3.25:	Schematic of a hot wire probe.	73

LIST OF FIGURES

Figure 3.26:	Schematic diagram of the thickness probe.	74
Figure 3.27:	Schematic of film thickness measurements by shadow method.	75
Figure 3.28:	Multi fiber-optic measurement system.	77
Figure 3.29:	Lens and photomultiplier arrangement.	79
Figure 3.30:	Light absorption methodology.	82
Figure 3.31:	Fluorescence technique for film thickness measurement.	83
Figure 3.32:	Rotating calibration cell.	85
Figure 3.33:	Emission spectra of acridine (10 ⁻⁵ moles/l) stimulated by ultraviolet radiation (365 nm).	88
Figure 3.34:	Laser scattering film thickness measurement system.	89
Figure 3.35:	Interferometric film thickness measurement technique.	91
Figure 3.36:	Experimental arrangement for spatial light absorption film thickness technique.	94
Figure 3.37:	Illustration of the required lighting arrangement for the spatial film thickness technique of Clegg (1969).	95
Figure 3.38:	Arrangements of point-electrode probes and probe-clusters of the S-PEP	97
Figure 3.39:	Arrangement of point-electrode probes of the SS-PEP and data-processing system.	98
Figure 3.40:	Multi-conductance film thickness measurement device.	100
Figure 3.41:	Pigment Luminance measurement system and test section.	102
Figure 3.42:	Fluorescent Imaging measurement system.	103
Figure 3.43:	Schematic of ultrasonic transmission device installed in a nuclear fuel rod.	105
Figure 3.44:	Illustration of ultrasonic transmission interpolating operation.	106
Figure 4.1:	Comparison of experimentally determined mean film thickness and predictive equation of Nusselt for falling water film with a stagnant airflow.	110
Figure 4.2:	Falling water film thickness profile along the test section midpoint, beginning approximately 1500mm below the inlet weir. ($u_1 = 2.1$ l/min, $v_g = 0$ m/s)	111
Figure 4.3:	A sample response trace for a localised film thickness measurement, for comparison with Figure 4.2.	112
Figure 4.4:	Schematic of photographic arrangement.	115
Figure 4.5:	Identification of light non-uniformity using image analysis software.	118
Figure 4.6:	Comparison of possible pixel components that could be used in the calibration of a 0.09g/l Biebrich Scarlet (red) dyed dodecylbenzene solution.	119
Figure 4.7:	Image of calibration cell.	121
Figure 4.8:	Determination of characteristic equation for thickness profile along wedge shaped calibration cell.	121
Figure 4.9:	Example of raw image obtained from the digital camera.	122
Figure 4.10:	Three test section images taken in rapid succession under identical flow conditions.	123

LIST OF FIGURES

Figure 4.11:	Illustration of separation of calibration strip and falling film region of interest from the remainder of the superfluous image.	125
Figure 4.12:	A typical calibration curve.	126
Figure 5.1:	Film image with a graphical plot of the unmodified film thickness versus longitudinal distance from top of image for a central strip of the image.	130
Figure 5.2:	Graphical plots of the modified and unmodified film thickness versus longitudinal distance from top of image for a central strip of the image presented in Figure 5.1.	131
Figure 5.3:	Film histogram table and plot generated for the film image in Figure 5.1.	132
Figure 5.4:	Illustration of falling film structure.	133
Figure 5.5:	Histogram tables and plots generated for the disturbance wave and substrate region of film image in Figure 5.1.	137
Figure 5.6:	Sample of sequential disturbance wave packet data for film image presented in Figure 5.1.	138
Figure 5.7:	Example Final Output Sheet for Film Image in Figure 5.1.	140
Figure 6.1:	Illustration of a hot-wire anemometer probe.	145
Figure 6.2:	Hydrogen bubble velocity measurement technique.	146
Figure 6.3:	Stereoscopic camera and test cell arrangement.	148
Figure 6.4:	Measurement schematic for mirrored wall stroboscopic particle visualisation.	150
Figure 6.5:	Experimental arrangement for original photochromic dye activation technique.	152
Figure 6.6:	Optical Arrangement used by Amenitskii et al. (1969).	155
Figure 6.7:	Film sampling channel.	157
Figure 6.8:	Schematic representation of results obtained for a cross-correlation coefficient R12 for a system with constant velocity.	161
Figure 7.1:	Kodak high-speed video camera unit.	164
Figure 7.2:	Typical high-speed camera image.	165
Figure 7.3:	Experimental arrangement utilised for light absorption based cross-correlation technique.	167
Figure 7.4:	Lamp Arrangement.	168
Figure 7.5:	Light Sensor and Housing.	168
Figure 7.6:	Control box electronic circuit.	169
Figure 7.7:	Typical sensor output.	170
Figure 7.8:	Plot showing manual method for individual wave celerity measurement.	171
Figure 7.9:	Cross-correlation coefficients plot to determine most likely disturbance wave transit time.	173
Figure 7.10:	Comparison of results obtained from the two measurement techniques for dodecylbenzene/air system under comparable flow conditions. (Air velocity $\sim 5\text{m/s}$).	175

LIST OF FIGURES

Figure 8.1:	Film images and corresponding spatial film thickness maps for free falling water films with increasing liquid flowrate (left to right). Range of liquid flowrates between 0.11 – 0.89 kg/m s.	180
Figure 8.2:	Film images and corresponding spatial film thickness maps for co-current air-water downflow at constant air velocity (7.4 m/s) with increasing liquid flowrate (left to right). Range of liquid flowrates between 0.11 – 0.89 kg/m s.	181
Figure 8.3:	Film images and corresponding spatial film thickness maps for co-current air-water downflow at constant air velocity (15.2 m/s) with increasing liquid flowrate (left to right). Range of liquid flowrates between 0.23 – 0.89 kg/m s.	182
Figure 8.4:	Film images and corresponding spatial film thickness maps for water falling films at constant liquid flowrate (0.57 kg/m s) with an increasing co-current downflow of air (left to right). Air flowrates 0, 4.9, 10.0, 12.5, 15.2 & 17.4 m/s.	183
Figure 8.5:	Film thickness profiles for a centrally located strip of the free falling images in Figure 8.1.	184
Figure 8.6:	Film thickness profiles for a centrally located strip of the falling film images in Figure 8.2.	185
Figure 8.7:	Film thickness profiles for a centrally located strip of the falling film images in Figure 8.3.	186
Figure 8.8:	Film thickness profiles for a centrally located strip of the falling film images in Figure 8.4.	187
Figure 8.9:	Comparison between current study and literature of free falling film mean film thickness values.	188
Figure 8.10:	Comparison of current mean film thickness data for falling water films with Equation 8.5.	190
Figure 8.11:	The influence of a co-current airflow on mean water film thickness.	191
Figure 8.12:	Comparison of a sample of the current study's mean film thickness data for co-current downflow with the study by Ueda & Tanaka (1974).	192
Figure 8.13:	Illustration of the possible film thickness measurement parameters utilising LAIT. Data presented is for free falling films of current study.	193
Figure 8.14:	Comparison of current data with literature for maximum film thickness for free falling films.	194
Figure 8.15:	Comparison of current data with literature for minimum film thickness for free falling films.	196
Figure 8.16:	Influence of a co-current downflow of air on the averaged maximum disturbance height for a variety of falling liquid film flows.	197
Figure 8.17:	Influence of a co-current downflow of air on disturbance wave celerity for the falling water film flows investigated in the current study.	198
Figure 8.18:	Comparison of the current wave celerity measurements with a sample of the available literature.	199

LIST OF FIGURES

Figure 8.19:	Influence of a co-current downflow of air on characteristic length of disturbance waves for the falling water film flows investigated in the current study.	200
Figure 8.20:	Comparison of characteristic lengths with results reported by Nencini & Andreussi (1982).	201
Figure 8.21:	Influence of a co-current downflow of air on mean substrate thickness for the falling water film flows investigated in the current study.	202
Figure 8.22:	Comparison between studies of ratio of substrate height to maximum disturbance/film height.	203
Figure 8.23:	Influence of a co-current downflow of air on the ratio of mean substrate height to maximum disturbance height.	204
Figure 9.1:	Film images and corresponding spatial film thickness maps for free falling dodecylbenzene films with increasing liquid flowrate (left to right). Range of liquid flowrates between 0.09 – 0.99 kg/m s.	207
Figure 9.2:	Film images and corresponding spatial film thickness maps for co-current air-dodecylbenzene downflow at constant air velocity (7.3 m/s) with increasing liquid flowrate (left to right). Range of liquid flowrates between 0.09 – 0.91 kg/m s.	208
Figure 9.3:	Film images and corresponding spatial film thickness maps for co-current air-dodecylbenzene downflow at constant air velocity (14.7 m/s) with increasing liquid flowrate (left to right). Range of liquid flowrates between 0.15 – 0.52 kg/m s.	209
Figure 9.4	Film images and corresponding spatial film thickness maps for dodecylbenzene falling films at constant liquid flowrate (0.52 kg/m s) with an increasing co-current downflow of air (left to right). Air flowrates 0, 5.2, 7.3, 9.7, 12.2 & 14.7 m/s.	210
Figure 9.5:	Film thickness profiles for a centrally located strip of the free falling images in Figure 9.1.	212
Figure 9.6:	Film thickness profiles for a centrally located strip of the falling film images in Figure 9.2.	213
Figure 9.7:	Film thickness profiles for a centrally located strip of a selection of the falling film images in Figure 9.3.	214
Figure 9.8:	Film thickness profiles for a centrally located strip of a selection of the film images in Figure 9.4.	215
Figure 9.9:	Comparison of mean film thickness values obtained for free falling dodecylbenzene films over the range of liquid flowrates investigated with the prediction of Nusselt (1916).	216
Figure 9.10:	Influence of co-current airflow on mean dodecylbenzene film thickness.	217
Figure 9.11:	Influence of flow conditions on mean dodecylbenzene disturbance wave amplitude.	218
Figure 9.12:	Influence of flow conditions on the mean characteristic length of dodecylbenzene disturbance waves.	219

LIST OF FIGURES

Figure 9.13:	Influence of co-current airflow on the mean dodecylbenzene disturbance wave celerity.	220
Figure 9.14:	Influence of flow conditions on the fraction of the interface covered by dodecylbenzene disturbance waves.	222
Figure 9.15:	Influence of flow conditions on the liquid hold-up fraction of the film contained in dodecylbenzene disturbance waves.	223
Figure 9.16:	Influence of flow conditions on the mean dodecylbenzene base substrate height.	224
Figure: 9.17	Influence of flow conditions on the ratio of mean substrate height and maximum disturbance height.	225
Figure 9.18:	Film images and corresponding spatial film thickness maps for free falling ethoxylated alcohol films with increasing liquid flowrate (left to right). Range of liquid flowrates between 0.09 – 0.76 kg/m s.	227
Figure 9.19:	Film images and corresponding spatial film thickness maps for co-current air-ethoxylated alcohol downflow at constant air velocity (4.9 m/s) with increasing liquid flowrate (left to right). Range of liquid flowrates between 0.09 – 0.76 kg/m s.	228
Figure 9.20:	Film images and corresponding spatial film thickness maps for co-current air-ethoxylated alcohol downflow at constant air velocity (10.0 m/s) with increasing liquid flowrate (left to right). Range of liquid flowrates between 0.09 – 0.28 kg/m s.	229
Figure 9.21:	Film images and corresponding spatial film thickness maps for ethoxylated alcohol falling films at constant liquid flowrate (0.28 kg/m s) with an increasing co-current downflow of air (left to right). Air flowrates 0, 2.6, 4.9, 7.4 & 10.0 m/s.	230
Figure 9.22:	Film thickness profiles for a centrally located strip of the free falling images in Figure 9.18.	232
Figure 9.23:	Film thickness profiles for a centrally located strip of the falling film images in Figure 9.19.	233
Figure 9.24:	Film thickness profiles for a centrally located strip of the film images in Figure 9.20.	233
Figure 9.25:	Film thickness profiles for a centrally located strip of the film images in Figure 8.4.	234
Figure 9.26:	Comparison of mean film thickness values obtained for free falling dodecylbenzene films over the range of liquid flowrates investigated with the prediction of Nusselt (1916).	235
Figure 9.27:	Influence of co-current airflow on mean ethoxylated alcohol film thickness.	236
Figure 9.28:	Influence of co-current airflow on mean ethoxylated alcohol disturbance wave amplitude.	237
Figure 9.29:	Influence of flow conditions on the mean characteristic length of ethoxylated alcohol disturbance waves.	239
Figure 9.30:	Influence of flow conditions on the mean ethoxylated alcohol disturbance wave celerity.	240
Figure 9.31:	Influence of flow conditions on the fraction of the interface covered by ethoxylated alcohol disturbance waves.	241

LIST OF FIGURES

Figure 9.32:	Influence of flow conditions on the liquid hold-up fraction of the film contained in ethoxylated alcohol disturbance waves.	242
Figure 9.33:	Influence of flow conditions on the mean ethoxylated alcohol base film substrate height.	244
Figure: 9.34	Influence of flow conditions on the ratio of mean ethoxylated alcohol substrate height and maximum disturbance height.	245
Figure 9.35:	Comparison plot for the three liquids of mean film thickness versus co-current downflow air velocity at three virtually identical liquid volumetric flow conditions.	247
Figure 9.36:	Comparison plot for the three liquids of mean disturbance wave height versus co-current downflow air velocity at three virtually identical liquid volumetric flow conditions.	248
Figure 9.37:	Comparison plot for the three liquids of mean disturbance wave length versus co-current downflow air velocity at three virtually identical liquid volumetric flow conditions.	249
Figure 9.38:	Comparison plot for the three liquids of mean disturbance wave celerity versus co-current downflow air velocity at three virtually identical liquid volumetric flow conditions.	250
Figure 9.39:	Comparison plot for the three liquids of the fraction of interface covered by disturbance waves versus co-current downflow air velocity at three virtually identical liquid volumetric flow conditions.	251
Figure 9.40:	Comparison plot for the three liquids of the liquid hold-up fraction of the film contained in disturbance waves versus co-current downflow air velocity at three virtually identical liquid volumetric flow conditions.	253
Figure 9.41:	Comparison plot for the three liquids of the mean base film substrate height versus co-current downflow air velocity at three virtually identical liquid volumetric flow conditions.	254
Figure 9.42:	Comparison plot for the three liquids of the ratio of mean substrate height and maximum disturbance height versus co-current downflow air velocity at three virtually identical liquid volumetric flow conditions.	255
Figure 10.1:	Comparison of Pols (1998) prediction of wave structure with data from the current study.	259
Figure A.1:	Comparison of measured viscosity and suggested values of Talens (1999) versus temperature.	278
Figure B.1:	Film image displaying total exclusion of light at much of the leading edge wave-substrate boundaries.	281
Figure B.2:	Trigonometrically based analysis of the standard photographic arrangement.	281
Figure B.3:	Schematic of the angle subtended by the edge of the light box.	283

LIST OF FIGURES

Figure B.4:	Graphical summary of the influence of the angle subtended by the edge of the light box on maximum allowable interface contact angle.	283
Figure B.5:	Trigonometrically based analysis of the non-standard photographic arrangement.	285
Figure B.6:	Measurement error (y/z) as a function of interface contact angle (θ).	286
Figure B.7:	Comparison plot of a sample of raw and corrected film thickness data after application of the correction for light arrangement induced measurement error.	288

LIST OF TABLES

Table 2.1:	Physical properties of the liquids under study at 20°C.	23
Table 3.1:	Summary of reviewed film thickness measurement techniques.	31
Table 4.1:	Specific dyes and their concentration applied in the current study.	120
Table 6.1:	Summary of reviewed liquid film velocity measurement techniques.	141
Table 8.1:	Range of experimental flow conditions employed for the investigation of water films.	178
Table 9.1:	Range of experimental flow conditions employed for dodecylbenzene films	206
Table 9.2:	Range of experimental flow conditions employed for ethoxylated alcohol films.	226
Table A.1:	Density values at 20°C.	277
Table A.2:	Liquid Surface Tension at 20°C.	279

Chapter 1

INTRODUCTION

The purpose of this chapter is to review the motivation and objectives of this study and detail the structure of this thesis.

1.1 MOTIVATION BEHIND STUDY

Falling film reactors are jacketed columns or clusters of columns where liquid and gas flow in annular or annular-mist flow. The gas phase is a mixture of a gaseous or vaporised reagent diluted with an inert carrier. Figure 1.1 presents a commercially available multi-tube film sulphonation reactor, utilised extensively in the manufacture of detergents. The figure shows the multiple reaction tube structure, where a thin organic reactant liquid film falls down, and completely wets, the internal walls while contacting a continuously fed inert gas-SO₃ vapour mixture travelling co-currently along the centre of the tubes. The SO₃ diffuses radially through the inert gas and reacts exothermically with the organic film to produce the sulphonic acid product, which dilutes and travels along with the reactant film. The reaction heat is primarily removed by a cooling water jacket, which encases the reactor tubes, however, a proportion of the reaction heat will also raise the temperature of the liquid film. The product, non-reacted organic feed and exhaust gas are removed from the lower outlet for separation and further treatment.

It is clear from the figure that falling film reactors are a very effective geometry in which to carry out fast exothermic gas-liquid reactions, because they allow easy removal of the heat produced. Currently, their industrial relevance lies in established applications in both sulphonation and chlorination; however, there is growing interest in their application for a wider range of reactions. This interest is motivated by the recent trend in the chemical industry for the substitution of traditional batch processes by continuous equivalents, in order to improve the reaction progress and safety conditions.

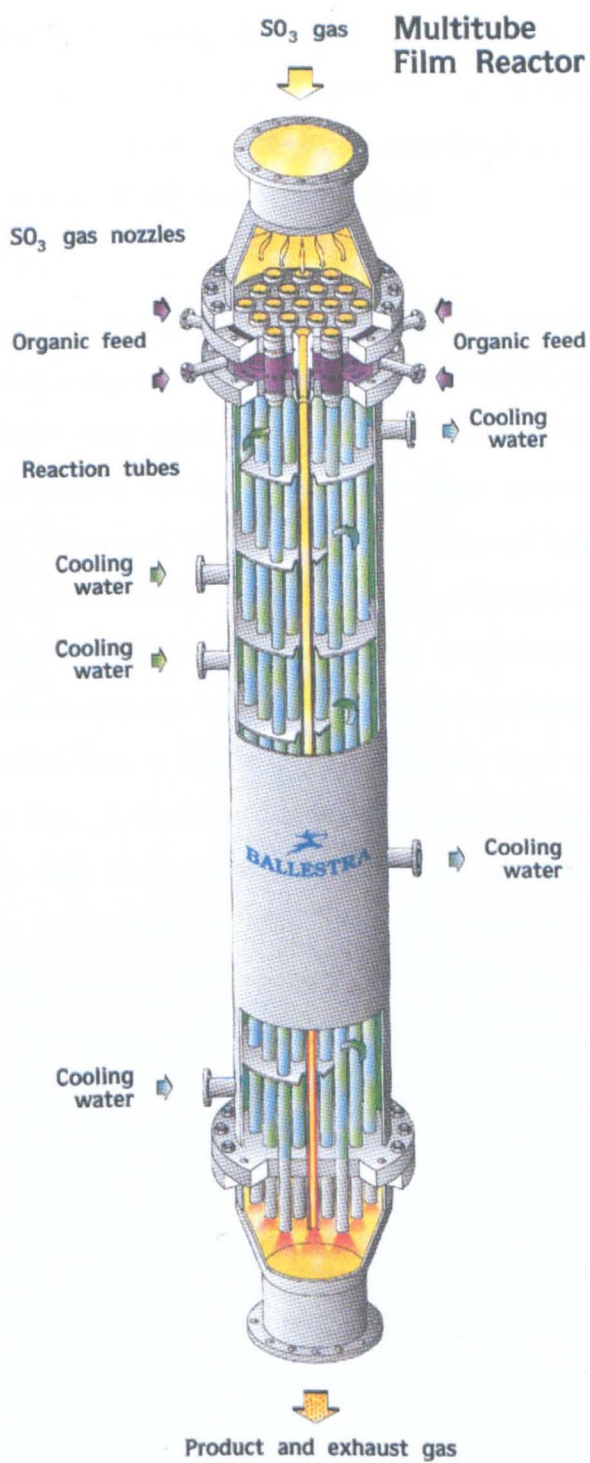


Figure 1.1: Sulphonation Multi-tube Film Reactor.

(Courtesy of Ballestra Sulphurex F Catalogue (1996))

The outstanding heat removal capabilities displayed by falling film reactors and recent improvements in catalyst technology have lead to the possibility of milder reaction conditions during reagent mixing than encountered in stirred batch reactors. Example reaction systems where this substitution is being considered are ethoxylation (Dicoi & Canavas (1993), Talens *et al.* (1998)) and hydrogenation.

To optimise and improve falling film reactors, soundly based physical models are required. Early models proposed by Johnson & Crynes (1974) and Davis *et al.* (1979) have been criticised for their assumption that the reaction takes place only at the interface, which is not borne out by observation. More recent models proposed by Gutiérrez *et al.* (1988), Dabir *et al.* (1996) include the effects of heat and mass transfer as well as reaction. However, these models assume a spatially averaged liquid film combined with empirically-determined mass transfer coefficients, but there is growing evidence that this is unsatisfactory, since the interface is dominated by ripples and larger disturbance waves which have a significant effect on the mass and heat transfer rates through and into the film. A further weakness with these empirically determined mass transfer coefficients is their development from studies on aqueous films, whose physical properties bear little resemblance to the industrially relevant organic films. Most recently, Talens (1999) reports some success with a new modelling approach where interfacial effects are associated with a roughness factor. However, as the author himself points out, the approach still utilises a spatially averaged film thickness whose accuracy is strongly dependent on gas-liquid flow conditions.

Clearly, if sound spatial knowledge of the hydrodynamics of falling film systems typical of these reactors were available, then the potential benefits in future modelling of these reactors would be enormous.

1.2 STUDY OBJECTIVES

The main objective of this study was the better understanding through experimental study of the interfacial characteristics of liquid falling films in the presence of a co current down flow of air, with emphasis on the physical and hydrodynamic conditions encountered in current falling film reactor technology, so that the information obtained

could be implemented in the enhancement of falling film reactor modelling. To meet this objective required the following steps:

- (i) Design, construction and commissioning of a purpose built flow facility to undertake the experimental investigation.
- (ii) Identification/design and implementation of measurement techniques to facilitate collection of the desired experimental data.
- (iii) Development of techniques to analyse and present the raw experimental data.
- (iv) Review the results obtained and comment on their significance.
- (v) Draw any conclusions from the study and make recommendations for future studies.

1.3 THESIS STRUCTURE

There are ten chapters (including this introduction) and three appendices:

Chapter 2 provides an overview of the experimental flow facility constructed for this study, including a detailed description of the individual components of the flow facility, the liquids under study, normal operating procedures and maintenance strategies.

Chapter 3 presents a critical review of alternative liquid film thickness measurement techniques with emphasis on their applicability to the film thickness measurement of falling films in the presence of co-current airflow, the flow regime of the current work.

Chapter 4 demonstrates how a novel adaptation of the light absorption based spatial film thickness technique, *i.e.* the Light Absorption Imaging Technique (LAIT), can be applied to obtain thickness information for a spatial region of a vertically falling film in both free falling and co-current flow systems.

Chapter 5 reviews the computer algorithm utilised in the analysis of the spatial film data generated by LAIT.

Chapter 6 presents a critical literature review of alternative liquid film velocity measurement techniques and summarise their suitability for application in the current study.

Chapter 7 describes in detail the methodology of the two time of flight based techniques applied in the measurement of one particular aspect of the liquid film velocity, the mean celerity of the large disturbance wave structures that are encountered travelling along the slower moving base film substrate.

Chapter 8 presents a selection of the experimental results obtained for wavy, vertical water films in both free falling and co-current air systems, that were primary utilised as a means of validation of the techniques employed in this study by comparison with the considerable data available for air-water systems in the literature.

Chapter 9 presents a selection of the experimental results obtained for wavy, vertical dodecylbenzene and ethoxylated alcohol films in both free falling and co-current air systems. The chapter also investigates the influence of the physical properties of the liquids on film interfacial characteristics by comparison of a sample of the results obtained for each liquid at similar flow conditions.

Chapter 10 suggests conclusions that can be drawn from this study and provides recommendations for future work.

Appendix A presents a detailed description of the methodology for acquisition of the physical properties (*i.e.* density, viscosity, surface tension) of the fluids utilised in this study.

Appendix B reviews the number of investigations undertaken into potential limitations of the light absorption film thickness measurement technique employed in the current work due to optical phenomena.

Appendix C provides a summary of the spatial film thickness and wave celerity data obtained for the three investigated liquids.

Chapter 2

EXPERIMENTAL FLOW FACILITY

2.1 INTRODUCTION

As stated in Chapter 1, the main objective of this work was an experimental study of the interfacial characteristics of falling liquid films in the presence of a co-current down-flow of air. This chapter describes the design, construction and commissioning of the experimental facility to carry out this work. Many of the design features were based on the recommendations of an internal report by Dr Frederico Talens, whose encouragement and assistance is acknowledged.

2.2 OVERVIEW OF THE FLOW FACILITY

The final revision of the experimental flow facility employed in this study is presented schematically and photographically in Figure 2.1 and Figure 2.2 respectively.

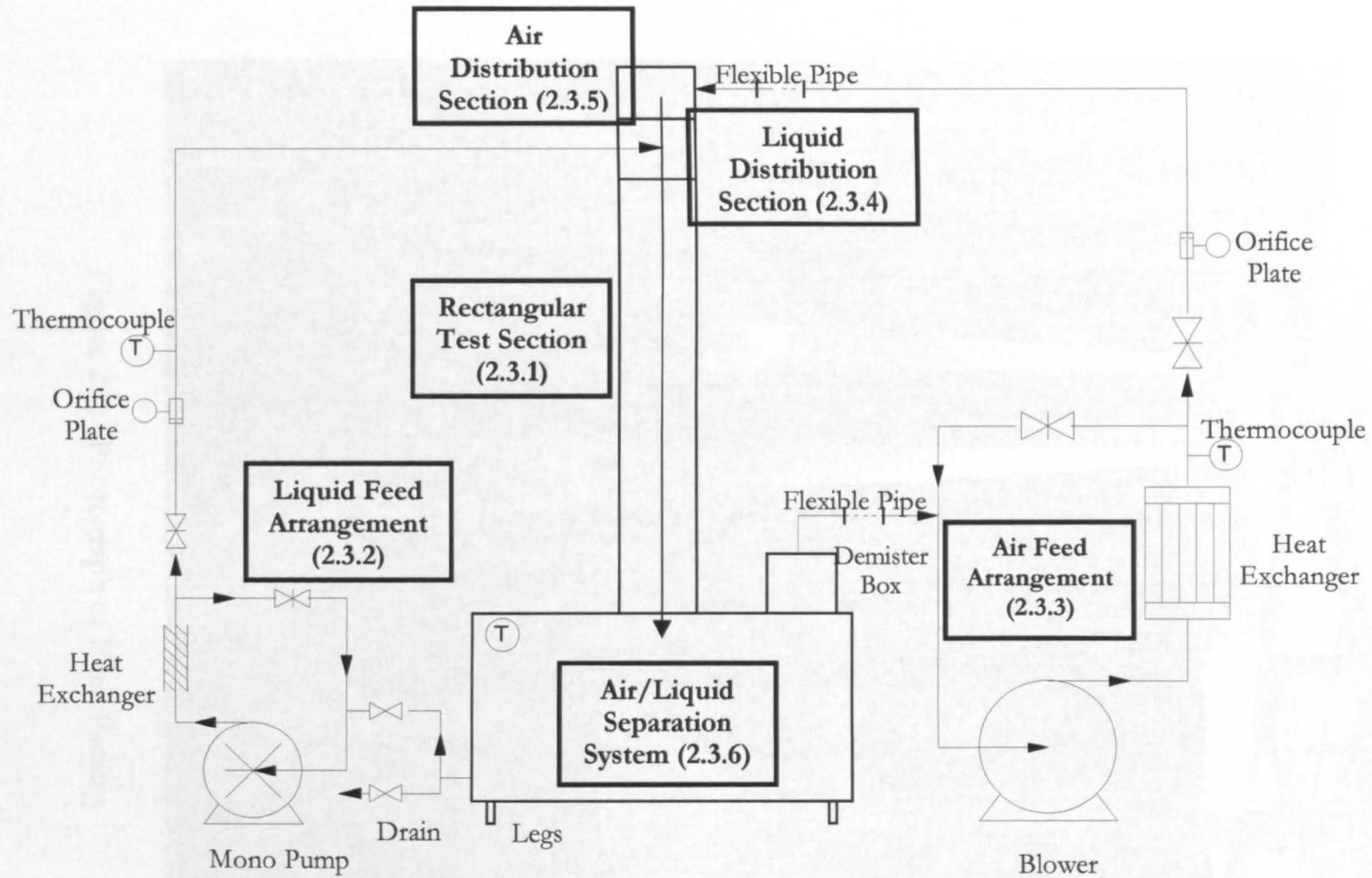


Figure 2.1: Schematic of Flow Facility.



Figure 2.2: Photograph of Flow Facility.

2.3. FLOW FACILITY COMPONENTS

2.3.1 Rectangular Test Section

Falling film reactors are predominantly of tubular design. However, this geometry is unsuitable for the application of optically based measurement methods, and in particular the light absorption imaging technique applied in this study, for the following reasons:

- (i) Light curvature due to the curvature of the tube.
- (ii) Light must pass through the liquid film twice on its journey through the tube.

These difficulties were avoided by the application of a rectangular geometry, where the falling liquid film was generated in such a manner that it was only allowed to flow on one of the surfaces. This configuration has the additional benefit of permitting an unobstructed view of the air/liquid interface, an essential requirement of the photographic aspect of the light absorption imaging technique. The actual test section employed is shown photographically in Figure 2.3.

The rectangular test section consisted of two sheets of 6mm thick toughened plate glass, 2000mm high by 153mm wide, sealed at the edges by a 13mm gap provided by plastic spacer strips. The height of the test section was determined by the available room height. The edges of the plate glass were ground flat at the point of



Figure 2.3: Photograph of rectangular test section.

manufacture to ensure a uniform surface for film contact. A metal frame supported the plates and spacers, and held them together using a number of metal bolts located along the metal frame perimeter. This configuration was designed for easy disassembly/reassembly of the test section to allow access to the internal surfaces of the glass plates for cleaning (see Section 2.6.1). The complete rectangular test section was held firmly in place with large angled brackets, attached to the plastic spacers, and fastened to the air/liquid separation tank located below it. Brackets between the ceiling and the air and liquid feed systems located above, and sitting on, the rectangular test section, provided further support. Vertical alignment of the test section was monitored using a spirit level, and was corrected by small adjustments to the height of the respective nut on the thread of the air-liquid separator tank “legs”.

2.3.2. Liquid Feed Arrangement

The liquid feed arrangement is shown photographically in Figure 2.4

Liquid was pumped to the liquid distribution system (Section 2.3.4), through 25mm i.d. copper pipe, by a mono positive displacement pump (Mono Pumps Ltd, Model D100L) from the air/liquid separation tank outlet. The pump was selected to provide sufficient capacity for the range of liquid flow conditions under study, and a recycle arrangement was incorporated into the feed pipe work using the system of gate valves shown in the design schematic (Figure 2.1). The recycle arrangement aided in flow regulation to the test section and allowed more sensitive changes in liquid flow conditions, by manipulation of the gate valves open level, than could be achieved by means of a conventional liquid feed.

Due to the relatively viscous nature of the organic liquids utilised during this study, some heating effects by the pump were anticipated. Therefore, in an effort to ensure the stabilisation of the liquid feed temperature, a heat exchanger was incorporated into the feed arrangement. This exchanger simply consisted of a 38mm copper pipe that encased approximately 330mm of a vertical section of the 25mm feed pipe, with cooling water flowing in the space between them. The exchanger was positioned after the pump outlet yet within the liquid recycle loop to ensure complete heat dissipation even at small

flowrates, where the liquid recycled to the pump was significantly larger than the flow to the test section.



Figure 2.4: Photograph of liquid feed arrangement.

A rotary piston flowmeter (KDG Ltd) was fitted to measure the liquid flowrate to the test section due to the proven ability of such meters to accurately measure volumetric flowrates of relatively viscous liquids. However, the rotary piston flowmeter installed was unsuitable to measure accurately small water flowrates, as the viscosity of water was at the lower end of the flowmeter's operating range. Also, because this flowmeter measures volume displacement rather than flow, it was necessary to time the movement of the dial over several minutes to obtain accurate readings. This is tedious, and makes it impossible to make accurate adjustments of the flow, so an orifice plate was designed to British Standards (BS 1042) and installed into the liquid feed line, with a manometer to

read the recorded pressure drop. A number of varying orifice plate diameters were used, depending on the flow range. The manometer was an inverted u-tube connected to the orifice plate tappings by lines filled with the liquid under study. A travelling microscope was made available, when necessary, for accurate measurement of small level differences (in the order of a few millimetres), encountered at the very lowest liquid flowrates. The rotary piston flowmeter was retained in position, and served as an invaluable tool in determination of the accuracy of the orifice plate under viscous conditions. A thermocouple was located after the orifice plate to allow the visual monitoring with a digital display of the liquid feed temperature into the test section. Careful monitoring of liquid feed temperature was particularly relevant in the case of the organic liquids, whose viscosities are especially sensitive to temperature fluctuations (see Appendix A).

2.3.3 Air Feed Arrangement

The air feed arrangement was designed in a similar manner to the liquid feed arrangement (Section 2.3.2), and is shown photographically in Figure 2.5.

To prevent problems with vapour loss and/or absorption of moisture when using organic liquids, the air was circulated in a closed loop of 75mm copper pipe by means of a 15kW blower (Secomak model – CL84/1) selected to provide adequate flows for the current work and any future experiments with this equipment. Using a conservative estimate of the head loss, the maximum air velocity in the test section, according to the manufacturer's data sheets, should be seventy metres per second, well above current requirements. A recycle loop helps control airflow to the test section. A temperature rise of up to sixty degrees could be expected through the blower, so a heat exchanger was fitted within the loop to the blower (made to order by Serck Marston), consisting of finned copper tubes carrying cooling water, with air on the shell side. An audible flow alarm was installed on the cooling water feed to warn of interruption of the cooling water supply and allow adequate time for shut down of the equipment. Temperature of the air supply was monitored by a digital display connected to a thermocouple installed in the air cooler outlet. Air flowrate was measured by an orifice plate, with the pressure drop recorded from a kerosene filled manometer, designed and positioned to British standards (BS1042). A bracket connected to the room ceiling, for extra rigidity, supports the air feed arrangement.



Figure 2.5: Photograph of air feed arrangement.

To minimise vibrational noise from the blower, flexible pipe sections were installed in both the inlet and return pipes to the test section, as shown in Figure 2.1.

2.3.4 Air Distribution Section

Uniform airflow distribution to the test section is critical to the observation and quantitative measurement of flow phenomena. It was achieved by the fluid distribution section shown schematically in Figure 2.6.

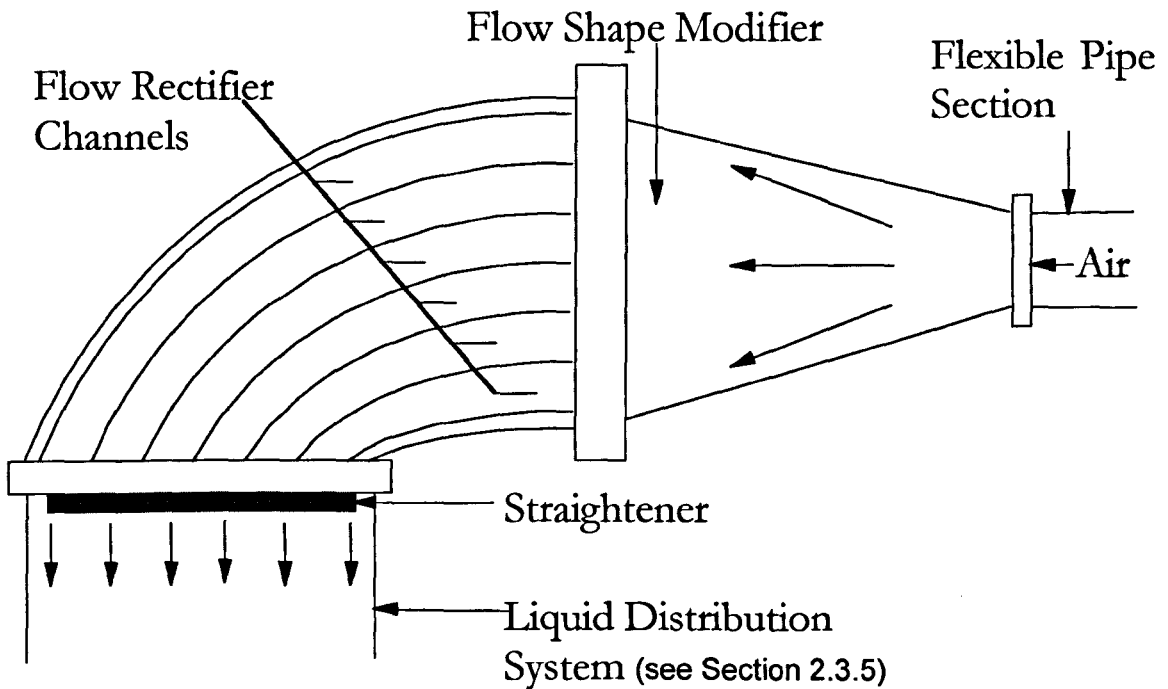


Figure 2.6: Schematic of air distribution section.

Air enters into the flow shape modifier through the flexible pipe section attached to the 75mm (3") copper pipe from the air feed arrangement (Section 2.3.3). The flow shape modifier was simply a shaped section of plastic moulded so that it gradually adapts the tubular flow into the rectangular cross-section flow required by the test section, and can be said to be analogous to the end of an extension pipe commonly found on vacuum cleaners. The airflow then passes into the flow rectifier channels, constructed of six Perspex rectangular channels, of equal cross section, moulded and glued together to form the bend shown in the figure. The purpose of these rectifier channels was to lessen the acuteness of the change in flow direction and attempt to equally distribute volumes of the airflow along the entire flow profile. The flow then enters the liquid distribution box after passing through a short (approximately 10mm deep) honeycombed cardboard strip for final straightening. The air distribution section was secured on top of the liquid

distribution box by metal bolts and given additional support by a bracket from the room ceiling. The tension of this bracket was slightly adjustable, to prevent adjustments to the alignment of the test section using the air/liquid separator legs from exerting potentially damaging strain on the flow facility.

During the commissioning stage, the success of the section at providing a uniform, straightened airflow distribution was investigated, by the introduction of a traversing pitot tube into the liquid distribution box. Initial flow distribution was observed to be poor, with most of the flow passing through the inner rectifier channels. This maldistribution was corrected by the trial and error addition/removal of small amounts of wire wool into the inlets of the rectifier channels and measurement of the resulting flow distribution. The flow distribution provided by the chosen wire wool arrangement still fluctuated around the mean flow point, which is consistent with this type of channelled flow, but there was little evidence of a serious maldistribution, such as a marked gradient profile along the horizontal axis. Additionally, observation of individual small waves across the horizontal axis of the test section show little evidence of their being more accelerated in certain regions of the test section, suggesting any residual maldistribution was short lived.

2.3.5 Liquid Distribution Section

Uniform distribution of the liquid film was probably the single most challenging aspect of the experimental application of this flow facility, and the uniform introduction of the liquid film has been an important design criteria since studies on such flows began. Review of the literature suggests several approaches:

- (i) A porous sinter inlet. (*e.g.* Stainthorp & Allen (1965), Stainthorp & Batt (1967), Webb (1975), Nencini & Andreussi (1982), Wasden & Dukler (1992), Mudawar & Houpt (1993a, b))
- (ii) A weir. (*e.g.* Dukler & Bergelin (1952), Jackson (1955), Portalski (1963), Portalski & Clegg (1972), Salazar & Marschall (1978a, b), Strumulo *et al.* (1985), Karapantsios *et al.* (1989), Lacey *et al.* (1991))

- (iii) A slit-type distributor. (*e.g.* Belkin *et al.* (1959), Ishigai *et al.* (1972), Chu & Dukler (1974, 1975), Takahama and Kato (1980), Aragaki *et al.* (1987))
- (iv) A quick shut-off valve. (*e.g.* Ueda & Tanaka (1974))
- (v) A nozzle. (*e.g.* Takahama *et al.* (1983), Ambrosini *et al.* (1996, 1998))

Considerable practical experience in the measurement of gas/liquid flows by the supervisors of this project has indicated the potential for approach (i) to be troublesome, particularly with relatively viscous liquids. The major difficulty they have encountered is pore blockage, caused by build-up of foreign material. Approach (v) was also discounted for similar reasons. Approach (iv) was discarded as unnecessarily complicated as no plans existed for utilisation of the facility for hold-up measurement methods. Little difference in the advantages/disadvantages of approaches (ii) & (iii) was obvious, therefore, the former approach was selected as there are several examples in the literature of its successful application in rectangular geometries similar to the one applied in this study. These include the study of Clegg (1969), which served as the basis of knowledge for the light absorption film thickness measurement technique developed for the current study.

The liquid distribution system, shown schematically in Figure 2.7, was encased in a clear Perspex box (approximately 180mm (H) x 165mm (W) x 125mm (D)) that was mounted on top of the rectangular test section. Clear Perspex was used as the material of construction for this box to allow visual inspection of the performance of the liquid distribution and air contact. This was a significant advantage, particularly at the commissioning phase. The liquid enters the distribution box through the liquid inlet, which was gauzed in order to prevent the randomly packed 12mm (1/2") ceramic beads escaping down the liquid feed. An underflow weir maintains the bulk of the ceramic beads in position at the liquid inlet, with both beads and underflow weir provided in an effort to even out film flow before entry into the test section. The liquid passes over a knife-edge weir, ground and polished smooth at approximately a forty five degree angle to prevent the development of artificial flow phenomena, and contacts with the air stream, if present, before flowing down on to the inner surface of one of the rectangular section glass plates. The top edge of this glass plate and the bottom of the plastic weir section strip were ground flat after installation to ensure a uniform transition surface.

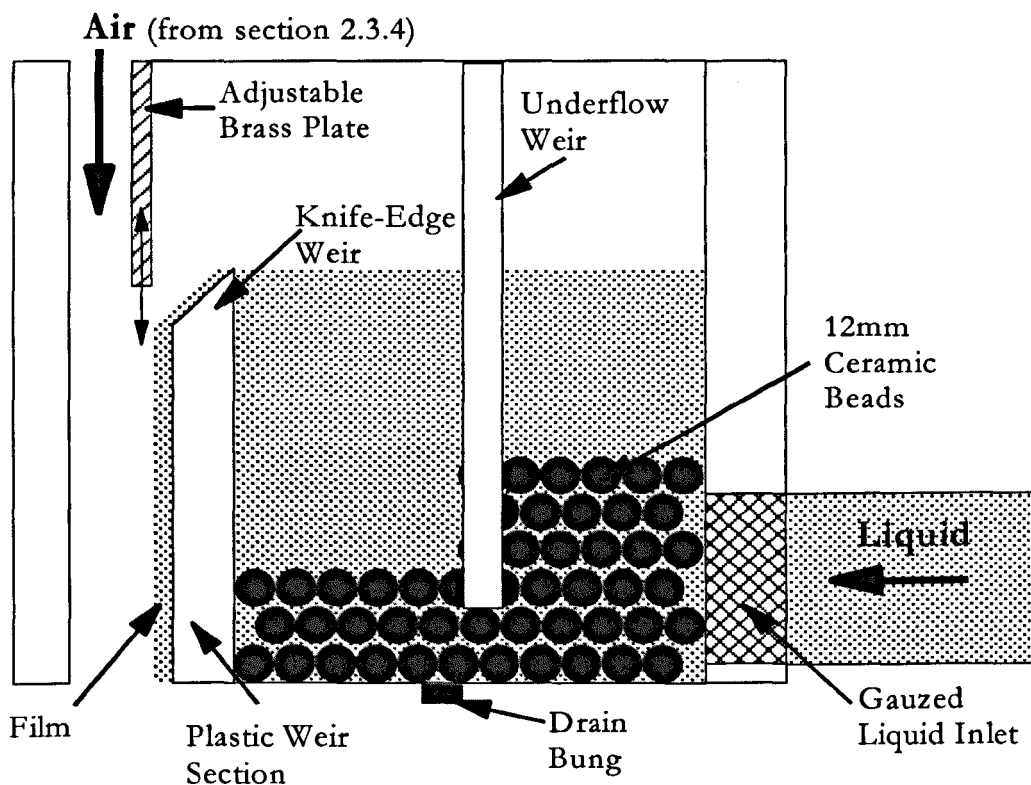


Figure 2.7: Schematic of liquid distribution section.

During commissioning of the flow facility, it was observed that jetting of the liquid over the weir on to the far glass plate occurred at high water flowrates. To combat this phenomenon a brass plate was installed in the distribution box. It was designed to be vertically adjustable in order that at high water flowrates it could be lowered in front of the weir, thus preventing liquid contact on the far side plastic section, and ultimately the far side viewing glass plate, and also reduce horizontal momentum for the falling film. A pair of guided screws made the vertical adjustments in brass plate position. The screws were designed to have a degree of movement within their tracks to allow small adjustments to the brass plate's vertical alignment to allow adjustment of the initial point of contact between liquid and air streams. However, the jetting phenomenon was not observed at any flowrate when the organic liquids replaced the water as the experimental fluid, and consequently the brass plate was removed during their study.

Another observation during commissioning was that solid contaminants and corroded metal particles, from the water and pump lining respectively, accumulated and settled in

the bottom of the distribution box. This settling feature of the distribution box was beneficial, although unintentional, as it allowed the continual removal of a large proportion of the unwanted solid contaminants from the system, and prevented much of the contaminants from travelling over the weir and interfering with measurements along the falling film. Removal of the contaminants from the distribution box was achieved periodically through the drain bung, primarily installed to allow draining of the box, and removal of the beads for cleaning, during liquid changeover.

Visual observation of the free falling liquid film allowed qualitative determination of the relative success or failure of obtaining a uniform liquid distribution, whilst horizontal film thickness distribution data obtained using the spatial film thickness measurement technique described in Chapter 4 provided a more quantitative approach. Success varied with the liquid under study, with the relatively viscous, low surface tension organic liquids providing a uniform distribution with little or no manipulation of the test facility. However, the relatively high surface tension characteristics of water ensured that obtaining complete wetting of the test surface at the lower liquid flowrates under study was not without difficulty. The gradual reduction of a high liquid flowrate to the desired flowrate was found to encourage continued wetting of the flow surface, and was employed in many instances. Additionally, when using water as the test fluid, a meniscus effect was observed over the knife-edge weir, which tended to create localised streaming of the liquid over the weir onto the test surface. However, visual observation showed that this streaming phenomena was short lived, with a more uniform distribution usually developing early on the journey down the test section, with the exact development distance dependent on flow conditions. At high water flowrate conditions it was observed there was a tendency for the film to wet the plastic spacer sides of the rectangular test section and ultimately to partially wet the viewing glass plate. Unfortunately, the introduction of a dynamic airflow only served to exacerbate this problem. This phenomenon limits the range of liquid and gas flows at which reliable quantitative interfacial data can be obtained, and the following approaches were attempted to eliminate it, or at the least, to extend the range of liquid flowrates that could be investigated:

- (i) The addition of plastic vanes on the plastic weir section (Section 2.3.5) to gently guide the liquid film away from the perimeter before entry into the rectangular test section. This approach was observed to have little influence on the phenomenon other than to lower the point along the test section at which initial wetting of the viewing glass plate begins. Additionally, visual observation showed that the plastic guide strips caused small artificial longitudinal flow currents across the liquid film that appeared to disrupt the natural formation of interfacial structure within the entry region of the rectangular test section. For this reason, the use of the plastic vanes was abandoned.
- (ii) The internal surfaces of the plastic spacer strips that constitute the sides of the rectangular test section were painted with a matt black paint. This was an attempt to inhibit the wetting characteristics of the plastic spacers and consequently act as a barrier to wetting of the viewing surface. This approach was observed to be successful at slightly extending the range of unaffected water flowrates.

Similar expansion of the liquid film onto the periphery of the viewing surfaces was also observed when utilising the organic liquids, with the air flowrate required for the onset of wetting of the viewing plate lowered significantly by increases in the viscosity of the film.

2.3.6 Air/Liquid Separation System

For the development of a closed system a method of separation of the two-phase air/liquid mixture and reintroduction of the single phases into their respective feed arrangements was required. As both the falling liquid film and air stream fall as continuous phases, the difficulty entailed in this separation was predominately the elimination or significant reduction of the remaining air in the liquid phase (*i.e.* bubbles) and liquid within the air phase (*i.e.* entrainment) after bulk separation of the phases. However, it was also necessary to prevent the falling liquid film from plunging into the liquid pool, which would cause significant extra air entrainment, which is hard to remove, especially in viscous liquids. Removal of bubbles from the liquid and drops from the air is essential otherwise both the mono-pump and the blower would suffer reduced efficiency, if not damage.

The major component of the implemented air/liquid separation system was a plastic vessel (600mm(W) x1500mm (L) x450mm (H)), located beneath the rectangular test section and sat on four adjustable legs used in alignment of the experimental test section. The liquid was returned to the mono positive displacement pump by piping at the bottom of the vessel with the airflow leaving at the top of the vessel. Sizing of this vessel was based on two criteria:

- (i) Ensuring the tank volume was sufficient to provide an estimated liquid residence time of ten minutes. This amount of time was considered long enough to allow the majority of air bubbles trapped in the liquid phase to make their way to the interface and escape.
- (ii) Providing sufficient volume above the bulk liquid to contain the airflow and limit mixing of the phases.

The air/liquid mixture enters the vessel through a rectangular segment cut out of the vessel lid and was diverted approximately forty-five degrees from the vertical by a plastic ramp. The ramp was incorporated into the design to prevent direct vertical plunging of the two-phase mixture into the bulk separation liquid, which would significantly increase bubble formation. A thermocouple was positioned on the ramp within the separator to monitor visually with a digital display the bulk temperature of the liquid returning to the separator, to aid in determination of the onset of stable temperature flow conditions. The vessel lid was manufactured from clear Perspex, as it was thought at the design stage that it would be beneficial to be able to visibly determine the separation effectiveness. In practice, however, a thin film of entrained liquid was permanently located on the lid obscuring internal viewing of the vessel. A drain valve was located on the feed to the mono pump for application when changing liquid inventories.

Liquid entrainment in the air phase was combated by the addition to the flow facility of a demister box (300mm(W) x450mm (L) x180mm (H)), positioned on top of the separation vessel over the air outlet and shown photographically in Figure 2.8.

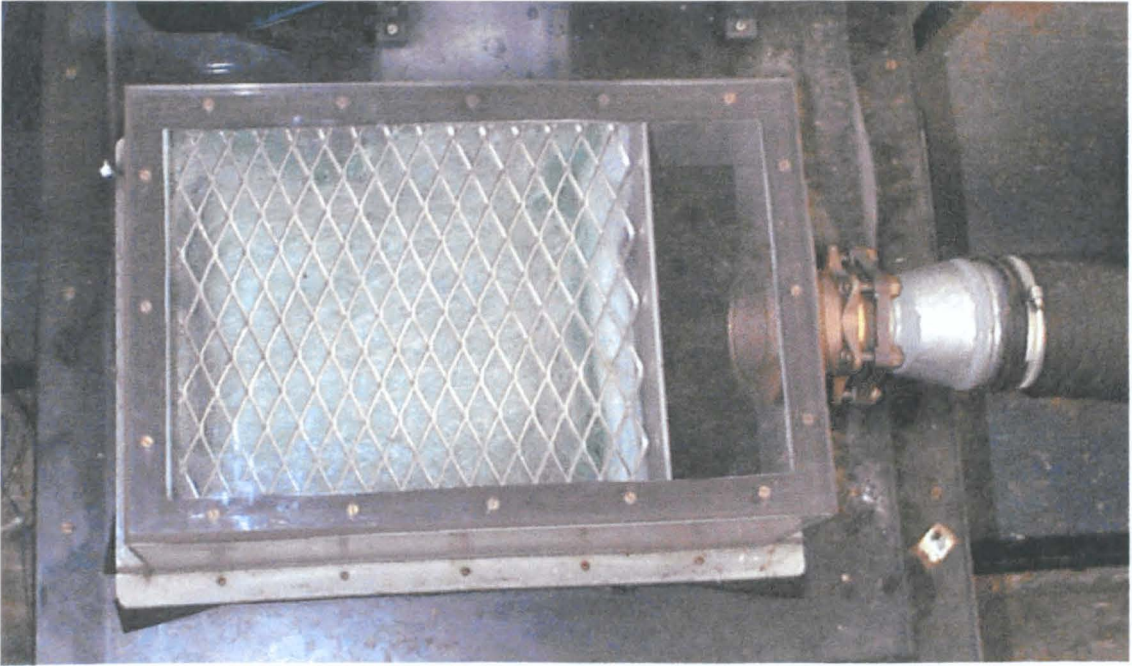


Figure 2.8: Photograph of demister box.

The box was filled with plastic meshing, used to capture the entrained liquid on the meshing fibres as it passes through the box towards the air blower feed. The wetting characteristics of the meshing were periodically checked to ensure that complete saturation had not occurred, as this would signal the removal of virtually any protection of the air blower from entrained liquid.

2.4 LIQUIDS UNDER STUDY

For the study of physical and hydrodynamic conditions encountered in falling film reactors it is important that the choice of liquids in this study reflect the physical properties of actual falling film reactor liquids. Therefore, after consultation with our industrial collaborators, Unilever Research Ltd, and review of the literature of previous modelling studies it was decided to use the liquids given in Table 2.1.

Table 2.1 presents the physical parameters of the liquids at a typical experimental temperature (20°C). A detailed description of the acquisition/derivation of these physical properties is presented in Appendix A. Water was chosen as the commissioning liquid, and to permit comparison with the literature, where the vast majority of hydrodynamic data available is for air/water systems. Dodecylbenzene and Ethoxylated

Lauyl Alcohol are common sulphonation/sulphation feed stocks, supplied to this study by Unilever Research Ltd. Dodecylbenzene was deemed particularly appropriate for application in this current study, as the sulphonation of this organic liquid is the basis of all recent published theoretical modelling of falling film reactors (*e.g.* Gutierrez *et al.* (1988), Dabir *et al.* (1996), Talens (1999)). The varied physical properties of the three liquids provided an ideal opportunity to investigate in detail their influence on falling film hydrodynamic properties and structure.

Table 2.1: Physical properties of the liquids under study at 20°C.

	Density / kg m ⁻³	Viscosity / mPa s	Surface Tension / N m ⁻¹
Water	1000	1	0.072
Dodecylbenzene	830	7	0.0315
Ethoxylated Alcohol	860	20	0.0325

2.5 OPERATING PROCEDURE

This section is included to review the operating procedures of the flow facility.

2.5.1 Start-Up

The procedure for start-up was as follows:

- (i) **Establish Liquid Film.** The mono pump was turned on after ensuring that the feed gate valve and recycle gate valve are fully closed and open respectively. This enables the liquid to re-circulate freely within the recycle pipework, including through the heat exchanger, limiting liquid heating and mechanical wear during the start-up process. The feed gate valve was then carefully opened in small increments until a flow on the manometer/rotary piston flowmeter was observed. At this point further opening of the valve was suspended until a small flow was witnessed crossing the weir and entering the rectangular test section. The reason for this cautious approach was to prevent

jetting of the initial liquid film over the weir and onto the viewing surface, as this could result in abandonment of the experimental run for cleaning and drying of the viewing surface. Further opening of the feed gate valve then continued until the valve was approximately three quarters open, followed by measured closing of the recycle valve to establish a high flowrate liquid film. No further adjustments were made to the flow conditions for several minutes to ensure complete wetting of the glass flow plate and allow thermal fluctuations in the liquid film to stabilise. Once these conditions were believed to have been met the liquid flowrate was then reduced to the approximate value required for the current experimental run, as indicated by the manometer. It was observed that for the liquid feed valve arrangement of this facility the recycle valve was best suited to large adjustments to the flowrate whilst the feed valve could be used in conjunction with it for final sensitive adjustments.

(ii) **Introduction of the airflow.** Once the required value for the liquid feed rate had been approximately met, the blower was activated after ensuring, as with the start-up of the liquid feed, that the feed and recycle valve were fully closed and open respectively. The airflow was then set to the desired flowrate in a similar manner to the liquid flow, *i.e.* open feed to three quarters, followed by incremental closing of the recycle where necessary. At this point final adjustment to the liquid flowrate was made as the airflow into the test section was observed to have a non-trivial influence on its value.

With the desired liquid and air flowrates established, the flow regime was given time, of the order of a few minutes, to develop and for an approximate thermal equilibrium to be created between the phases. As the cooling water for the heat exchangers is obtained from an external source whose temperature is controlled by atmospheric conditions and the intermittent usage by others, temperature drift was common and monitored on the digital display from the strategically located thermocouples. Additional heating of the phases over long periods of time of the running flow facility, believed to have been caused by the lighting used in the photographic aspects of this study, was also recorded. The required measurements could then be undertaken and flowrates adjusted to the appropriate level for the next measurement using the methodology of valve adjustment detailed in the start-up procedure.

2.5.2 Shut-down

The procedure for both planned and emergency shutdown was straightforward, using emergency stop buttons on the starter motor boxes for the mono pump and blower. These boxes were strategically located to provide easy access. As much of the experimental work in this study required the removal of all incident light sources, the boxes were painted with fluorescent paint to highlight their placement.

In the case of a planned shutdown, it was preferred that the liquid flow be stopped first as the airflow was quite good at ensuring nearly all residual liquid was removed from the test section. This was particularly important as the liquids of this study were dyed, and the dyes were capable of staining the test section if the liquid was free to remain or evaporate.

2.6 MAINTAINANCE

2.6.1 Test Section Cleaning

The optical nature of much of the experimental work undertaken in this study necessitated great importance being placed on ensuring that the rectangular section was free from any material that could obscure or distort visualisation of the air/liquid interface. With the majority of solid flow contaminants contained by and removed from the liquid distribution box (see Section 2.3.5), the greatest source of obstruction of the viewing surface was from liquid separated from the liquid film itself. The observed mechanisms of this liquid separation from the film were:

- (i) **Entrainment.** Liquid is sheared from the disturbance waves travelling along the interface by the action of the cocurrent airflow and deposited on the viewing plate. Fortunately, significant entrainment was only observed at the higher airflows investigated.
- (ii) **Spreading.** Observed at the higher liquid flowrates investigated in this study, where the liquid film traverses the plastic spacer sides of the rectangular test section and partially wets the periphery of the viewing surface. The methods attempted to correct this phenomenon are discussed in Section 2.3.5.

- (iii) **Jetting.** Jetting of the liquid over the weir directly onto the viewing surface. Observed initially during commissioning of the facility using water and corrected using the adjustable brass plate discussed in Section 2.3.5. However, jetting was also possible at start up of the liquid feed into the test section if the initial feed to the facility was set too high.

Mechanisms (i) and (ii) represented the upper flow range limits at which reliable quantitative data could be obtained using the optical measurement technique in this study.

Additionally, under certain external environmental conditions, condensation could be observed to occur on both the internal and external surfaces of the viewing glass plate. The condensation could be temporarily removed from an area, to allow measurements to continue, by heating the viewing glass in that area using a hot-air blower.

The water marks left by the mechanisms detailed above were exacerbated by the liquids being dyed, therefore, regular, often daily, cleaning of the test section was required. As stated in section 2.3.1, many of these problems were anticipated at the design stage of the facility and the test section was purposely designed for easy disassembly/reassembly. When removing/reinstalling the viewing glass plate from the test section, medical gloves were used to prevent fingerprints and oil/sweat from hands being deposited on the glass. With the viewing glass plate removed, the flow plate could be cleaned in situ.

Many different cleaning materials were tested during the course of this study, with most being effective at removing dyed smudges and watermarks by application in small amounts using a clean cloth or paper towel. For more stubborn stains, alcohols were often used. The glass plates were then left to dry before reassembly of the test section.

2.6.2 Changeover of Liquid Inventories

The changeover of liquid inventories was facilitated by the use of a drain valve on the air/liquid separation vessel and a similar drain valve on the liquid feed pump. As the dyes used in the liquids, and the organic liquids themselves, were a relatively expensive

resource, it was desired to recover as much of the liquid inventory as possible for future application. Once the bulk of the liquid inventory had been recovered and stored, hot soapy water was pumped into, around, and out of the facility for a number of hours. This was to ensure that the facility internals were clear of the dyed liquid. In the case of the organic liquids, during the pumping of hot soapy water around the flow facility, any residual organic layer was skimmed from the air/liquid separation vessel using buckets and stored for safe disposal. With the liquids being dyed, it was visually easy to detect when the facility was clean (*i.e.* no trace of the liquid dye remained). The facility was then drained of the soapy water, and tap water introduced and pumped once-through the facility, until removal of the detergent content of the water could be assured. The facility was then drained and left to dry overnight before introduction of the new test liquid.

Chapter 3

LIQUID FILM THICKNESS MEASUREMENTS

Review of the Literature

3.1 INTRODUCTION

The importance of liquid films in a wide variety of industrial processes has led to extensive experimental investigations into the phenomenon of film flow. In particular, knowledge of the thickness of these liquid films is useful in equipment design. Moreover, in most two-phase gas/liquid flow regimes the interface between liquid film and gas is far from linear, consisting of fast moving waves travelling over a relatively slower moving liquid film substrate. The presence of these interfacial waves is known to have a major influence on the mass and heat transfer characteristics of the film, therefore, knowledge of the structure of the liquid film interface is vital in understanding the precise effects related to these flow phenomena.

As film thicknesses in two-phase applications are generally less than a few millimetres, accurate measurement is difficult, and this has led to the development of a diverse range of measurement techniques. The purpose of this chapter is to critically review these measurement techniques in detail with emphasis on their applicability to the falling film thickness measurement in the presence of co-current airflow, the flow regime of the current work. This review was felt to be necessary for a number of reasons:

- (i) In order to set the film thickness measurement technique chosen for this work in context, and to make fair comparisons with data obtained using other techniques, it was felt necessary to obtain detailed information on these techniques so their strengths and weakness could be compared.
- (ii) Although countless experimental investigations have been carried out, only a few publications present detailed information on measurement methods.
- (iii) Previous reviews of film thickness measurement methods available in the literature (*e.g.* Collier & Hewitt (1964), Hewitt (1978, 1982), Alekseenko *et al.* (1994), and Graf (1996)) were found to be either outdated, brief in detail,

- (iv) incomplete or a combination of these weaknesses. However, the reviews given above as examples must be credited as being the starting point of much of the present work.

Initial review of the literature identified around twenty distinct film thickness measurement techniques, making apparent the necessity for a classification method to give a coherent structure to this chapter. Collier & Hewitt (1964) proposed a classification for film thickness measurement techniques based on the measurement range of the technique. The three groups considered in the classification are:

- (i) **Film average methods.** This group incorporates techniques where the average film thickness is measured over a considerable length of film. There has been little recent study using film average methods due predominantly to their inability to provide information on local interface phenomena (*i.e.* waves) where much of the research interest is directed today. As information on the structure of the interface is desired in the current work, these techniques were not considered for application. However, a brief review of the available techniques is included for completeness.
- (ii) **Localised methods.** This group incorporates techniques that give a reasonably localised measurement (of the order of a few millimetres to a few centimetres) of the thickness of the film but from which it is impossible to deduce a point instantaneous value. The most commonly implemented film thickness measurement techniques (*i.e.* conductance and capacitance probes) belong to this group. This is probably due to their relative ease of use and general applicability to most flow systems.
- (iii) **Point methods.** Methods attributed to this group include all in which continuous or statistical information can be obtained at a point in a liquid film. These methods are generally harder to implement and analyse than localised methods and thus have not been as extensively applied.

However, due to the age of this classification, it does not include a growing area of film thickness measurement using **spatial methods**. Spatial methods involve the performance of a number of point or localised measurements simultaneously in different

areas of the film in order to build up a global picture of the film thickness structure for the area under study. These techniques potentially offer a wealth of information, particularly on the three dimensional wave structures that have been reported as travelling on liquid films. Naturally, these potential benefits over single, point or localised measurement techniques come at a cost, the increase in resources in both implementation and analysis relative to their single measurement counterparts.

Table 3.1 shows a summary of the reviewed film thickness techniques, classified using an adaptation of the Collier & Hewitt measurement range method, to include spatial techniques. The numbers in brackets refer to the specific section of this chapter where the technique is described.

Table 3.1: Summary of reviewed film thickness measurement techniques.

Film Average (3.2)	Localised (3.3)	Point (3.4)	Spatial (3.5)
Hold –up Measurements (3.2.1)	Capacitance Probes (3.3.1)	Needle Contact Probe (3.4.1)	Photographic Light Absorption (3.5.1)
Film Conductance Method (3.2.2)	Conductance Probes (3.3.2)	Hot Wire Probe (3.4.2)	Multiple Electrode Probes (3.5.2)
Weighing Method (3.2.3)	Radioactive Absorption (3.3.3)	Shadow Method (3.4.3)	Multi-Conductance Probe (3.5.3)
	Radioactive Emission (3.3.4)	Fiber-Optic Techniques (3.4.4)	Pigment Luminance Method (3.5.4)
	Acoustic Method (3.3.5)	Light Absorption Techniques (3.4.5)	Fluorescent Imaging (3.5.5)
	Ultrasonic Pulse-Echo Method (3.3.6)	Fluorescent Techniques (3.4.6)	Ultrasonic Transmission (3.5.6)
		Laser Scattering Method (3.4.7)	
		Interferometric Methods (3.4.8)	

3.2 FILM AVERAGE TECHNIQUES

3.2.1 Hold-up Measurements

Hold-up methods were arguably the preferred film thickness measurement techniques prior to the emergence of localised methods such as the conductance technique. These methods simply consisted of the isolation of a section of film and measurement of the liquid volume within this isolated section, an early example of which is presented by Hewitt *et al.* (1961). It is in the isolation of the film where the main difficulties in implementation arise, and several techniques have been developed for different flow regimes. In falling films, the most frequently adopted method is to divert the outlet flow to a collection device whilst simultaneously stopping the feed. It is in the co-ordination of this simultaneous event that the possibility of measurement error occurs. Both mechanical and electrical systems have been developed to combat this source of error.

Hewitt & Lovegrove (1963) gives an example of the application of a manual hold-up system for film thickness measurement of air-water mixtures in upward annular flow in a 1 ¼ inch (32mm) bore tube. They managed the rapid isolation of the section of tube by using two rotating plug valves operated by linked levers, shown schematically in Figure 3.1. The total amount of liquid retained in the section is measured to determine the average film thickness. This method makes the assumption that the liquid held up and measured consists entirely of liquid from the film. This is not strictly true, as part of the liquid will often flow in the gas core. The authors point out that this is negligible in climbing films at the low flowrates studied within their report but question the validity of the method at high mass flowrates. Hughmark & Pressburg (1961) report a similar study on vertical upward co-current air-liquid flow using electrical switching by solenoid valves.

Ueda & Tanaka (1974) report the application of a hold-up method for measuring the mean liquid film thickness of a downward air/water flow in a 28.8mm vertical tube. The method is simplistic, using only one shut-off valve on the liquid feed with a linked moveable drain receiver at the bottom of the test section to collect the film. The data presented compares favourably with previous experimental work and predictive equations for mean liquid film thickness measurements of falling film flow without cocurrent airflow. However, for falling film flow in contact with cocurrent airflow, the

authors acknowledge that the liquid film flowrate should be corrected by subtracting the entrained droplet flowrate, which was measured experimentally by sampling.

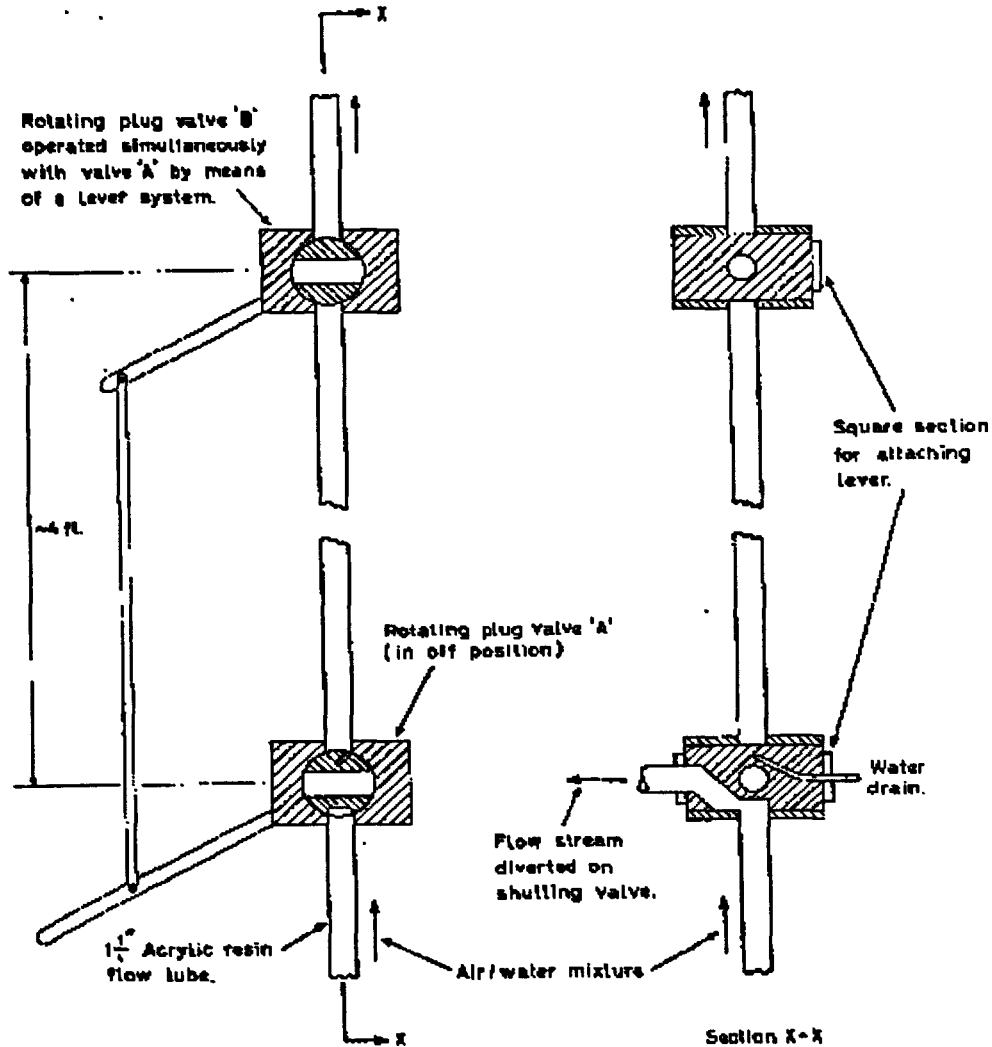


Figure 3.1: Linked valve arrangements for hold-up measurements. (Taken from Collier & Hewitt (1964))

Tailby & Portalski (1960) and Portalski (1963) report a similar application of the hold-up technique for falling liquid films for a range of liquids of differing viscosity, while Yih & Hsu (1985) apply a similar methodology to film thickness measurements on free falling non-newtonian liquid films.

3.2.2 Film Conductance Method

The film conductance method is the measurement of the conductance of a length of film and relating this to the thickness of the film. Electrodes are inserted flush into the wall at the boundaries of the film length to be measured and are connected to some form of instrumentation to analyse the results. In many instances, it is necessary to make the film conducting by adding appropriate electrolytes. An early application of the film conductance method is reported by Grimley (1945), who applied it in the comparison of film thickness on the inside and outside of a small diameter (0.7cm) vertical tube. Cassagrande *et al.* (1962) as part of the CISE team developed and used the film conductance method to measure mean film thickness for argon/water mixtures in vertical upward film flow in a 25mm diameter tube. A simple schematic of their film conductance measurement components is given in Figure 3.2.

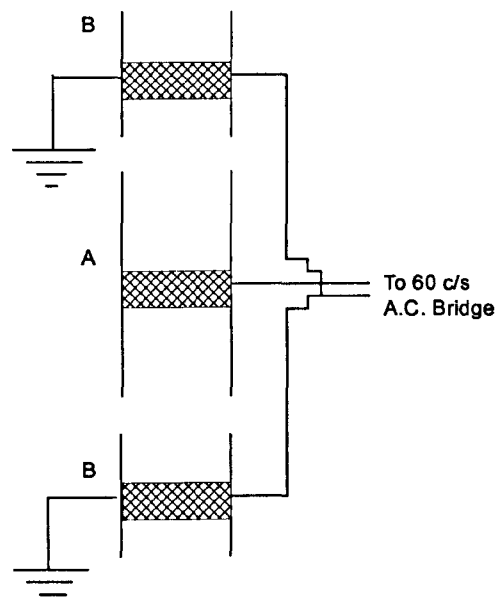


Figure 3.2: Schematic of film conductance measurement components.
(Adapted from Collier & Hewitt (1964))

They measured the mean conductance between electrode A and earthed electrodes B, situated 250mm apart, using a 60 Hz Ac Bridge. The authors found that the results were highly reproducible, however, Hewitt & Lovegrove (1963) in comparative tests on the film conductance method found that the method invariably underestimated the mean

thickness. They attributed this underestimation to the wavy nature of falling films and non-linearity along the film length.

3.2.3 Weighing Method

The principle of the weighing or counterbalance method is identical to the Hold-up measurement method (Section 3.2.1) but involves the replacing of the isolation and drainage procedures with an arrangement that allows weight analysis of the experimental test section during operation.

Collier and Hewitt (1964) point out that for the results from this method to be accurate, precautions should be taken in the design. In particular, careful design is required for the entry and exit to the test section in an effort to reduce systematic errors due to the friction and forces induced by the experimental supports. They suggest the implementation of a null-deflection balance arrangement with a force balance carefully formulated to account for all the forces imposed on the experimental section.

Kamei and Oishi (1954) used the method for average film thickness measurements of falling films with liquids such as water, soap and millet-jelly solutions. They suggested that the entrance and exit unsteady regions of flow could be neglected for towers longer than about 250 cm. They reported good agreement with theoretical predictions in laminar flow but results deviated markedly in turbulent flow and with the introduction of gas flow. The authors, quite correctly, attributed these errors to wave formation on the film and unaccounted force elements on the balance that suggests considerable caution when using this method.

A more recent application of a weighing method for mean film thickness measurement of falling liquid films on the outside of a vertical tube is reported by Aragaki *et al* (1987), and a schematic diagram of the apparatus used is given in Figure 3.3. The cylindrical test section (3) was fixed to one end of a lever by means of a connecting shaft, with the other end of the lever attached to the strain gauge load transducer (4). A number of vertical tubes with differing diameters were used, with the reported results comparing favourably with other studies.

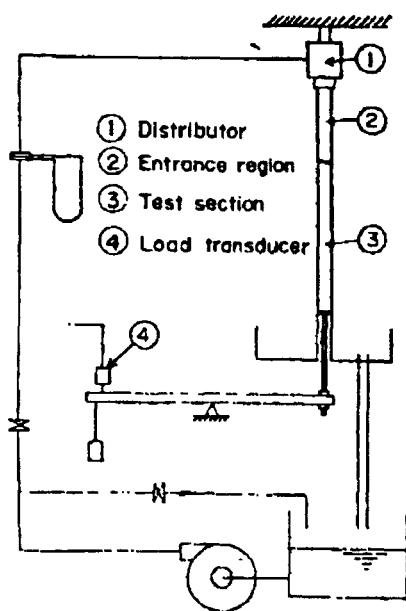


Figure 3.3: Schematic diagram of weighing method apparatus.
(Taken from Aragaki *et al.* (1987))

3.3 LOCALISED TECHNIQUES

3.3.1 Capacitance Probes

Capacitance probes are a popular alternative to conductance probes (Section 3.3.2) and optical techniques (Sections 3.4.2 – 3.4.5) where the test fluid is non-conductive, opaque, or immiscible with dyestuffs or a combination of these properties. The principle of this method is that, because of the usually significant difference in di-electric constant between liquids and gas, a pair of probes will give a localised measurement of the capacitance that will be function of the thickness of the film between them. The basic variants on capacitive thickness transducers/probes are shown schematically in Figure 3.4.

Dukler & Bergelin (1952) and Taliby & Portalski (1960) report early applications of capacitance probes in measuring the thickness of falling films over flat vertical surfaces. They formed a condenser using a combination of the wetted metallic vertical surface and a small cylindrical probe with axis perpendicular to it (Figure 3.4(b)). The cylindrical probe (typical diameter in the order of a few millimetres) is positioned a few millimetres distance away from the test surface. It is desirable that the electrode diameter be as small

as possible to measure more accurately any fluctuations in thickness of the film surface. However, the reduction of electrode area decreases the output voltage and lowers the signal-to-noise ratio. Therefore it is undesirable to make the electrode area too small. The optimum electrode diameter and its distance from the test surface of the cylindrical probe appears to be determined in most reported cases by trial and error, however, Fujita & Katoh (1985) report a theoretical analysis of the effect of probe diameter on the accuracy of measurement.

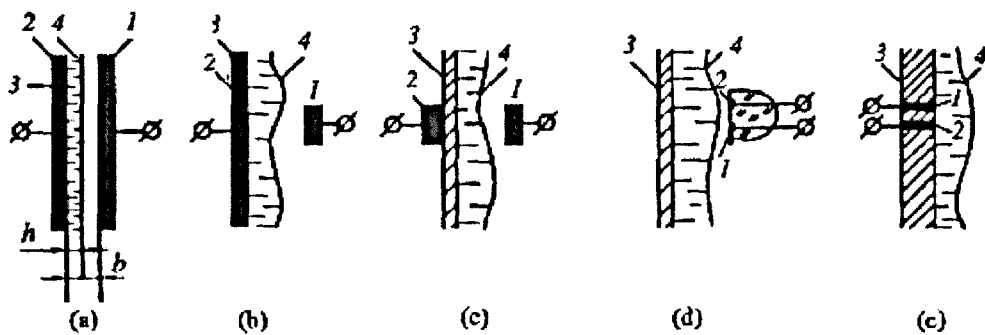


Figure 3.4: Variants on capacitive thickness sensors. 1, 2 – first and second capacitor plate, 3 – wall, 4 – liquid film. (Taken from Alekseenko *et al.* (1994)).

Other applications of this capacitance probe configuration in more recent falling film studies are presented by Takahama & Kato (1980) in falling films without gas flow and by Fujita & Katoh (1985) for falling water film measurements over a ring attached to a vertical cylinder. Aragaki *et al.* (1987) used a similar configuration for falling film measurements on vertical tubes, utilising a separate copper tube within the acrylic test cylinder as the reference electrode. Most recently, Ambrosini *et al.* (1998) used this capacitance probe technique for film thickness measurements of a water film falling down a flat plate. All the studies reported above present results generally consistent with other studies using alternative film thickness techniques

Ozgu *et al.* (1973) suggested that this external capacitance probe measurement technique has limited sensitivity due to the transverse orientation of the liquid film and capacitance probe. Furthermore, they criticised the method due to its restriction to geometries where the probe does not interfere with the flow field. In response to these criticisms, they developed a capacitance probe measurement technique, which locates both

electrodes/transducers of a capacitance circuit in the surface over which the liquid film flows (Figure 3.4(e)). The advantages reported by the authors for this configuration are maximum capacitance variation with changes in film thickness giving high resolution, no probe interference with the flow field and adjustable electrode spacing to optimise signal for local film conditions. Ozgu *et al.* (1973) developed and tested two different electrode geometries, 'ring' and 'rod' probes.

Ring probes are a pair of concentric metallic electrode rings mounted flush into the annular test section with their detecting surface shaped to match the contour of the surface over which the film flows. Rod probes are a pair of metallic cylindrical electrodes that are mounted flush into the test section at pre-determined distance in a similar manner to ring probes. Leskovar *et al.* (1979) and Sun *et al.* (1982) report improvements on the original design of ring and rod probes for application within vertical annular flows. They concluded that their ring arrangements were adequate for the measurement of film thickness from near zero up to a value of about 4-6 mm. They also tested the feasibility of ring probes for average film thickness measurements with a large dynamic range, but agreed with the original conclusion of Ozgu *et al.* (1973) that rod probes were better suited for local measurement. This is clearly due to the fact that ring probes can only give an average film thickness around the perimeter of the ring/tube. The major advantage of rod probes over ring probes is that their spacing is easily adjustable, allowing optimisation of the signal for local film phenomena for improved resolution. However, it is also reported that rod probes have a lesser range of applicability in film thickness measurements than their ring counterparts (from near zero to 3mm). Disappointingly, there do not appear to be any further application of either 'ring' or 'rod' probe configurations in falling film measurement within the literature. However, Keska & Fernando (1992) report a similar application utilising capacitors, consisting of two plates mounted on the same plane over which the fluid flows, in an experimental study on horizontal flow in a square channel. The authors investigated the effect of the shape, gap and area of the plates on capacitor response and obtained data that correlated well with models for this flow system available in the literature. Little information on applications of the other probe/transducer configurations (Figure 3.4(a), (c), (d)) for falling film thickness measurements could be found in the literature.

For the measurement of film thickness under transient conditions such as wavy flow, the response of the capacitance circuit and associated recorder must be sufficiently rapid to match the phenomenon. Two possible methods have been suggested for the measurement of capacitance. They are measuring the variations in voltage across the capacitor by polarising it, and incorporating the capacitor in a bridge circuit or a capacitance dependent oscillator. In practice, the latter method is favoured due to the lower power dissipation from the detecting surface of the probe. This is a significant advantage as power dissipation from the detecting surface of the probe will increase the probe temperature and change the characteristics of the reading of the film flowing over it. To combat probe temperature increase, Benn (1972) suggested the use of a thermistor mounted near the end of the detecting surface of the probe which could monitor any changes in probe temperature and inject a voltage accordingly into the output to counteract the increase. However, no practical application of this thermistor could be found in the literature.

Noise is a significant area for concern in using capacitance probes in film thickness measurements. Noise in this case can be defined as any external contribution to capacitance, which is added to the capacitance meter output. The two major causes of noise in capacitance probes are capacitance from external sources beyond the locality detected by the electrodes (*i.e.* background noise), and capacitance generated by movement of the leads or other connecting device between the electrodes and the output device. Noise due to the former can be reduced or even eliminated by shielding of the electrodes from the external environment. Leskovar *et al.* (1979) mounted their probes with an attaching block that contained a metallic box designed to screen out local noise. All other literature sources studied for this review utilising capacitance probe have used similar shielding methods. Researchers have adopted no standard method, however, all researchers have highlighted the necessity in combating noise caused by movement. Benn (1972) suggests that a way of overcoming this problem is to use charge amplifiers with special cables but indicated they are difficult to use when the signal is static (D.C). The author also proposes the use of a “backing off” system that injects an opposite signal to the output that cancels out the effect of the noise, and the possible use of rigid tubes to connect the electrodes to the output device. Ozgu *et al.* (1973) simply shielded the wires with a single cable but joined the cables together to eliminate any ambient effects on the capacitance measurements.

In the simplest version of transducer, *i.e.* a plane condenser (Figure 3.4(a)), a two dimensional approximation of the relation between electric capacity C and thickness b of a plane liquid layer, assuming the relative dielectric permeability of the liquid approaches 1, can be represented by:

$$C = \frac{\epsilon_0 s}{(b-h)} \quad (3.1)$$

where, ϵ_0 is the electric constant and b and s are respectively the distance between the plates and their area. It is often advantageous to linearise the output signal because of the non-linear relationship between changes in capacitance and film thickness. Linearisation can be achieved by data analysis or by digital/analogue means with the appropriate circuitry. The accuracy of linearisation can be checked and modified at the calibration stage.

For the more complex geometries, Figure 3.4(b)-(e), more rigorous calibration is required. Most researchers are in agreement that it is advisable at least to calibrate each probe with its test fluid in some simple geometry. Calibration of capacitance probes has been achieved by both static and dynamic methods. Benn (1972) favoured a static method of calibration that involved the creation of a number of plastic calibration standards of known thickness and di-electric constants. These standards were presented to the bottom face of the probe making certain that the film was flat to the face of the probe. The output was recorded and plotted against the known film thickness. It is unclear to this author whether a capacitance probe would react identically regardless of fluid being utilised, so it is the opinion of this author that it is still preferential to use the working fluid. Most other static calibration methods consist of simply putting measured amounts of the test fluid over the probe, and determining the output response. The results can be plotted in relation to the film thickness in some manner for ease of interpretation.

Sun *et al.* (1982) proposed and used a dynamic method of calibration (*i.e.* continuously running test fluid of known thickness over the electrodes). The thickness of the film was determined by running the test fluid, in this case water, through a previously calibrated

turbine flowmeter before it entered the test apparatus. The flowmeter readings were converted to thickness of the falling film using the equations quoted by Wallis (1969):

At low flowrates the film flow is laminar and will obey the Nusselt equation:

$$\delta = \left(\frac{3\mu_f Q_f}{\pi g \rho_f D} \right)^{1/3} \quad (3.2)$$

where, δ is the film thickness, g the gravitational acceleration term, μ_f the water viscosity, ρ_f the water density, Q_f the volumetric flowrate, and D the tube diameter.

At higher flowrates the film flow becomes turbulent (δ now is proportional to $Q_f^{2/3}$). The onset of turbulence can be deduced from the film Reynolds number defined as:

$$\text{Re} = \frac{4\rho_f Q_f}{\pi D \mu_f} \quad (3.3)$$

Sun *et al.* (1982) suggest that a reasonable fit to the entire water flow region can be obtained if laminar flow conditions are assumed for $\text{Re} < 3000$ and turbulent flow conditions are assumed for $\text{Re} > 3000$. However, the accuracy of a calibration using a theoretical prediction of film thickness for all flow conditions must be questioned.

3.3.2 Conductance probes

Conductance probes are probably the single most extensively used time varying film thickness measuring device, and as such, a vast number of literature references on their use have been reported. The principle of this measuring technique is similar to capacitance techniques and many of the problems of measurement are inherent in both techniques. Basically, conductance is measured using a circuit containing a pre-determined electrode configuration and the readings are amplified and displayed by some output device. The conductance of the fluid under investigation can also be artificially enhanced, for example, by the addition of salt (NaCl, KCl) into water systems. Film thickness can be determined from these conductance measurements if a calibrated

relationship, preferably linear, can be established between the two parameters within the range of measurements. In pursuit of the extension of a linear range and improved resolution, three distinctive conductance probe types have been developed as schematically illustrated in Figure 3.5.

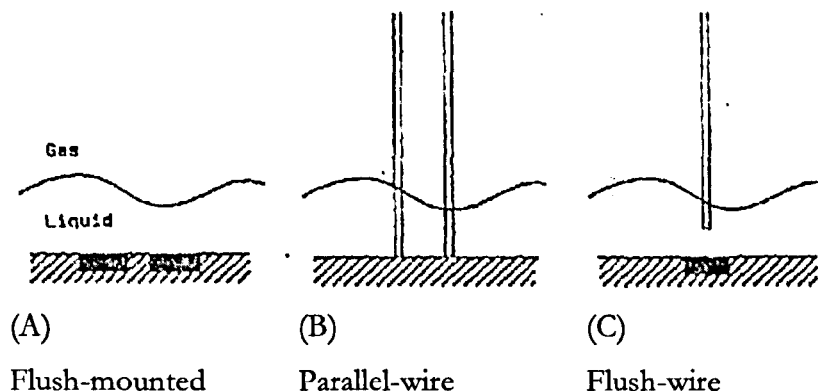


Figure 3.5: Schematic diagram of differing conductance probe types.
(Adapted from Graf (1996))

3.3.2.1 Flush-mounted

Flush-mounted conductance probes involve the measurement of conductance between two electrodes mounted flush in the insulated surface over which the film is passing. Coney (1973) found that these probes have an effective resolution only for film thicknesses less than the distance between probes. However, if the distance between electrodes is too great, highly localised measurements are not possible. This naturally leads to compromise, and the results from Coney (1973) infer that flush probes are effective over a film thickness range of only up to about 2 mm. This lack of range is compensated by their non-disturbance of the film flow, which is not true of the other conductance probe variants.

A number of electrode geometries for flush mounted conductance probes have been reported:

(i) **Two pin electrodes.** These electrodes are probably the easiest to manufacture. A simple schematic is shown in Figure 3.6.

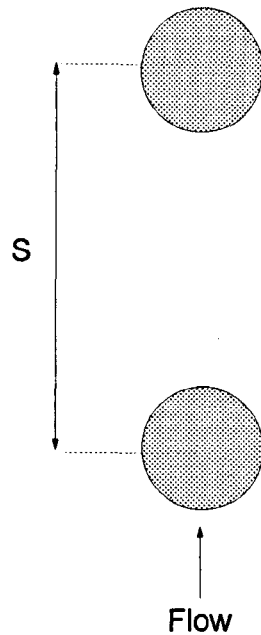


Figure 3.6: Schematic of two-pin electrodes.

Two metal pins are mounted flush and machined to match the shape of the surface. They are usually mounted in position by epoxy resin or an expanding mandrel. Azzopardi *et al.* (1979) report a typical application of flush conductance probes, with each probe consisting of a 1.59mm diameter electrode. An earthed annular electrode, of 6.35mm internal and 9.58mm external diameter, surrounded the measuring electrode. This “guarding” of the measuring electrode is commonplace in conductance probe application.

Examples of the application of flush conductance probes for vertical upflow of air-water mixtures within 30 mm to 42 mm i.d. vertical tubes are reported by Bennett & Thornton (1961), Collier & Hewitt (1961), Hewitt *et al.* (1962), Hall Taylor *et al.* (1963), Gill *et al.* (1962, 1963, 1969), Hewitt & Lovegrove (1969), Whalley *et al.* (1973), Azzopardi *et al.* (1979), Martin & Whalley (1983), Asali (1985) and Okada & Fujita (1992).

Of most relevance to the current study, Webb & Hewitt (1975) and Takahama *et al.* (1983) report their application in air/water downward vertical annular flows in a 1 1/4” (32mm) and 30mm tube respectively.

(ii) **Parallel-strip electrodes.** These electrodes are more difficult to manufacture than two-pin electrodes, however, they have the advantage of approaching a two

dimensional geometry and are thus easier to model. A simple schematic is given in Figure 3.7.

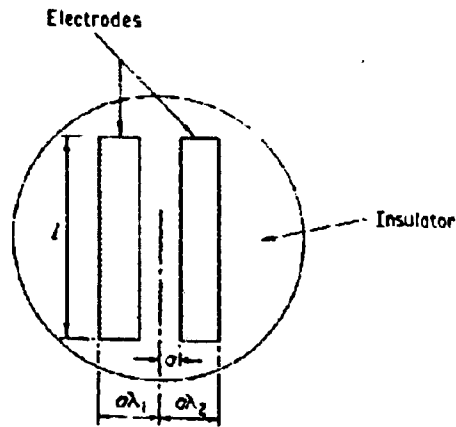


Figure 3.7: Schematic of parallel-strip electrodes.
(Taken from Coney (1973)).

The electrodes consist of two parallel strips mounted flush to the surface and perpendicular to the direction of flow. However, if the separation distance of the parallel conductors is not small compared to their length, there will be end effects. Coney (1973) modified the above arrangement to limit any end effects by segmenting one of the electrode strips into three parts and insulating the individual segments with paper impregnated with perspex cement. The outer segments now became 'guard' electrodes for the central measuring segment. A schematic of this modified electrode arrangement is given in Figure 3.8.

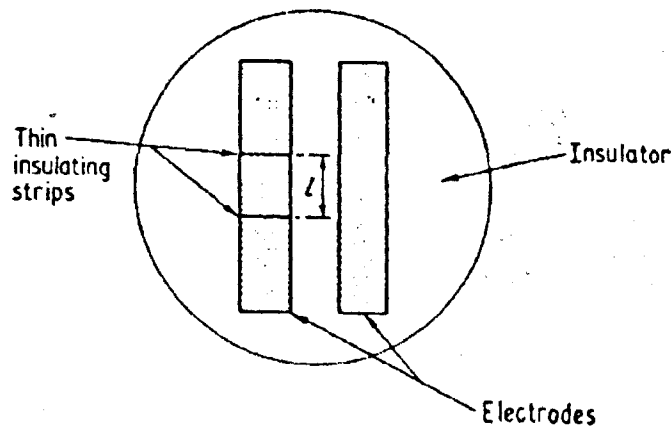


Figure 3.8: Schematic of segmented parallel-strip electrodes.
(Taken from Coney (1973)).

The advantages of this guarded arrangement over the simple parallel-strip electrodes were reported to be increased range and resolution in the direction parallel to the strips.

Examples of parallel-strip electrodes being utilised in film thickness measurements are reported by:

Telles & Dukler (1970) for free falling films in a vertical rectangular conduit 6" (152 mm) by 3/4" (19 mm) in cross-section.

Webb & Hewitt (1975) and Chu & Dukler (1974, 1975) in downward annular two-phase flow in 1.25" (32mm), 1.50" (38 mm) and 2" (51mm) vertical tubes respectively.

Nash & Freeman (1980) in upward annular two-phase flow in a 1.25" (32mm) vertical tube and by Laurinat *et al.* (1984) in 1" (25mm) and 2" (51mm) i.d. tubes in horizontal annular gas-liquid flow.

(iv) Ring electrodes. Comparable to the ring electrode geometry used in capacitance measurements (Section 3.3.1.). These probes simply consist of a number of metal ring electrodes built flush with the tube inner surface at a set distance apart. Clearly this geometry is limited to measurement of the cross-sectional averaged thickness around the tube. Applications of conductance ring electrodes in vertical pipes are reported by Kulov *et al.* (1979) utilising three ring electrodes for thickness measurements in downward two-phase flow in a 25mm tube, and by Asali *et al.* (1985) using a pair of annular metal electrodes in measurements in vertical upward annular flow in a 2.29cm diameter tube.

(iv) Concentric electrodes. Hewitt (1982) reported that these electrodes are particularly convenient for application in metal-walled channels. As Figure 3.9 indicates, with this probe configuration the wall usually acts as one electrode, and a central pin as the other. No evidence in the literature could be found of any relevant study measuring local film thickness using such a configuration, however, application of the geometry is commonplace in void fraction measurement.

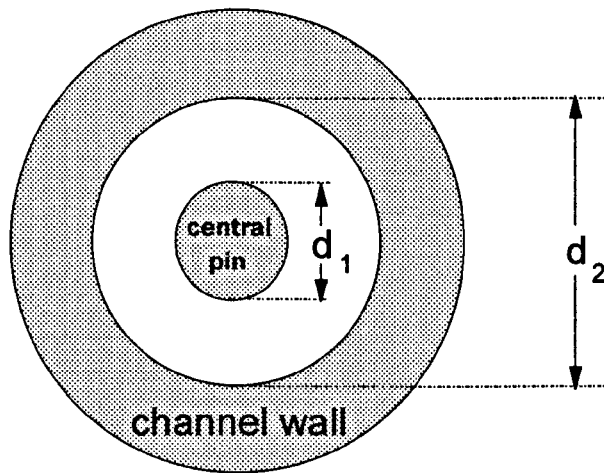


Figure 3.9: Schematic of concentric electrode.

Recently, this configuration has been modified by use of a concentric cylinder as the earth electrode rather than the pipe wall, for example by Wolf *et al.* (1996) in the study of waves in vertical upward annular flow.

(v) **Ring/Rod Combination.** Recently, Fukano (1998) has reported the application of a flush electrode probe configuration consisting of two concentric rings and one circular rod at the centre of the two rings, and this arrangement is shown schematically in Figure 3.10.

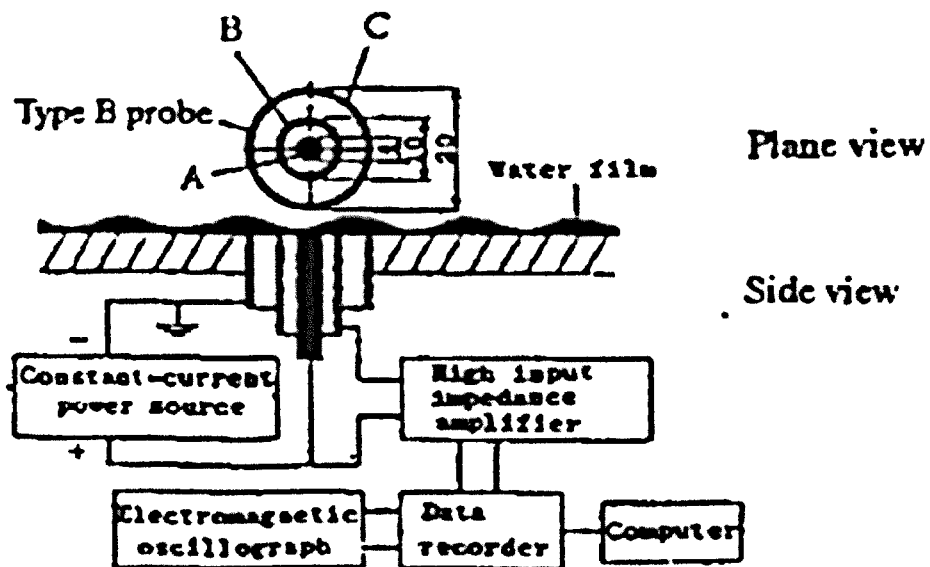


Figure 3.10: Schematic of ring/rod combination probe.
(Taken from Fukano (1998))

The inner ring and rod are used as the sensor electrodes, with the measured thickness averaged over their locality. The outer ring acts as a grounded guard electrode. Currently, application of this probe geometry has been limited to wave studies in horizontal rectangular ducts.

3.3.2.2 Parallel-wire

Parallel-wire conductance probes consist of two thin parallel metallic wires stretched through the film normal to the wall over which the film flows. The wires are usually manufactured of platinum based alloys (*e.g.* platinum-rhodium) to ensure stable performance. The wires can be anchored in an insulating material at the wall and lacquered-insulated over one half of their length to allow thickness variations to be monitored on one side of a pipe only. Wire spacing can be controlled by accurate positioning at the wall insulating material and by the use of wire tension. A schematic of an application on a vertical cylindrical column, as used by Koskie *et al.* (1989), is shown in Figure 3.11.

In this example two platinum-rhodium alloy wires of 0.08 mm diameter are stretched through two insulated holes drilled into the flow column at a distance of 0.51 mm. The wires are connected to the power supply and fixed with a screw on the column support rod at one end, while at the other end they are passed over glass bearings and connected to tension maintaining weights.

Parallel-wire conductance probes have been found to give a linear response in a wider range of film thickness and to allow a more localised measurement to be undertaken than their flush-mounted counterparts. For these reasons it is easy to understand why parallel wire probes have quickly become the most popular implementation of conductance film thickness measurement since their earliest reported applications by Swanson (1966) and Miya *et al.* (1971). However, wire probes do have negative and potentially limiting features that should be considered before application. The most significant of these features are the inevitable disturbance of the flow and the modifications of the interfacial surface caused by the wetting of the wires.

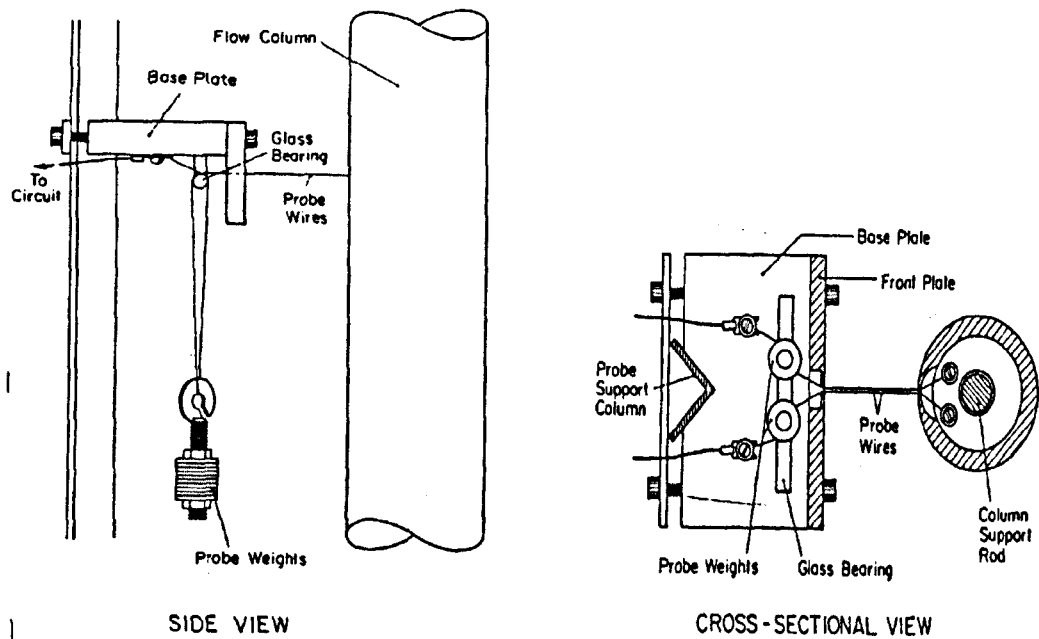


Figure 3.11: Parallel-Wire Conductance Probe installed on a vertical cylindrical column.

(Taken from Koskie *et al.* (1989))

Naturally, the choice of wire thickness is critical to their successful operation. The wire diameter must be minimised to have negligible disturbance effect on the flow and yet large enough to be sensitive to electrical resistance with respect to the entire liquid film height. Koskie *et al.* (1989) realised that the disturbance of the bulk film, and the subsequent wake formation, introduces the possibility of the phenomenon of vortex shedding having a detrimental effect on the probe results. If the wires begin to shed alternating vortices they will begin to vibrate normal to the flow. Since the resistance with respect to the liquid will vary with the spacing of the wires, vibration will cause a fluctuating resistance and be detected as noise in the output signal. They suggest that a certain range of Reynolds numbers based on the wire diameter should be avoided, where these Reynolds numbers are most likely to produce coherent vortices. An alternative solution is the movement of the natural frequencies of the wires outside of the coherent shedding range by controlling their tension.

In a wavy film, where the liquid height is continually changing, a decrease in height will often still leave a temporary liquid layer adhering to the probe which will indicate a higher liquid film height than can be observed. However, Brown *et al.* (1978) report that this introduction of a certain amount of dynamic lag had been experimentally

investigated by Pearlman (1963), who found the errors to be negligible and the response of the probe to be virtually instantaneous.

Examples of the utilisation of parallel wire conductance probes in film thickness measurement are given by:

Zabaras *et al.* (1986) and Lacey & Dukler (1994) for upward annular gas-liquid flow in a 2" (51mm) tube.

Koskie *et al.* (1989), Wasden & Dukler (1989, 1992), Karapantsios *et al.* (1989), Karapantsios & Karabelas (1990, 1995), Lacey *et al.* (1991) and Mudawar & Houpt (1993a,b) for free falling films on the internal and external surface of a 2" (51 mm) vertical pipe.

Nencini & Andreussi (1982) for downwards annular flow in a 24 mm vertical pipe.

3.3.2.3 Flush-wire

Murav'ev *et al.* (1984) first discussed and reported the combination of flush and wire conductance electrodes in the hope to create a probe configuration that would have the advantages, and limit the disadvantages, of both these electrodes. The authors claim to have achieved an increase in accuracy and linearity of the measurements over flush and wire probe electrode configurations using the systems shown schematically in Figure 3.12, however, little data or further application could be found to substantiate these claims.

Figure 3.12 shows one stainless steel electrode, the reference electrode, having a large surface and this is placed into the liquid at some fixed distance from the point of measurement. The second electrode, the measurement electrode, consists of a thin platinum filament, about 30 μ m in diameter, immersed to the entire depth of the film normal to its surface. Ensuring that the linear dimension of the reference electrode in the plane of the film and the distance between the electrodes are much greater than the diameter of the measurement electrode, allows the resistance between the electrodes to be related to the film thickness.

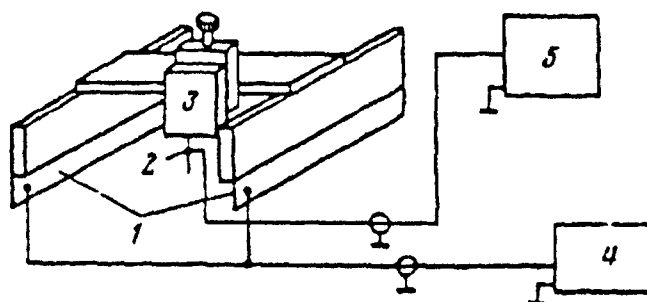


Figure 3.12: Flush wire film thickness measurement circuit: 1) reference electrodes; 2) measurement electrode; 3) micrometer conveyor; 4) low frequency generator; 5) measurement block.

(Taken from Murav'ev *et al.* (1984))

Kang & Kim (1992a) developed an alternative flush-wire conductance probe geometry (see Figure 3.5(c)) in an effort to increase the spatial resolution for continuous measurements of film thickness above what was available by conventional flush-mounted and wire probes. In this configuration the flush-wire conductance probe consists of an electrode mounted flush to the wall over which the film flows and a vertical wire electrode inserted/suspended from the opposite wall. Kang & Kim (1992a) reported that they found their probe configuration to be easier to set-up and handle than previous implementations of conductance probes. In contrast to Murav'ev *et al.* (1984), they present considerable evidence to suggest that this probe configuration compares favourably with other conductance probes.

For flush-wire probes, many of the difficulties reported earlier with the utilisation of wire probes, such as wire wetting, still exist. However, as the wire is only partially within the film, wire induced phenomena are naturally less significant. Additionally, Murav'ev *et al.* (1984) state that flush wire probes should be restricted to liquids without mechanical impurities. They comment that particles, especially fibrous ones, can induce a sharp increase in hydrodynamic resistance and perturbations at the site of the probe, and can also cause deformation of the filament/wire electrode.

3.3.2.4 Electronic Circuitry

Obviously, the electronic circuitry used for conductance probes has become more sophisticated in line with the rapid developments in electronics generally. The circuit arrangement utilised by Kang & Kim (1992a), and typical of current applications is presented in Figure 3.13.

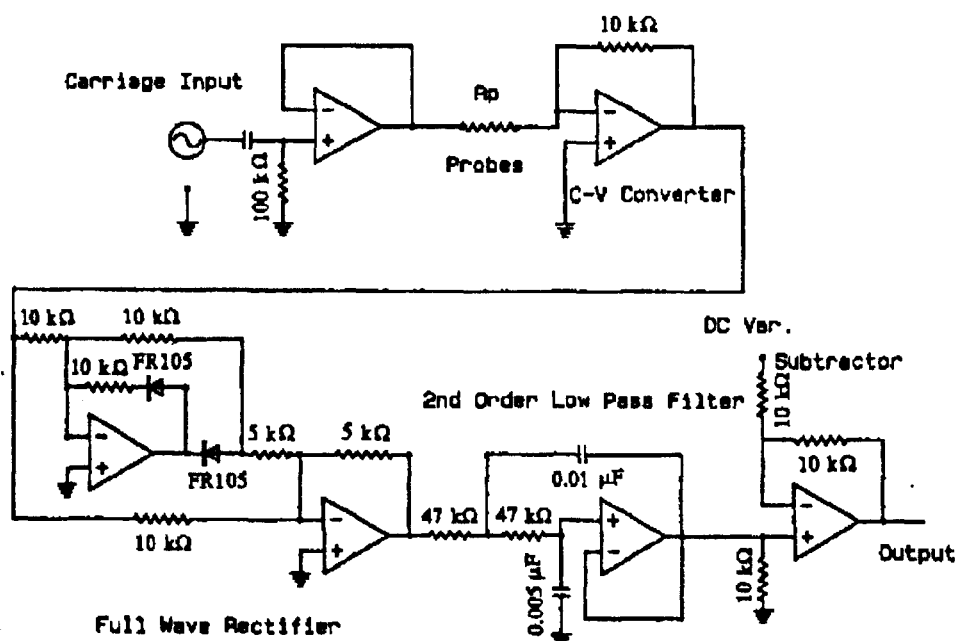


Figure 3.13: Example of electronic circuitry used in conductance probe application.

(Taken from Kang & Kim (1992))

Basically, it involves the application of a high frequency, constant amplitude AC voltage from a sine wave signal generator across the electrode/wire pair and measuring the film thickness dependent voltage drop across some form of resistor. In the case of flush-wire probes, the flush electrode introduces the signal and the output is taken from the wire. The signal is then usually rectified, smoothed and amplified for recording by analogue or more recently by digital means. Low conductivity liquids (*e.g.* water) are often used and amplification of the signal will increase the spatial resolution of the output.

Lacey & Dukler (1994) deviated from the standard AC circuit arrangement outlined above by not using a sine-wave carrier frequency. They applied instead a single, very short duration square wave to the probe for the time interval of each measurement and then the reading was taken after the transient had decayed. They found this arrangement

to be extremely linear with conductance, and produce no measurable interaction with other probe locations.

Alternative arrangements have been proposed. Fukano *et al.* (1971) proposed a constant electric current method, in which a DC power source was used. The application of direct current systems has been avoided by most workers, as disturbing electrochemical phenomena and deposits on the surface of electrodes make application potentially more difficult. However, Fukano (1998) in a recent review of his application of constant electric current methods, concludes that they could be particularly advantageous in thin liquid flow. This is because the output from conductance probes utilising a constant electric current method becomes highly sensitive to the change in film thickness when the film is thin due to the increase in electrical resistance.

Interaction between conductance probes is a potential source of considerable error unless steps are taken to prevent it. Traditionally, a transformer isolating the probes from the voltage source and output device is employed, and is found to greatly reduce the interference between adjacent probe pairs. Alternatively, Koskie *et al.* (1989) achieved isolation of their wire probes by using magnetic coupling. Where multiple probes are being used, Brown *et al.* (1978) also suggests that to eliminate the possibility of cross-talk, simultaneous readings ideally should not be taken for different probes at multiple channels. This idea was re-iterated by Lacey & Dukler (1994) who developed their circuitry to prevent this.

The choice of signal wave frequency is critical to the successful operation of the probe. At low frequencies, the conductance properties between electrodes is affected by a number of capacitive and resistive elements that arise at the electrode-electrolyte interface commonly referred to as 'double layer' effects. Coney (1973) describes this electrode double layer effect by stating that, because electrical conduction in liquids used (*e.g.* water) involves ions rather than electrons, a process of charge transfer must take place at the interface between the metallic electrodes and the film of liquid. This charge transfer will involve the transfer of protons across electrical double layers of ions on the surface of the electrodes, which will need a certain significant activation energy, supplied by the applied potential difference between the probes across the system. The double layer will increase in thickness, and thus increase the resistive properties of the system, as

the excess potential difference increases. Unfortunately, this excess potential difference or 'overvoltage' will build up during the experiment, rather like a capacitor charging, which will affect the probe sensitivity and increase the likelihood of rogue measurements. Therefore, it is naturally beneficial to choose a frequency high enough to negate the double layer effect. Kvurt *et al.* (1981) did extensive study on the influence of frequency on measurement results and came to the conclusion that frequencies not lower than 50-100 kHz should be adopted. This range is typical of the minimum values for signal frequency adopted since the original Coney *et al.* (1973) study.

3.3.2.5 Calibration

Calibration of conductance probes has presented many problems to researchers, resulting in extensive study of this aspect of the probes. Overall, review of the literature suggests that the creation of simulated films of known thickness has become the predominant calibration method for conductance probes. However, direct calibration of conductance is not without experimental difficulty. Due to the sensitive relationship between conductivity and the environment surrounding the system, a major difficulty is observed in the maintaining of a constant liquid condition (*i.e.* conductivity, temperature, level of contaminants *etc.*) during film thickness measurements. One possible solution, as adopted by Coney (1973) for example, is the use of reference probes in the inlet stream to record and compensate for the changes in condition. Bennett *et al.* (1961) controlled the conductivity in their experimental runs by adding small amounts of copper nitrate to the liquid sump. However, the addition of conductivity buffer such as copper nitrate may have an effect on the film characteristics, and should probably be avoided if possible.

An alternative to direct calibration is theoretical calibration, which requires knowledge of the exact relationship between film thickness and conductance. Early attempts at the establishment of the theoretical film thickness-conductance relationship were largely unsuccessful. An example of an early attempt to theoretically model flush-mounted conductance probes was undertaken by Hewitt *et al.* (1962). The basis to their approach was that if flush probes are considered to be equivalent to probes that project into the full thickness of the film, then the current field between them will be equivalent to that

between two long supported wire conductors. This equivalency then allows the following equation to be valid:

$$G = \frac{\pi\gamma}{\ln \left[\frac{a}{r} + \sqrt{\frac{a^2}{r^2} - 1} \right]} \quad (3.4)$$

where, G (Ω^{-1}/cm) is the conductivity per unit length between two parallel wires, r (cm) is the radius of the wires, $2a$ (cm) is the axial spacing, and γ ($\text{ohm}^{-1} \text{cm}^{-1}$) is the specific conductivity in a homogeneous medium.

As the authors themselves point out, this equivalency is not entirely valid as the flush probes do not project full distance into the film and therefore, Equation 3.4 will over-predict conductivity values for a given thickness. It was not until Coney (1973) that a satisfactory model for conductivity/film thickness relationship (for flush-mounted probes) was presented. The theory only strictly applies to a system that has a two-dimensional geometry, which implies that if the separation of the conductors is not small compared to their length, then end effects will occur and create discrepancies between theory and system. The resulting equations can be presented in non-dimensionless form:

$$G^* = \frac{G}{\sigma l_1} \quad (3.5)$$

where, G^* = dimensionless conductance, G = actual conductance (Ω^{-1}), σ = electrical conductivity of the liquid ($\Omega^{-1} \text{m}^{-1}$), and l_1 = characteristic conducting length dependent on probe geometry (m).

and:

$$h = \frac{m}{l_2} \quad (3.6)$$

where, b = dimensionless film thickness, m = actual film thickness (m) and l_2 = characteristic actual length dependent on probe geometry (m).

For two-pin electrodes (see Figure 3.6), defining $l_1 = l_2 = s$, where s is the probe spacing gives:

$$\frac{G}{G^*} = \frac{m\sigma}{h} \quad (3.7)$$

For segmented parallel-strip electrodes (see Figure 3.8), defining $l_1 = l$ and $l_2 = a$ where l and a are the probe active length and half-spacing respectively, gives the following equation:

$$G^* = \frac{K(M)}{K(1-M)} \quad (3.8)$$

where, $K(M)$ is a complete elliptical first order integral, defined by

$$K(M) = \int_0^{\pi/2} (1 - M \sin^2 \theta)^{-1/2} d\theta \quad (3.9)$$

where, M is given by

$$M = \frac{\sinh^2[\pi(\lambda - 1)/2h]}{\sinh^2[\pi(\lambda + 1)/2h]} \quad (3.10)$$

and, λ is the ratio of λ_1 to λ_2 . (where, λ_1 and λ_2 are distances of the outer edges of the two electrodes from the mid-point of the central insulating strip as shown on Figure 3.7).

Coney's results can also be applied to concentric electrode geometries (see Figure 3.9), defining $l_1 = l_2 = d_2 - d_1$, which gives for the linear region;

$$G^* = \frac{2\pi h}{\ln(d_2/d_1)} \quad (3.11)$$

Brown *et al.* (1978) presented a linear dependence between conductance and film thickness, for parallel-wire conductance probes (see Figure 3.5 (B)), in the form of the equation:

$$G = \frac{\pi\sigma h}{\ln\left(\frac{d}{r}\right)} \quad (3.12)$$

where, d and r are the distance between wires and wire radius respectively.

The main drawback in using theoretical calibration is the need to rely on the probe geometry being machined precisely as a cylinder, ring *etc.* which in practice cannot be guaranteed. Even the smallest deviation from a perfect geometry can cause significant errors between theory and practice. Therefore, it would be inadvisable to rely on theoretical calibration alone and some practical direct calibration of the probe to be implemented to substantiate the theory is essential. The two possible approaches to direct calibration are:

(i) **Static.** As discussed above, each probe will have its own unique conductance characteristics, which necessitates some form of individual calibration and direct static calibration has always been the preferred technique for conductance probes. A popular approach, first used by Bennett *et al.* (1961), was a static calibration device using inserts, and an example is shown schematically in Figure 3.14.

As Figure 3.14 shows, the device consists of a 1.25 in. bore Perspex tube, a , which contains the electrodes mounted as they would be in the actual experimental rig. The electrodes are sleeved on a base block, b . A concentric rod, c , of is also mounted in the base as shown and the annular space between the rods filled with liquid of the appropriate conductivity, preferably the liquid under test. This liquid simulates a film of known thickness and conductance measurements can be taken. Concentric rods of differing diameters can be used to achieve a range of film thickness/conductance

measurements. Clearly, this method relies on precise machining for the results to be meaningful. Another disadvantage to this technique, also caused by machining limitations, is that it is virtually impossible to achieve measurements at spacing typical of thin films (e.g. substantially less than 1 mm). Additionally, Collier & Hewitt (1961) suggest results from this insert calibration device even at larger spaces are suspect, since variations of the order of up to half a millimetre could practically be expected in the linearity of the concentric tube diameters. In an attempt to improve the range of this calibration device, Hewitt *et al.* (1962) allowed the position of the electrodes to be adjusted, and the concentric rod was also supported to allow movement. This rod movement was recorded on dial gauges and allowed more accurate measurements over smaller ranges of simulated film-thickness. Similar static calibration methods have been made by amongst others Hewitt & Lovegrove (1969), Webb (1970b), Telles & Dukler (1970), Coney (1973), Chu & Dukler (1974).

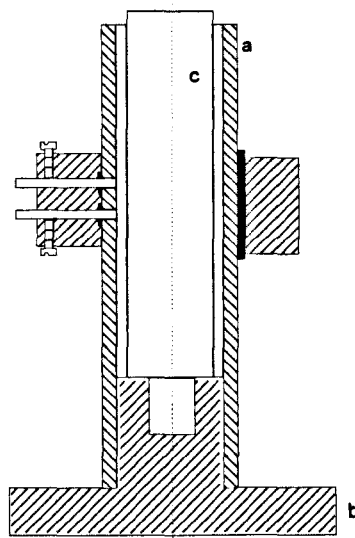


Figure 3.14: Inserts calibration device.
(Taken from Bennett *et al.* (1961))

More recently, Koskie *et al.* (1989) improved on previous static calibration techniques by removing the necessity of inserts, and a schematic of their calibration set-up is given in Figure 3.15. In this arrangement a needle probe is attached to a micrometer and positioned close (<1 mm) to the probe. The output of the probe was recorded when the needle touched the film. By repeating this procedure for different heights of liquid a calibration curve can be built up.

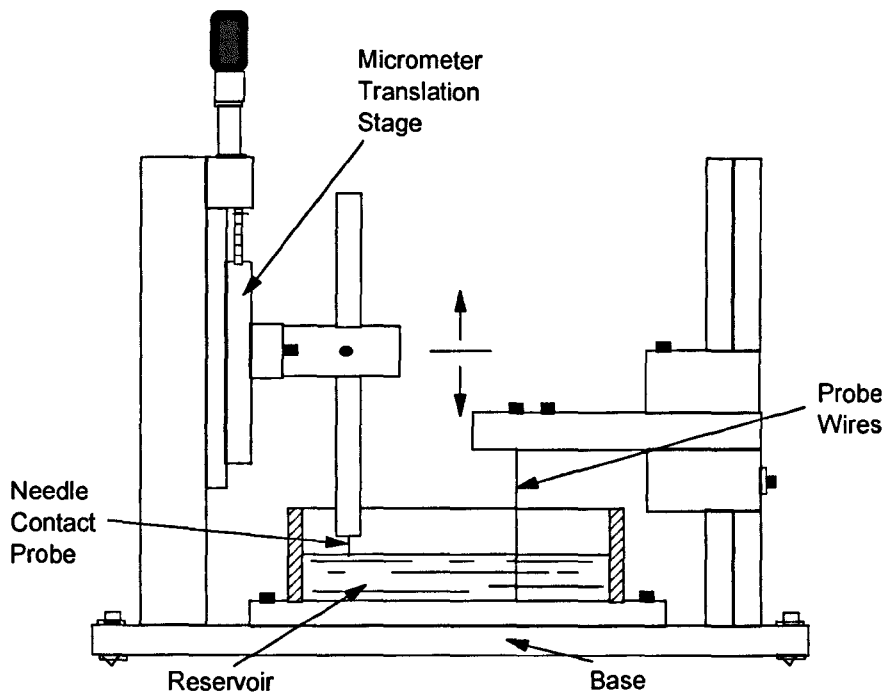


Figure 3.15: Static calibration equipment
(Taken from Koskie *et al.* (1989))

Specially designed calibration equipment has not always been used. Zabarás *et al.* (1986), working on vertical upward co-current annular flows, simply sat their test section horizontal and blocked the ends. They then introduced a series of liquid levels whose heights were determined with a cathetometer, accurate to 0.01mm, and measured the corresponding conductivity.

One potential serious limitation of static calibration is that it neglects any possible influence that a rapid change in film height, i.e. waves, have on the performance of conductance probes.

(iii) **Dynamic.** With the potential difficulties and limitations of direct and static calibration, such as varying liquid physical properties on conductance and the neglect of wave influence, Kang & Kim (1992a) proposed an indirect dynamic alternative. Using the assumption that the probability of the liquid existence at any height is unique for a constant liquid flow rate, they propose that it would be easier to calibrate the probe indirectly using this fact. They acquired the probability data of the liquid's existence at a

given height using the well-established needle-contact probe (Section 3.4.1). Figure 3.16 shows the concept of their calibration using probabilities.

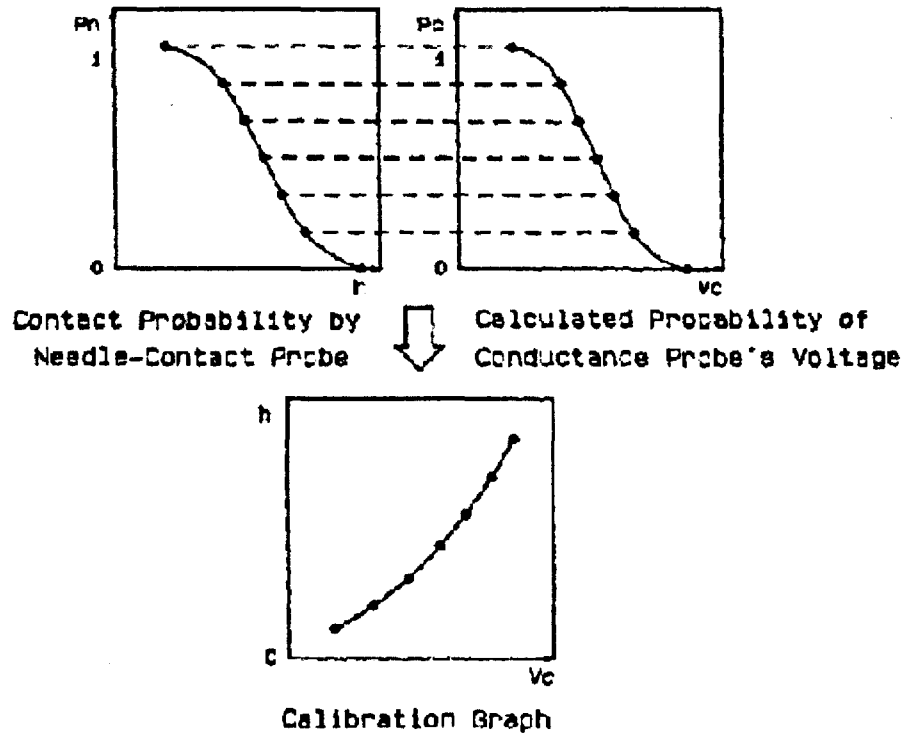


Figure 3.16: Concept of the calibration method using probabilities.
(Taken from Kang & Kim (1992a))

The contact probability, Pn_i , of the needle probe at any chosen height h_i , is given by:

$$Pn_i = f(h_i) = \frac{t_n}{t_t} \quad (3.13)$$

where, t_n and t_t are the sum of the liquid contact times and total measuring time respectively.

The output of the conductance probe, Vc_i at height h_i is given by:

$$Vc_i = f(\sigma, s, h_i) \quad (3.14)$$

where, σ is the conductivity of the probe and s the status of the probe. If the conductance probe has good resolution and the data acquisition is fast enough to allow the assumption that the conductivity and status of the probe are constant during the period of measurement, then the output voltage V_{c_i} only depends on the film height. The probability P_{c_i} of the conductance being then larger than any voltage V_{c_i} at film height b_i can be expressed as:

$$P_{c_i} = f(V_{c_i}) = \frac{t_c}{t_t} \quad (3.15)$$

where, t_i and t_c are the total time and the sum of the times above voltage V_{c_i} respectively. As at any film height b_i the probabilities of P_{n_i} and P_{c_i} must be equal, therefore the relationship between height b_i and voltage V_{c_i} , i.e. calibration graph, can be obtained from the probabilities of P_{n_i} and P_{c_i} in Equations 3.13 and 3.15 respectively. Figure 3.17 outlines the experimental calibration procedure.

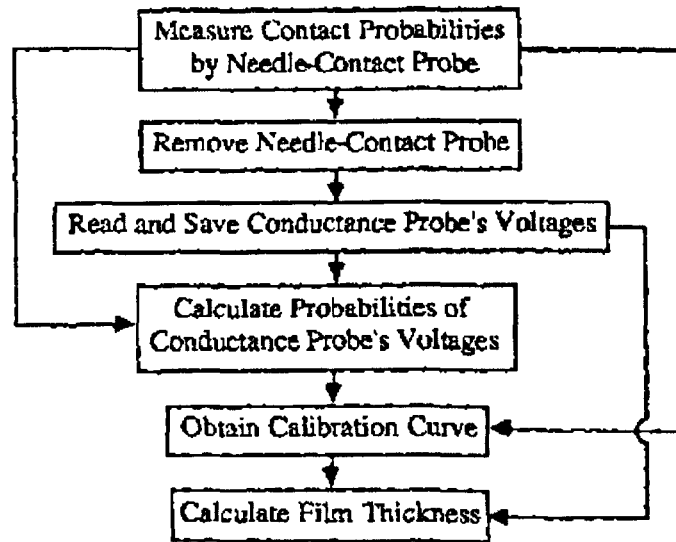


Figure 3.17: Example of dynamic calibration procedure.
(Taken from Kang & Kim (1992))

If the problems associated with accurate needle contact probe measurement (Section 3.4.1) can be overcome, then this dynamic calibration technique can be considered as possibly the most reliable and accurate conductance probe calibration technique to be

presented to date. The calibration can be achieved “on-line” with the elimination of the uncertainty of changing environmental properties on conductivity.

3.3.3 Radioactive Absorption Techniques

Radioactive absorption techniques have been utilised to obtain localised measurements of film thickness virtually since interest in this phenomenon began. These techniques have lost favour in recent years due largely to their obvious potentially hazardous nature and small observed benefit over other techniques. All the radioactive absorption techniques are based on the absorption of radiation by the film and detecting the loss of intensity via a detector. Naturally, the main difference between techniques is the radioactive source, and this review will look at the techniques available.

3.3.3.1 X-Ray Absorption Technique

The principle of the technique is that for instantaneous X-ray absorption:

$$h = -\frac{1}{\mu} \text{Log} \frac{i}{i_0} \quad (3.16)$$

where, h is the thickness, μ the linear absorption coefficient of the material, i the emergent intensity, and i_0 the incident intensity of the monochromatic collimated beam. Hence, the instantaneous material thickness h can be determined if the values of the other variables are known at one instant.

Solesio *et al.* (1978) developed this technique for film thickness measurements and reported success at measuring films of 1mm average thickness flowing down an inclined plane at intervals of one millisecond with a precision finer than 50 μm . Their experimental set-up is shown schematically in Figure 3.18.

The methodology consists of the production perpendicular to the film base of a fine collimated beam of X-rays, 0.5 mm in diameter, from the X-ray tube. This beam is partially absorbed by the film and the non-absorbed remainder is detected and measured on a photomultiplier. The output from the photomultiplier is then directed towards an

analog to digital convertor whose output is recorded. Solesio *et al.* (1978) found X-ray absorption not easy to utilise but believed it provided a good comparative method for other techniques due to its fast response times and point information. This claim is supported by favourable comparison data obtained with a parallel conductance probe arrangement, recorded simultaneously with the x-ray data at virtually the same location.

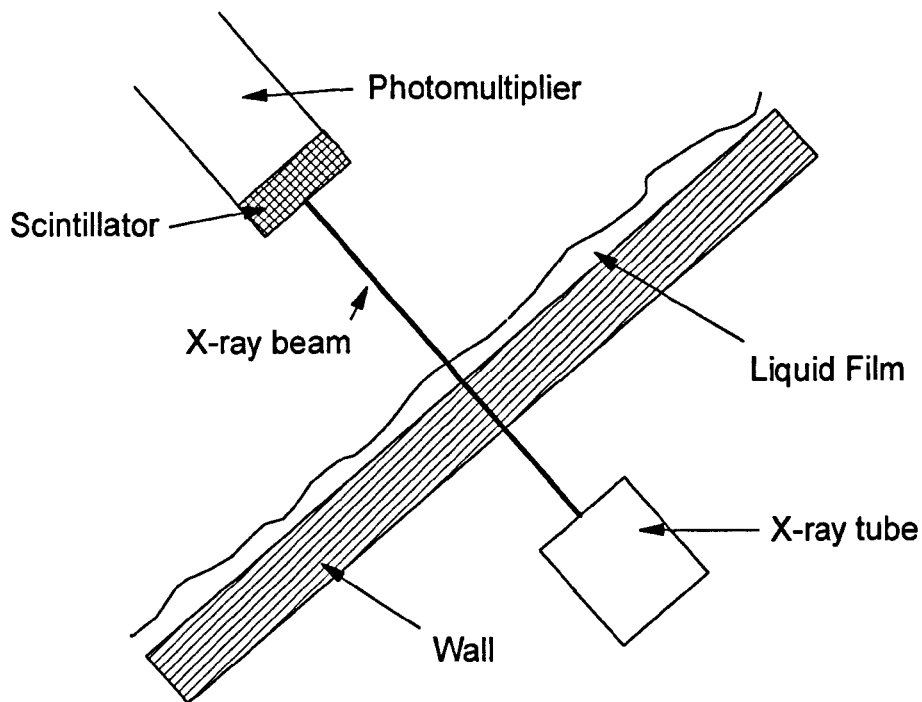


Figure 3.18: X-ray absorption measurement technique.

(Taken from Solesio *et al.* (1979))

3.3.3.2 Beta Ray Attenuation Method

Absorption of both beta and gamma rays has long been a traditional method for measuring the density of gas-liquid mixtures. One novel example of this is given by Cravarolo *et al.* (1961) who used beta-ray absorption or 'attenuation' for measuring the density of gas-liquid mixtures flowing in circular ducts in the dispersed region. Their approach to the technique was novel, and of interest to this review, due to their use of a small sized source (4 mm by 4 mm) introduced inside the flowstream. This source could be placed in different positions along the duct diameter, thus allowing density measurements and thus film thickness in a non-uniform absorbing medium, such as a falling film wavy interface. The major components of the experimental set-up were the source positioned within the wall of the test assembly and a Geiger Müller Counter

placed directly opposite. The counter was lead shielded to reduce the influence of background radiation on the device. The source chosen, a mixture of the practically pure beta emitters Sr^{90} and Y^{90} , was chosen as a compromise between sensitivity, range limitations and sufficiently long half-life. Naturally, this mixture would have to be optimised for utilisation in film thickness measurements. Calibration was achieved dynamically by using mixtures of known density within the range of experimental study and adaptation is required for film thickness measurements possibly by the use of real or simulated liquid films of known thickness, as per the microwave waveguide technique reviewed in Section 3.3.3.3.

The authors claim to have had reasonable agreement with other density measurement methods but do not include any data within their report. Applications of this method for liquid film-thickness measurements could not be found, and this is almost certainly due to the hazardous aspects of this technique and the wealth of alternatives.

3.3.3.3 Microwave Techniques

El-Sayed *et al.* (1983) experimented with the use of microwave waveguide methods to determine their practicality for measuring liquid hold-up in various flow regimes, in particular in co-current flow of a gas and water based solutions. In a refinement of this work, Roy *et al.* (1986) presented a simple experimental demonstration of how a microwave waveguide technique can be used for the non-intrusive measurement of the instantaneous local thickness of a falling liquid film. A schematic of the measurement system used to achieve this is given in Figure 3.19.

The concept behind the technique is that the 'loss' of intensity of microwaves travelling along the wave guide and through the test section, i.e. between the generator & detector, is a function of the local thickness of the film. The width of waveguide determines the local measurement spacing of the technique, and was 1.5 cm for this demonstration. Great care was taken in ensuring there was no leakage of energy from the measurement system, which could detract from the accuracy of the measurements due to interference from nearby objects. The authors also gave consideration to the frequency of microwaves to be used, to ensure the frequency used was low enough that the depth of

penetration and wavelength in the liquid are much larger than the thickness of the liquid film.

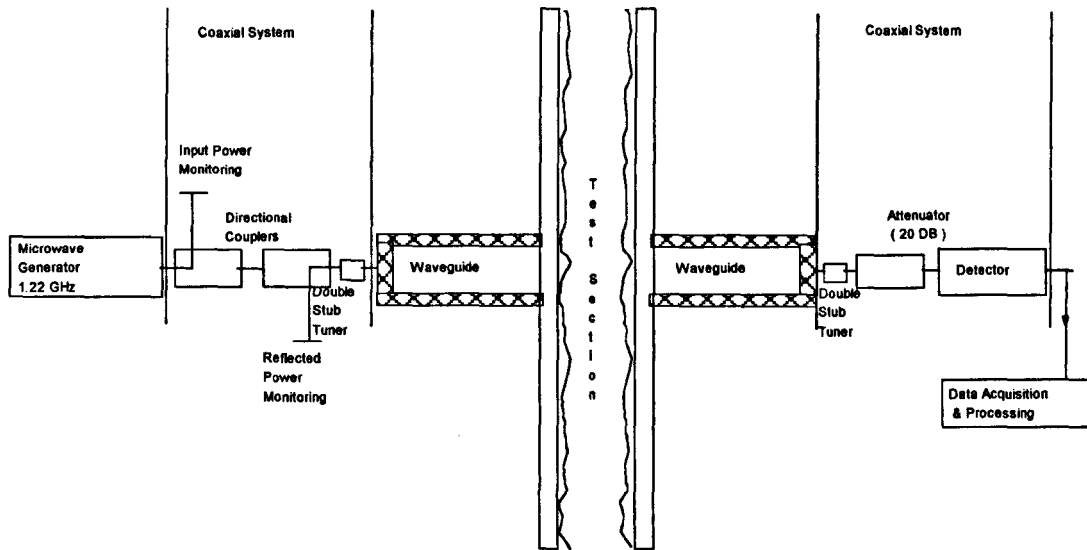


Figure 3.19: Microwave Waveguide Measurement Section.
(Adapted from Roy *et al.* (1986))

Calibration was achieved statically by the insertion into the initially water filled test section of concentric polyfoam cylinders of known diameters that could simulate air density at the microwave frequencies used. Measurements were taken of the changes in output voltages in the detector these insertions caused in reference to the dry test section. Attempts to calibrate the test section dynamically by using water films of known thickness were also made.

The authors noted that by changing the height of the waveguide, the extent of localisation could be altered allowing some degree of flexibility in the study of time-varying local phenomena. They also state their belief that the method is suitable for both tubular and rectangular test sections. Disappointingly, little data is presented for comparison with alternative techniques.

More recently, Root & Kaufman (1992) present an alternative microwave technique for measuring the thickness of thin liquid or solid films and coatings by utilising the resonance properties of microstrip structures, and a schematic of a microstrip resonating structure for use in film thickness measurement is given in Figure 3.20.

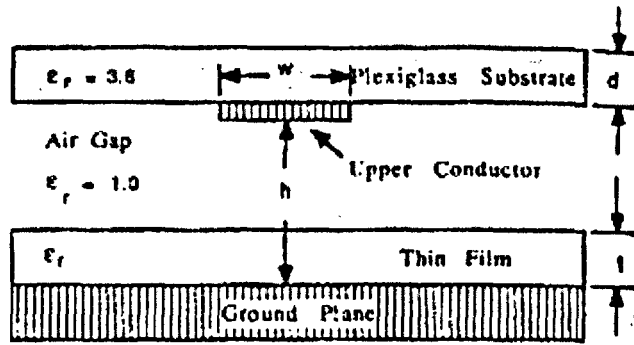


Figure 3.20: Microstrip resonating structure used in film thickness measurement.

The basis of the technique is that the resonant frequency of the microstrip structure is a function of the relative permittivities and thicknesses of the materials that are located between the strip conductor and ground plane, and thus the resonant frequency will vary with varying liquid film thickness. The resonance of the microstrip can be converted to a correlatable dc output voltage with inexpensive electronics, for recording by standard data logging methods. The exact relationship between resonance and film thickness can simply be pre-determined by calibration using films of known thickness to build a calibration curve.

Currently, application of the device is reported to be limited to static liquid films, however, adaptation of this low cost, non-intrusive technique to dynamic two-phase flow systems appears straightforward. The main advantage of this measurement technique over waveguide techniques is that all the microwave components are internal to the instrument and require no expensive microwave test equipment. Comparison of the experimental results obtained for water films approximately 1mm in thickness with measurements taken with a needle probe suggests measurement accuracy of around 1-2%.

3.3.4 Radioactive Emission Techniques

In radioactive emission techniques a radioactive substance is dissolved in the flowing liquid and measured by a detector brought up to the film. The amount of liquid in the

locality (*i.e.* the film thickness) will be proportionally related to the radiation detected at that locality.

One relevant example of the technique is given by Jackson (1955) who used a yttrium-91 salt dissolved in varying viscosity liquids flowing down the inner wall of a vertical tube and detected the radioactivity emissions by means of a shielded Geiger-Müller Tube. Naturally, the localisation of the technique is determined by the size of detecting tube utilised. A schematic of the experimental construction is given in Figure 3.21.

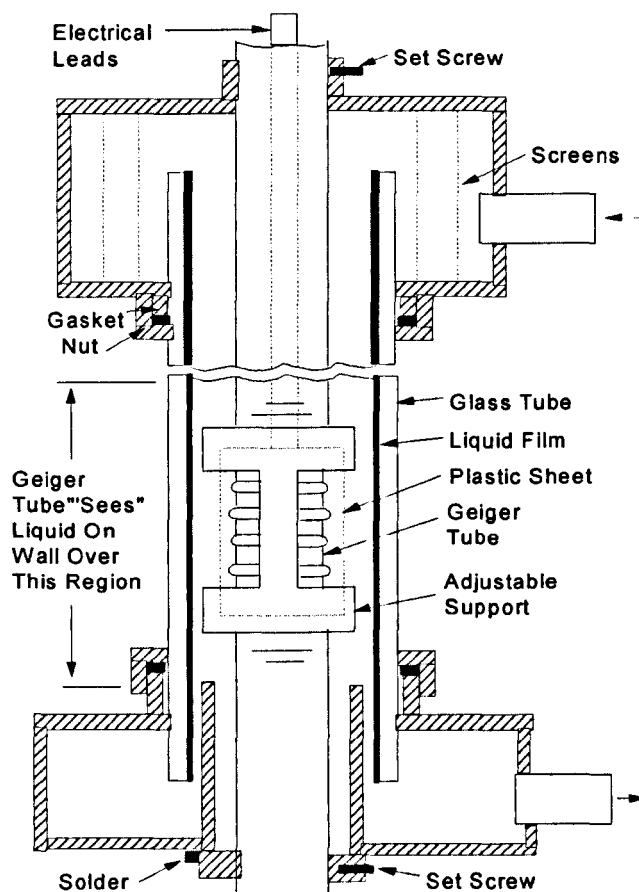


Figure 3.21: Schematic of column construction for film thickness measurement utilising radioactive emissions. (Adapted from Jackson (1955))

Calibration was achieved by the creation of static films of known thickness by use of a micropipet and the corresponding activity recorded. Sampling of the flow at intervals was required due to partial adsorption of the radiation by the liquid in the film. However, as pointed out in a previous review of this measuring technique by Collier & Hewitt (1964), no correction is made for the reduced contribution of the outer layers of

the film compared to those closer to the detector. They expressed concern that this will cause significant errors in film thickness measurements when a wavy interface is present.

Further application of radioactive emission techniques for film thickness determination could not be found since the study reviewed above, but such techniques have been utilised in mean density and velocity determinations, that are possibly open to adaptation.

3.3.5 Acoustic Method

The principle of this technique is that the variation in mechanical Q-factor of a medium, defined as the ratio of the energy transported and transmitted by the sound wave to that absorbed by the medium, is proportional only to the thickness and density of the medium. Bezrodnyy & Antoshko (1992) presented an experimental method for measuring the flow of falling films based on these acoustic properties of the liquid film, and their experimental measuring unit is presented in Figure 3.22.

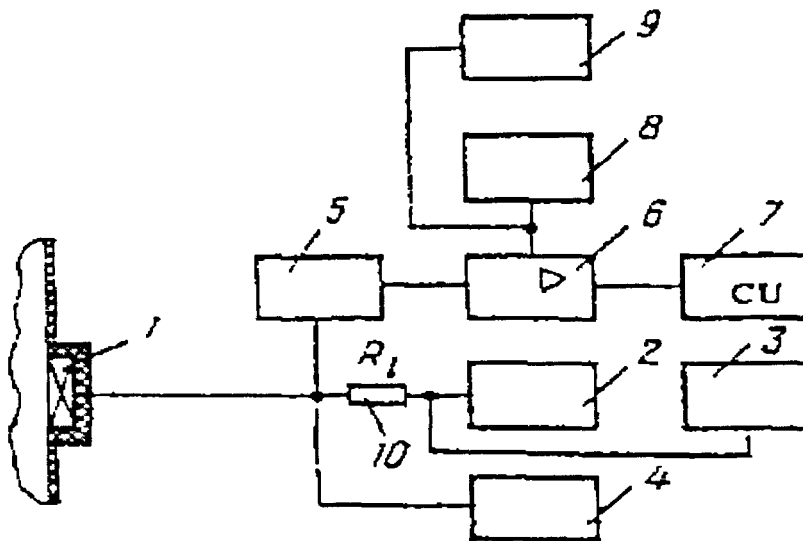


Figure 3.22: Block diagram of the unit for measuring the thickness of a liquid film by the acoustic method.

1)Ceramic piezoelectric emitter; 2)signal generator; 3)frequency meter; 4)oscillograph; 5)microvoltmeter for ac current; 6)differentiating amplifier; 7)correction unit; 8)integrating dc voltmeter; 9)high-speed recorder; 10) load resistance.
(Taken from Bezrodnyy & Antoshko (1992))

A piezoelectric emitter made of a radially polarised ceramic ring (8mm in diameter) is used as the film thickness sensor. It is mounted flush to the wall and excited by a sinusoidal voltage of the frequency produced by a signal generator. The voltage at this emitter is measured by means of an alternating-current microvoltmeter. This voltage is converted into a linearised analog dc signal, which is fed to a differentiating amplifier with a correction unit, with the variation in signal being a function of the thickness of the liquid film.

Clearly, the sensitivity of the method is directly related to the emitting surface area, however, it is not just a question of having as high a surface area as possible as this will be detrimental to interfacial resolution. Calibration was achieved by the needle contact method (see Section 3.4.1). The authors claim the method to be simple to implement, non-intrusive and have generally applicability to falling film measurement in the range of 0 – 2.5 mm thick with an error not exceeding fifteen percent.

3.3.6 Ultrasonic Pulse-Echo Method

Starkovich *et al.* (1980) first demonstrated that commercially available ultrasonic testing equipment could be used in the measurement of liquid film thickness relevant to this review; however, the technique is similar to sonar that has been employed in naval applications since a time considerably before 1980. The basis of all ultrasonic film thickness measurement methods is a pulse-echo approach. This involves the measurement of the transit time of a sound wave transmitted and received by a single ultrasonic transducer. The transit time can be combined with knowledge of the speed of sound in water to determine the liquid film thickness. This approach is complicated if the transducer is located external to the test section by the fact that the ultrasonic pulse will first be partly reflected by the solid wall/liquid interface before further partial reflection at the liquid/air interface, and also any subsequent interfaces. Therefore, the ultrasonic signal must be analysed to determine the true signal from the liquid/air interface before true transit time can be evaluated.

The original study presented results obtained for static and dynamic water films ranging between 1-10mm in thickness on both horizontal and inclined surfaces, which were in good agreement with results obtained by needle contact probe (Section 3.4.1). Dallman

(1981) extended this original study to falling liquid films as thin as 0.02mm in a cylinder and Chang *et al.* (1982) further developed the technique in liquid film thickness measurements in a variety of flow regimes in horizontal gas-liquid flows. Chun *et al.* (1984) reported further development in a study to measure the effects of wall thickness and ultrasonic frequency on liquid film thickness measurement, using the measurement system and test section geometries shown in Figure 3.23.

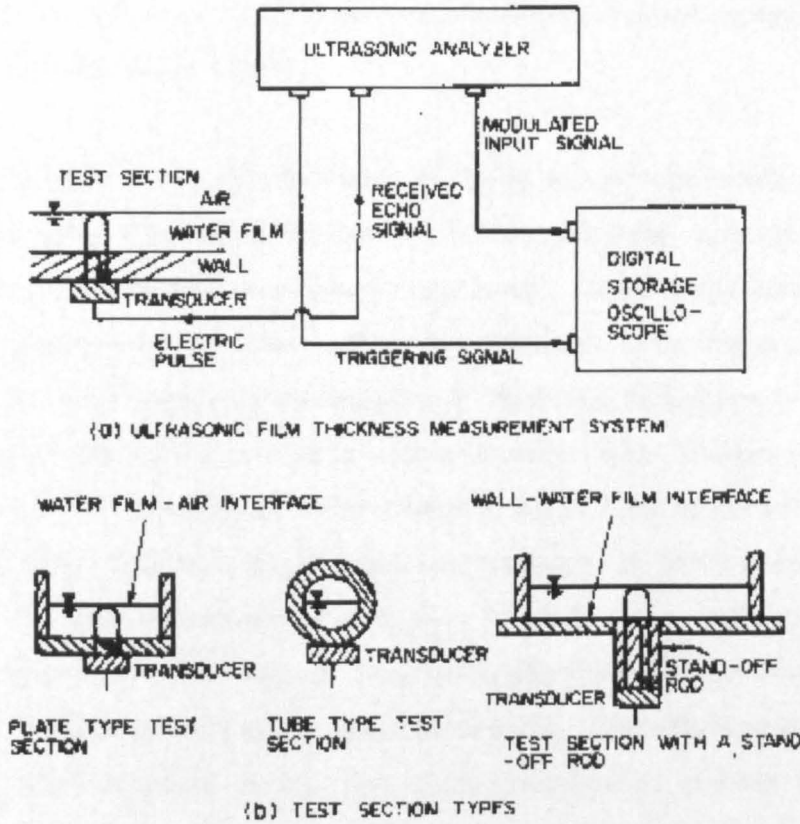


Figure 3.23: Ultrasonic liquid-film thickness measurement system and test section geometries.
(Taken from Chun *et al.* (1984))

From this study, the authors came to the conclusion that the ultrasonic pulse-echo method could be successfully implemented if:

- (i) The tube wall thickness is greater than the minimum wall thickness given by:

$$\frac{NV_w}{2f} \tag{3.17}$$

where, N is the number of ultrasonic pulse periods, V_w is the speed of the ultrasonic wave in the wall material, and f is the frequency of ultrasonic wave.

- (ii) the acoustic impedance of the tube is low enough such that the peak point of echo from the liquid film/air interface remains distinguishable.

The authors also suggest that these restrictions can be removed in practical application if a standoff rod manufactured of a low acoustic impedance material is employed, with an example illustrated in Figure 3.23(b).

More recently, Serizawa *et al.* (1994) report the application of a pulse-echo technique in horizontal two-phase flow using 5 MHz and 10MHz ultrasonic waves produced from 12.7mm and 3.2mm diameter transmitters respectively. Of particular interest from this study is the simultaneous application of an interferometric laser displacement method (Section 3.4.8), which highlights the inability of ultrasonic techniques to measure the thickness at the sharp edges of the liquid surface associated with disturbance waves. This is due to poor detection sensitivity to the inclination angle of the reflection interface, and angles above about four and nine degrees were found to be immeasurable using the 3.2mm and 12.7mm transmitter respectively. However, the technique does have potentially considerable advantages in industrial application over the more established film thickness techniques such as the conductance probe. The ultrasonic transmitter can be easily attached/detached to the pipe under investigation without the need for modification, and if the velocity of sound through the liquid under investigation is known then no calibration is required.

3.4 POINT METHODS

3.4.1 Needle Contact Probe

The needle contact probe has always been a popular film thickness measurement device, and this popularity is probably due to the simplicity of its application to virtually any type and size of conducting liquid film flow. Recently, it has been primarily utilised as a calibration or comparative device for other more sophisticated probes. A schematic for a typical needle contact probe arrangement is given in Figure 3.24.

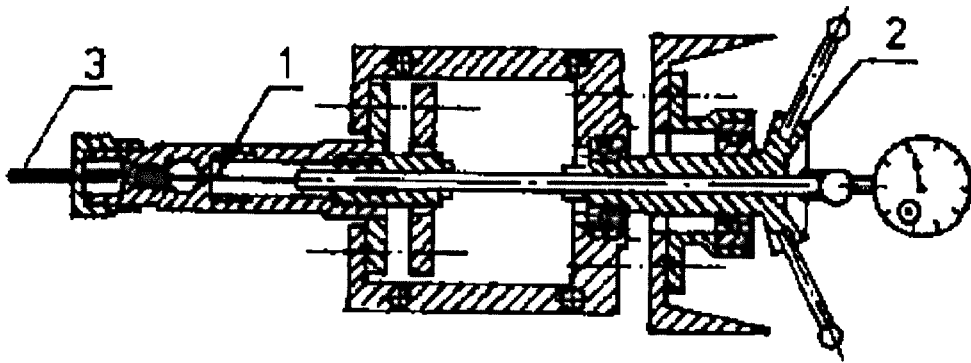


Figure 3.24: Typical needle contact device used for film thickness measurements.

1-Needle, 2-Driving mechanism, 3-Wall electrode.
(Taken from Kirillov *et al* (1978)).

The probe usually consists of a needle, electrically insulated except for the tip, mounted on a moveable rod that can be brought to the surface of the film. An electrode is placed flush on the wall on which the film flows, directly opposite the needle tip. When the needle tip makes contact with the surface of the film a conduction path is made between the needle and the wall electrode allowing this contact to be recorded electronically. A micrometer or some form of dial gauge can measure the previously calibrated distance from the wall electrode. This first contact will be with the wave peak, i.e. the maximum film thickness. Butterworth *et al.* (1972,1973) utilised an electrical pulse generator and pulse counter attached to the flush probe and needle respectively to determine the film/probe contact time from the pulses counted, with similar devices used in all other relevant applications. If subsequent measurements of the contact time are made for long time periods at several points spaced deeper within the film, a film thickness probability distribution can be established for that needle point placement. The probe will first register permanent contact with the film at the wave trough, giving a base film thickness. By evaluation of the area under the probability distribution curve, the time-averaged film thickness for that point can be determined. Subsequently, the probe can be easily moved to other positions along/around the wall allowing information on local and global phenomena to be obtained.

Calibration of the 'zero' position when the tip of the needle is in contact with the wall has presented some problems. Hewitt *et al.* (1962) found that a needle, which was under

the influence of a spring, could be slightly “bent” when being in placed in contact with the wall causing error of the order of tens of thousandths of an inch. They solved this by manipulating short lengths of standard rod around the inside of the tube and underneath the tip of the probe using a magnet outside the tube. They claim to have achieved reproducible fixing of the zero position within 0.0002 of an inch.

By far the biggest area of concern with the use of the needle contact probe is the distortion induced in the liquid flow field when the probe is immersed in the liquid, and in particular the phenomenon of contact hysteresis. This involves the needle being in extended contact with the liquid due to the ‘dragging-out’ of a filament of liquid when the wave subsides, and the continued detection of the conduction path until this filament of liquid is eventually broken. The magnitude of these liquid/needle contact problems will obviously depend on needle geometry and the surface tension, viscosity, density and velocity of the liquid. The effect of needle geometry can be reduced by the use of very fine wires or sewing needles, however, Yablounik & Khaimov (1972) studied the contact hysteresis phenomenon under free falling liquid film conditions and found that it may cause an increase in indicator readings as high as twenty six percent. The authors point out that this error value will decrease with increasing gas flows, however, it should also be noted that there will be an inevitable severe misdistribution of any dynamic gas flow by the contact probe located within the test section, questioning the applicability of the technique when utilised under these conditions.

Examples of needle-probe application in the determination of falling liquid film thickness measurements are given by:

Ishigai *et al.* (1972), Takahama & Kato (1980) and Fujita *et al.* (1986) for flow on the outer surface of a 60 mm diameter vertical tube, 45 mm diameter vertical tube and 45 mm diameter vertical tube with a downward step respectively.

Ito & Tomura (1979) and Nosoko *et al.* (1996) on flow down a 165 mm wide inclined plate, and 205 mm vertical plate respectively.

Strumolo *et al.* (1985) for flow on the inside of a 50 mm i.d. vertical pipe.

3.4.2 Hot-wire Method

This probe is based on the principle of the hot-wire anemometer traditionally utilised for velocity and wall-shear stress measurements. Two alternative approaches have been adopted by researchers in implementing a hot-wire probe for falling film thickness measurement.

Ishigai *et al.* (1972) used a technique identical in application to that of the needle contact probe (Section 3.4.1), simply replacing the needle probe with a hot-wire probe. Their motivation was to extend the application of the needle contact probe to liquids with low conductivities. Their experimental arrangement is shown schematically in Figure 3.25.

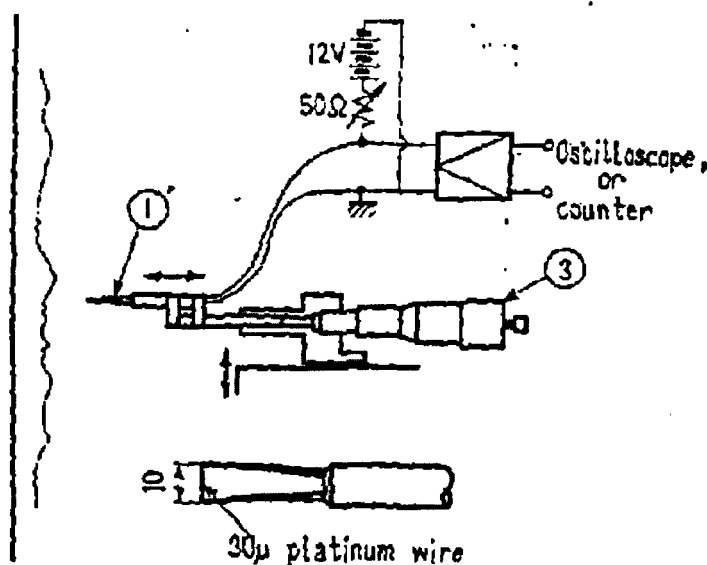


Figure 3.25: Schematic of a hot wire probe. Bottom section of diagram shows detail of (1). (3)-micrometer head.
(Taken from Ishigai *et al.* (1972))

In this case, when the constant current heated 30 micron platinum wire touches the film surface, the wire's temperature and thus resistance fall sharply due to the enhanced heat transfer capabilities of the liquid relative to air, and a pulse signal is given outputted to the counter. Clearly, this method has all the difficulties and limitations associated with needle contact probes, and these are presented within that section of review.

Lyu & Mudawar (1991) utilised an alternative hot-wire approach, consisting of a 0.0254mm diameter platinum-10% rhodium wire stretched across the gas-liquid interface

and heated by a constant current. This probe arrangement and support is shown schematically in Figure 3.26.

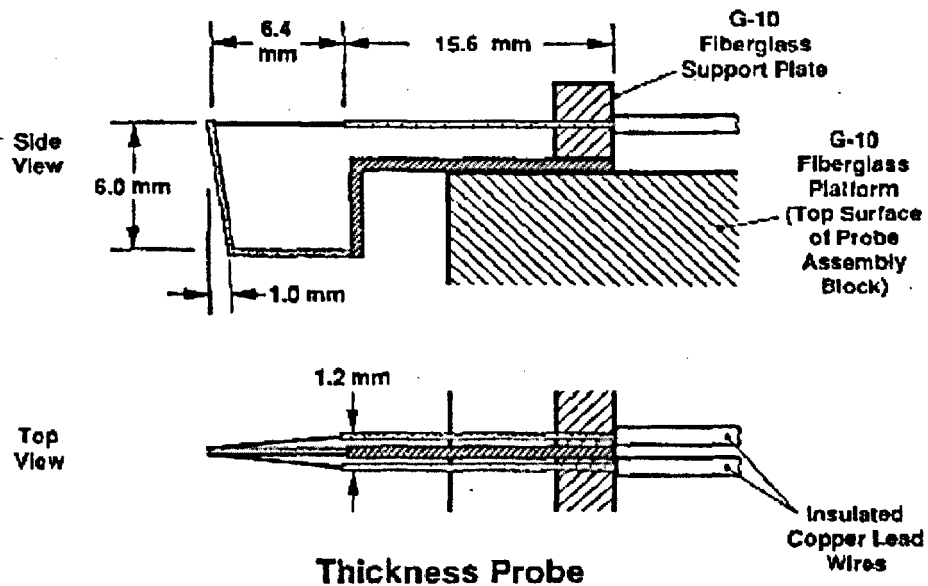


Figure 3.26: Schematic diagram of the thickness probe.
(Taken from Lyu & Mudawar (1991))

As with the alternative approach, the technique relies on the temperature/resistance of the measuring wire depending on the greatly differing heat transfer properties of the liquid and air. However, in this arrangement the voltage signal becomes a function of the film thickness due to the strong dependency of the total electrical resistance on the length of wire submerged within the liquid. A disadvantage of this probe arrangement for film thickness measurement is that the heat transfer between the wire and liquid is also a function of the velocity of the film, the basis of the application of hot-wire probes in local velocity measurements. Therefore, this method requires in situ calibration at every flow rate under study, and this was achieved using a standard needle contact probe (3.4.1) before each run. Another obvious disadvantage of the technique is the intrusive nature of the probe. On a positive note, the authors claim the measurement resolution and response time of the thickness probe to be determined at 0.05 mm and 0.14 ms, respectively. Disappointingly, no comparative data with other measurement techniques was presented.

3.4.3 Shadow Method

Kapitsa & Kapitsa (1949) developed this measurement technique for use on pioneering experiments on wave flow of viscous falling films. The technique is based on the focusing by a lens of the rays of a powerful light source (mercury lamp) on the outside surface of the measuring test section. The rays illuminate the test section in one point and hit the liquid film tangentially, causing the formation of a shadow in the shape of the film interface. Arnold & Hewitt (1967), in experiments to determine the influence of fluorescein solutions used in the fluorescence technique (3.4.6) on wave behaviour, captured these silhouettes of the film interface using a microscope arrangement and a high speed camera film exposed at a rate of 1000 frames per second. Calibration to obtain actual film thickness measurements was achieved by exposing a number of frames with the measuring section dry at the beginning of each run. Using a pointer at a known distance from the dry surface as a reference allows the position of the interface to be determined in the rest of the frames. A similar shadow photographic application is reported by Belkin *et al.* (1959) for film thickness measurements of a film falling on the outer surface of a 0.934" and 0.935" (~24 mm) diameter rod.

Clearly, the data analysis requirements for these early applications of the shadow method are laborious. Nakoryakov *et al.* (1976), in a study of roll waves on a vertical film of fluid, reported a shadow-measuring device, which enabled the acquisition of instantaneous film thickness measurements that could be recorded electronically. This device was refined by Alekseenko *et al.* (1985a) for the study of wave formation on the outside of a 60mm diameter vertical tube, and a schematic of their measurement device is given in Figure 3.27.

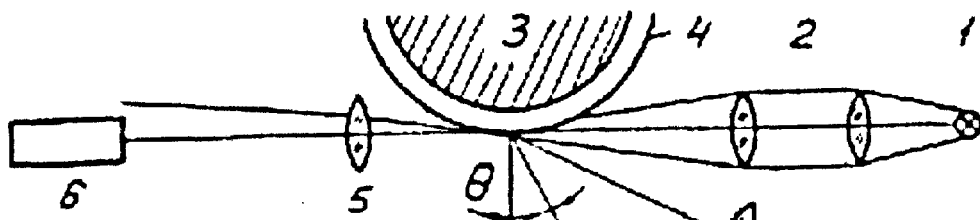


Figure 3.27: Schematic of film thickness measurements by shadow method. 1) Mercury lamp 2) Condenser 3) Test section 4) Liquid film 5) Objective lens 6) Photoelectron multiplier. (Taken from Alekseenko *et al.* (1985a))

In this arrangement, the fluctuations of the film shadow are intensified by an objective lens (5) and projected through a narrow slit to a photoelectron multiplier (6) and recorded in the analog or digital form. The potential advantages of the technique are the non-disturbance of the flow, very high spatial resolutions achieved and low measuring error (claimed to be in the region of 0.5 to 5 percent). Calibration is often a challenging experimental consideration for optically based techniques; however, no information on their method is provided.

3.4.4 Fiber-Optic Techniques

The use of fiber-optic techniques for the measurement of film thickness was first considered by Ohba *et al.* (1984), as an alternative to the dominant impedance (*i.e.* conductance and capacitance) probes which cannot be utilised in certain environments. Examples of these environments are when dielectric fluids, such as insulator oil Freon, are to be used and when there is a lot of electrical noise, for example, in the case of an evaporative cooled cable for power transmission. A schematic of their multi fiber-optic measurement system can be seen in Figure 3.28.

The sensor pick-up head is mounted flush to the wall surface on which the film flows. This pick-up head consists of seven optical fibres joined tightly to each other in parallel, with the six receiving fibers surround the transmitting fiber. Light, emitted by the laser through the objective lens, travels along the transmitting fiber into the liquid and is reflected at the interfacial surface. This reflected light is then collected by the six receiving fibers, each equipped with a photodetector at its opposite end. Light intensity received by each of the fibers has a different value corresponding to the position of the fiber, and is dependent on both film thickness and the inclination angle to the surface with respect to the wall surface. Thus, if the output from the six photodetectors is calibrated and processed, inclination angle and more importantly film thickness can be evaluated. In this study the authors reported the use of two types of graded fibers, with either a fifty micron or eighty micron core diameter.

Ohba & Origuchi (1985) present a technique for calibration of the light intensity received by each fiber as a function of the thickness and the inclination angle of the liquid film. The technique consists of theoretical analysis, based on the geometrical optics and

knowledge of the beam emitted and by experimental work where the liquid film is replaced by a plane mirror surface.

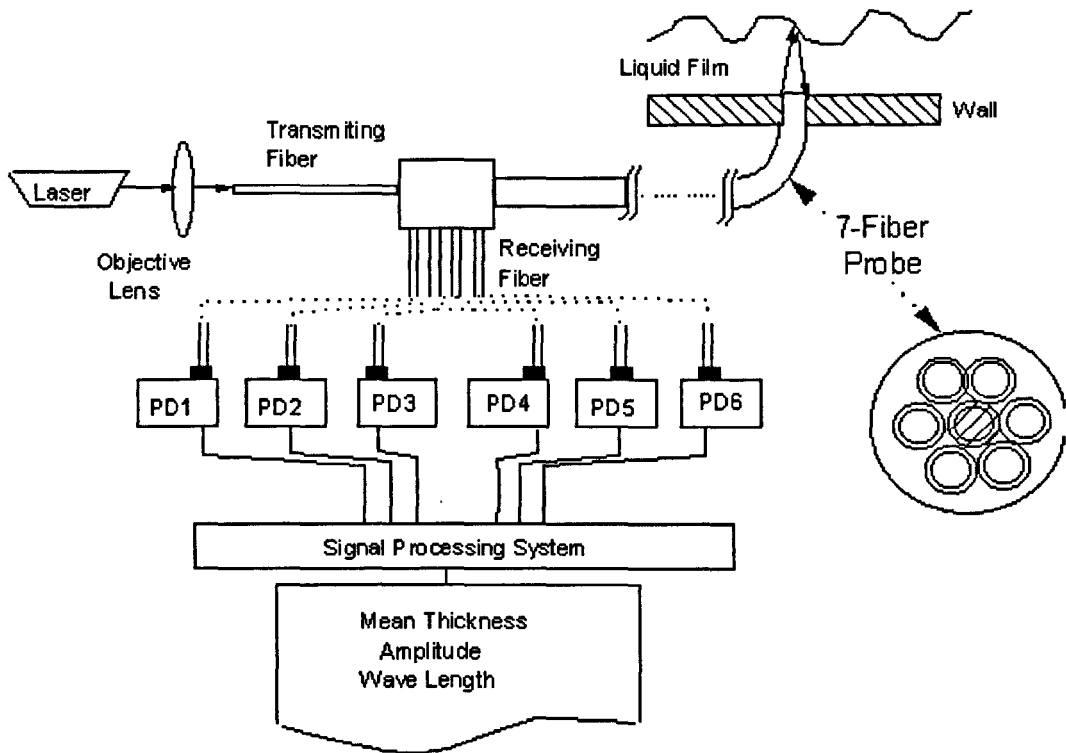


Figure 3.28: Multi fiber-optic measurement system.
(Taken from Ohba *et al.* (1984))

The viability of this measurement technique was investigated further by Ohba *et al.* (1985) using a computer simulation to model various waveforms and predict the sensor's response. The authors believed that computer simulations could accurately predict the sensor response because the theoretical model used to obtain the relationship between light intensity and film thickness accurately expressed the actual phenomenon. However, Than *et al.* (1993) is critical of this theoretical model's development using a mirror surface by an image method to represent the liquid film, as this neglects the important effect of interfacial refraction. Subsequently, Than *et al.* (1993) reported their development of a theoretical model which does account for the phenomenon of interfacial refraction.

The other benefit of computer simulations of multi-fiber optic sensors was in highlighting the sensor's ineffectiveness at accurately measuring films thinner than about one millimetre. Hence, Ohba *et al.* (1992) developed a mono-fiber optic film sensor to

improve film thickness measurements in this range. The mono-fiber optic sensor is identical to the multi-fiber optic sensor in application but only consists of one fiber that acts as both transmitter and receiver. Naturally, it only allows the measurement of the thickness of the film at the crest and trough of the interfacial wave where the inclination angle of the surface is zero. Similar calibration techniques and computer simulation work to those used for multi-fiber sensors are reported. Additionally, the authors report a study of the sensors effectiveness in film thickness measurements in annular flow in a vertical tube, and conclude the mono-fibers range of thickness measurement to be between about 0.02mm to 2mm.

Recently, Yu & Tso (1995) have developed simulation software for both multi-fiber and mono-fiber studies. They used an approach based on the principle of the virtual image using vector analysis and claim good agreement with reported measurements. They conclude that an appropriate range for use of the multi-fiber optic sensor is between 1 - 4 mm and that below 1 mm the mono-fiber sensor should be preferred, and these ranges are close agreement to the figures quoted by Ohba and his co-workers. However, they also remark that these values are probably highly dependent on the aperture of the fibers used.

3.4.5 Light Absorption Techniques

Light absorption techniques are based on the well known Lambert-Beer Law which states that the intensity I of a light beam after passing through a liquid layer of thickness t can be described by the following equation:

$$I = I_0 e^{-kt} \quad (3.18)$$

where, I_0 is the original intensity and k is the absorption coefficient.

In practice, this traditionally involves the passing of a monochromatic light beam through a liquid film and detecting the intensity of received light on the other side of the film by some form of photo device, and Figure 3.29 illustrates this with an early experimental arrangement.

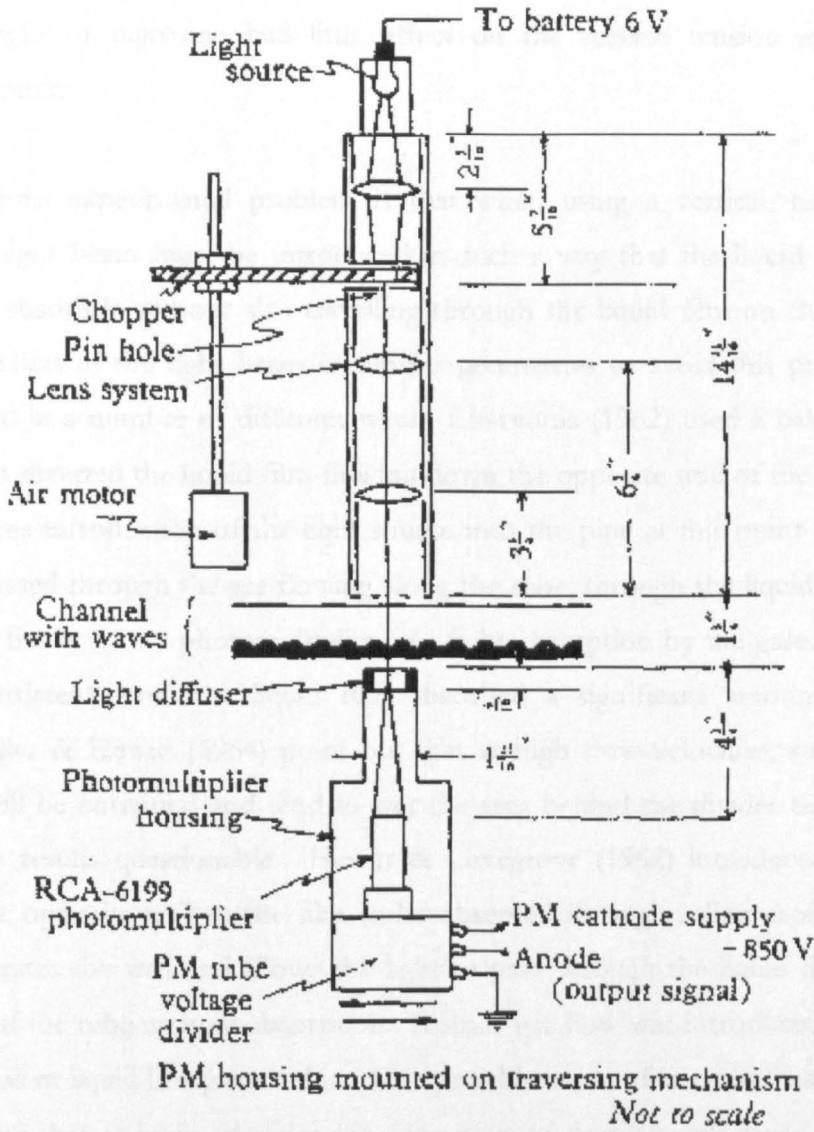


Figure 3.29: Lens and photomultiplier arrangement.
 (Taken from Lilleht & Hanratty (1961))

Practical problems in the implementation of the technique have shaped its design. One such problem is that the absorption coefficient, k , of typical test liquids, such as water, for white light is too low to be capable of detecting small changes in the thickness of the liquid. This problem has been traditionally solved by the additions of small quantities of dye to the liquid film to dramatically increase the absorption of white light, however, this is potentially an area of concern about the validity of the technique. The addition of a dyestuff could potentially alter the test liquid properties, and of particular concern is the fact that a number of dyestuffs are very surface active and could artificially effect the interfacial shape. The most common choice of dye reported in the literature is nigrosine,

a black dye, as a study by Crozier *et al.* (1961) showed that concentrations as high as 2.17% by weight of nigrosine had little effect on the surface tension and density properties of water.

Another potential experimental problem is that when using a vertical, tubular pipe geometry the light beam must be introduced in such a way that the liquid film being measured can absorb it without also travelling through the liquid film on the opposite wall. Introduction of the light beam in tubular geometries to avoid this problem has been attempted in a number of different ways. Charvonia (1962) used a bakelite “film divider”, which diverted the liquid film flowing down the opposite wall of the glass tube, to allow the free introduction of the light source into the pipe at this point. The light source then passed through the gas flowing along the tube, through the liquid film to be measured and finally to the photomultiplier. As light absorption by the gaseous flow is virtually non-existent, only the liquid film absorbed a significant amount of light. However, Collier & Hewitt (1964) point out that at high flow velocities, some of the liquid phase will be entrained and tend to wet the area behind the divider thus making the absorption results questionable. Hewitt & Lovegrove (1962) introduced the light beam from the opposite wall to the film to be observed through a fine capillary. The capillary penetrates the wall and allows the light to pass through the liquid film on the opposite wall of the tube without absorption. A small gas flow was introduced along the capillary to prevent liquid being sucked in. One possible cause of error in these methods is the possibility that at high velocities the formation of droplets will cause significant absorption of the light before it reaches the liquid film. In order to avoid this potential problem, Stainthorp & Allen (1965) used an optical system which was aligned so that two narrow beams of light were brought to focus just inside the inner wall of the test tube on which the film to be examined flows. The light from each beam was collected by photomultipliers positioned within the core of the tube thus eliminating the influence of the film on the opposite wall and the majority of the gaseous region. Clegg (1969) employed a simpler solution to the problems associated with the introduction of the light beam. The test section used was not annular, but of rectangular cross-section. The nigrosine dyed film was allowed to pass down a vertical glass sheet that was illuminated by a flash tube through a diffuse screen, used secondarily to enclose the gas flow. The optical positioning requirements of such a configuration are discussed in detail when considering this techniques spatial counterpart (Section 3.5.1).

Probably the largest area of concern in the utilisation of the light absorption technique in film thickness measurements is the reduction of the intensity of light received by the detector by means other than absorption, *i.e.* scattering and refraction at the air/liquid interface. In wavy flow, the surface of the film can be rough enough so that a potentially significant amount of the light contacting it will be scattered and refracted away from the detector. If the angle of the wave is sufficiently acute, even reflection of the light can become significant. Hewitt & Lovegrove (1962) investigated this phenomenon for vertical upward flow by comparing the light absorption of dyed and un-dyed water and found that there was little difference, indicating non-absorption elements were completely dominant. However, Lilleleht & Hanratty (1961) carried out studies of non-absorptive loss of intensity in their system, stratified horizontal flow, and found it to be only of the order of a few percent. This apparent contradiction was discussed by Hsu *et al.* (1969) in their review, and they came to the same conclusion as Hewitt & Lovegrove that the films created by Lilleleht & Hanratty in their study were significantly thicker than the thin films of Hewitt & Lovegrove. This perceived non-applicability of the technique for point measurements in thin liquid films resulted in its abandonment by Hewitt and his co-workers, and led them into the development of the fluorescent technique (see Section 3.4.6), a modification of the light absorption technique where both incident and removed beams are in line from the same side. In defence of the traditional absorption technique, it should be also noted that other studies on falling films using this technique (Charvonia (1961), Stainthorp & Allen (1965), Stainthorp & Batt (1967), Clegg (1969), Portalski & Clegg (1972) and Azzopardi (1977)), generally report results that compare favourably with results from more established techniques.

Calibration of the light absorption techniques detailed above was most commonly achieved statically using a specially designed calibration cell. The cell is filled with the dyed liquid under study and either the cell is capable of variable known thickness or of fixed thickness and the dye concentration is varied. In each case the light absorption equipment allows a simple calibration curve between thickness and received intensity to be established.

More recently, a novel light absorption technique has been developed. The technique was first demonstrated by Wittig *et al.* (1992) and subsequently utilised by co-workers

(Samenfink *et al.* (1996), Elsäßer *et al.* (1997,1998) and Roskamp *et al.* (1998)) in studies on shear driven liquid films. A simple schematic of their light absorption methodology is given in Figure 3.30.

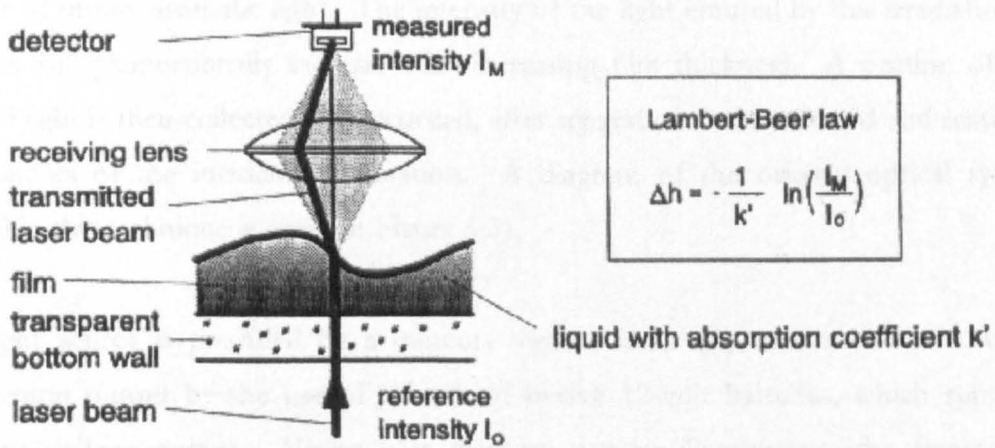


Figure 3.30: Light absorption methodology.

(Taken from Elsäßer *et al.* (1997))

In this arrangement, a laser using a near infra-red wavelength of 1462 nm replaces the white light source. At this wavelength strong absorption effects occur in liquids such as water, water/glycerin or alcohols without the need of enhancement with the addition of a dye. For example, a 1mm thick water film leads to an intensity reduction of more than 95%, enabling high-accuracy thin film thickness measurements. Additionally, a correction laser beam of near visible wavelength, 673 nm, is superposed onto the infrared beam in the system. The light from this beam is virtually unabsorbed, as the absorption coefficient for visible light is very low. This visible light beam can therefore be used for intensity loss detection in the optical path or reflection loss detection at the air/film interface, and the intensity signal of the infrared laser beam can be corrected with this visible light signal to improve overall accuracy. Present applications of this laser light absorption technique are limited to horizontal liquid films in rectangular ducts, and viability of the technique in vertical flows to date is untested.

3.4.6 Fluorescence Technique

As stated in the review of the light absorption technique in Section 3.4.5, the fluorescence technique was developed and first reported by Hewitt *et al.* (1964) as a

replacement for the traditional light absorption approach which was believed by these workers not to be applicable to thin liquid films. The principle of the technique is that a fluorescent dyestuff is added (e.g. 0.1g/litre of sodium fluorescein by Hewitt *et al.* (1964)) into the circulating liquid that forms the liquid film under study and this is irradiated with a beam of monochromatic light. The intensity of the light emitted by this irradiation of the film will proportionally increase with increasing film thickness. A portion of this emitted light is then collected and recorded, after separation from reflected and scattered components of the incident illumination. A diagram of the original optical system applied in this technique is given in Figure 3.31.

The light source is provided by a mercury vapour lamp (A) maintained at constant illumination output by the use of a bank of twelve 12-volt batteries, which supply a constant voltage output. Under blue mercury vapour illumination, the fluorescent dyestuff used, sodium fluorescein, has a peak emission observed in the green band. Therefore, to achieve a monochromatic beam, the light from the lamp is passed through a condensing lens and glass filters (B) to filter out the ultra-violet and mercury green components. The resulting blue light is passed through prisms (C), reflected from a half-silvered mirror (D) and passes into an objective lens system (E) which focuses the incident beam of blue light into a narrow cone through the wall of the channel (F) and into the liquid film (G). The incident beam of blue light causes an isotropic fluorescent emission from the dissolved dyestuff, which is reflected partially back into the objective lens system, through the half-silvered mirror and into the barrel of the spectrometer (H). The spectrometer separates the emitted light from the portion of the incident light that was reflected and scattered back and the intensity is measured using the photomultiplier (I). Later studies by researchers using this technique, such as Anderson & Hills (1974), replaced the spectrometer with a narrow-band-pass-filter arrangement, and this simplifies greatly the instrumentation required. The output from the photomultiplier is fed to a microammeter (J) or recorded using an oscilloscope and camera system (K). The whole of the flow tube, apart from a window where the incident beam can enter, is blacked out in order to eliminate the effect of neighbouring light. A full description of the method can be obtained in the patent submitted by Hewitt (1966).

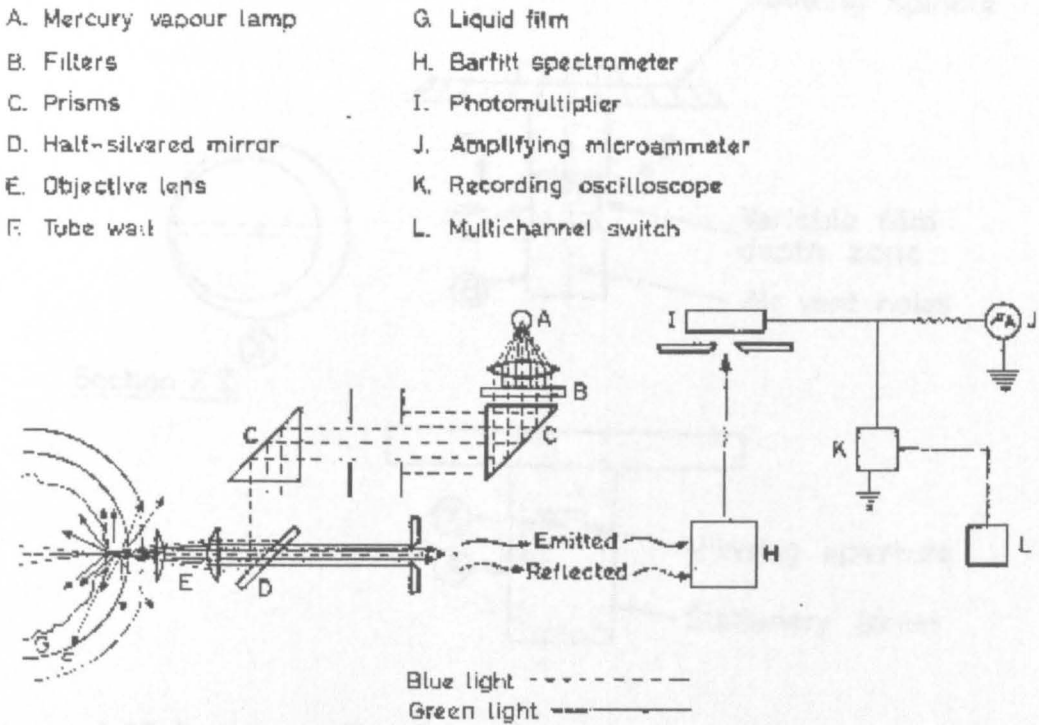


Figure 3.31: Fluorescence technique for film thickness measurement.
(Taken from Hewitt *et al.* (1964)).

Since its conception, it was realised that the response of this fluorescence technique, as with any optical technique, is critically linked to the flow conditions and physiochemical properties of the film under study. With this in mind, calibration was attempted by simulating the exact geometry of the tube and liquid properties of the film. Hewitt *et al.* (1964) used a reference tube, with identical geometry and liquid concentration to that used in their experimental apparatus. Additionally, a wetting agent was added to the liquid to suppress wave growth (i.e. give a laminar film) and the film thickness was calculated or directly measured using the needle contact method (see Section 3.4.1). This gave them accurate and reproducible calibrations, however, they reported that it was not possible to obtain thickness measurements above 0.03" (0.76 mm) as surface waves began to appear, and distort the thickness value, even with the addition of wetting agents. To obtain calibrated thickness measurements above 0.03" (0.76 mm) a rotating mechanical calibration cell was developed. A schematic of this cell is given in Figure 3.32.

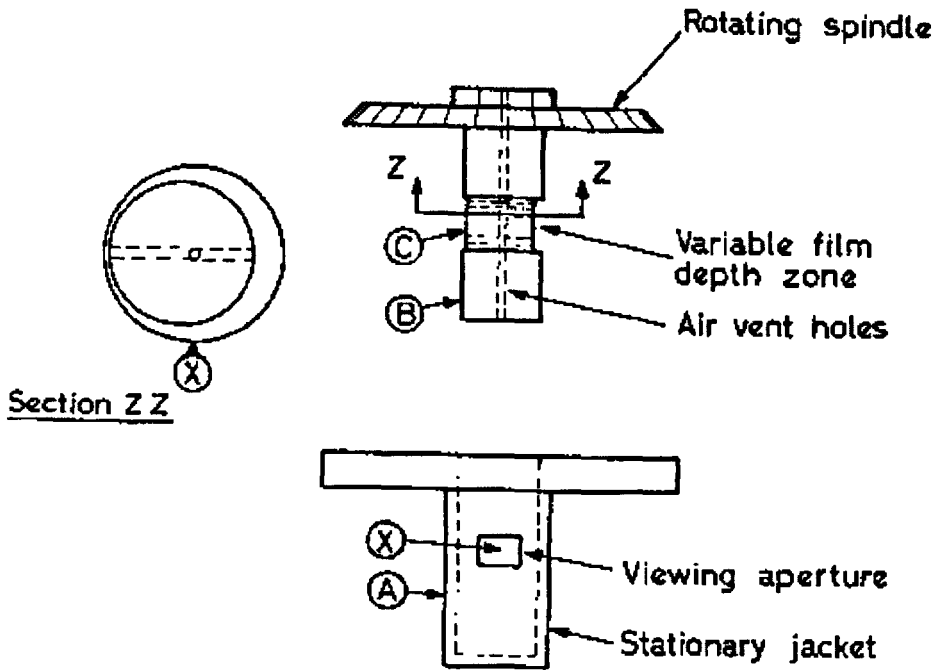


Figure 3.32: Rotating calibration cell.
(Taken from Hewitt *et al.* (1964)).

It consists of a cylindrical pot (A) of identical geometry and material of construction to their experimental tube with a close fitting transparent plug (B) inside. Part of the plug was machined away to leave an eccentric rod (C), which allows the introduction of the working fluid between the rod and pot. As the plug is rotated, the distance between the rod and pot (point X) will vary cyclically at known film thickness values. The corresponding intensity can be metered using the spectrometer and recording arrangement as used for the experimental set-up. A full range of calibration measurements can be achieved by using plugs of various sizes. Most future studies have continued the use of, or derivatives of, the rotating cell as the primary calibration device for the fluorescent technique.

Hewitt *et al.* (1964) also considered and examined some of the possible objections or disadvantages involved in using the fluorescence technique. These include:

- (i) The effect of the film on the opposing part of the tube. The importance of this film was tested by using a blackened plate down the centre of the

tube. It was discovered that the blackened plate made no appreciable difference to the output signal. Therefore, it was concluded from this that the film on the opposite surface has no influence on the results.

- (ii) The reflection of mercury green light. It was observed that the filters cannot completely remove the entire green band from the incident illumination or the part reflected back. The influence of the remaining green light, which will also be proportional to film thickness, was tested by using pure water in the flow tube. There was found to be no significant difference over a wide range of flowrates.
- (iii) The influence of the dyestuff on surface phenomena. It is widely accepted that even small quantities of surfactants can have dramatic effects on interfacial phenomenon. Comparing the surface tension, viscosity and density values of the working fluid with the corresponding values for pure water was used to test the influence of the sodium fluorescein on interfacial properties, and no appreciable difference was found. Observation also indicated no visible difference caused by the dye on the frequency and velocity of the large disturbance waves.

Azzopardi (1978) carried out further critical examination of the fluorescence technique for film thickness measurement. He noted that the photomultiplier output/film thickness relationship was not linear but dependent on the dye concentration. He also investigated the theoretical basis for the technique and developed an expression for the intensity, I , of fluorescent light received by the detector. As with standard light absorption techniques, this theoretical basis assumes that absorption occurs according to the Lambert-Beer's law:

$$I' = I_0 e^{-k_1 cx} \quad (3.19)$$

where, I' , I_0 are the intensities at $x = x$ and $x = 0$ respectively, k_1 is the absorption coefficient, c is the dye concentration and x is the distance into the film. By considering a thin element of thickness dx at x and considering the fluorescence response, you arrive at the following expression:

$$I = \int_0^d \frac{EaI_0k_1c}{1+k_2c} \exp(-k_1cx - k_3\sqrt{cx} + k_4cx) dx \quad (3.20)$$

where, I_0 is the incident intensity, E the fluorescence efficiency, a the fraction of fluorescence received by the detector, k_2 a self-quenching coefficient, k_3 and k_4 are self-absorption coefficients and d is the film thickness. This integration can then be carried out numerically, and the resulting values were found to compare favourably with experimental calibration data.

More recently, a further development of the fluorescence technique is reported by Schmitt *et al.* (1982), with later refinements by Driscoll *et al.* (1992). The optical arrangement was further simplified by creating the monochromatic excitation beam using an argon laser operating in the green range. Their work was motivated by developing a technique for time-resolved measurements of liquid film thickness on the tip of air-blast atomisers, however, adaptation for falling liquid films should not be difficult due to the similar film thickness and interface phenomena under consideration.

Hewitt & Nicholls (1969) present favourably comparable data for the simultaneous application of this fluorescent and a conductance technique in film thickness measurements in upward annular two-phase flow and Anderson & Hills (1974) present a study using the technique in bends. However, in the literature the application of this technique in falling films appears limited to a novel adaptation by Schwanbom *et al.* (1971). The motivation of this application was to obtain simultaneous film thickness and penetration level of absorption of an alkaline gas into a falling acid liquid film (*i.e.* NH_3/HNO_3 (*Aqueous*) system. The practical application of this 'double-ray' technique is similar to the original technique developed by Hewitt. They replaced the fluorescein dyestuff with acridine, a dye whose fluorescence response is pH dependent. The film is exposed to ultraviolet light and a lens collects the emitted light before being divided into two-parts which are filtered and focused on a photomultiplier. Even though the emissivity of acridine shows different characteristics throughout the pH range, at wavelength λ_1 (see Figure 3.33) the emissivity is independent of pH (the isoemissive point). Combined with knowledge at another filtered wavelength, *e.g.* λ_2 , outside the

range of acid pH's, allows the simultaneous measurement of the film thickness and absorption/neutralisation layer thickness during gas absorption into the film

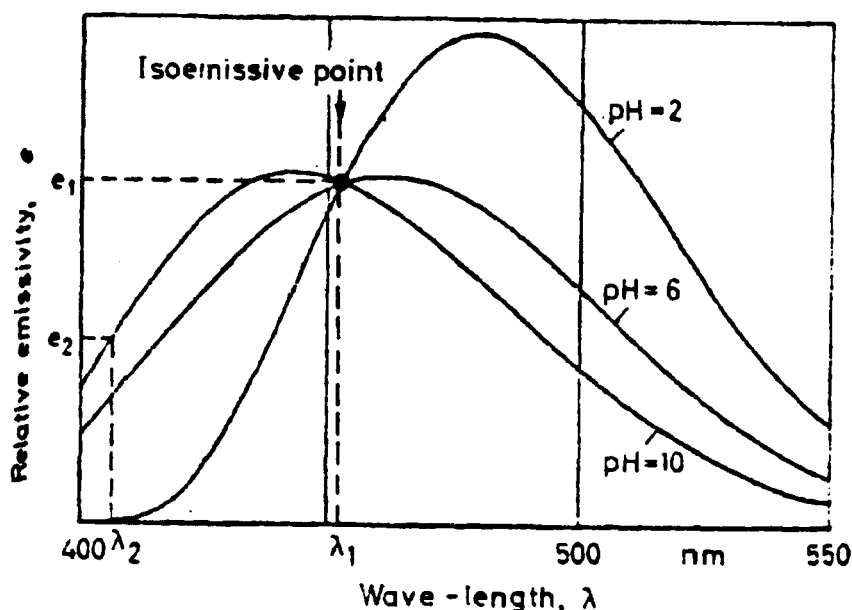


Figure 3.33: Emission spectra of acridine (10^{-5} moles/l) stimulated by ultraviolet radiation (365 nm). Taken from Schwanbom *et al* (1971).

Azzopardi (1978) also critically examined the double-ray technique, with his major concern being the validity of the method if there is a non-uniform distribution of the dyestuff within the liquid film. This non-uniform dye distribution is probable in a reaction system such as the one described. He concluded that until further information was made available any enthusiasm for the technique should be tempered.

3.4.7 Laser Scattering Method

This optical method was proposed and first reported by Salazar & Marschall (1975) as an alternative technique to capacitance probes (3.3.1), which they believed to have inherent disadvantages (*i.e.* non-linear response and poor resolution for small waves). The principle behind the technique is that film thickness is proportional to, and can be measured by detecting changes in, the length of a column of scattered light shining through a liquid film and transparent surface. Figure 3.34 shows schematically the implementation of this principle.

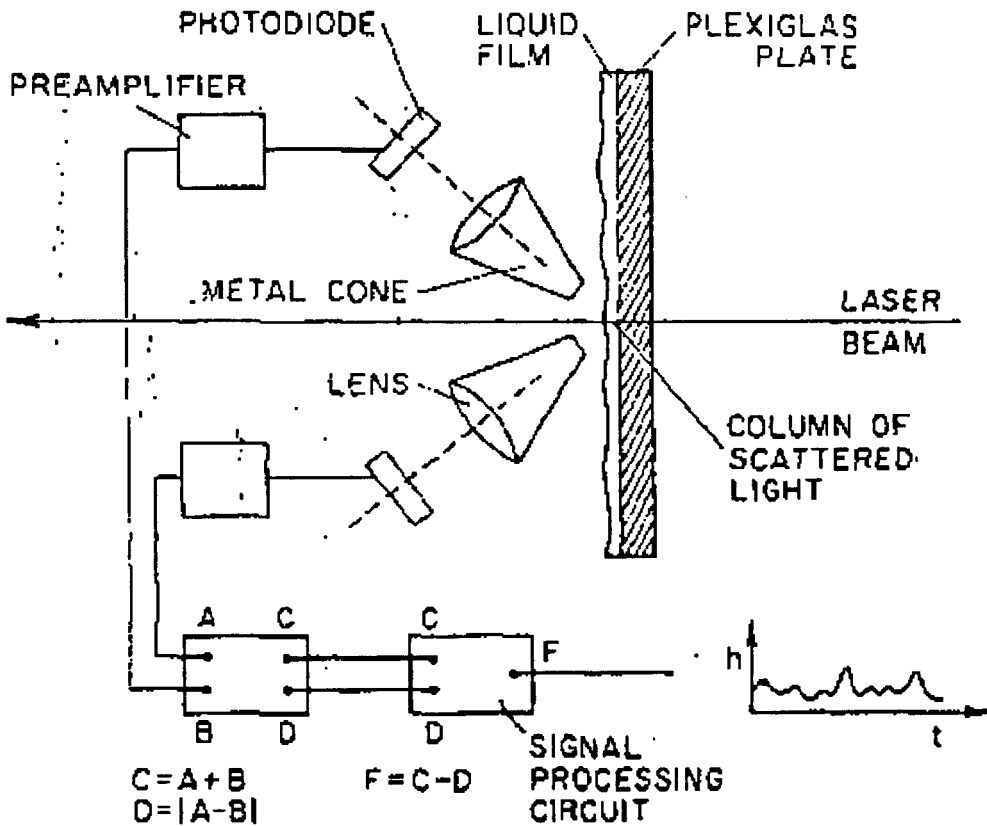


Figure 3.34: Laser scattering film thickness measurement system.
(Taken from Salazar & Marschall (1975))

A He-Ne laser beam, approximately 1.5mm in diameter, is generated and passed through a liquid film falling on a Plexiglas plate. The laser beam is visible due to particle and molecular scattering. Primarily, spherical latex particles, average diameter of 0.087 microns and 0.005 % particle volume to liquid volume, suspended in the film produce this scattering. The particles small size and spherical shape was chosen to:

- (i) Minimise the effect of the effect of viewing the scattered light through a distorting interface (the water surface),
- (ii) Prevent migration of the particles across streamlines creating a significant concentration gradient, and
- (iii) Ensure particle orientation has no effect on scattering intensity.

The particle concentration was chosen to optimise the scattering intensity against particle interference of the film. The light detection instrumentation employs a short focal lens, 25mm in diameter with a 25mm focal length that produces an image of the column of scattered light on the face of a photodiode. A black metal cone with a 6mm-diameter hole at the apex is used over the lens to help ensure that stray reflections do not strike photodiode surface. The measurements are taken in a darkened room to minimise the external light falling on the photodiode. Two identical photodetector systems are used to eliminate the effect of specular reflections from the irregular liquid surface that would only strike one detector at a time. This is achieved by an electronic circuit that subtracts the difference between the two signals from the sum, resulting in a signal that is proportional to the lower photodiode voltage that should represent the effect of scattering only. As the film thickness changes, the column of light changes in length and the amount of light received by the photodiode changes also, and by monitoring the output of the system a record of film thickness can be obtained after calibration.

Original calibration attempts were reportedly achieved with a range of horizontal static films of liquid measured by a micrometer mounted above the film to establish a calibration curve. When Salazar & Marschall (1978a) utilised a more sophisticated calibration, using the optical equipment set up on the test facility, the authors reportedly ran into difficulty. They found it was not possible to keep a constant signal for zero film thickness and witnessed large shifts in the calibration curve throughout the test. They came to the conclusion that slight unintentional motion of the laser during the test was responsible for these large shifts. However, as the calibration curve gradient was observed to remain constant, they found it possible to set up the film thickness correlation by means of a reference value, measured in a draining film before every measurement.

Salazar & Marschall (1978a, 1978b) report application of the laser scattering method in falling film thickness measurements down a 35.67cm wide Plexiglas plate. The authors report good correlation with data obtained by Portalski & Clegg (1972) using the light absorption method.

3.4.8 Interferometric Methods

Interferometric methods rely on the way in which light reflectivity changes as a function of the incident angle at an interface between two differing media. Unterberg (1961) reported an early application of an optical interference method for measuring the thickness of liquid film flow. The method consisted of photographing and measuring the fringes appearing when a wide beam of monochromatic light illuminates a film. Interference occurs at the superposition of light beams reflected from mirror wall and film surface. However, the author reports that this application is limited to film thickness measurements not exceeding 25 microns.

More recent applications for liquid film thickness measurement, have used more sophisticated light generation and optics, and one such arrangement is shown schematically in Figure 3.35.

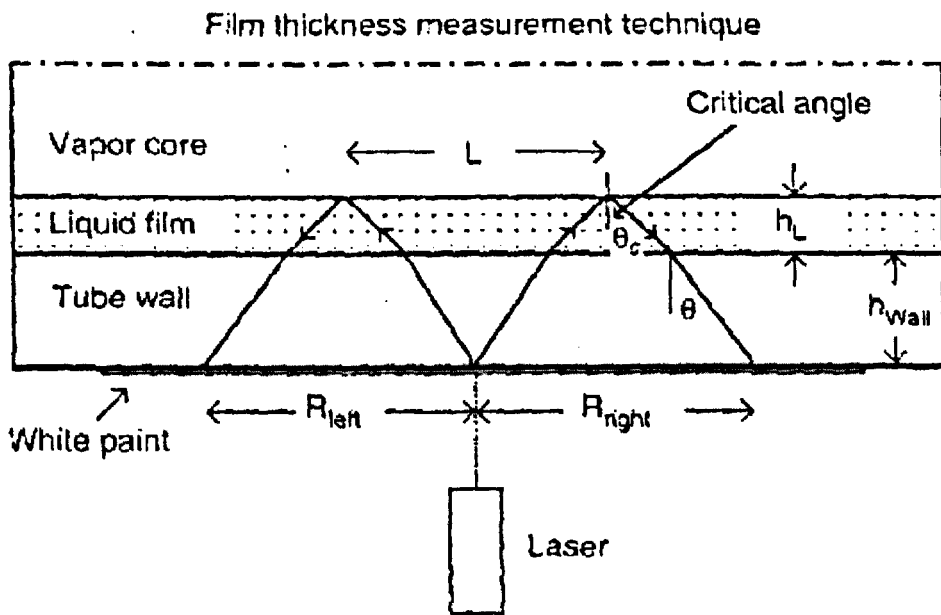


Figure 3.35: Interferometric film thickness measurement technique.
(Taken from Hurlburt & Newell (1996))

Hurlburt & Newell (1996) utilised a 5 mW He-Ne laser aimed at a transparent white coating attached to the surface of a clear 1" (25mm) i.d. horizontal tube, which generates a point source of light with diffuse light travelling hemispherically toward the liquid-vapour interface. Light rays at an angle less than the critical angle are primarily

transmitted with the remainder reflected back to the white coating. The distance from the point source that this reflected light reaches the white coating, R , can be geometrically related to the film thickness, h_L , by the following expression:

$$R = R_0 + 2h_L \tan \theta_c \quad (3.21)$$

where, θ_c is the critical angle, and R_0 is the contribution due to wall thickness given by:

$$R_0 = 2h_{wall} \tan \theta \quad (3.22)$$

where, h_{wall} is wall thickness.

In reality, this contribution is constant and can simply be found by measuring R with no liquid in the tube. The reflected light images were recorded using a video camera with the shutter speed set between 1/1000 and 1/10000 of a second, with approximately 16 sample frames processed at each operating condition. To check the validity of the technique, the film thickness of stagnant water films were measured using the technique and compared to measurements taken using callipers. It is reported that over the range of measurements considered (0.5 - 1.2cm) the methods showed agreement within 1%. However, the authors do discuss some potential significant errors and limitations inherent to the technique, with the major of these being limitation to flows which surface slopes less than about five degrees. This concern is of particular relevance as surface slope higher than five degrees are common in many of the interfacial structures observed on falling films with and without the influence of a dynamic airflow. Shedd & Newell (1998) report further refinements to this method to reduce the cost of implementation and automate the data collection. The authors replaced the laser with a relatively low cost, high-brightness light emitting diode and automated the system by capturing the image of the light reflected from the liquid surface by a charge couple device camera, digitising the image by a framegrabber board and processing it using custom software. They claimed to have produced film thickness measurements using this system that are accurate to within 0.01mm and present data obtained in horizontal annular flow for both rectangular and circular test sections.

The application of similar interferometric methods to film thickness measurement of falling liquid films is reported by Nozhat (1997) and Karimi & Kawaji (1996) and to draining liquid films by Irons (1995) and Keeley *et al.* (1989). In these studies the interference pattern was captured photographically or by use of position sensitive photodetector cells. Coney *et al.* (1989) reports a novel dual laser beam interferometric method for wavy film thickness measurement. Similar in application to single laser beam interferometric methods, the extra laser beam removes the necessity of a reflective surface and is capable of giving information on the instantaneous surface slope.

3.5 SPATIAL METHODS

3.5.1 Light Absorption

Clegg (1969) reports probably the first example of the application of a spatial method to liquid film thickness measurement. The technique is an extension of a light absorption method reviewed in Section 3.4.5, and was primarily developed to investigate film thickness (Clegg (1969)) and interfacial area increase (Portalski & Clegg (1971)) of falling liquid films on wetted wall columns and was later adapted by Azzopardi (1977) for film thickness measurement of falling liquid films in a cross air-flow. The principle of the technique is the acquisition of photographs of a dyed flow, with the light density of the photographed film recorded at any point being proportional to the amount of dye and therefore the thickness of the film at that point. A schematic of the experimental arrangement utilised by Clegg (1969) is given in Figure 3.36.

A nigrosine dyed film was allowed to pass down a vertical glass sheet of rectangular cross-section (21”(W) x 7/8”(D) x 84”(H)) that was illuminated by a flash tube through a diffuse screen, used secondarily to enclose the gas flow for co-current and counter-current airflow investigations. The rectangular column is used to eliminate the light introduction and optical difficulties encountered with tubular geometries, reviewed in Section 3.4.5. A 5” by 7” plate camera was used, with the shutter synchronised with the 200 μ sec duration flash. The camera is fitted with graduated concentric filter to provide an even illumination of the image. Both camera and flash could be raised or lowered in order to photograph any region of the column. The developed photographic plates were scanned by a densitometer coupled to a data logger for subsequent feeding into a computer. The densitometer signal was sampled every 0.25 seconds, which corresponds

to a movement of 0.265mm on the photographic plate and 0.755mm on the wetted wall column.

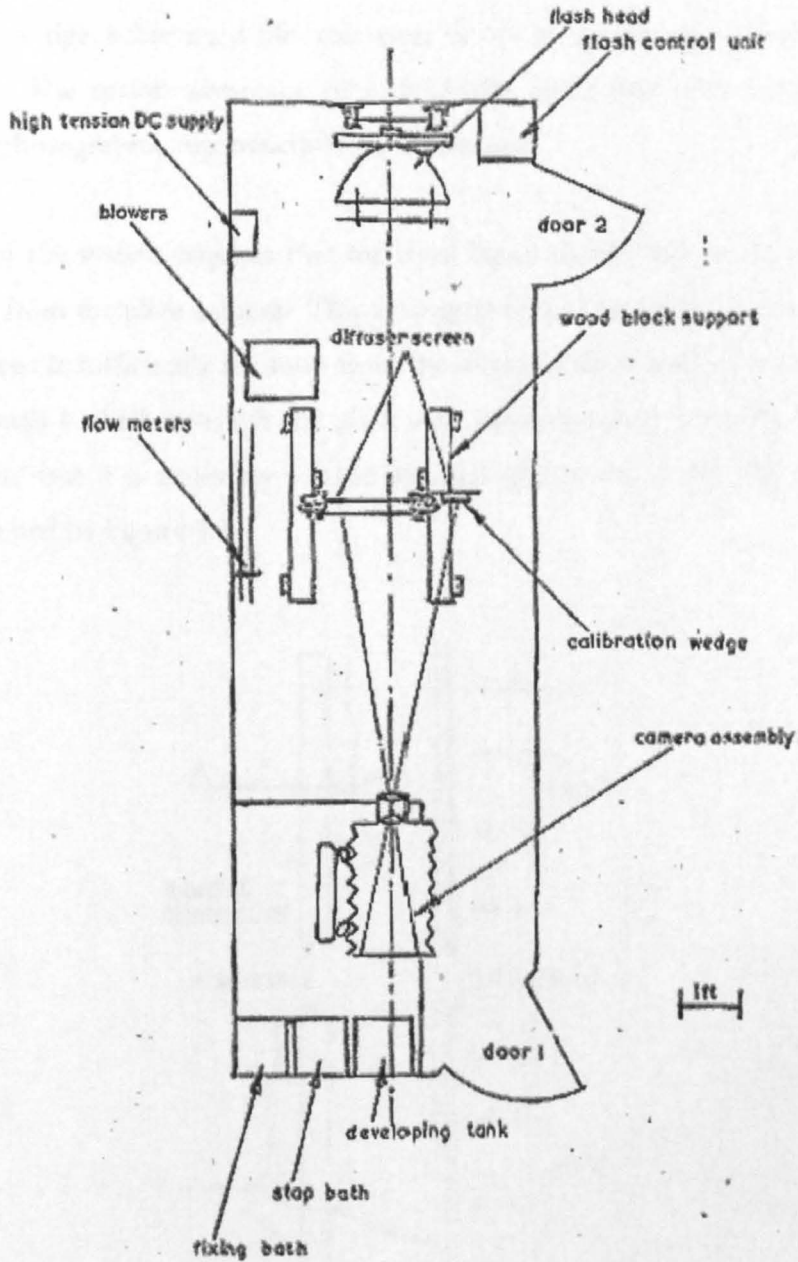


Figure 3.36: Experimental arrangement for spatial light absorption film thickness technique.
(Taken from Clegg (1969))

To calibrate the apparatus it is necessary to relate the voltage output from the densitometer to the film thickness corresponding to the measured density from the

photographic plates. This was achieved by a calibration wedge consisting of two rectangular glass plates (4" x 12" x 1/8" thick), clamped together and filled with the dyed liquid being passed down the column. The wedge was photographed in the same frame as the falling film, so that the densitometer could be passed along the centre line of the image of the wedge, achieving a film thickness versus image density calibration curve for each frame. The major advantage of individually calibrating each frame is that the necessity of photographic reproducibility is eliminated.

The optics of the system requires that the dyed liquid should fall on the far side of the wetted plate from the plate camera. This arrangement was necessary as it is assumed that the camera lens is sufficiently far away from the wetted wall in order that the rays of light passing through it shall have left the glass plate approximately normally to its surface. For this to be true it is necessary for the diffused light to enter the film interface first. This is illustrated by Figure 3.37.

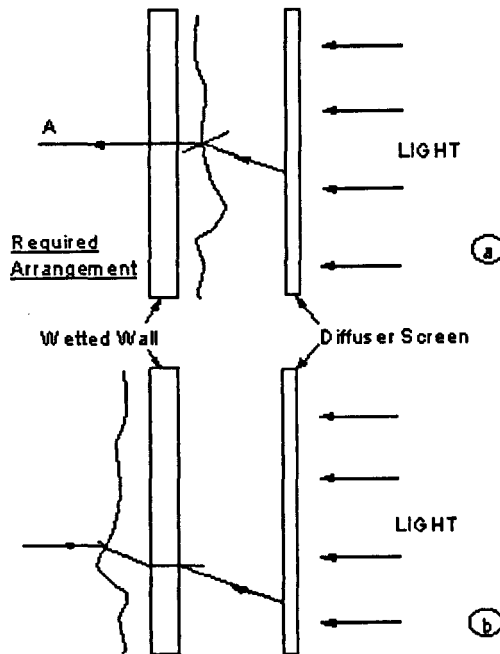


Figure 3.37: Illustration of the required lighting arrangement for the spatial film thickness technique of Clegg (1969).

Figure 3.37 demonstrates that all rays of light passing into the lens, such as A in part (a) of the figure, must have entered the glass plate normally. This is the case since any ray of

light which leaves a parallel sided glass block normal to its surface must have entered it normal to its other surface. This relationship is expressed in Snell's law, where:

$$\frac{\sin(\alpha_i)}{\sin(\alpha_r)} = \mu \quad (3.23)$$

where, α_i is the angle of incidence, α_r is the angle of refraction, and μ is the refractive index..

For the alternative arrangement given in part (b) of Figure 3.37, the light will still enter the lens normal to the glass plate, however, it will not travel the film by the shortest distance, leading potentially to significant errors in the measured thickness.

3.5.2 Multiple Electrode Probes

This section reviews the multiple electrode probe configurations developed by Sekoguchi and co-workers in their studies of interfacial structure and flow regimes in vertical gas-liquid two-phase flows.

Sekoguchi *et al.* (1985) reports the development of a spatial measurement device, the Super Multiple Point Electrode Probe (S-PEP), whose basic measuring element is the needle contact probe (Section 3.4.1). However, this film thickness measurement device consists of 409 needle contact probes located strategically over the cross-section of interest, with an example of their arrangement shown in Figure 3.38.

Each probe is constructed from 100 μm diameter platinum wire, sharpened to form a tip angle of 20° . The wires are electrically insulated, except for their tips, by coating with a thin resin film. They are assembled in 23 clusters of 17 probes and one cluster of 18 probes, with each cluster fixed on a stainless steel trap (see Figure 3.38(a)). The probes were arranged with spacings from 50 μm to 3.2mm over a tube radius of 12.9mm, with the bases of the clusters clamped in 24 equally spaced slots on the periphery of the tube (see Figure 3.38(b)). However, these probe spacings are system dependent, being optimised for spatial resolution of the observed film phenomena in the geometry under study. The probe spacing values quoted above were adopted by Sekoguchi *et al.* (1985) in

experiments on air-water two phase upward flow in a 25.8mm i.d. vertical tube, used to test the performance of this measuring system. The data processing system used in this study allowed 4.5s of signal to be recorded at a 1kHz probe-sampling rate. Sekoguchi & Takeishi (1989) report the development of a computer algorithm to process this data in order to determine the gas-liquid interface by comparing the signals of individual neighbouring probes.

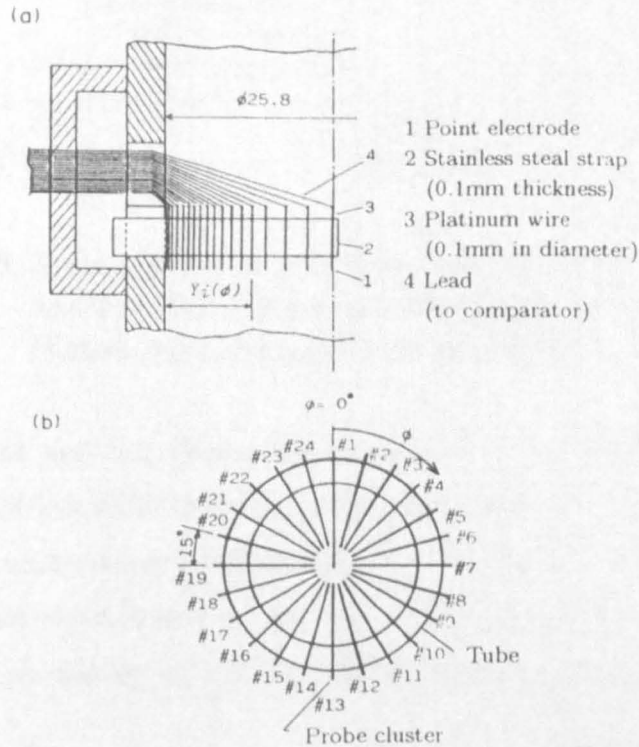


Figure 3.38: Arrangements of point-electrode probes and probe-clusters of the S-PEP:
 (a) arrangement of point-electrode probes on a strap;
 (b) arrangement of probe-clusters around the periphery.
 (Taken from Sekoguchi & Mori (1997))

More recently, Sekoguchi & Mori (1997) report the utilisation of an improved instrument system with higher sensing resolution in both the sampling time and the radial distance near a tube central core. The Semi-Supermultiple Point Electrode Probe (SS-PEP) device is shown schematically in Figure 3.39.

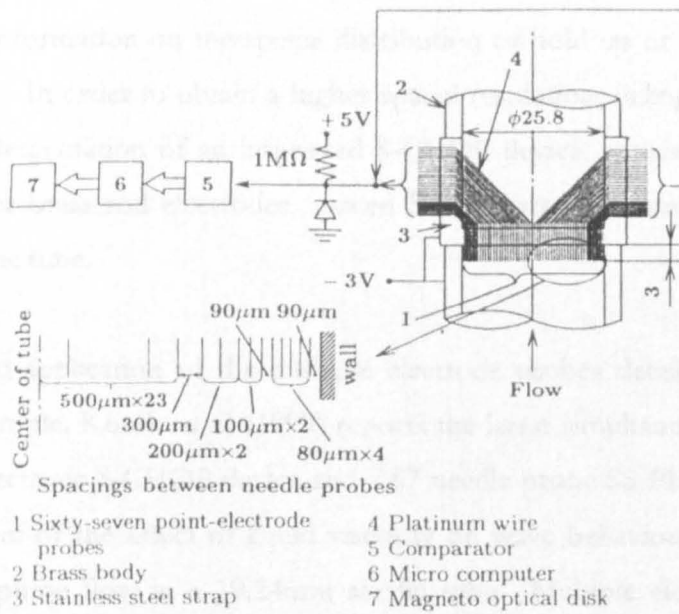


Figure 3.39: Arrangement of point-electrode probes of the SS-PEP and data-processing system.
(Taken from Sekoguchi & Mori (1997))

The specification of each individual probe is identical to that used on S-PEP devices, however, the two devices differ in spacing arrangements and improved electronics on the SS-PEP that allow an increased sampling frequency of 20 kHz. The SS-PEP device has been applied to both vertically upward and downward two-phase flows with a wide range of flow rates of gas and liquid, covering bubble plug, huge wave and annular flow regimes.

3.3.1 Multiple Electrode Probe

Sekoguchi and co-workers report a third multiple electrode probe spatial measurement device, referred originally as the Supermultiple Ring Electrode Probe (S-REP) and more recently as the Supermultiple Cross-sectional Mean Liquid Holdup Probe (S-CHOP). These devices are reported in studies where they were applied in conjunction with S-PEP and SS-PEP devices. The change in name from S-REP to S-CHOP appears to have occurred when implementation using rod rather than ring probes was considered. The original S-REP named devices and initial S-CHOP named device appear to be the same device, that simply consisted of 94 pairs of 5mm spaced, flush, 0.5mm thick ring shaped electrode conductance probes arranged axially with a spacing of 25mm over the tube length of 2325mm. Each pair of ring shaped electrodes can only provide the time-

varying cross-sectional mean liquid holdup value at the locality, however, collectively can reveal limited information on the spatial distribution of hold up or film thickness along the tube length. In order to obtain a higher spatial resolution, Sekoguchi & Mori (1997) report the implementation of an improved S-CHOP device, consisting of 266 pairs of 0.5mm diameter brass rod electrodes, spaced 5mm apart, and mounted flush with the inside wall of the tube.

Refinement and application of the multiple electrode probes detailed above is still on going. For example, Kondo *et al.* (1999) reports the latest simultaneous application of a 266 pair rod electrode S-CHOP device and a 67 needle probe SS-PEP device, applied in the measurement of the effect of liquid viscosity on wave behaviour in vertical upward gas-liquid two-phase flow in a 19.24mm acrylic tube. Multiple electrode probes have successfully been utilised by Sekoguchi and co-workers to improve knowledge of gas liquid interfacial characteristics in vertical flows, however, the devices are still open to potential areas of criticism. Clearly, the S-PEP and SS-PEP devices still retain the intrusive properties of their needle probe constituents. Kang & Kim (1992b) criticised the resolution of the S-PEP device, stating the limitation of the device to identifying the liquid's existence at only 17 fixed points along the film thickness direction. Another obvious criticism relates to the resources required in application of multiple electrode probe devices. With hundreds of probes and associated electronics involved, the devices must be costly in both time and financial resources.

3.5.3 Multi-Conductance Probe

Kang & Kim (1992b) report the development of a multi-conductance probe to measure the instantaneous spatial liquid film thickness, and in particular the three dimensional wave forms which are observed in thin liquid film flow. The probe is basically an extension of their development work on the flush-wire conductance probe (Section 3.3.2.3), and a schematic of their multi-conductance probe is presented in Figure 3.40.

The probe consists of a large built-in flush electrode, made of a brass plate 75mm long, 150mm wide and 4mm thick, and eleven platinum wire electrodes, 0.05mm in diameter with an effective length of 5mm, supported by stainless steel tubes. The front ten wire electrodes were uniformly aligned 4mm apart along the width of the flow, with the

eleventh electrode located 5mm (for horizontal flow) or 25mm (for vertical film) downstream from the tenth probe for wave velocity measurements. The wire diameter and the formation of the probe were chosen in this way as to prevent electrical or mechanical interference between the wires. The measurement system was located at the centre of the measurement channel, covering 36mm of the width, and the wire probes were connected to a translation stage for precision placement. Eleven sets of electrical circuits were used, one for each wire probe with the data processed three dimensional and contour maps of the interfacial surface.

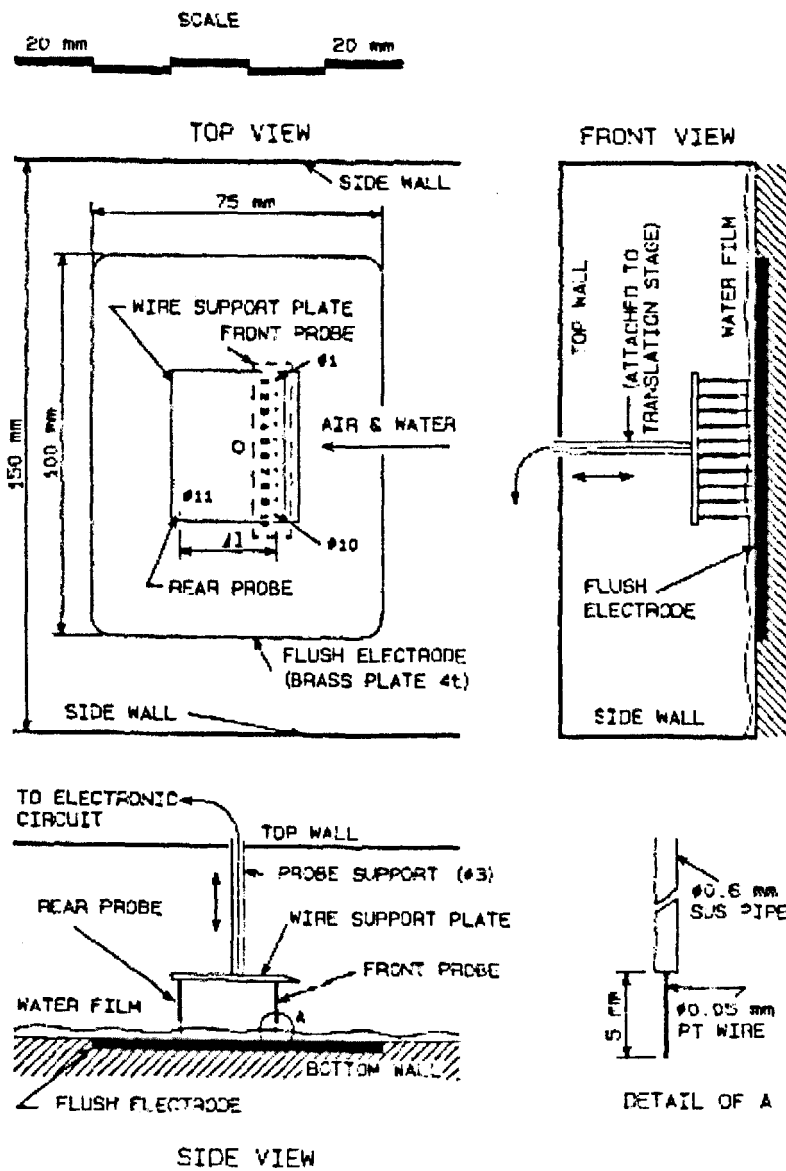


Figure 3.40: Multi-conductance film thickness measurement device.
(Taken from Kang & Kim (1992b))

Calibration was achieved using the indirect method proposed by Kang & Kim (1990a) and reviewed in Section 3.3.2.5. Both horizontal and vertical liquid film experiments were conducted, and an attempt was made to qualitatively confirm the validity of the results of the measurement technique by comparing the spatial maps recorded with real photographs. This measurement technique is capable of giving a low spatial resolution for each wire, thought to be less than 0.1mm, indicating a high accuracy. However, this application is restricted to 10 wires across a 150mm wide duct resulting in a very poor global resolution. As with all wire probes, this measurement systems intrusive nature is also open to criticism, especially if the number of wire probes utilised is increased in search of enhanced global resolution.

3.5.4 Pigment Luminance Method

Hagiwara *et al.* (1983) reports probably the earliest application of pigment luminance to spatial film thickness measurement. The technique was applied in flow visualisation studies of downward annular two-phase flow in a 26.4mm i.d. acrylic pipe. The basis of the technique was the visualisation of scattered light from fine TiO₂ particles suspended in the liquid film. Assuming that the particles are dispersed evenly throughout the liquid film, the intensity of the photographically recorded light at any point on the image can be taken to be proportional to the number of particles present at that point in the film and thus the film thickness at the point. The authors adopted the technique for visualisation purposes only, making no attempt to obtain quantitative film thickness data. Application of the pigment luminance method (PLM) to quantitative spatial film thickness measurement is reported by Ohba & Nagae (1993) and with further refinements by Ohba *et al.* (1996) in studies on interfacial waves in vertically upward air-water annular flow. The measurement scheme and test section utilised by the latter study is shown in Figure 3.41.

The application of a 200 frames per second high-speed video camera allows dynamic study of the spatial film thickness structure over an approximately 20cm length of pipe. Figure 3.41 (b) shows a water tank attached around the pipe in order to correct the light refraction of a tubular geometry. The figure also shows a black thin board strategically located within the tube to act as a light absorption object with the secondary purpose of reducing any disturbances caused by the airflow.

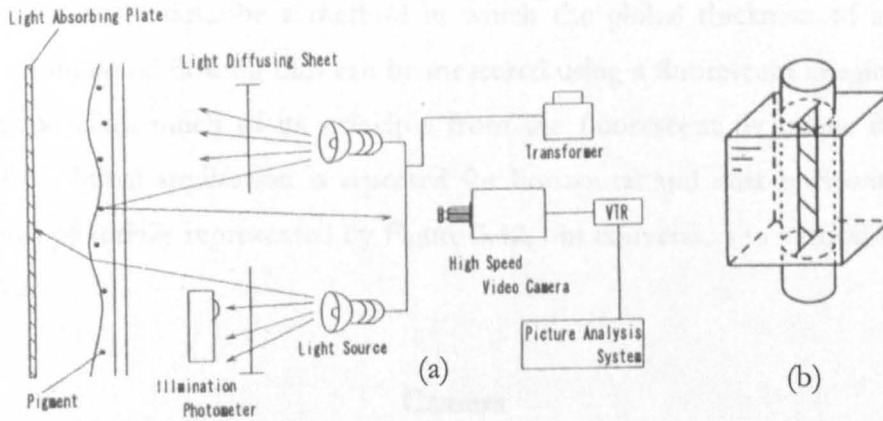


Figure 3.41: Pigment Luminance measurement system and test section.
(Taken from Ohba *et al.* (1996))

Calibration of the system to obtain the relationship between luminance and film thickness was achieved by replacing the test section with a transparent vessel filled with water with a very small amount of the white TiO_2 pigment intermixed in. The incident light intensity can be regulated by varying the voltage across the source light lamps and measured by illumination photometer. The calibration curve can be obtained from processing of the luminance image. Ohba *et al.* (1996) also report the development of a theoretical relation between luminance, B , and liquid film thickness, δ , based on the exponential decay law:

$$B = \frac{1}{2} I_0 R_{TD} \left(1 - \exp \left[- \frac{3m_{TD}a}{\rho_{TD}d_{TD}} z \right] \right) \quad (3.24)$$

where, subscript $_{TD}$ refers to the TiO_2 particles, R is the reflectivity, m is the particles mass to total pigment mass ratio, a is the mass of pigment intermixed into water by volume, and ρ and d is the particle density and diameter respectively.

Comparison between theoretical and experimental results showed good agreement for liquid films less than about 1.5mm, and above this figure it was witnessed that marked differences appeared which the authors attributed to the sensitivity of the video camera.

3.5.5 Fluorescent Imaging

Johnson *et al.* (1997) describe a method in which the global thickness of a dynamic surface of a thin liquid flowing film can be measured using a fluorescent imaging system. The technique takes much of its principle from the fluorescent technique detailed in Section 3.4.6. Initial application is reported for horizontal and near horizontal (0-40°) flow systems, pictorially represented by Figure 3.42, but conversion to vertical systems is not complex.

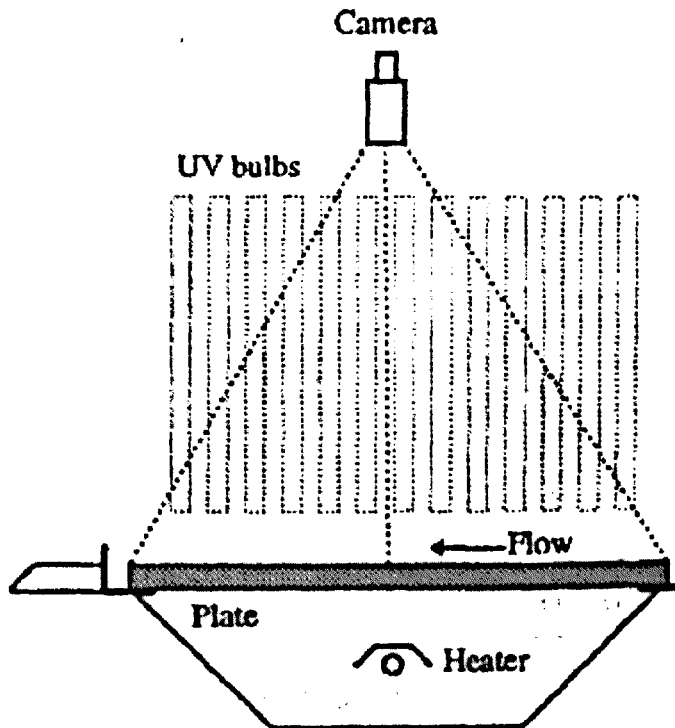


Figure 3.42: Fluorescent Imaging measurement system.
(Taken from Johnson *et al.* (1997))

A near-ultraviolet (UV) broad light source is supplied by two banks of 40 inch UV bulbs that flank the camera facing the fluid substrate surface of area up to approximately 0.8m by 1.0m. The broad source UV light illuminates a thin fluid film such that each volume element in the fluid receives approximately equal incident light energy per unit volume. A small concentration of fluorescent solution, fluorescein, dissolved within the measuring liquid produces a characteristic emission band, which is sighted along a line almost perpendicular with the fluid surface and received by a charge couple device (CCD) camera. A large area filter is applied over the UV bulb bank to remove any trace from the UV light of other spurious light to which the CCD camera is sensitive. A

smaller filter is placed on the camera to narrow its receptivity to the emission spectra of the fluorescent solute. The camera lens can be adjusted to permit fluid spatial viewing areas between $2 \times 3\text{cm}^2$ and $50 \times 70\text{cm}^2$. The CCD camera is attached to a PC with digital analysis software and is capable of producing a time series of digital images, at a time interval of approximately half a second using the video grabbing equipment of this study. The digital images produced are made up of a number of pixels that vary in the size of flow area that they represent, dependent on viewable flow area. For example, for the largest viewing dimension of 70cm available in this study, each pixel represents a 1.5 cm segment of flow. Each pixel amplitude or greyscale value is a linear representation of the amount of fluorescent solute in the sightline of the camera, and after appropriate calibration, the thickness of the film. Calibration is achieved by using increments of known film thickness within the experimental facility, and relating the pixel values obtained in digital images to film thickness by means of a calibration curve.

The largest potential source of error using this technique is the variation of UV illumination intensity, quoted by the authors as high as fifteen percent. In the present study, the authors averaged out this fluctuation during the calibration. A possible improvement would be to develop a calibration system, such as implemented in the light absorption technique detailed in Section 3.5.1, where calibration and digital image are combined to eliminate any influence of light intensity variations.

3.5.6 Ultrasonic Transmission

Kamei & Serizawa (1998) present a novel adaptation of the Ultrasonic Pulse-Echo Method (Section 3.3.6), developed primarily for spatial and temporal measurements of the film thickness around a nuclear fuel rod. The nuclear fuel rod was simulated by locating the device on the inside of a 1000mm long 15mm O.D. vertical tube surrounded by a 30mm I.D. vertical tube. The flow over the nuclear fuel rod was simulated with an air-water flow travelling concurrently upward between the tubes. A schematic of this ultrasonic transmission device installed within the simulated nuclear fuel rod is presented in Figure 3.43.

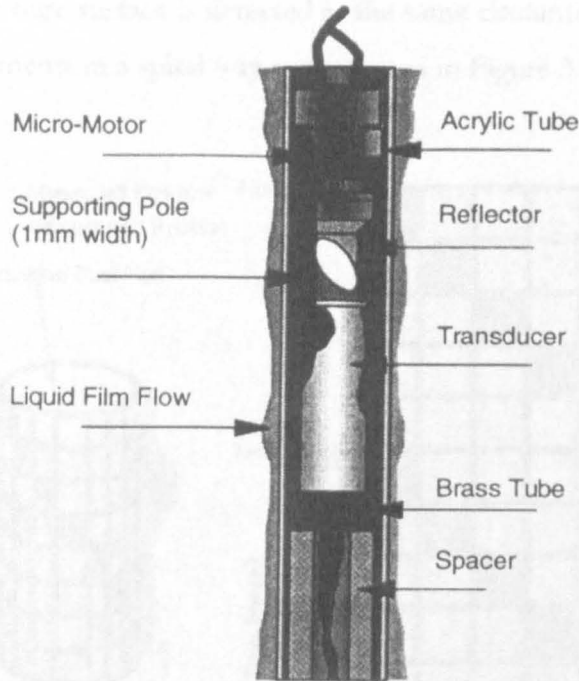


Figure 3.43: Schematic of ultrasonic transmission device installed in a nuclear fuel rod.

(Taken from Kamei & Serizawa (1998))

The device is located within a small brass tube and consists of a transducer, reflector and micro-motor. The 6.4mm diameter transducer is inserted co-axially with the tube, and emits/receives a 10MHz ultrasonic wave at a frequency of 10 kHz. The ultrasonic wave beam from the transducer surface expands along the direction of its propagation with a 1.6-degree angle, before reaching the aluminium reflector located 8mm away, which is rotated by a micro-motor at 15,000 rpm creating a scanning time of 4ms per round. The reflector has a flat surface inclined at 45 degrees with respect to the transducer to cast the ultrasonic pulse waves toward the liquid film flow located about 7.5mm away. This measurement system results in an approximately 0.9mm diameter ultrasonic wave being reflected at the gas-liquid interface. The 10,000 reflected signals received by the transmitter a second are fed to a personal computer fitted with an analogue to digital converter board, and the attached data acquisition system is capable of storing 1.6s of the signal.

The analysis of the data for temporal film thickness measurements is identical to the approach detailed in Section 3.4.6, however, the spatial distribution of the liquid film

thickness around the tube surface is detected at the same circumferential position at two consecutive measurements in a spiral way as illustrated in Figure 3.44.

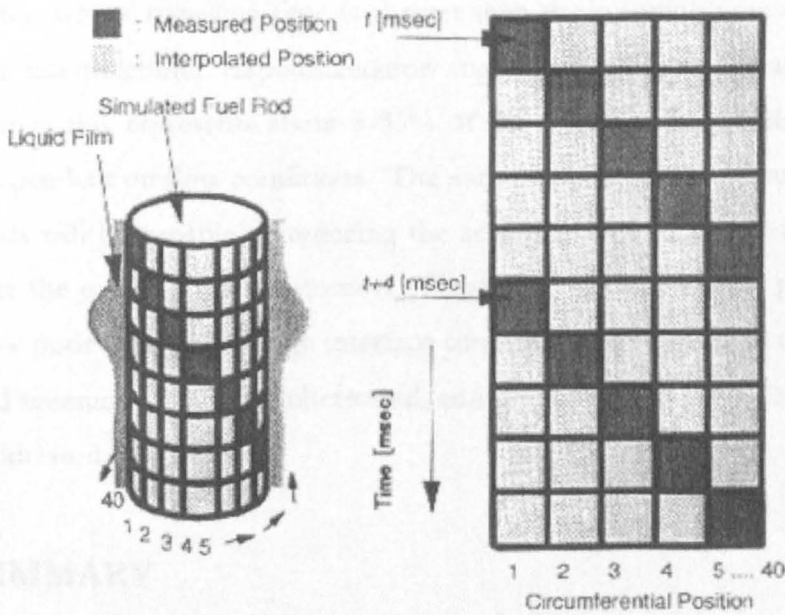


Figure 3.44: Illustration of ultrasonic transmission interpolating operation.
(Taken from Kamei & Serizawa (1998))

Therefore, to reconstruct 2-dimensional images of the liquid film it is necessary to interpolate the signals using:

$$V(i) = \frac{V(t+4) - V(t)}{40} i + V(t) \quad (3.25)$$

where, $V(i)$ is the interpolated value at time i and $V(t+4)$ and $V(t)$ are measured liquid film thickness (where 4 denotes scanning time of 4ms and 40 is the number of circumferential measurement positions during one scanning). This operation is done for each measurement location around the tube, and allows the creation of time-spatial contour plots of the flow.

In order to assess the accuracy of the technique, the authors made measurements for comparison using their ultrasonic transmission device and a needle contact probe (Section 3.4.1) in a pool of stationary water, with both results showing good agreement.

The authors state the actual measurement error to be $75\mu\text{m}$ in water using the current device assuming the sound velocity to be 1500m/s , this error being equal to a half wavelength of the ultrasonic wave. It is also noted by the authors that surface waves on the liquid film whose travelling time is shorter than the scanning time will be distorted through the interpolation. Experimentation suggests that for the measurement set-up reported above this represents about 5-35% of the total number of disturbance waves detected, dependent on flow conditions. The authors point out that future improvement in electronics will be capable of reducing the scanning time to improve resolution and limit further the extent of this distortion. However, no discussion is presented in this work of how poor reflection at high interface contact angle (reported in their earlier work on localised measurements using ultrasound, and described in Section 3.4.6), has been or could be addressed.

3.6 SUMMARY

The diverse range of film thickness measurement techniques reviewed in this chapter makes a “Best Buy” recommendation difficult. It is this author’s opinion that it is easier to consider the suitability of the techniques depending on the type of film thickness measurements required. For localised information on interfacial film thickness it is easy to recommend the application of conductance/capacitance probes unless resolution, fluid properties, or measurement location prevent their use. They are accurate, relatively inexpensive and simple to apply, and this is reflected in their popularity in the literature. For global information on interfacial structure this author would recommend the application of one of the emerging optically based spatial film thickness measurement techniques, such as fluorescence, pigment luminance or the light absorption technique developed in this study. Where location prevents the application of an optically based spatial technique then the multiple probe based techniques are possible alternatives. However, these techniques are resource intensive and to date have a much lower spatial resolution than their optical counterparts.

It is hoped that this chapter has provided a valuable reference for future studies involving liquid film thickness measurement.

Chapter 4

LIQUID FILM THICKNESS MEASUREMENTS

The Light Absorption Imaging Technique

4.1 INTRODUCTION

The purpose of this chapter is to present a detailed review of the novel spatial film thickness measurement technique, the Light Absorption Imaging Technique (LAIT), developed for application in this study.

The chapter begins by describing the evolution of this technique from the spatial light absorption technique pioneered by Clegg (1969), and reviewed in Section 3.5.1 of Chapter 3. The remainder of the chapter is devoted to a detailed description of the methodology of the latest revision of LAIT.

4.2 EVOLUTION

As stated in the summary of Chapter 3, the spatial light absorption technique pioneered by Clegg (1969) potentially offers a wealth of information about the film structure of a large spatial region of falling film yet it has been virtually unused. Almost certainly a major factor in the virtual abandonment of the technique by subsequent researchers is the cumbersome densitometer image analysis method. This is best illustrated by considering that the densitometer employed was only capable of sampling a point every 0.25 seconds, therefore, it would take to over 8 hours to analyse one of the images, containing 125,000 individual measuring points (*i.e.* pixels), obtained in the current study.

Therefore, from the inception of this study it was decided that due to the potentially unrivalled information that it could bestow about the interfacial characteristics of falling films, it was desirable to apply the photographic technique of Clegg but improve the image analysis aspects of the technique. This was considered possible by utilising some of the major advances in computer technology, and computer image analysis methods in particular, that have occurred over the past 30 years.

Initial application of the technique in this study was limited to water as the test fluid, for direct comparison with the original results of Clegg (1969) and the considerable volume of water film thickness data available in the literature. The Clegg technique, detailed in Section 3.5.1, was reproduced as closely as possible, except for the following modifications:

- (i) A standard 35mm black & white camera replaced the considerably more expensive application of a 5" x 7" plate camera used in the original study. Preliminary test photographs using both a hired plate camera and a 35mm camera showed little of the resolution advantages expected for a plate camera if care was taken at the 35mm picture processing stage.
- (ii) The densitometer and data logger arrangement were replaced by scanning the photographs directly into a personal computer. Film thickness was related to the black & white image intensity using variations in pixel greyscale values derived from the calibration cell. The software and methodology were similar to those described in Section 4.3.4.

Visual inspection of the resultant photographs, for flow visualisation purposes, provided initial optimism that the technique had been faithfully reproduced. However, doubts arose about the technique's qualitative accuracy during the image analysis stage. Calibration of film thickness to greyscale pixel intensity was expected to follow a Lambert-Beer Law type relationship (Eqn 4.1), however, this was often not the case. The problem was exacerbated by the need to extrapolate on occasion beyond the range of the upper limit of the calibration cell, set in hindsight too low at 1.5mm. Due to the curing action of the silicon sealant beneath the calibration cell glass plates, a gap between the plates approximately four hundred microns in width opened up. This gap forced further extrapolation of the calibration curve below the lower cell width limit. In the case of water falling films, whose base thicknesses are often less than four hundred microns, the gap often resulted in a large percentage of point values relying on extrapolated information.

Analysis of the results suggested the doubts were well founded. The vast majority of previous studies on falling water films in the absence of gas flow, observed a relatively

close agreement between the Nusselt predictive equation (Eqn 8.3) for the thickness of laminar falling films and the experimentally determined mean film thickness. Figure 4.1 presents the water mean film thickness data obtained using this early adaptation of the Clegg technique plotted with the Nusselt predictive equation.

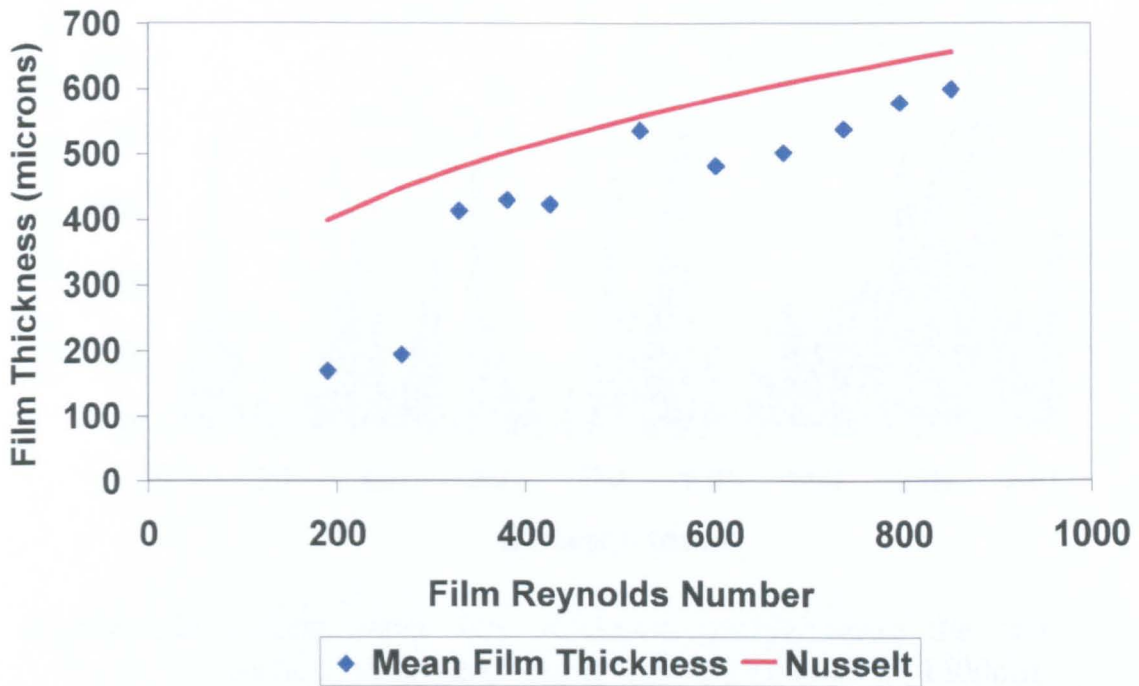


Figure 4.1: Comparison of experimentally determined mean film thickness and predictive equation of Nusselt for falling water film with a stagnant airflow.

The figure demonstrates that the experimentally determined mean film thickness was on average twenty percent lower than the figure suggested by Nusselt, and there is particular deviation at the lower film Reynolds numbers (*i.e.* lower water flowrates). This marked deviation at the lower water flowrates coincides with the application of measurement data that is particularly reliant on extrapolation of the relevant calibration curve.

Further evidence of disparity with the water falling film data available in the literature is evident with closer examination of the film thickness data from which the points on Figure 4.1 are derived. Figure 4.2 presents a film thickness profile along the midpoint of the test section obtained for the lowest water flowrate, and is typical of most of the data

obtained, which suggests that the base film thickness is virtually indistinguishable from zero.

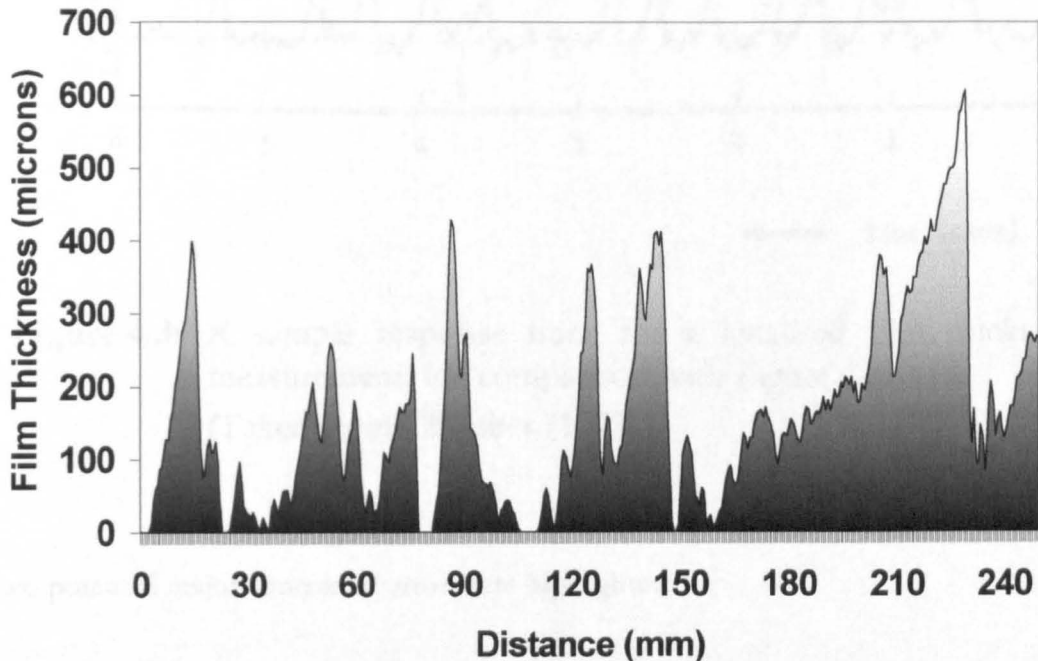


Figure 4.2: Falling water film thickness profile along the test section midpoint, beginning approximately 1500mm below the inlet weir. ($u_l = 2.1$ l/min, $v_g = 0$ m/s)

The prediction of an indeterminate base film thickness is not supported by observation or the literature. Figure 4.3 presents a sample response trace for a localised film thickness measurement, at a similar liquid flowrate to that presented in Figure 4.2, of a falling water film taken from Thwaites (1973).

The data for Figure 4.3 was obtained by application of electrical conductivity probes in a 25mm i.d. pipe; however, it is typical of the results available throughout the literature. The figure clearly suggests that a base film thickness nearer two hundred microns should be expected.

A review of the technique was then undertaken to attempt to highlight the causes of these observed discrepancies with the literature and propose solutions to correct them.

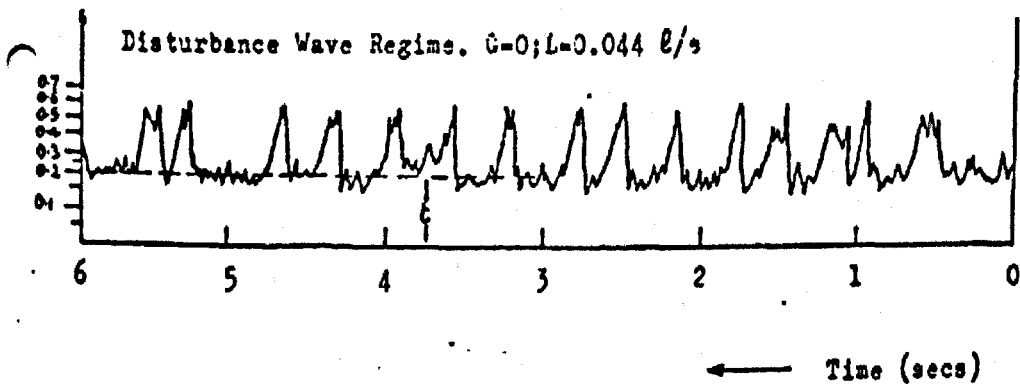


Figure 4.3: A sample response trace for a localised film thickness measurement, for comparison with Figure 4.2. (Taken from Thwaites (1973)).

Two potential major sources of error were highlighted:

- (i) **Calibration cell.** It was agreed that the need for extrapolations at both ends of the calibration cell was a potentially large source of error. Therefore, the calibration cell was widened to represent a larger range of film thickness (to approximately 4mm) and the point of contact between the wedged glass plates more securely clamped to limit the measured gap between them to approximately 100microns.
- (ii) **Photographic Processing.** A conscious effort was made to duplicate the rigorous uniform photographic processing procedure indicated by Clegg (1969). However, visual inspection of the pictures where the calibration curve did not follow the expected Lambert-Beer Law relationship identified their processing as the probable source of error. Common in all these pictures was their exhibition of varying degrees of underdevelopment, indicating that constant photographic processing conditions had not been achieved. As the development time and temperature had been kept virtually constant for all processing, this implies that changes in processing chemical quality may have been responsible for the variations. Any underdevelopment of the pictures

resulted in the loss of resolution at the lower greyscale (thickness) measurement range, and this was confirmed by re-processing of the picture negative. This could possibly explain the lack of any distinguishable base film and the lower than expected mean film thickness values. Re-processing of all the pictures from the negatives was possible; however, with the uncertainty surrounding the calibration it was considered better to abandon the entire experimental set. The opportunity to eliminate entirely the photographic processing and scanning stage became possible with the acquisition of a digital camera, which stores the pictures digitally before direct transfer to a personal computer. Not only did the digital camera sidestep any processing concerns, it produced colour images (the importance of which is discussed in the next paragraph) and was found to significantly reduce the time required for picture processing.

A further refinement to the technique was discovered by chance, when water was replaced by dodecylbenzene as the test fluid. Naturally, the water-soluble nigrosine dye utilised previously was insoluble in the organic dodecylbenzene, and it was our original intention to simply replace this with an organic soluble version of the nigrosine dye. However, tests indicated that the organic nigrosine dye was only partially soluble in dodecylbenzene, and therefore, an alternative dye must be utilised. During calibration tests with a readily soluble organic red dye, Biebrich Scarlet, and employment of the colour digital camera, it was observed that the blue and green components of the RGB (red, green, blue) pixel were considerably more sensitive to subtle differences in dye colour and thus calibration cell thickness than the previously utilised intensity value, which is a combination of the RGB components and heavily influenced by the dominant red component. The benefits that lead from the application of this discovery were:

- (i) Calibration of a selected film thickness range over the entire 256 pixel range was now possible with minimal effort by small changes in dye concentration
- (ii) The amounts of the dye required were reduced by about a factor of 8 for the organics and a factor of 25 for water. This has the

potential to lower dye procurement costs and limit further any possible influence of the dye on the interfacial characteristics of the falling film.

The refinements described above were implemented to form the current revision of the light absorption imaging technique, whose methodology is described in detail in the next section. More information on the results obtained from the original modification to the Clegg technique described in this section and some results from the extensive water data collected are presented elsewhere by Clark *et al.* (1998, 1999).

4.3 METHODOLOGY

4.3.1 Theory

As with all light absorption techniques, this technique was based on the Lambert-Beer Law, which states that the intensity I of a light beam after passing through a liquid layer of thickness t can be described by the following equation:

$$I = I_0 e^{-kt} \quad (4.1)$$

where, I_0 is the original intensity and k is the absorption coefficient.

Therefore, this law implies that if a liquid film flowing under uniform lighting conditions could be recorded photographically, then the recorded intensity of the photographic image representing a point on the film is, after appropriate calibration, a measure of the thickness of the liquid film at that point.

4.3.2 Experimental Arrangement

4.3.2.1 Overview

The photographic arrangement required for the implementation of this technique, using the flow facility detailed in Chapter 2, is shown schematically in Figure 4.4.

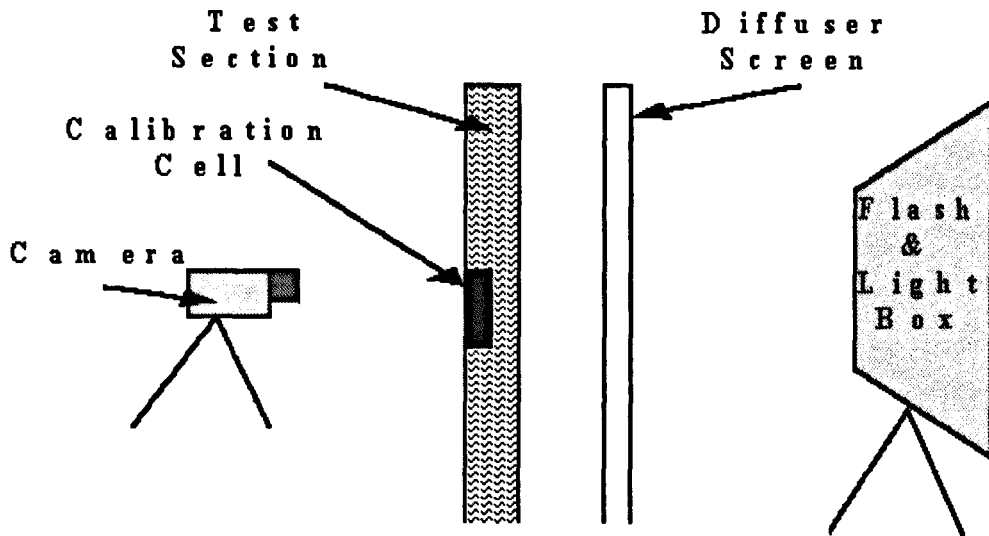


Figure 4.4: Schematic of photographic arrangement.

4.3.2.2 Test Section Geometry

As previously stated in Section 2.3.1, a rectangular geometry where the falling liquid film was generated in such a manner that it was only allowed to flow on one of the surfaces was identified as the optimal test section geometry for application of optical measurement techniques such as LAIT. In review, the rectangular geometry described overcomes the difficulties of curvature and introduction of the light source associated with a more conventional tubular geometry.

4.3.2.3 Photographic Arrangement

A digital camera (Kodak, Model DC-120) was mounted approximately 1000mm behind the glass flow plate of the rectangular test section at the desired measurement height using a standard camera tripod. For measurements at heights beyond the range of the tripod alone, a stage was constructed to safely hold camera, tripod and photographer. The stage was modular by design, for simple adjustment of its wooden base to facilitate measurements at virtually any test section height. The digital camera was linked electronically by cable, to ensure simultaneous firing, to an external commercially available flash and light box (Elinchrom, Model 250-R). The choice of flash was dictated by the ability to generate high flash speeds, to ensure practically complete freezing of the film during measurement. The Elinchrom model used in this study was capable of

achieving flash speeds of up to $1/6500^{\text{th}}$ of a second, equivalent to a movement during this duration of only approximately 0.3mm of the fastest components of the interface. As the flash box was primarily designed for photographic portrait work, another incorporated feature was the provision of light from a standard bulb to represent the flash conditions during inactivity. This feature was particularly useful in the setting up of flow measurement conditions and providing a light source for the operator between measurements. The flash box was located approximately six hundred millimetres in front of the viewing glass plate of the rectangular test section and mounted on a large adjustable retort stand to ensure that it was centrally positioned at the height of the digital camera.

The necessity for the photographic arrangement described above, with the source (flash) located in front of the liquid film and the receiver (camera) behind it, was highlighted by Clegg (1969) and is detailed in the review of his technique in Section 3.5.1. Clegg (1969) reported that the opposite photographic arrangement, with the source behind the liquid film and receiver in front, could lead to potentially significant errors. However, the dodecylbenzene results reported here were, for reasons of convenience, carried out with the light behind the film, so an analysis of the magnitude of the possible errors was conducted and is presented in Appendix B. To summarise, it was found that the errors were dependent on interface slope and found to be negligible for angles up to approximately plus or minus forty five degrees. As the vast majority of interfacial contact angles are well below these criteria, measurement error will be negligible.

4.3.2.4 Uniform Lighting

As stated in the theory of this technique, uniform lighting conditions are fundamental in any valid application of this technique. To achieve this criterion the following steps were taken:

- (i) All possible external sources of light were located and removed. This primarily involved the painting of all windows within the room housing the flow facility with black matt paint.

- (ii) Although the flash was already located behind a material diffuser screen, which appeared in initial tests to be quite an efficient means of ensuring uniformly diffuse light, the entire flash box arrangement was placed behind a large translucent plastic diffuser screen (2000mm (H) x 1200mm (W)). This had the added benefit of being a fairly efficient thermal barrier between the light source from the inactive flash unit and the flow rig.

Clegg (1969) fitted the plate camera in his study with a graduated concentric filter to ensure evenly recorded illumination between central and peripheral regions of his photographic print. However, this was unnecessary in this study as the digital camera provided a similar automatic option.

The relative success at achieving uniform light conditions was tested using a standard hand-held photographic light meter (Calumet) at random points between the test section and camera, and virtually uniform conditions were recorded by the light meter for the implemented photographic arrangement. Analysis of blank images of the film region (Figure 4.5(a)) appeared to confirm general uniformity, however, checks on the mean pixel value suggested there was a small but measurable non-uniformity over the image. This was tested and confirmed using commercially available image analysis software (Adobe Photoshop 5) by exaggerating the pixel contrast (Figure 4.5(b)).

Figure 4.5(b) clearly demonstrates the gradient in light output intensity that is centred on the flash light source, and suggests that the material diffuser screen and translucent plastic diffuser screen were not completely effective. Further analysis of the pixel values from the blank images (*i.e.* an image with no liquid present in test section or calibration cell) showed that there was an approximate twenty percent range of values around the mean pixel value. This would lead to significant errors in measurement. Therefore, a procedure was developed to correct for the relationship between changes in light intensity and distance from the flash light source, and is described in the image analysis (Section 4.3.4).

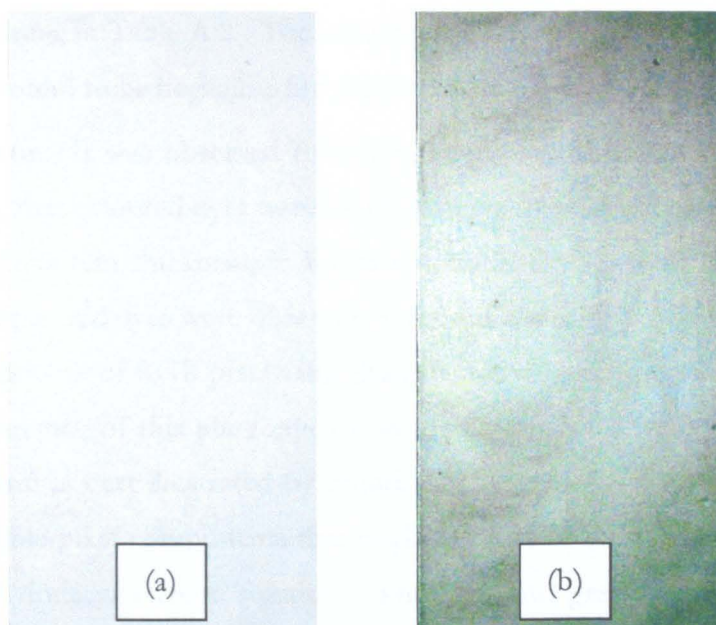


Figure 4.5: Identification of light non-uniformity using image analysis software. (a) = raw blank image, (b) = exaggerated contrast image.

4.3.2.5 Dyes Used

The addition of small quantities of dye to clear or translucent test liquids, to enhance the light absorption properties of the fluid so that small changes in liquid film thickness can be detected, is an essential component of light absorption based film thickness measurement techniques. Initial application of this light absorption technique used water soluble black nigrosine dye, in an effort to reproduce the measurement procedure of Clegg (1969) as closely as possible. However, black nigrosine dye was replaced in favour of coloured dyes in the refinements to this technique discussed in Section 4.2. The prerequisite requirements in the choice of these coloured dyes were:

- (i) **Solubility.** Clearly, it is vitally important that the dye be soluble, preferably highly soluble, in the water or organic based liquid under test, otherwise, uniform distribution of the dye in the bulk liquid cannot be assumed.
- (ii) **Surface Activity.** As the influence of surface tension on air/liquid interface shape was to be investigated, it was important to ensure that the dyes were not significantly surface active, as is the case for many dyes. Surface activity was tested at the laboratory scale using a torsion balance. Appendix A presents, for comparison, the surface tension of dyed and non-dyed

solutions, in Table A.2. The influence of the dyes utilised on surface activity was found to be negligible for the concentrations applied in this study.

- (iii) **Colour.** It was observed from commonly available blue and red indicator dyes, that coloured dyes were more sensitive to small changes in dye intensity, and thus film thickness, in the less dominant RGB pixel constituents. For example, red dyes were observed to be more sensitive in their blue and green component of RGB pixel value than the red value or greyscale intensity. The importance of this phenomenon in the current work is discussed in Section 4.2 and is best illustrated by Figure 4.6. Figure 4.6 is a comparison of the possible pixel components that could be used in the calibration of a 0.09g/l dyed dodecylbenzene solution. The blue and green pixel component can clearly be seen to considerably extend the pixel range for the film thickness range to be measured, minimising the thickness range represented by a single pixel (*i.e.* resolution).

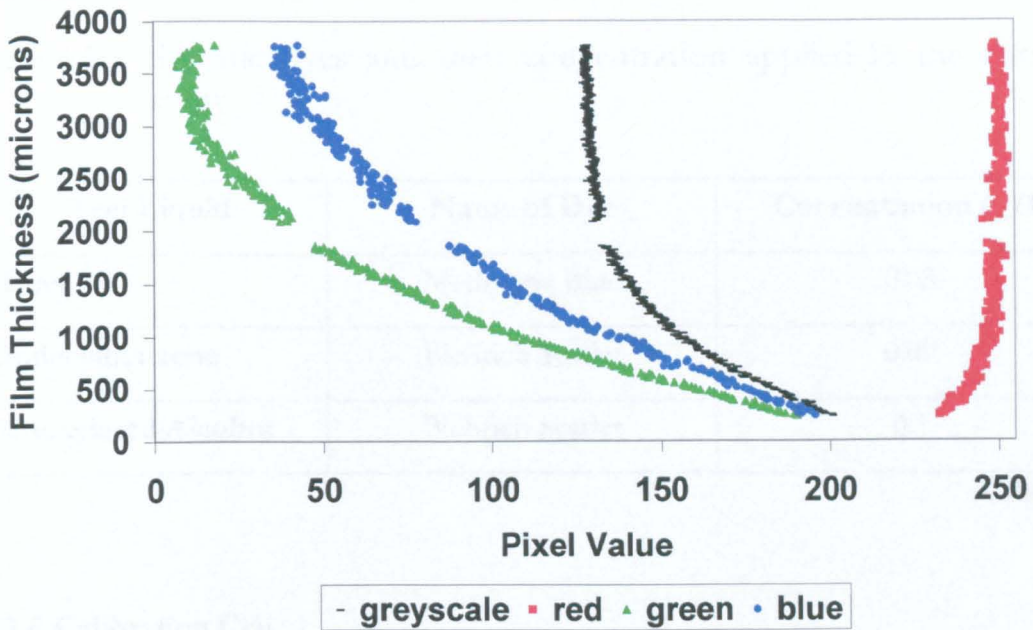


Figure 4.6: Comparison of possible pixel components that could be used in the calibration of a 0.09g/l Biebrich Scarlet (red) dyed dodecylbenzene solution.

The optimum dye concentration could be considered reached when the required film thickness range of the test fluid is represented by the majority or complete (0-255) pixel

range. Initially, optimum dye concentration was estimated by the addition of measured amounts of dye into some of the pure test liquid in the calibration cell, and then visually observing the cell through a complimentary filter (*e.g.* red filter for a blue dye). The filter showed the gradulation of the dye colour in the calibration cell as a greyscale image, and the observer deduced which dye concentration provided the best greyscale variation from white (bottom) to top (black). Near the completion of this study, a more sophisticated approach was developed to determine the optimal dye concentration. This optimisation was achieved by the progressive addition of small amounts of known dye into the bulk liquid and measuring the resolution range obtained across the calibration cell. The monitoring of resolution range was accomplished by comparison of the plots generated from images taken of the calibration cell, presented in a similar format to Figure 4.6, at differing dye concentrations.

The specific dyes used and their concentration in each of the test liquids for the current study is presented in Table 4.1

Table 4.1: Specific dyes and their concentration applied in the current study.

Test Liquid	Name of Dye	Concentration (g/l)
Water	Methylene Blue	0.03
Dodecylbenzene	Biebrich Scarlet	0.09
Ethoxylated Alcohol	Biebrich Scarlet	0.1

4.3.2.6 Calibration Cell

Calibration of the technique was achieved by the construction of the wedge shaped cell (200mm (H) x 65mm (W)) shown in Figure 4.7.

The cell was constructed of two (174mm (H) x 50mm (W)) glass plates cut from a larger 6mm toughened glass plate that was surplus to requirements in the construction of the

rectangular test section. The glass sections were clamped in a wedge formation by a surrounding metal framework so that the graduated distance between the glass sections was between approximately zero and four millimetres. Silicone sealant was used to coat the underneath of the touching surfaces of the glass sections to ensure that any slight gap between them was watertight. The exact distance between the glass plates along their length was measured at a number of points using feeler gauges, and this information was graphically charted (Figure 4.8) to obtain the characteristic equation for the thickness profile.

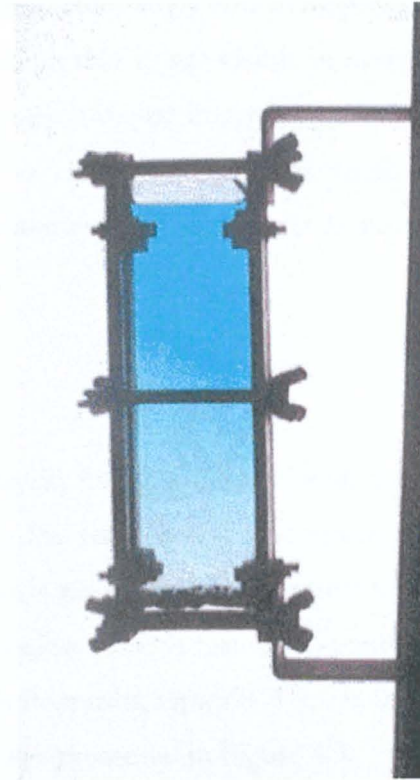


Figure 4.7: Image of calibration cell.

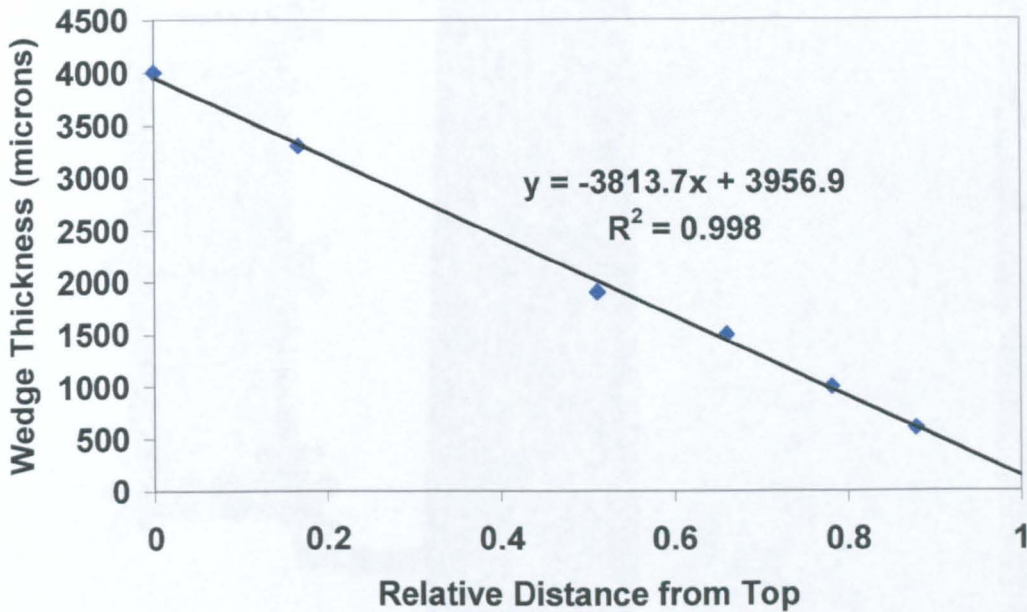


Figure 4.8: Determination of characteristic equation for thickness profile along wedge shaped calibration cell.

The cell was filled with a sample of the dyed liquid under study and strategically bolted to the test section adjacent to the area under study so that it was visible in every recorded image. The inclusion of the calibration cell in each digital image permitted individual calibration of the images, which is essential to compensate for the small variations observed in flash output intensity during measurement and also removes any obligation for the uniform processing of the digital images.

4.3.3 Measurement Procedure

The flow facility is set to the desired air and liquid flow conditions using the operating procedure detailed in Chapter 2 (2.5). During the time interval incorporated to allow stable flow conditions to persist, final adjustments are made of the camera viewing area, utilising the zoom lens, to ensure optimum inclusion of both test section and calibration cell in the digital image. A number of digital photographs, typically 3-5, are then taken in rapid succession, with a typical resultant raw image presented in Figure 4.9.

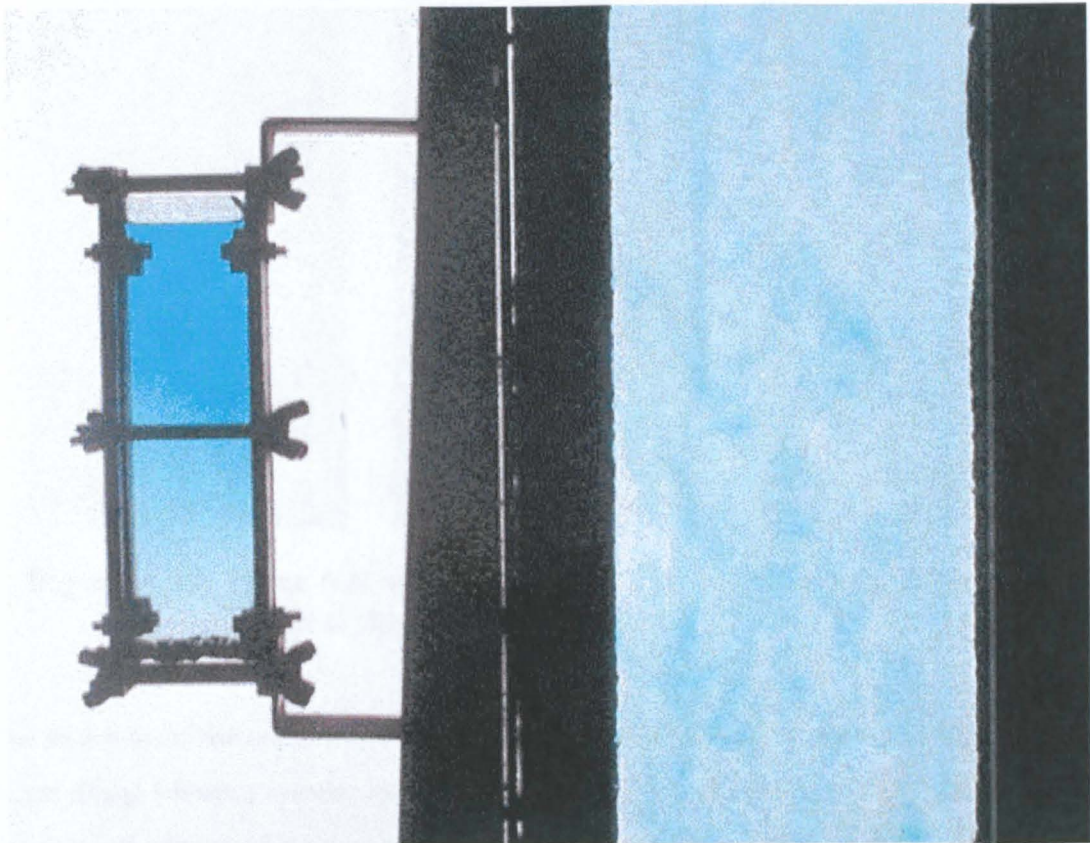


Figure 4.9: Example of raw image obtained from the digital camera.

Multiple images are necessary at each of the flow conditions for the following reasons:

- (i) To accurately determine the mean properties of the liquid film structure.
- (ii) To help ensure the capture of any interfacial phenomenon present that exhibits a longer wavelength than the measurable region of test section.

The necessity of multiple images to characterise the falling film is illustrated by Figure 4.10, which presents three images taken in rapid succession at identical flow conditions. Reliance on the first of the images, where a large disturbance wave is not present, as typical of the flow conditions would clearly result in both ignorance of the interfacial phenomenon travelling along the film and a significant underestimation of the mean properties of the falling film

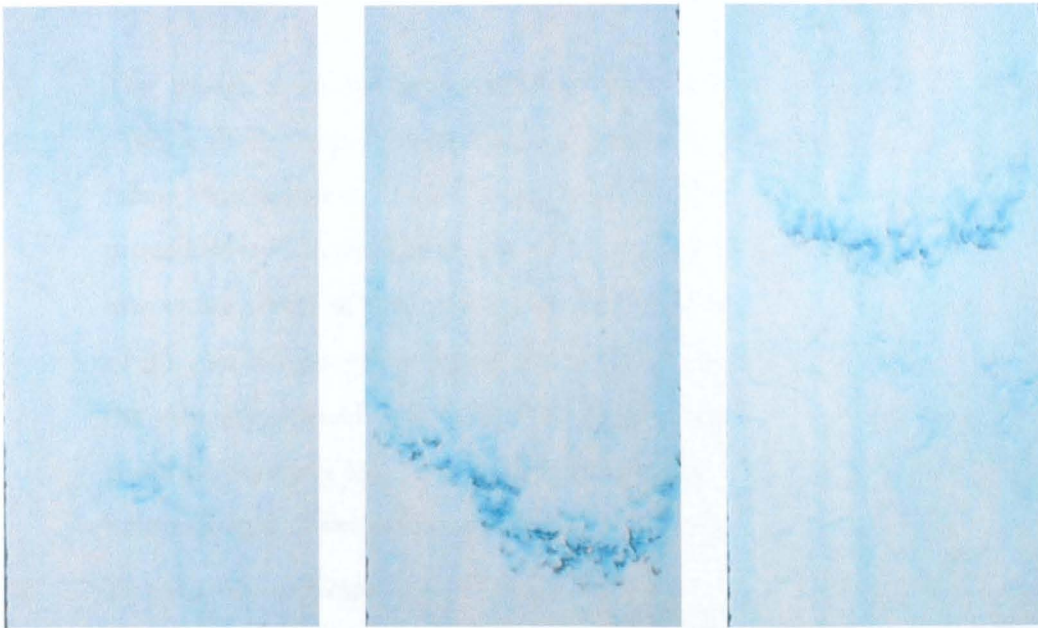


Figure 4.10: Three test section images taken in rapid succession under identical flow conditions.

The selection of the images that best represent the properties of the liquid film was aided by an image viewing system incorporated on the digital camera. This feature allowed viewing and editing of the recorded images at the point of measurement.

Figure 4.10 also highlights the phenomenon of total light exclusion from the film image, which is discussed in detail in Chapter 5 (Section 5.2.2) and Appendix B.

The flow facility could then be adjusted to the next flow regime to be investigated and the next set of images recorded. Once the experimental runs were completed, or the digital camera was filled to capacity (approximately 70 images), the digital camera was removed from the tripod and connected to a personal computer to download the recorded images.

4.3.4 Image Analysis

With the recorded digital photographs securely stored on the personal computer as bitmap images, analysis of the images could begin. The following steps were performed in the analysis of each image:

- (i) The image is loaded into commercially available image analysis software (Adobe Photoshop 5) to separate a central strip of the calibration cell and the falling film region of interest from the rest of the superfluous image, and this procedure is illustrated in Figure 4.11. A standard falling film region, 150mm (the entire width of the column) by 300mm in length, was extracted from all of the raw images. This region was usually equivalent to about two thirds of the viewable area of the falling film on each image. The falling film region could be precisely sized to the dimensions quoted above by reference to the known height of the calibration cell also present on the image.
- (ii) The analysis software is then utilised further to resize the calibration strip and falling film images to the desired standard pixel dimensions (i.e. 25(W) x 400(L) and 250(W) x 500(H), respectively). The utilisation of standard pixel dimensions throughout this study simplified any comparative data analysis and software written for batch processing of the images. A 250-pixel width was chosen as the standard for the film image due to the limitation of Microsoft Excel spreadsheet software to 256 columns. Microsoft Excel was the basis application of the software algorithms written to extract the

interfacial characteristics from the data resulting from this technique (see Chapter 5).

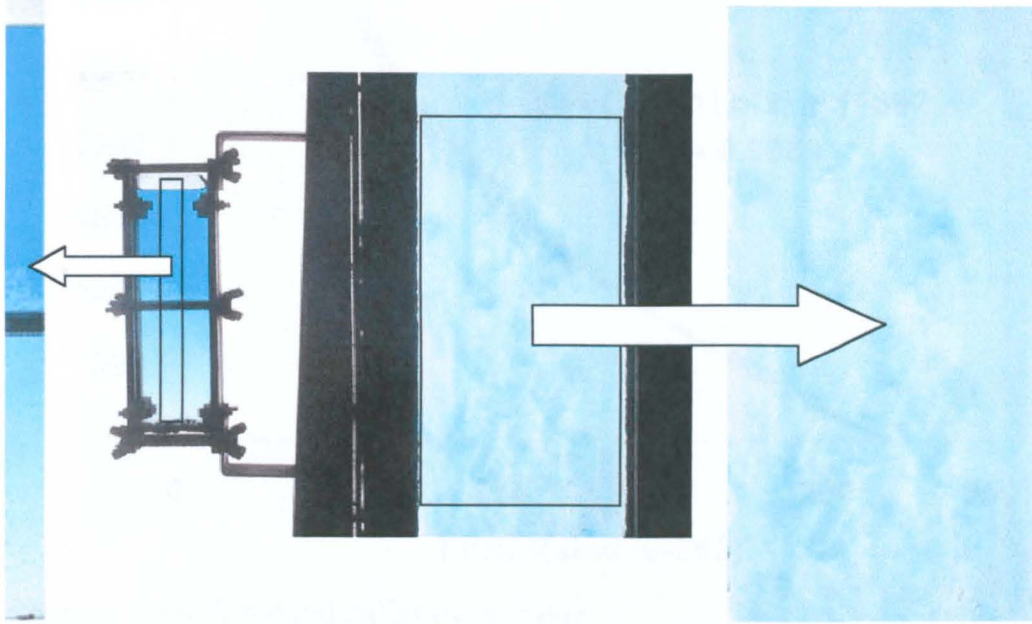


Figure 4.11: Illustration of separation of calibration strip and falling film region of interest from the remainder of the superfluous image.

- (iii) The image of the central strip of the calibration cell was then loaded into MATLAB 5 and the RGB (red, green and blue) pixel values extracted from the bitmap image and stored in the form of a 3-dimensional matrix. This matrix is then modified to reduce the contents to only the most film thickness sensitive pixel colour, determined using the procedure detailed in Section 4.3.2.5 (iii). The resulting two-dimensional matrix is then stored in the form of a Microsoft Excel spreadsheet.
- (iv) Calibration of the falling film image could then be achieved by relating the characteristic equation for the calibration cell thickness profile (Figure 4.8) with the pixel values from the calibration strip image. When plotted graphically a thickness against pixel value calibration curve and characteristic equation was generated. A typical example is presented in Figure 4.12. The gap in the data points in Figure 4.12 relates to the location of the central support bar (see Figure 4.7).

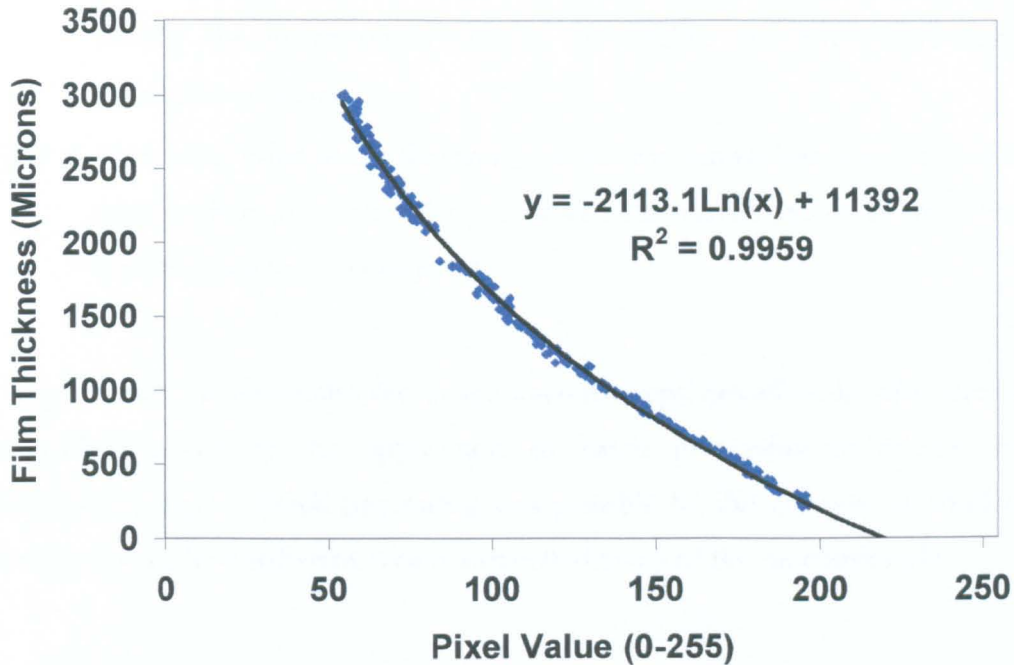


Figure 4.12: A typical calibration curve.

- (v) Step (iii) is repeated using the falling film image.
- (vi) The falling film image pixel values were then corrected for the light non-uniformity discussed in Section 4.3.2.4. This was achieved in several stages. The first stage was the identification of the centre of the flash light source on the raw images by analysis of the pixel values of a horizontal and vertical strip of a raw blank image (*i.e.* an image with no liquid present in test section or calibration cell). This was made possible by using the assumption that output from the flash light source was radially constant, confirmed to be valid from separate checks. This stage was necessary each time the camera's position was adjusted, however slightly. After identification of the light source centre, the next stage was to determine the distance of each film image pixel from this point. The next stage was the construction of a correction equation for modification of the image pixel values in relation to their distances to the light source centre, by a ratio of their value to a reference value. The reference value was chosen as the value associated with the mean distance of the calibration cell image strip from the centre of the light source. This choice of reference simplified matters, by ensuring that the corresponding

modifications required for the calibration cell pixel values were small enough to be ignored. The final stage was the utilisation of a computer program to modify the image pixels one by one within the spreadsheet using the correction equation.

- (vii) Each pixel value of the film image within the spreadsheet was then converted into the film thickness value it represents by substitution into the calibration equation generated in step (iv).

The time needed to undertake the image analysis steps described in this section was significantly reduced by the application of batch processing techniques on the photographic images. Batch processing was possible by the creation of small macro routines in the analysis software, which automated many of the repetitive tasks.

Chapter 5

LIQUID FILM THICKNESS MEASUREMENT

Analysis of the Spatial Film

5.1 INTRODUCTION

Chapter 4 demonstrates how a novel adaptation of the light absorption spatial film thickness technique (*i.e.* LAIT) can be applied to obtain thickness information for a spatial region of a vertically falling film. Currently, each application of the technique results in the spatial representation of the film by one hundred and twenty five thousand individual localised measurements of film thickness contained within a two hundred and fifty column by five hundred row spreadsheet.

Global analysis of the spatial film data is possible through averaging and histogram based techniques, however, specific analysis of localised and global substrate film and disturbance wave physical characteristics requires a method of categorisation of these components of the film.

The purpose of this chapter is to review the computer algorithm utilised in the analysis of the spatial film data. The algorithm was written using the Microsoft Visual Basic for Applications (VBA) language present within Microsoft Excel. VBA is an object-orientated computer language, which requires that the algorithm is built up from individual subroutines or modules of specific function. The structure of this chapter is to describe the mechanics and reasoning behind each of the modules in turn, presenting examples of their output where relevant.

The algorithm was utilised in batch analysis of all spatial film thickness data obtained for the three liquids under investigation. Analysis techniques utilised for specific portions of the film data are detailed in the appropriate section of the results (Chapters 8 & 9).

5.2 ANALYSIS OF THE SPATIAL FILM DATA

5.2.1 Edge Effects

Accurate analysis of the entire image of the spatial film was complicated by the influence of the following phenomena at the edges of rectangular test section:

- (i) Light reflection shadows from the plastic spacer strips.
- (ii) Flow disturbances caused by edge effects.
- (iii) Localised wetting of the glass viewing plate by liquid bridging the plastic spacer strips.
- (iv) Minor inaccuracies in the cutting of the film image from the rest of the superfluous image, resulting in small black strips of rectangular test section framework being included at the vertical edges of the film image.

Therefore, it was believed prudent that all analysis of the spatial film data ignored the first 2.4% of data (*i.e.* six data columns) from each vertical edge, reducing the number of film thickness analysis points to one hundred and nineteen thousand. However, small amounts of erroneous data were still included at the edges of many of the film images (highlighted as a consequence of the investigation into rogue points caused by light exclusion, see Section 5.2.2), which tends to suggest that any edge data exclusion should be at least doubled in future analysis attempts.

5.2.2 Correction of Rogue Points Caused by Total Light Exclusion

The purpose of this module was to modify rogue points caused by total exclusion of the light source by refraction. The presence of this optical phenomenon is directly related to the contact angle between air and liquid phases, and this relationship is quantified and discussed in detail in Appendix B. The phenomenon was visualised in the current study at wave-substrate boundaries under certain flow conditions where relatively high interface contact angles were present, represented on the film image by pixels totally devoid of light (*i.e.* black).

The program module analyses each measurement point in turn, column by column, determining the air-liquid interface contact gradient between the current and previous point. If the value of this gradient exceeds forty-five degrees (upward slope) the measurement point value is modified to an exactly forty-five degree gradient equivalent. Similarly, if the value of this gradient is less than minus forty-five degrees (downward slope) the previous measurement point is modified to an exactly minus forty-five degree equivalent. Forty-five degrees was chosen as the trigger value as this is consistent with the values determined in Appendix B for the maximum interface contact angle obtainable before the occurrence of total light exclusion.

To demonstrate the necessity of this module, Figure 5.1 presents a film image of ethoxylated alcohol falling where total exclusion of light can clearly be seen at many of the leading edge wave-substrate boundaries. Also provided in the figure is a graphical plot of film thickness versus distance for a central longitudinal strip of the film image.

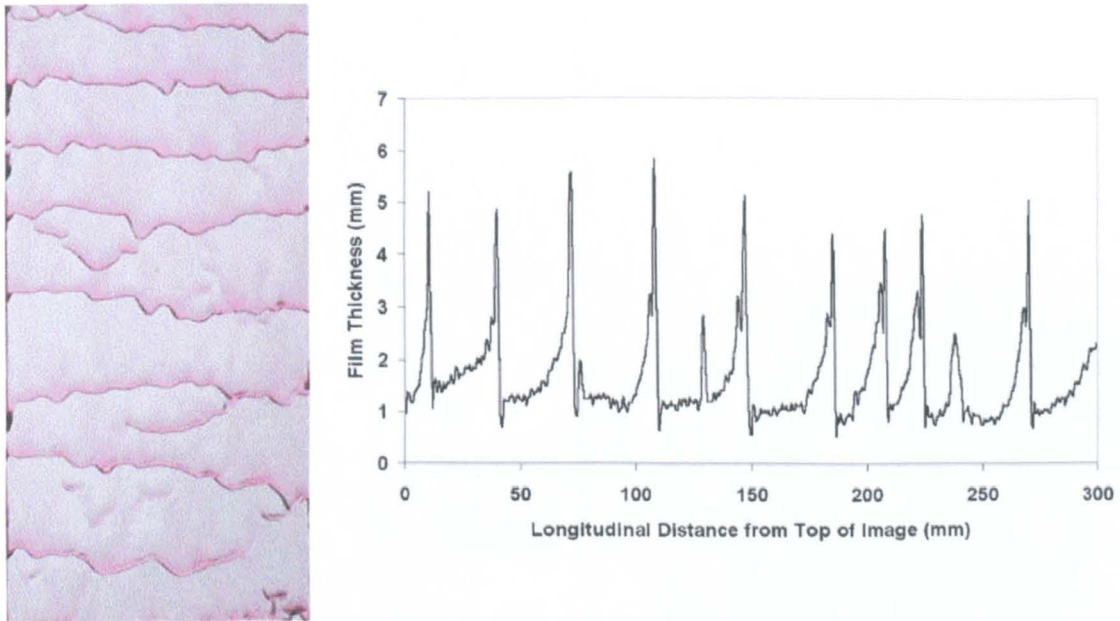


Figure 5.1: Film image with a graphical plot of the unmodified film thickness versus longitudinal distance from top of image for a central strip of the image.

The graphical plot demonstrates the artificial exaggeration of the wave peaks caused by the points of total light exclusion at the leading edge of the disturbance waves. These

black points manifest themselves in the analysis as comparably much high film thickness values than the rest of the image. This is due to their relevant RGB pixel value being or approaching zero, whereas the rest of the image’s relevant RGB pixel values are generally much higher as they contain at least some measurable pigmentation of the appropriate colour.

To demonstrate the effectiveness of this module at modifying these rogue values to more realistic levels, Figure 5.2 presents the film thickness versus distance from the top of the above image for a central longitudinal strip after modification of film thickness data with the ModifyRogueCode module. The unmodified values are also included to aid comparison

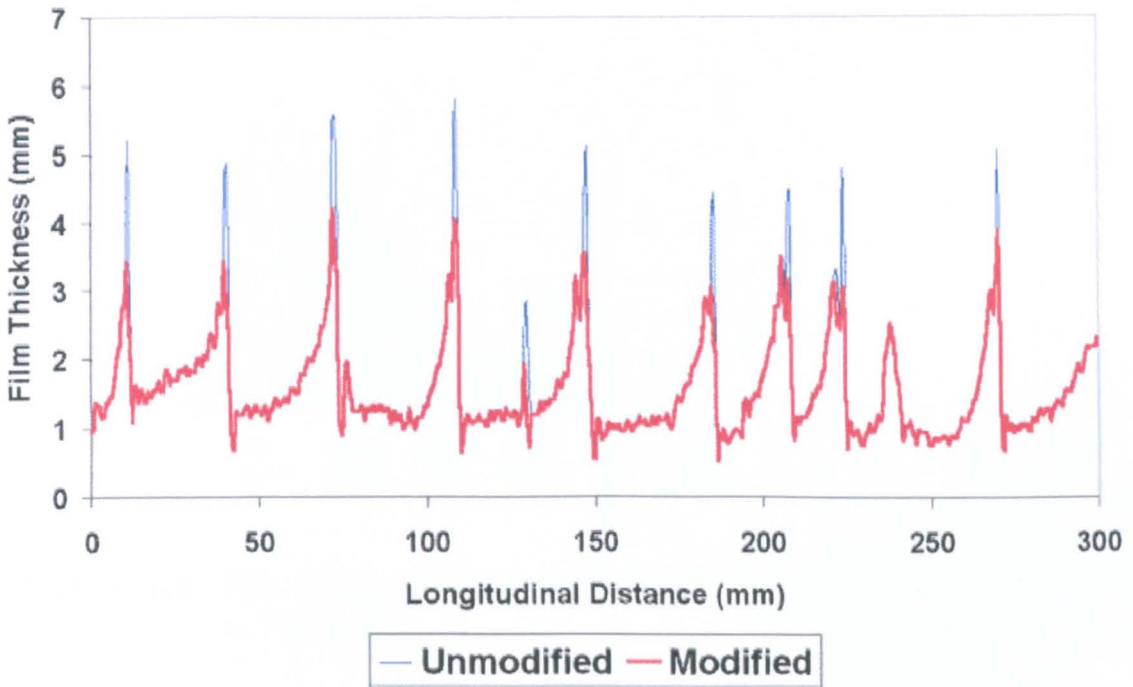


Figure 5.2: Graphical plots of the modified and unmodified film thickness versus longitudinal distance from top of image for a central strip of the image presented in Figure 5.1.

Clearly, the film thickness spikes caused by the light excluded points have been clipped and the modified wave profile is more consistent with disturbance wave structures reported in the literature. However, the module is not capable of removing all rogue

measurement points and is particularly ineffective when the black region covers more than one pixel in depth. More complex methods at modification were attempted but were prone to accidental modification of data unrelated to the phenomenon.

5.2.3 Generation of a Histogram of the Spatial Film

This module simply obtains the maximum, mean and minimum film thickness value of the film data and generates both in tabular form and graphically a histogram of the entire film thickness points within ten equally sized bins. Figure 5.3 presents an example of the film histogram table and plot generated by this module for the film image in Figure 5.1.

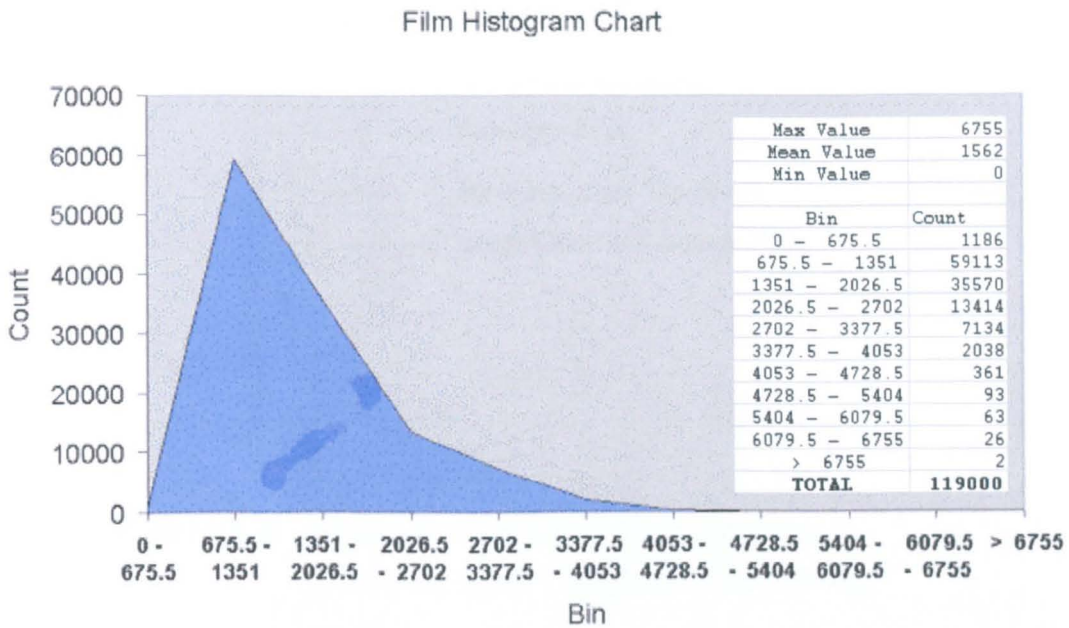


Figure 5.3: Film histogram table and plot generated for the film image in Figure 5.1.

The film histograms generated by this module were particularly useful at providing a simple way to overview the global film thickness characteristics and facilitate comparison of these characteristics with other films. They further provided a means to quantify the errors in thickness measurement due to light exclusion that were still present after the modification of the majority of these points by the module reviewed in the previous section. When present, these errors appear as a cluster of data in the highest bins of the histogram and represent film thickness heights at the high end of the calibrated thickness

range, usually far removed from the rest of the spatial thickness data for the investigated film.

5.2.4 Categorisation of the Film Data

Any categorisation of the film data is non-trivialised by the apparent random nature of the interface, illustrated by Figure 5.4.

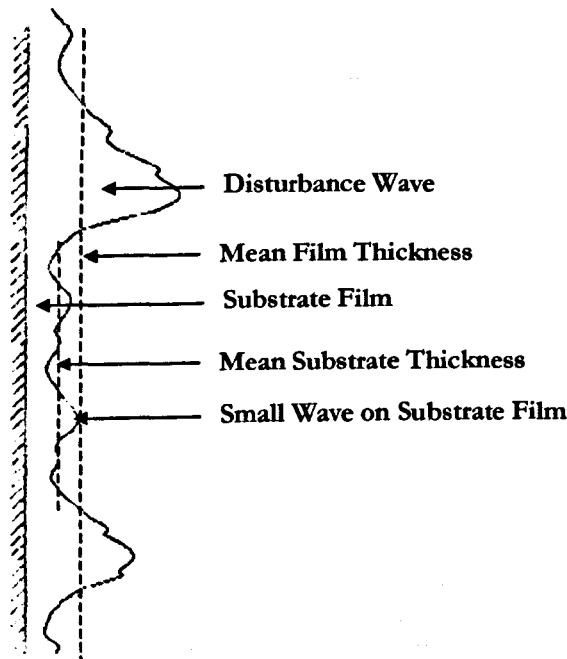


Figure 5.4: Illustration of falling film structure.
(Adapted from Chu & Dukler (1974)).

However, the figure also illustrates that categorisation is possible by considering separately the two main constituents of the film.

- (i) The wavy substrate base film layer.
- (ii) Disturbance waves.

The purpose of this module is to categorise the film thickness data into these disturbance and substrate regions.

Literature indicates that categorisation of temporal film thickness data has been applied in several previous studies, and of these, the categorisation by Chu & Dukler (1974) was considered the most suitable for adaptation to the current work. Their method involves the categorisation of the interface into three classes of wave by the following criteria:

1. A large (disturbance) wave exists if an excursion in film thickness is found such that:

$$h_{\max} > \{h\} \text{ and } h_{\min}, h'_{\min} < \{h\}$$

2. A small wave exists on the substrate if for that excursion:

$$h_{\max}, h_{\min}, h'_{\min} < \{h\}$$

3. A small wave exists on large waves if one of three possible conditions are detected:

$$h_{\max} > \{h\}, h_{\min} > \{h\}, h'_{\min} < \{h\}$$

$$h_{\max} > \{h\}, h_{\min} < \{h\}, h'_{\min} > \{h\}$$

$$h_{\max} > \{h\}, h_{\min} > \{h\}, h'_{\min} > \{h\}$$

where, $\{h\}$ is the mean film thickness, h_{\max} is the film thickness at the crest of the wave, h_{\min} is the film thickness at the trough in front of the wave and h'_{\min} is the film thickness at the trough at the back of the wave.

These criteria imply that disturbance waves can be considered as large fluctuations that take place about the mean film thickness with the minimum and maximum film thickness associated with the wave being on alternate sides of the mean, and that the entire contents of the substrate appear to be completely below the mean film thickness. This appeared consistent with visual observation of the film data generated, therefore, attempts were made by this author to develop algorithm coding to utilise the criteria directly. Initial techniques involved stepping through the data, column by column and identifying regions where the criteria were successfully met. However, the resulting codes were cumbersome, prone to bugs and required hours of running time for each film image, therefore, a simpler approach was sought

It became apparent quite quickly that identification of small waves on the disturbance waves (Criteria 3) was the most difficult criterion to implement. The trailing edge wave slopes, where the small waves described by Chu & Dukler should be found, were often not as smooth as Figure 5.4 suggests but covered in perturbations that made wave identification difficult. Without further study at higher image resolutions, i.e. the trailing edge being represented by a greater number of points, it is difficult to deduce whether the general roughness of the trailing edge is a natural phenomenon or a resolution limitation. Therefore, it was decided for the current study to abandon Criterion 3 and consider the disturbance wave as a whole. To further reduce complexity and computational time required, Criterion 2 was simplified to consider the substrate film as a whole, rather than treating the base film and waves separately. Implementation of these simplifications allowed the reduction of the module code to the following methodology:

- (i) **Copy the bulk of the disturbance wave points onto a separate disturbance wave specific spreadsheet.** Criterion 1 implies that film thickness points with a value greater than the mean film thickness should only be related to disturbance waves, therefore, all film thickness values ten percent greater than the mean value were automatically considered as disturbance wave points. The addition of a ten percent tolerance was found to be necessary through experience to avoid the inclusion of points that were clearly associated with the substrate film but had values slightly greater than the mean thickness value, particularly when the film region was substrate dominated.
- (ii) **Find wave trailing edge points and add to disturbance wave specific spreadsheet.** The purpose of this code loop is to step forward through the points, column by column, until the first point identified in (i) is reached. This point triggers the code to step back through the row of data to identify points associated with the trailing edge of the disturbance wave. The code continues to step back through the row of data, while adding these points to the disturbance wave specific spreadsheet, until it encounters the trigger point that has a value smaller than the next point to be stepped to. This trigger point represents the

trailing wave edge minimum point, h'_{\min} , for that one column wide slice of the disturbance wave. The code then returns to the point at which the stepping back was triggered, and continues stepping forward through the data, until reaching the next disturbance wave region initial trigger point that was identified by (i). Here the stepping back loop is activated once again and the whole process continues until the entire film data has been scrutinised.

- (iii) **Find wave leading edge points and add to disturbance specific spreadsheet.** This code loop works in a similar manner to that in (ii) but instead is triggered by the all the last points of the column wide disturbance wave strips, where it steps forward through the data until being triggered by a point whose value is smaller than the next point. Therefore, the loop identifies the film data points associated with the leading edges of the disturbance waves and adds them all to the disturbance wave region spreadsheet to complete these regions. The trigger point represents the leading wave edge minimum point, h_{\min} , for that column of the disturbance wave region.
- (iv) **Any points not associated with disturbances are assumed substrate and copied to separate spreadsheet.** This portion of code simply identifies any points not previously added by (i)-(iii) to the disturbance wave region spreadsheet to be assigned to a substrate film specific spreadsheet.

Visual observation of the resulting classification suggests that although simplistic, the method described above is quite effective at accurate categorisation of the film data.

5.2.5 Generation of Histograms for the Disturbance Wave and Substrate Regions of the Film

As with the generation of the entire spatial film histogram (Section 5.2.3), these modules simply obtain the maximum, mean and minimum film thickness values of the disturbance wave and substrate region classified film data and generate both in tabular form and graphically a histogram of the film thickness points for each region within ten

equally sized height bins. An example of these histogram tables and plots is presented in Figure 5.5

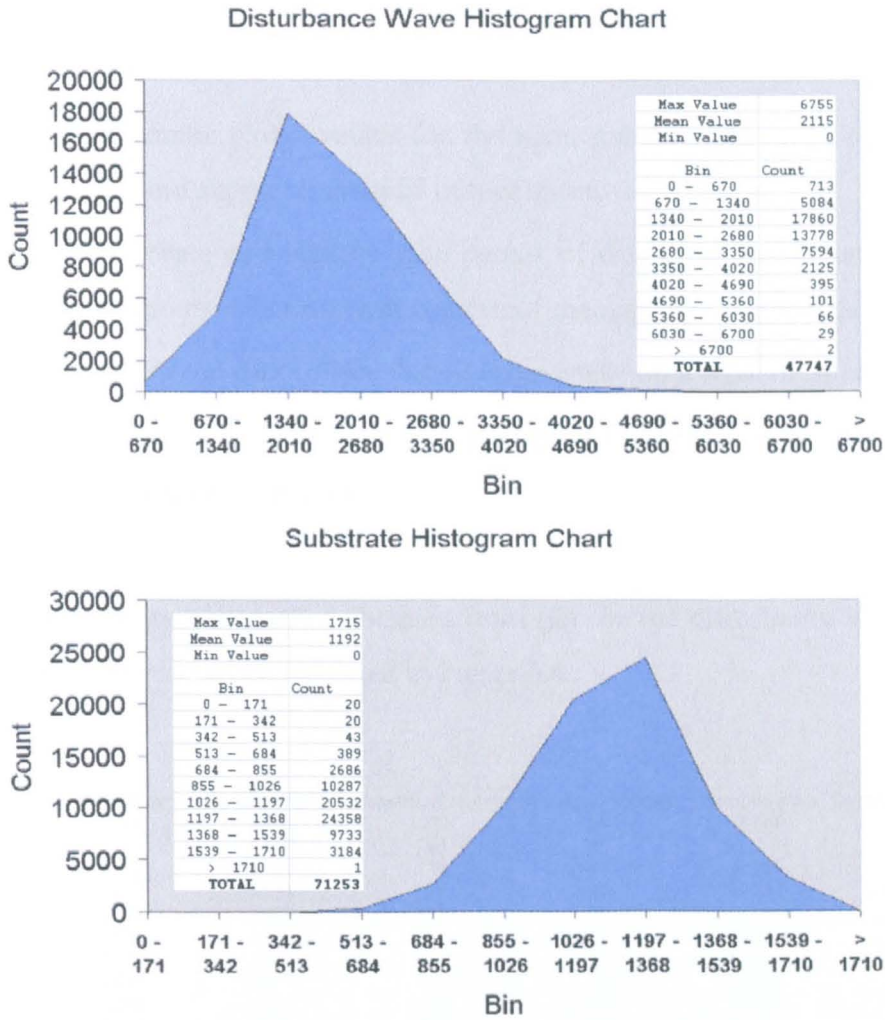


Figure 5.5: Histogram tables and plots generated for the disturbance wave and substrate region of film image in Figure 5.1.

These histograms provided a simple means to visualise the film thickness components that made up the substrate and disturbance wave regions. Their ability to ascertain a globally averaged dimension to these regions through the minimum, mean and maximum values was complicated by the inclusion of tiny amounts of erroneous data that exaggerate the minimum and maximum values. However, true minimum and maximum values are clearly evident from the histogram graphical plot.

5.2.6 Collation and Analysis of Disturbance Wave and Substrate Film Data Packets

The objectives of these two program modules is identical, except for their application to either the disturbance wave or substrate region of data:

- (i) Determine global values for the sum, number and mean of the region data and supply to the final output sheet.
- (ii) To collate and identify each packet of data's size, minimum, mean and maximum values on each column of their specific regional data sheet.
- (iii) Output the data collected in (i) sequentially on a separate sheet.
- (iv) Obtain global averages of the packet data identified in (ii) and supply this to the final output sheet.

A sample of this sequential output obtained from (iii) for the disturbance wave data for the film image of Figure 5.1 is presented in Figure 5.6.

WaveNumber	WaveMinStart	WaveMaxValue	WaveMinFinish	WaveCellNumber	WaveCellSum	WaveMeanValue
1	3346	3953	1531	35	78756	2250
2	1531	6479	559	49	130190	2656
3	1612	4209	338	40	92345	2308
4	1408	4161	250	25	56744	2269
5	1531	3900	338	25	54685	2187
6	1572	6244	646	33	114857	3480
7	1531	3241	819	20	42808	2140
8	1449	4083	338	27	65215	2415
9	3171	4016	1449	27	62000	2296
10	1449	5655	1284	27	76742	2842
11	1367	1734	1242	8	12322	1540
12	1449	2773	990	22	45697	2077
13	1449	3973	338	21	46788	2228
14	1612	3262	70	19	40122	2111
15	1367	3920	383	36	83330	2314
16	1408	3100	1200	21	43613	2076
17	1408	3812	383	26	59527	2289
18	2700	3262	1612	21	43953	2093
19	1325	4935	776	25	59209	2368
20	1408	3150	1074	22	42486	1931

Figure 5.6: Sample of sequential disturbance wave packet data for film image presented in Figure 5.1.

Global averaging of the packet data provided a straightforward means to obtain representative values of the physical structure for the disturbance wave and wavy

substrate regions. This information provided a comprehensive means to study the influence of flow conditions on physical structure of the films.

5.2.7 Determination of Area and Volume Relationships for the Disturbance Wave and Substrate Film Regions

The purpose of this module is to supply to the final output sheet the area and volume relationships of the disturbance wave and substrate regions relative to the entire spatial film. This information is particularly valuable when considering mass transfer aspects through the system.

The percentage area associated with each region is simply determined from the number of data points allocated. For volume determination it is assumed that the disturbance waves travel independently over the substrate. Therefore, the fraction of the film volume held up within the disturbance waves can be expressed by:

$$\frac{((D_{mean} - S_{mean}) \times D_{num})}{F_{mean} \times F_{num}} \quad (5.1)$$

where, D, S and F represent the disturbance wave, substrate and entire film region data points, and subscripts mean and num denote mean value and total number of points of the specified region, respectively.

5.2.8 Final Output

To ease visualisation of the information determined during the spatial film analysis, all pertinent data was collated on to a separate final output sheet, illustrated in Figure 5.7 for the example used throughout this section.

For each of the fluids investigated, the final output sheets for all flow conditions investigated were then combined to create the tabular summary of the spatial film data provided for reference in Appendix C.

	Raw
Mean Film Thickness	1562
Sum of Disturbance Points	100993108
Number of Disturbance Points	47747
Mean Disturbance Height	2115
Mean Disturbance Wave Min Start	1411
Mean Disturbance Wave Max	3374
Mean Disturbance Wave Min Finish	976
Mean Disturbance Wave Cell Number	19
Mean Disturbance Wave Length	11674
Mean Disturbance Wave Height	2084
Sum of Substrate Points	84984725
Number of Substrate Points	71253
Mean Substrate Height	1192
Mean Substrate Min Value	961
Mean Substrate Max Value	1505
Mean Substrate Cell Number	31
Mean Substrate Length	18435
Number of Disturbance Wavelets	2454
% Area Covered By Disturbance Waves	40.12%
% Area Covered By Substrate	59.88%
% Volume Contained in Disturbance Waves	23.71%

Figure 5.7: Example Final Output Sheet for Film Image in Figure 5.1.

Chapter 6

LIQUID FILM VELOCITY MEASUREMENT

Review of the Literature

6.1 INTRODUCTION

The measurement of velocities in falling films is an even more challenging problem than measurement of film thickness. Velocity measurement is made non-trivial not only by the thinness of such films, generally less than a few millimetres, but also by the existence of a velocity profile within the film. For wavy falling films, measurement is further complicated by the interfacial structures (*e.g.* disturbance waves) that travel virtually independently over the base substrate film at substantially greater velocities than the substrate. Finally, the difficulties described above are exacerbated by the range and magnitude of the measurement velocities, reaching several meters per second in highly turbulent air-liquid flows.

In an effort to overcome the experimental challenges that film velocity measurements present, a diverse range of velocity measurement techniques has been developed. Additionally, review of the literature suggests that the desired component of the liquid film velocity also restricts the choice of measurement technique. Velocity profile measurement within liquid films has mainly been limited to smooth films or the base substrate layer, with little application to the measurement of profiles within wavy films. Techniques developed for wave velocity measurement are limited to these structures, with information on the velocity of the base substrate layer only indirectly available with knowledge of the thickness of the film.

Table 6.1 presents a Summary of reviewed film velocity measurement techniques, with appropriate classification of their measurement capabilities.

Table 6.1: Summary of reviewed liquid film velocity measurement techniques.

Velocity Profile Measurement (6.2)	Wave Celerity Measurement (6.3)
Receiving Vessel Method (6.2.1)	Fast Stopwatch Method (6.3.1)
Ultra Microscope Technique (6.2.2)	Direct Photographic Measurement (6.3.2)
Pneumometric Method (6.2.3)	Paired Film Thickness Probe Output (6.3.3)
Hot-Wire Anemometry (6.2.4)	
Hydrogen Bubble Technique (6.2.5)	
Stereoscopic Photography (6.2.6)	
Mirrored Wall Stroboscopic Particle Visualisation (6.2.7)	
Photochromic Dye Activation Technique (6.2.8)	
Laser Doppler Anemometry (6.2.9)	

The purpose of this chapter is to critically review the alternative techniques available and summarise their suitability for application in the current study.

6.2 VELOCITY PROFILE MEASUREMENT

Since the earliest interest in liquid films, there has been a desire to have knowledge of the velocities within them to validate the parabolic velocity profile predicted by laminar film flow theory. As with film thickness measurement, the earliest techniques developed were mainly intrusive in nature, however, most researchers would agree that their usefulness in thin falling film measurement is questionable. The non-intrusive techniques that have been developed and applied over the past thirty years to replace these intrusive techniques and extend measurement into wavy films are predominantly optically based, but with many of these techniques involving the addition of tracer particles, their actual non-intrusivity has also been questioned.

6.2.1 Receiving Vessel Method

Described in the review by Alekseenko *et al.* (1994), this method involves the insertion of a sharp-edged vessel into the liquid film and then measuring the flow rate of the removed liquid. The average local velocity can then be determined by the following formula:

$$u = \frac{Q(y_2) - Q(y_1)}{s_{1,2}} \quad (6.1)$$

where, y_1, y_2 are the distances from the receiving vessel to the wall, $Q(y_1), Q(y_2)$ are the flow rates through the receiving vessel and $s_{1,2}$ is the cross sectional area corresponding to the vessel displacement from y_1 to y_2 .

Clearly, for wavy film flow the technique is limited to measurement of the actual average velocity for a displacement range less than the height of the continuous substrate layer. The accuracy of the technique is also questionable when considering the strong disturbances to the film flow by the receiving vessel. Therefore, it is not surprising that applications of this technique in wavy film environments could not be found.

6.2.2 Ultra Microscope Technique

The technique has been extensively applied for measurement of velocities in single-phase liquid flows; however, Grimley (1945) probably reports the only application of the technique for thin falling films. It uses streak photography, with side illumination of small (1-10 μ m) tracer particles, to obtain velocity profiles. Due to the limitations imposed by the available technology of the time, the author had difficulty interrupting the light source rapidly enough to allow the observing microscope to obtain traces of a realistic measurement length. Therefore, the author overcame this by moving the microscope along the film at an equal speed to the particles, making the particles appear stationary for measurement purposes, with the velocity directly obtained from the microscope displacement. Naturally, the necessity of the microscope displacement results in a much larger than desired averaging locality.

6.2.3 Pneumometric Method

This method has traditionally been applied in the measurement of the velocity profile within the continuous substrate residual layer of a dynamic liquid film. The velocity is calculated on the basis of the dynamic head measured using a standard head tube. A recent application in velocity profile measurement of turbulent vertically falling films is presented by Gimbutis (1998) using a 0.26mm o.d., 0.18mm i.d. tube capable of traversing the film from both sides.

However, the intrusive nature of the tube applied in the pneumometric method brings into question the validity of application of this technique in thin film measurements.

6.2.4 Hot-Wire Anemometry

The fundamental principle behind hot-wire anemometry is that the heat transfer from a thin filament heated by a constant electrical current is directly related to the velocity of the fluid receiving the heat.

Hot-wire anemometry has been used extensively in many aspects of two-phase flow for the determination of velocity fluctuations, wall shear stress and local void fractions,

however, limited examples have been reported for velocity measurements within liquid films. One such application of hot-wire anemometry in the measurement of horizontal liquid film velocity profiles is reported by Atkinson & Caruthers (1965). They used a hand made probe, illustrated in Figure 6.1, and shaped it in such a way that the hot-wire is the first element of the probe to touch either the fluid interface or the bottom of the channel to allow exploration of the total thickness of the film.

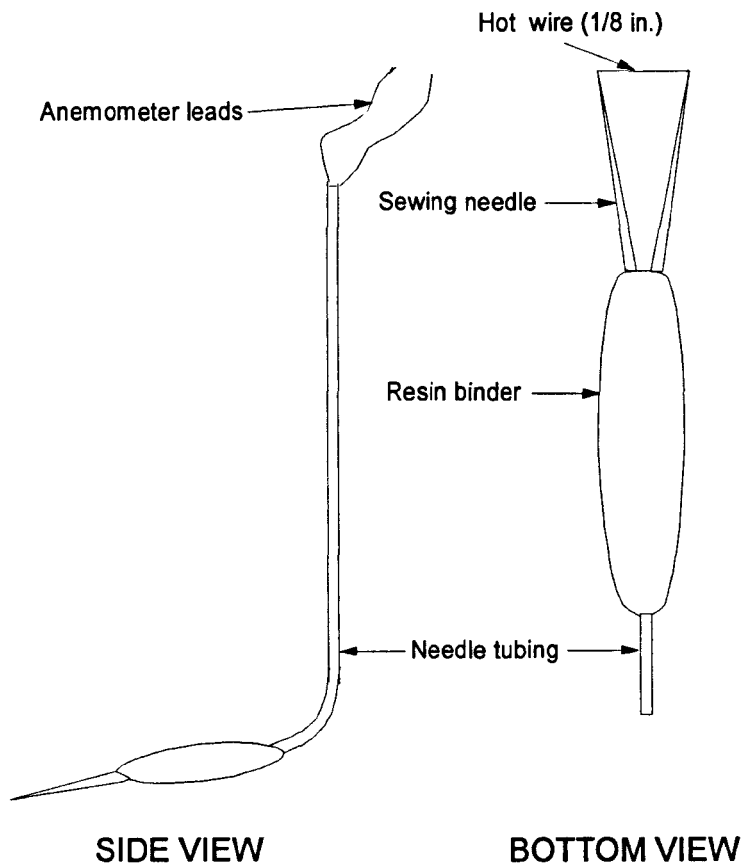


Figure 6.1: Illustration of a hot-wire anemometer probe. (Taken from Atkinson & Caruthers (1965)).

The probe was supported by an aluminium traversing mechanism, with a dial indicator attached to the traversing plate to allow probe positioning to be located within 0.005 in. Calibration was achieved directly for each profile measured by a comparison for various flowrates between the surface velocity of a small particle passing over the measuring section and the output signal. Velocity measurements were then taken at small incremental steps into the liquid film. Ueda & Tanaka (1975) reported the application of a similar methodology for velocity profile measurements on inclined falling films. The

results achieved from both studies were consistent with the parabolic profile presented by other measurement techniques.

6.2.5 Hydrogen Bubble Technique

Thomas & Rice (1973) adapted the hydrogen bubble visualisation method for the measurement of velocity profiles in thin liquid films on an inclined plane wall of up to four degrees from the horizontal, utilising the experimental facility illustrated in Figure 6.2.

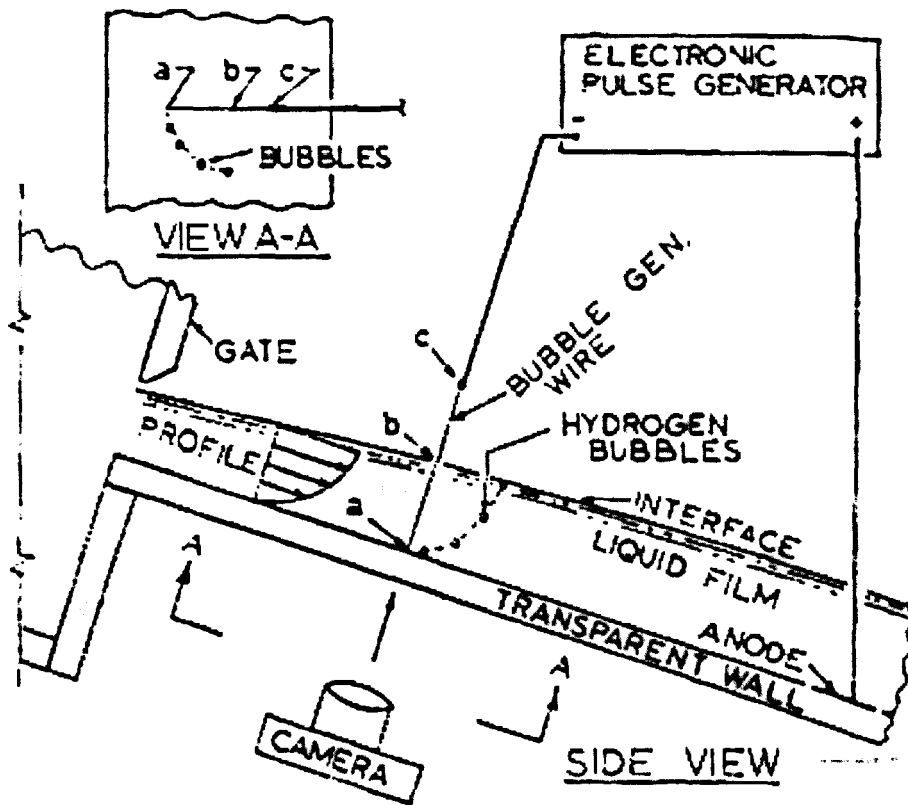


Figure 6.2: Hydrogen bubble velocity measurement technique. (Taken from Thomas & Rice (1973)).

The technique involves the electrolytic generation of a fine row of hydrogen bubbles on a 0.001inch diameter tungsten wire orientated diagonally through the liquid film and perpendicular to the mean flow direction. The fine hydrogen bubbles were then swept away immediately by the flow and recorded photographically on a plane parallel to the bottom of the transparent flow channel. This approach effectively amplified the film

thickness by a factor of approximately twenty for observation purposes and bypassed the necessity of a side view. A small amount of NaCl salt was added to the liquid film to improve conductivity of the water. Ito & Tomura (1979) utilised a virtually identical methodology in the determination of the velocity profile for a falling liquid films on inclined plates up to approximately fifteen degrees from the horizontal.

Both studies present parabolic velocity profiles that compare favourably with theoretical analysis and comparative measurement techniques, however, the inevitable disturbance of the flow, admittedly small, caused by the thin tungsten wire ensures that some concern must still remain on this methods suitability in thin liquid film measurements, particularly in turbulent regimes where a two dimensional flow cannot be assumed.

6.2.6 Stereoscopic Photography

Stereoscopic photography was developed by Nedderman (1961) to allow velocity profiles in thin (*circa.* 1mm) films of liquid. The method is based on the production of a pair of stereoscopic photographs of tracer particles flowing within the film. The original camera and test cell arrangement employed is shown pictorially in Figure 6.3.

The author reports obtaining a linear calibration, and the best results, when the camera axes were co-planar with the cell axis. The cameras were focussed by moving them bodily on two-way sliding tables, whose displacement was calibrated to 0.001inch using a screw feed. The tracer particles are lit with a flashing light so that they appear on the photographs as rows of dots. Analysing these photographs so that the two images of a particular point were both under the cross wires of their respective calibrated stereoscopic eyepiece, allowed velocities to be obtained from the distance between two successive dots. Alternatively, particle velocity could be calculated on the basis of track length if pulse illumination is utilised.

Nedderman investigated as potential tracer particles air bubbles, glass beads and oil dispersions and found that air bubbles gave the best photographs and were small enough to have negligible drift velocity. The bubbles were generated by bleeding air through a needle valve into the suction of a circulating pump. This generation within the

circulating system gave enough time for the large bubbles to rise to the surface and burst, leaving only the small bubbles to enter the films. Spherical particles were also preferred, as asymmetric particles will appear brighter on one photograph than the other, leading to confusion in matching the dots on the photographs. The lighting for the photographs was also found to be critical; backlighting caused the necessity of corrections for depth and side lighting caused displacement of the bubbles to one side. Therefore, the bubbles were lit from both sides, with the average position of the two images giving the central position of the bubble. A photographic flashlight was utilised to generate the light as it removed any need to synchronise the camera shutters, which would be necessary under normal light.

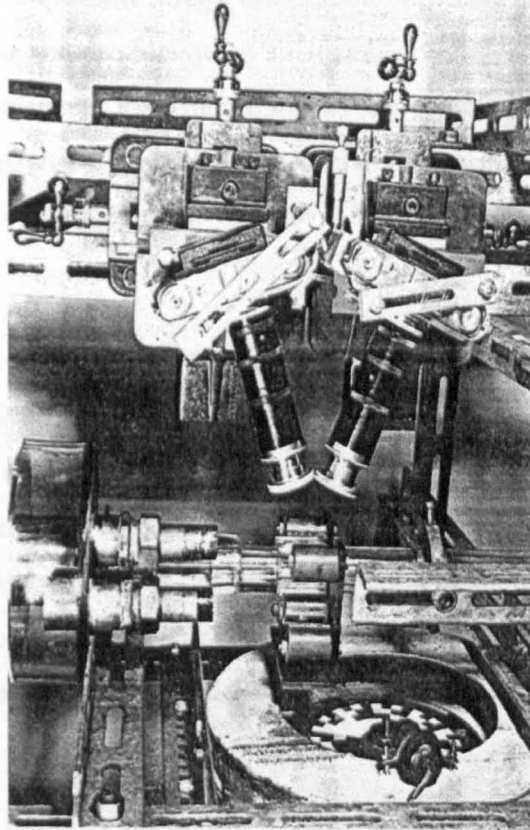


Figure 6.3: Stereoscopic camera and test cell arrangement. (Taken from Nedderman (1961)).

Wilkes & Nedderman (1962) present actual measurements of velocity profiles in falling liquid films within a 10ft long, 1" diameter, Perspex tube. They found that in almost all cases the velocity profile was very nearly parabolic, which is consistent with the other

velocity profiling techniques reviewed in this chapter. A major disadvantage of this method, reported by the authors, is that it takes several minutes to obtain one reading from the photographs, making it rather unsuitable for fluctuating flow when a large number of readings are necessary for a reasonable average.

The original stereoscopic technique was adapted and improved by Azzopardi (1977) who utilised refraction through a large angle prism, which forms both halves of the stereoscopic picture on one frame. This removes the necessity of one of the two cameras used by Nedderman and his co-workers. However, the varying length of light paths within the prism caused the formation of a phenomenon described by the author as a 'coma', *i.e.* a tail of light from the object towards the edge of the photographic film. This coma was tolerated; as it did not obscure the image, only blur it. A further problem associated with the use of the prism was the production of an area of overlap at the centre of the prism. This overlap made it difficult to differentiate between objects from the sides of the prism. Grinding the apex of the prism away until a 1mm wide face parallel to the front face was produced masked the overlap.

Elkins *et al.* (1977) utilised a similar prism approach for a horizontal liquid film flow; however, they additionally report hardware and software requirements for scanning the data to automate film reading. This method significantly reduces much of the tedious and time-consuming analysis requirements of the stereoscopic technique, which is probably the major drawback of the technique over comparable techniques reviewed in this chapter. It is reasonable to believe that with the considerable advances in computer and image analysis technology over the past twenty years that the method could yet be refined further.

6.2.7 Mirrored Wall Stroboscopic Particle Visualisation

Developed by Cook & Clark (1971), this technique was based on the stereoscopic photography technique reviewed in the previous section. The principle of this method was to measure the depth of the tracer particle by utilising a mirror as the flow surface. When viewed at an angle, the apparent displacement between particle and reflection will determine the particle depth from simple geometry and the laws of refraction. The

author utilised one-micron aluminium oxide particles as the tracer, chosen as a compromise between size and brightness. The particles were recorded photographically with a high-speed film and analysed directly from the negatives with a 10x microscope. The author asserts the technique to be capable of depth measurements within four microns and velocity measurement accuracy within one percent. However, he concedes the technique is limited to a region of negligible surface curvature.

An improvement on this method is reported by Nakoryakov *et al.* (1977) and later by Alekseenko *et al.* (1985b) for the measurement of instantaneous, rather than only mean, velocity profiles in vertical wavy falling films. The measuring schematic is presented in Figure 6.4.

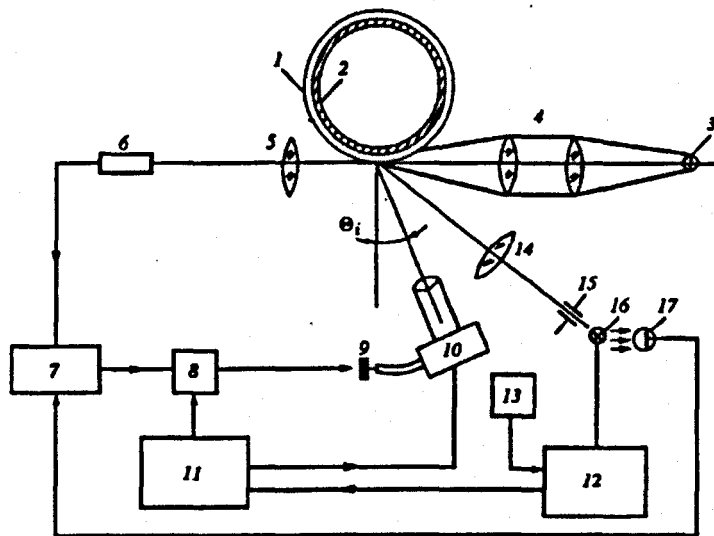


Figure 6.4: Measurement schematic for mirrored wall stroboscopic particle visualisation: 1-liquid film, 2-test section, 3-mercury lamp, 4-lens, 5-objective, 6-photomultiplier, 7-loop oscillograph, 8-electromagnet, 9-cable release, 10-camera, 11-synchronisation unit, 12-stroboscope, 13-sound frequency generator, 14-lens, 15-slit, 16-flash unit, 17-photodiode.

(Taken from Alekseenko *et al.* (1994))

A detailed description of the methodology is provided by Alekseenko *et al.* (1994), and is summarised in the following paragraph:

In this arrangement, a small concentration of 1-5 micron aluminium particles are introduced into the liquid film (1), flowing down the external surface of the stainless steel test section (2) which is polished to a mirror finish. The measurement begins with the recording of the wavy film profile on photographic paper by the loop oscillograph (see shadowgraph method, section 3.4.3). After a set time period a voltage is supplied to the electromagnet (8) by the oscillograph. The electromagnet triggers the opening of the camera shutter (10), by means of the cable release (9), while simultaneously closing the synchronisation contacts on the camera. This event triggers the synchronisation unit (11) to initiate the stroboscope (12), which generates a series of short pulses toward the pulse lamp (16). The frequency of the pulse repetition is given by a sound frequency generator (13). The light from the pulse lamp illuminates a small section of the film through the slit (15) and long focus lens (14). The double tracks of the particles are photographed at an angle $(\theta)_i$ to the normal of the wall. Finally, after a set period of time, the synchronisation unit switches off the electromagnet and the camera shutter is closed. The whole process can be repeated as necessary.

The results reported for the technique appear consistent with comparable techniques.

6.2.8 Photochromic Dye Activation Technique

Hummel and his co-workers originally developed the photochromic dye activation technique as a non-disturbing flow visualisation technique. The original experimental arrangement utilised by Popovich & Hummel (1967) is presented in Figure 6.5.

The methodology consists of the addition of essentially colourless tracer, 2(-2, 4-dinitrobenzyl)-pyridine dissolved in ninety five percent ethyl alcohol, to the liquid flow under consideration. On exposure to high intensity light produced by a xenon-filled electronic flash tube, and introduced by focusing on a parabolic mirror, the essentially colourless solution will turn blue due to a tautomeric shift in structure before reverting to its colourless form within a few milliseconds after the light has ceased. The photoactive blue tracer, seen as a line, was recorded photographically through the triggering of a second flash tube up to approximately two milliseconds later by an electronic time-delay circuit. To record the tracer photographically the illumination light was first passed

through two filters that ensure that only light at the required wavelength, where the difference in optical density between colourless and coloured solution is the greatest, can continue on into the liquid film.

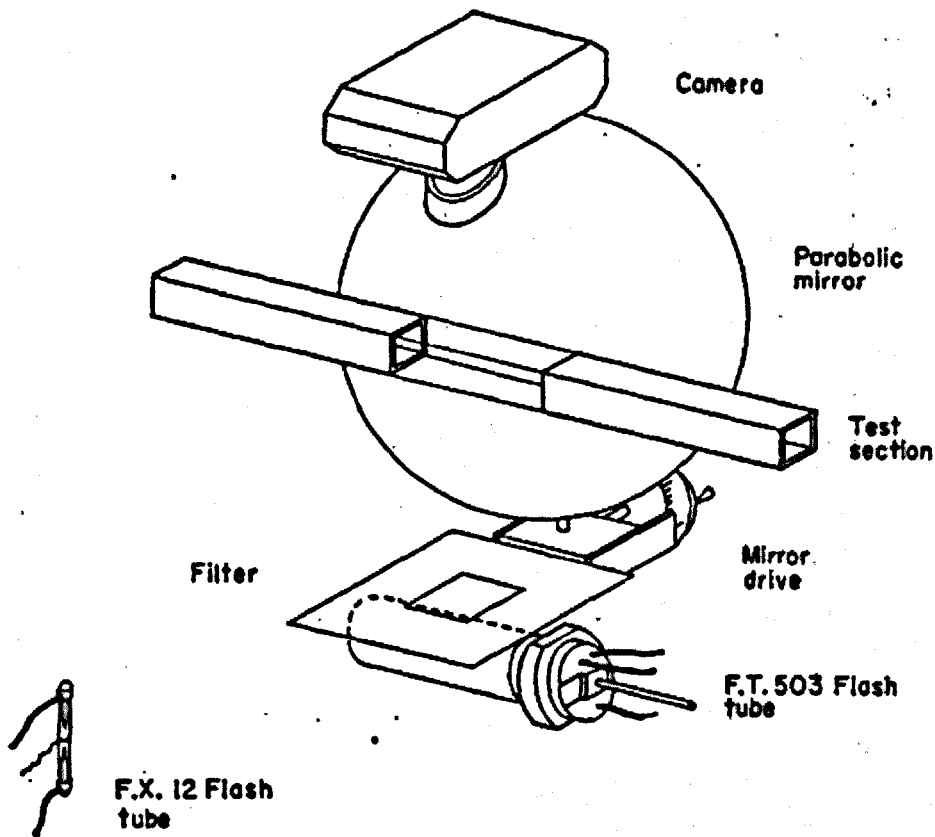


Figure 6.5: Experimental arrangement for original photochromic dye activation technique.
(Taken from Popovich & Hummel (1967)).

The method was improved by Frantisak *et al.* (1969) with the introduction of the light utilising a ruby laser beam with an appropriate harmonic generator to reduce the beam to the appropriate wavelength and induce the tautomeric reaction of the dye. Additionally, they recorded the dye trace utilising a high-speed camera that was capable of speeds of up to ten thousand frames per second. Optical distortion caused by their utilisation of a round glass tube was reduced by the application of a Plexiglas box positioned around the tube and filled with the liquid under study. The application of an optical correction box is a common feature with all subsequent applications of the technique that utilise tubular test geometries. Fogwell (1986) reports an extensive study into the optimal matching of

the refractive indexes of the working fluid and the walls of the test section, in order to provide an undistorted image of the trace that removes the refraction effects of a curved boundary between the tube wall and working fluid and tube wall and surroundings.

Ho & Hummel (1970) applied the technique to obtaining average velocity distributions within vertical falling liquid films of various viscosities. They observed that the thin falling films required extremely fine dye-traces, and when they attempted to utilise the high speed video camera photographic technique of Frantisak *et al.* (1969) they found the resolution of the photographs too poor for quantitative measurements. Therefore, they retained the laser light introduction arrangement and reverted to the original photographic technique of Popovich & Hummel (1967), a 35mm still camera with the proper attachments and lens. The parabolic results achieved compare favourably with the other velocity profile measurement methods reviewed in this chapter.

Dunn & Smith (1971) questioned the belief that the technique accurately portrays the fluid motion within turbulent films. They reported, in their measurements of turbulent momentum transfer in rough pipes, that the confidence in the quality of quantitative measurements, such as velocity profiles, could only be high in turbulent flows if the time between activation and photography was small compared with the smallest eddies and that the velocity is measured in the direction of mean motion.

The non-disturbing nature of the technique has also been questioned. Humphrey *et al.* (1974), utilising the technique during a study of the fluid dynamics of drop formation and coalescence, reported the observation of the nucleation of tiny gas bubbles along the dye trace at the same time the trace was formed. Upon formation, the bubbles within the drop rose to the drop interface, apparently dragging some of the induced dye trace along with them. They concluded that this activation-induced nucleation was the result of differences in surface properties between solutions of the two forms of dye rather than local heating by the laser light, which is thought only to be in the order of a rise of one and a half degrees Celsius.

More recently, the photochromic dye-activation technique has been applied by Martin (1984) for measuring liquid phase velocity profiles in vertical two-phase flow, by Kawaji *et al.* (1993) and Karimi & Kawaji (1996) for instantaneous velocities and profiles in vertical gas-liquid flows and by Sutharshan *et al.* (1995) for liquid film velocities in horizontal annular flow. As one would expect, the equipment has been refined as technology allows. Sutharshan *et al.* (1995) reports the application of a high-speed video camera to record the dye traces and analysis with PC-based digital analysis software, capable of tracking the initial dot and subsequent traces frame by frame using pixel location and intensity.

The insolubility of the favoured dye for this technique in water-based systems has resulted in the current limitation of this technique to organic test fluids; however, Douglas (1988) reports an extensive study in the search of photosensitive materials for use in the water phase of air-water systems. This study indicated the potential suitability of triarylmethane and polymethane dyes, and was followed by studies that screened these possible dyes (Enos & Douglas (1989a)), with a trial application of the best candidate, photochromic triarylmethane dye sulphite (Enos & Douglas (1989b)).

6.2.9 Laser Doppler Anemometry

Amenitskii *et al.* (1969) report probably the earliest use of a Laser Doppler Anemometry (Velocimetry) system in the measurement of velocity profiles in liquid films. They utilised two laser generated incident beams to scatter light off half-micron polystyrene particles introduced into the flow of glycerol-water mixture falling down a vertical glass plate. The Doppler effect produces a frequency change in the scattered light, where the frequency difference indicates the speed of the particle by the following equation:

$$\Delta f_D = \frac{2U}{\lambda_0} \sin \frac{\alpha}{2} \quad (6.2)$$

where, Δf_D is the Doppler frequency difference, U is the flow speed, λ_0 is the laser wavelength in vacuum, and α is the angle between the two incident beams in vacuum.

A beam splitting plate, in the optical arrangement shown in Figure 6.6, generated the incident laser beams.

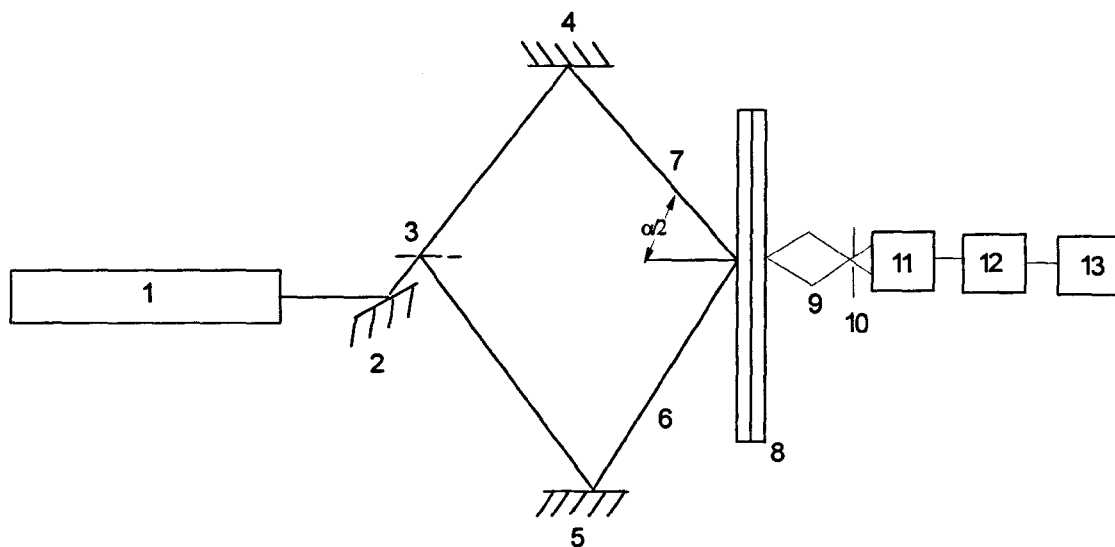


Figure 6.6: Optical Arrangement used by Amenitskii *et al.* (1969).

The He-Ne Laser (1) generates a beam which is reflected by a mirror (2) and falls on the beam-splitting plate (3), which gives two beams of equal intensity. Mirrors (4 & 5) direct the beams to lenses (6 & 7) whose focal points lie at 8. The scattered light is collected by a lens (9) and passed to a photomultiplier (11) after passing through the stop (10). The photomultiplier signal then goes through an amplifier (12) to the spectral analyser (13). A similar optical arrangement was utilised by Semena & Mel'nichuk (1978) in their study of mean velocity distributions in falling films.

Oldengarm *et al.* (1975) later improved on this original optical arrangement by replacing the beam-splitting plate with a rotating differential grating. The rotating differential grating splits the focused beam from the laser into one zero order and pairs of higher order beams. The two first order diffracted beams are used, with the higher order diffracted beams being blocked by a diaphragm. Since the grating is rotating, and the particles of water travelling through the interference fringe pattern formed in the measured volume are moving at a constant velocity in a direction, which is related to the

direction of rotation, it causes an apparent Doppler frequency shift that can be analysed to determine velocity using Equation 6.2.

The advantages reported of this rotating grating over the beam-splitting plate are:

- (i) The beams will always cross each other, even if there is slight misalignment.
- (ii) The optical path lengths of the beams are equal.
- (iii) The independence of the beam configuration and the angle between the plane of the grating and optical axis.
- (iv) The alignment parameters will not strongly influence each other.

The importance of these advantages is particularly clear if you consider the severe alignment requirements imposed when measuring the small volumes of fluid encountered in falling films. However, no evidence of the application of a rotating grating over the beam-splitting plate by subsequent researchers could be found.

More recent applications of laser Doppler anemometry in measurements of velocities within vertical or draining falling films have been made by Strumolo *et al.* (1985), Keeley *et al.* (1989) and Mudawar & Houpt (1993b).

The results obtained from all the Laser Doppler studies reported in this review show good agreement with velocity profile measurements obtained using the other techniques reviewed in this chapter. The potential disadvantages in applying this technique over other comparable techniques are related to the equipment costs, the man-hour intensive nature of setting up the equipment and the optically based technical problems associated with the technique. The most important of these optical technical difficulties encountered being the effects of interfacial refraction and scattering. These effects can be minimised by bringing the beams closer to the point of measurement using suitable light guide tubes or specially modified test sections, such as the film sampling channel utilised by Mudawar & Houpt (1993b) and presented in Figure 6.7.

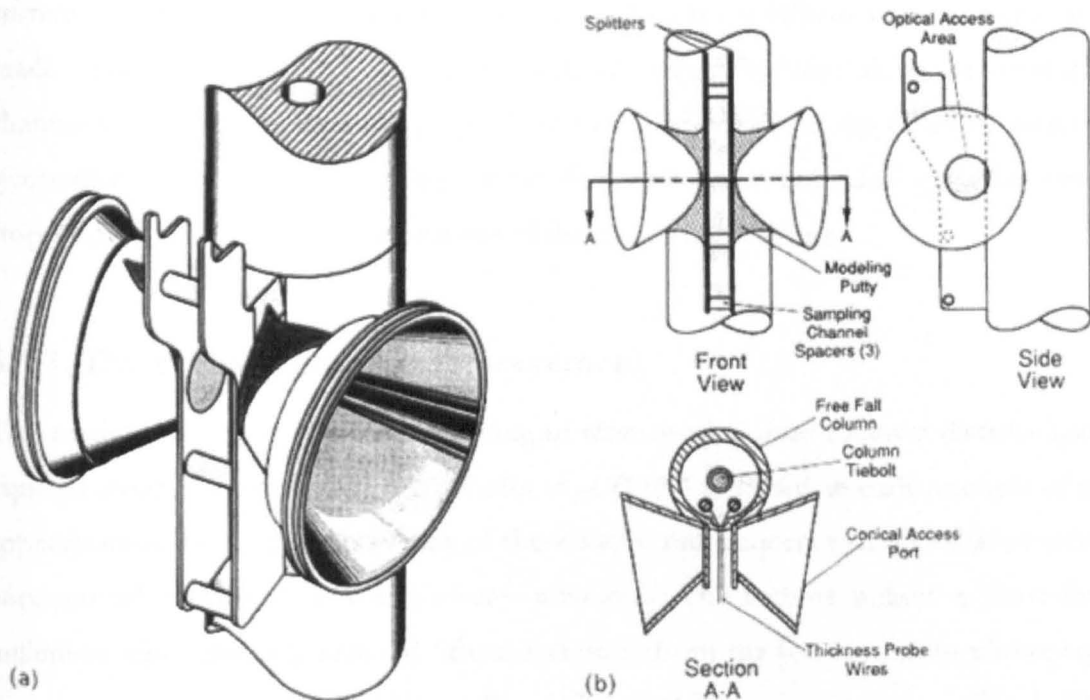


Figure 6.7: Film sampling channel: (a) isometric view, (b) schematic drawing.

(Taken from Mudawar & Houpt (1993b))

6.3 DISTURBANCE WAVE CELERITY MEASUREMENT

The wave celerity measurement techniques reviewed in this section are all essentially time of flight techniques, where the time required for a wave travelling between two fixed points, or conversely the distance travelled by the wave over a fixed time, is measured.

6.3.1 Fast Stopwatch Method

The application of a fast stopwatch is probably the simplest and least accurate technique for disturbance wave velocity measurement. Portalski (1973) reported the application of a fast stopwatch in the measurement of the velocity of artificially generated waves travelling along liquid films flowing down a smooth vertical plate. However, the waves were timed over the entire length of plate (213cm) and therefore, the wave velocity recorded is only a global average value. As a consequence, no account of the initial acceleration of the falling wave is made and localised wave velocity at any particular point

along the film cannot be deduced. Utilising a similar approach, Craik (1966) measured the velocity of waves travelling along thin horizontal films in contact with a counter-current airflow. However, in this study more localised wave velocity measurements were made. The authors marked off twenty centimetre length sections along the measuring channel with pieces of measuring tape fixed to the underside of the channel, sprinkled lycopodium powder on the surface of the film, and timed individual particles with a stopwatch as they traversed one or more of the measuring sections.

6.3.2 Direct Photographic Measurement

This method simply involves the recording of wave motion over a known distance using rapid photography techniques. Hall Taylor *et al.* (1963) reported an early example of the application of this method in a study of the velocity and frequency of disturbance waves encountered in vertical annular air-water mixtures. The authors utilised a thirty-five-millimetre ciné camera positioned fifteen feet away from the test section to photograph the disturbed, tangentially illuminated, liquid film at thirty two frames per second. The distance travelled by the disturbance waves was determined through reference to a blackboard with white distance markers taped along its length at one foot intervals, mounted adjacent to the test section tube and within the image of the camera. After completion of the required photographic measurements, the negatives were developed and projected. The velocities of the disturbance waves were then recorded by noting their position in successive frames.

This general approach was adopted by Nedderman & Shearer (1963) and improved by Hewitt & Lovegrove (1969) utilising enhanced ciné frame rates of up to eighty and two thousand frames per second respectively.

More recently, Ohba & Nagae (1993) analysed the frequency and velocity behaviour of individual waves in upward annular air-water flows using the cathode ray tube (CRT) display of a high-speed video monitor. The authors chose two fixed points along the flow direction and visible on the CRT, with the velocity calculated simply from the time given on the video display that was needed to travel the distance between these points.

The major limitation of the direct photographic techniques described is the time consuming and tedious nature of the analysis required, to obtain sufficient individual wave velocity measurements to characterise the local average flow.

6.3.3 Paired Film Thickness Probe Output (Cross-Correlation)

This is the most common technique utilised in the measurement of local wave phase velocities in liquid films. The technique is based on the principle that if a probe is used to measure a local parameter it will provide results in the form of a time-varying fluctuating curve. If another probe is located directly downstream at known distance, and the wave structure remains relatively static over this distance, this probe will also produce a similar fluctuating curve. Therefore, the local velocity of the wave can be deduced from the time-shift between the probe outputs.

By far the most common local parameter used in this velocity measurement method in liquid films is film thickness, with a variety of differing probe types being utilised:

Fujita *et al.* (1985) and Aragaki *et al.* (1987) utilised the time-series data from a pair of electric-capacitance probes (see Section 3.3.1).

Hewitt & Lovegrove (1969), Hewitt & Nicholls (1969), Gill *et al.* (1969), Webb (1970), Sergeev *et al.* (1975), Thwaites *et al.* (1976), Nencini & Andreussi (1982), Takahama *et al.* (1983), Sekoguchi *et al.* (1984), Azzopardi (1986), Okada & Fujita (1993) and Mudawar & Houpt (1993a) amongst many others report the utilisation of the output from a pair of conductance probes (see Section 3.3.2).

Ohba *et al.* (1992) utilised a twin fiber optic liquid film sensor system (see Section 3.4.4).

Stainthorp & Batt (1967) utilised results obtained by a light absorption technique (see Section 3.4.5).

Hurlburt & Newell (1996) utilised an interferometric system (see Section 3.4.8).

Jones & Whitaker (1966) reported the utilisation of a novel approach. The technique is based not on surface position (thickness), but rather on the slope of the surface. The authors utilised the deflection from a pair of light beams of fixed distance apart. A

photomultiplier tube measured the magnitude of the deflection of each beam, with both photomultiplier outputs plotted simultaneously on a strip-chart recorder. The advantages of such a technique are the simplicity of the electronics and optical system required. Naturally, the major limitation of this approach is the inability to simultaneously obtain information on the film thickness.

The simplest analysis method to obtain wave velocity is direct comparison of the probe outputs. For example, for the light beam deflection method described above, the wave velocity, C , was directly calculated from the strip-chart by the following:

$$C = \frac{x_b u}{x_a} \quad (6.3)$$

where, x_b is the distance between light beams, u is the velocity of the strip-chart and x_a is the distance between the peaks representing the wave on each photomultiplier output. Similar direct comparison is reported in the literature with the application of film thickness probes.

A more sophisticated method of comparison of the probe outputs is available utilising cross-correlation, and has become the standard analysis technique for wave velocity determination from paired probe output. A cross-correlation coefficient can be computed over a statistically significant amount of time and Hewitt (1982), in his review of measurement techniques, defines this cross-correlation coefficient, R_{12} , by:

$$R_{12}(\tau) = \frac{\int_0^T f_1(t) f_2(t + \tau) dt}{\int_0^T f_1^2(t) dt} \quad (6.4)$$

where; $f_1(t)$ is the measured quantity at one point as a function of time, $f_2(t + \tau)$ is the quantity measured at a downstream point at time $t + \tau$, and the averaging is done over a sufficiently long time T such that $R_{12}(\tau)$ is constant with T .

The value of $R_{12}(\tau)$ reaches a maximum (see Figure 6.8) at $\tau = \tau_m$

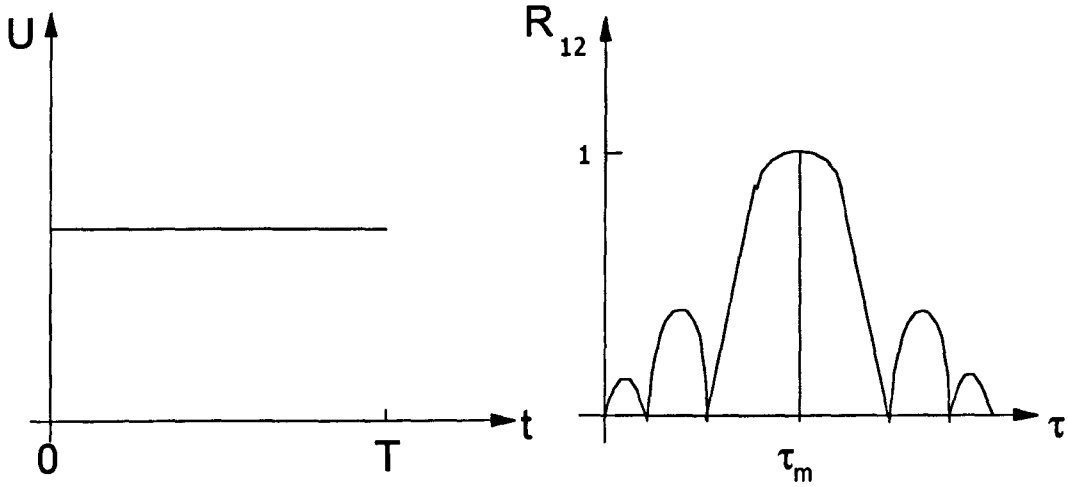


Figure 6.8: Schematic representation of results obtained for a cross-correlation coefficient R_{12} for a system with constant velocity. (Taken from Hewitt (1982)).

where τ_m is the most likely transit time of the fluid between the measuring stations. The fluid velocity U is then given by:

$$U = \frac{z_{12}}{\tau_m} \quad (6.5)$$

where, z_{12} is the distance between measuring stations.

6.4 SUMMARY

Although film velocity profile measurements were not undertaken in this study it is hoped that the literature review presented here will be valuable reference for future work in this area. It is clear from this review that profile measurement is well established for laminar films, however, the limited application to the wavy nature of falling films is an indication of the difficulties inherent in such experimental systems.

For disturbance wave celerity measurement, it is evident from the literature that cross-correlation of paired film thickness probes output is the preferred option. The technique

not only works in tandem with localised film thickness investigations, it is also probably the most sophisticated method to date.

Chapter 7

LIQUID FILM VELOCITY MEASUREMENT

Disturbance Wave Celerity

7.1 INTRODUCTION

As stated in the introduction to Chapter 6, the measurement of velocities in falling films is an even more challenging problem than measurement of film thickness. The purpose of this chapter is to describe in detail the methodology of the two time-of-flight based techniques applied in the measurement of one particular aspect of the liquid film velocity, the velocity/celerity of the large disturbance waves that are encountered travelling along the slower moving base film substrate.

7.2 DIRECT PHOTOGRAPHIC MEASUREMENT

The availability to this study of a high-speed video camera (Kodak, Model Ektapro EM) illustrated in Figure 7.1, presented an opportunity to visualise the flow dynamics of the interfacial phenomena travelling on the falling film and investigate any influence on these phenomena of a co-current air stream. In particular, the camera permitted the development of a simple technique to measure the celerity of the large disturbance waves encountered on the film.

The methodology utilised is similar to the technique described by Ohba & Nagae (1993) that is reviewed in Chapter 6. The high-speed camera was positioned to view an area of the falling film between approximately 1.7 and 1.8 metres below the inlet weir. The viewing image has a definition of 240 pixels horizontal x 200 vertical x 625 grey levels, with an example presented in Figure 7.2. The test section was lit by two sodium lamps, positioned angularly behind the camera and focussed on the test section area of interest. Two strips of masking tape were then stuck on to the outer surface of the test section viewing plate at a measured distance apart (79mm). Their placement was perpendicular to the flow direction, across the entire test section width and within the viewable region of interest.



Figure 7.1: Kodak high-speed video camera unit.

The liquid and air flows within the flow facility were then set to the desired level using the methodology detailed in Chapter 2. Once uniform flow conditions were satisfactorily established, the camera was triggered to record approximately two seconds of the flow image at five hundred frames per second, stored within the instrument's solid-state memory. The recorded image was then played back at reduced speed (*e.g.* eight frames per second) where individual disturbance waves could be monitored and the frame numbers at which they passed between the masking strips noted. In an attempt to provide a consistent representation of the flow regime from a small sample of disturbance waves, waves that showed the following characteristics were ignored from the analysis:

- (i) Waves travelling on or close to the edges of the test section.
- (ii) Waves that coalesced with other waves.
- (iii) Waves whose structure was not stable over the length of the viewable area.

The individual disturbance wave celerity, u (m/s), could then be simply determined from the following equation:

$$u = \frac{Rx}{F_1 - F_2} \quad (7.1)$$

where, F_1 is the frame number when the leading edge of the disturbance wave is in contact with the upper edge of the lower masking strip, F_2 is the frame number when the leading edge of the disturbance wave is in contact with the lower edge of the upper masking strip, R is the frame rate of the camera (fps), and x is the distance between the masking strips (m).

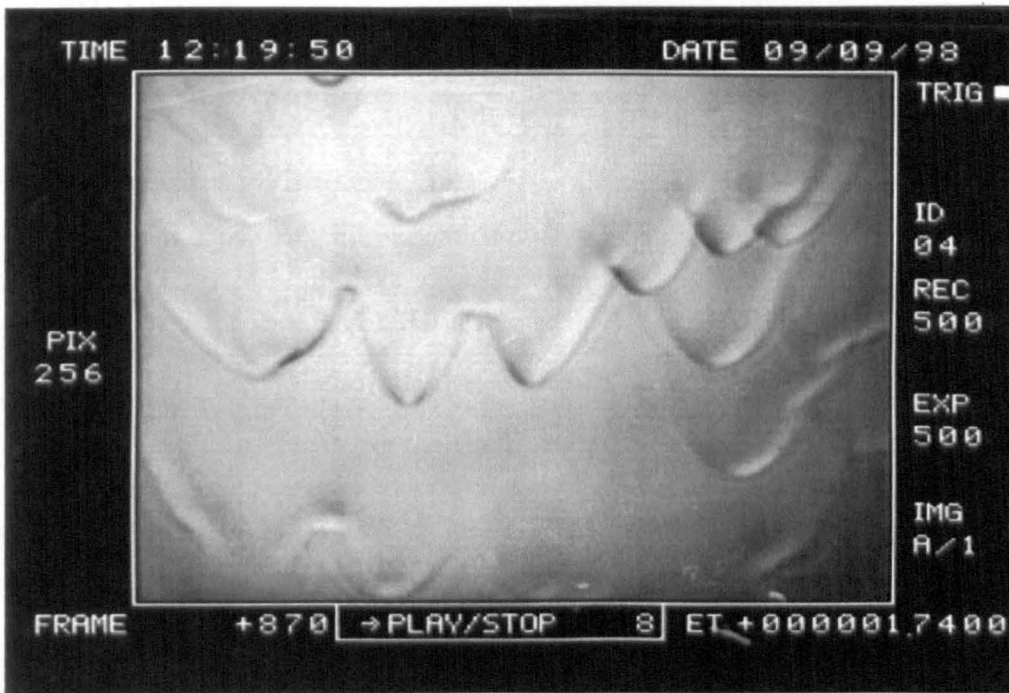


Figure 7.2: Typical high-speed camera image.

This wave monitoring process was repeated for several (typically five to ten) different waves within the recorded image, to build up an averaged local celerity value for the given flow conditions. Finally, the recorded images were archived onto a standard video recorder tape to allow for future examination and flow visualisation.

The major drawbacks encountered in the utilisation of this technique were the tedious, repetitive analysis required and the subjectivity required in the choice of disturbance waves. For the vast majority of flow conditions investigated, the waves observed were far from homogeneous, varying markedly in size and shape. Naturally, more confidence in the averaged celerity values could be expected by extension of the number of disturbance waves sampled at each flow condition, however, this would also substantially increase the already heavy time resources required. As a consequence, an alternative technique was sought that would remove the human subjectivity elements and reduce the analysis resources required. This led to the development and application of the light absorption based cross correlation technique reviewed in the following section.

7.3 LIGHT ABSORPTION BASED CROSS CORRELATION METHOD

The application of cross correlation of paired probe output signals in the determination of disturbance wave celerity is well established, and a detailed review of the alternative methods is presented in Chapter 6. In summary, for a light absorption based technique the outputs from a pair of photosensitive detectors are utilised. When these detectors are being stimulated by constant source of white light, which has passed through the liquid film, then Lambert-Beer Law dictates that their output will be related to the local thickness of the film.

A technique based on light absorption was chosen for the following reasons;

- (i) Such a technique would be complementary to the light absorption imaging technique (LAIT) applied in film thickness measurement.
- (ii) It was also hoped that the temporal data obtained could be calibrated to give localised film thickness data for comparison with the spatial data obtained from LAIT.

Implementation of the technique reviewed in this section highlighted that (ii) could not be satisfactorily achieved with the resources applied within the time frame allocated, and

was subsequently abandoned. However, it will be shown that for disturbance wave celerity measurements, quantitative film thickness data is not necessary.

The experimental arrangement utilised is shown schematically in Figure 7.3.

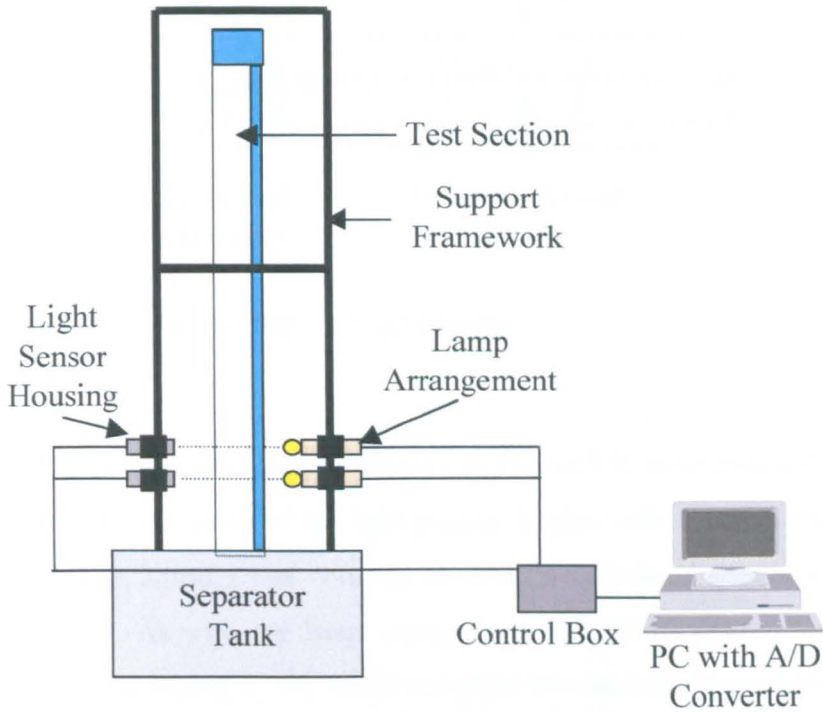


Figure 7.3: Experimental arrangement utilised for light absorption based cross-correlation technique.

The dyed liquids applied the LAIT film thickness technique were reused, as the dyes dramatically increased the absorption of white light and thus thickness sensitivity. For easy assembly/de-assembly, a modular support framework was constructed around the test section and mounted on the gas/liquid separator tank lid. The white light sources were provided by the lamp arrangements, positioned on the framework with the use of retort clamps, approximately eight centimetres apart in the vertical plane and illuminating an approximately 10mm diameter region at the centre of the rectangular test section. An individual lamp arrangement is illustrated in closer detail in Figure 7.4.

The lamp arrangement simply consists of a 0.5W lens end vacuum lamp and holder that is securely fastened to the flat surface on one end of a 115mm length of wooden dowel.

A lens bulb was utilised to allow simple focussing of a substantial proportion of the output onto the receiver. Wooden dowel was preferred as its surface curvature aided the grip of the retort clamps.

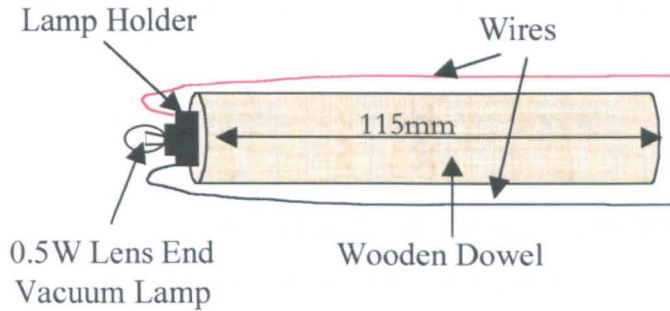


Figure 7.4: Lamp Arrangement.

The light sensor housings, shown schematically in Figure 7.5, were attached opposite the lamp arrangements in the plane of the light passing horizontally through the test section area of interest. The housing was constructed from a cylindrical section (16mm (D) x 44mm (L)) of PVC. As with the lamp arrangement, a cylindrical housing section was preferred to facilitate gripping by the retort camps to the modular framework.

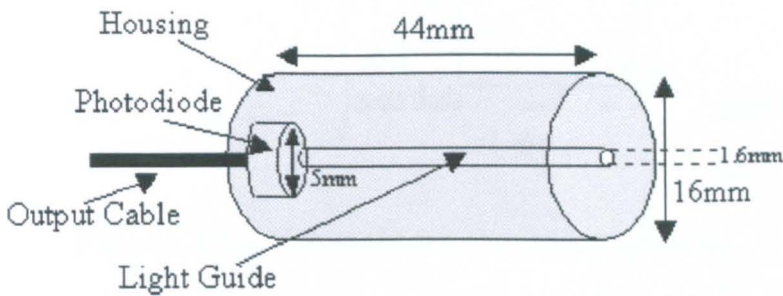


Figure 7.5: Light Sensor and Housing.

Light enters the sensor housing through a 1/16" (1.6mm) hole drilled along the core of the solid PVC housing. This core acted as a collimating light guide, which minimised the amounts of incident and non-localised reflected light that could reach the light sensor. The influence of external light sources was tested by simply turning on and off the room lights while monitoring the sensor outputs, showing no measurable influence. The light

sensors utilised were commercially available 5mm diameter photodiodes, secured in a drilled out cavity at the far end of the housings. Outputs from the photodiodes were sent to the control box on 1mm flexible sheathed coaxial cable.

The experimental arrangement was controlled from a purpose built box whose electronic circuit is presented in Figure 7.6. In summary, the electronics was powered by a 12V supply, with the photodiode output passed through an operational amplifier to provide the 0-5Volt Output to be sent to the PC. The 12V power supply also powered the pair of lens lamps, whose current input could be manipulated individually by means of variable resistor pots located on the external facing of the box.

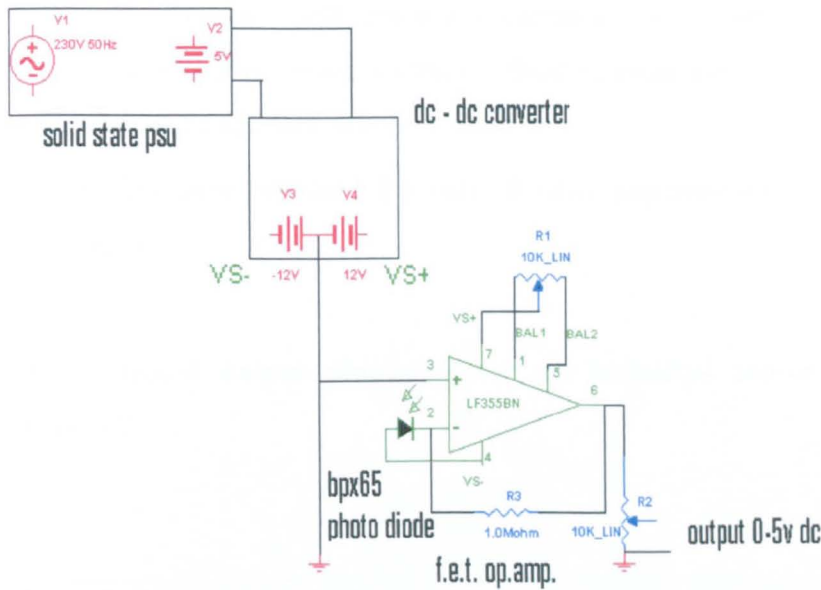


Figure 7.6: Control box electronic circuit.

The PC utilised contained a two-channel analogue to digital conversion card (Pico Technologies, Model No. AD-100). The real-time outputs from the light sensors could be visually displayed on the PC monitor using the data acquisition software provided with the signal conversion card. This software was also able to trigger logging of the data to archive files for subsequent analysis.

The measurement methodology applied was as follows:

- (i) With the flow facility off and the test section empty, small careful movements to their horizontal and vertical positions aligned the lamps and sensors. Accurate alignment was made substantially easier with the real-time voltage output displayed on the PC monitor. With the lamp current intensity at full power, alignment was considered to have been successful when the full 5 Volt output was received by the photodiode light sensor and recorded on the PC monitor display. The lamp current was then incrementally reduced until the point at which a significant reduction in signal output was recorded. This was necessary to maximise the operational lifetime of the bulbs.
- (ii) The flow conditions within the flow facility to be measured were established utilising the methodology detailed in Chapter 2.
- (iii) The data acquisition software was triggered to store 5 seconds of output at 2 millisecond intervals, a total of 2500 measurement points recorded simultaneously for each sensor.
- (iv) (ii) & (iii) were repeated for each desired experimental measurement condition.

An example of the typical output obtained from an individual sensor is plotted graphically in Figure 7.7.

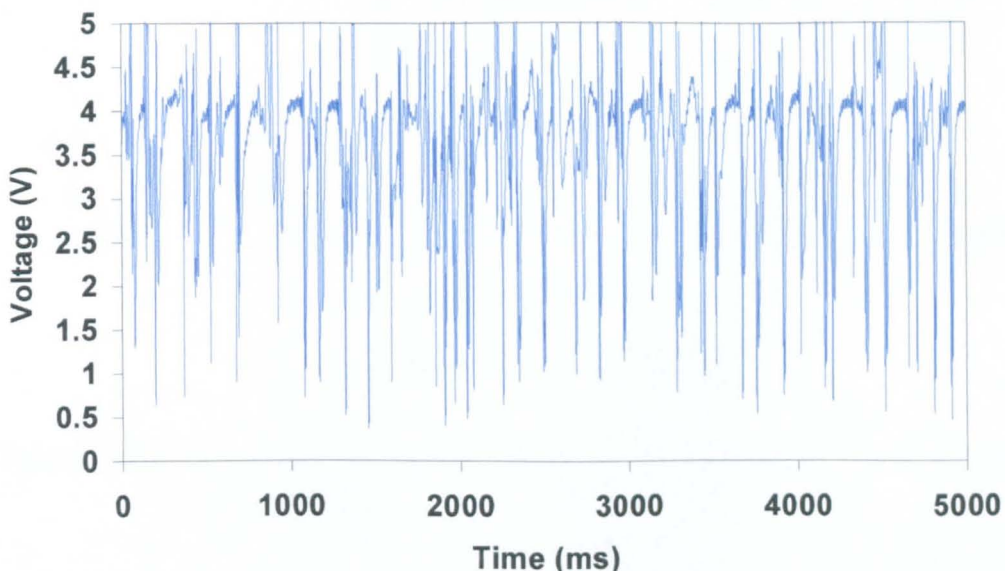


Figure 7.7: Typical sensor output.

Figure 7.7 clearly shows periodic dips in the output voltage. The voltage dips represent points at which the thicker, and thus more light absorbent, disturbance waves have crossed the light beam. The signal also indicates points around the voltage dips at which voltage spikes above the reading representative of the base substrate are measured. At first glance this appears to indicate the presence of troughs in the film base substrate, both before and after disturbance waves. However, it is the author's belief that refraction effects occurring at high angular wave slopes have exaggerated the magnitude of any such troughs. The same phenomena is visible in the LAIT images as a white band before the leading edge of each large wave and is also represented as a trough in the spatial data (see Figure 5.1). However, no such deep troughs have been reported when using other film thickness measurement techniques, suggesting the effect is probably an artefact of the light absorption technique.

Determination of the celerity of individual disturbance waves could be achieved manually by application of a graphical plot such as shown in Figure 7.8.

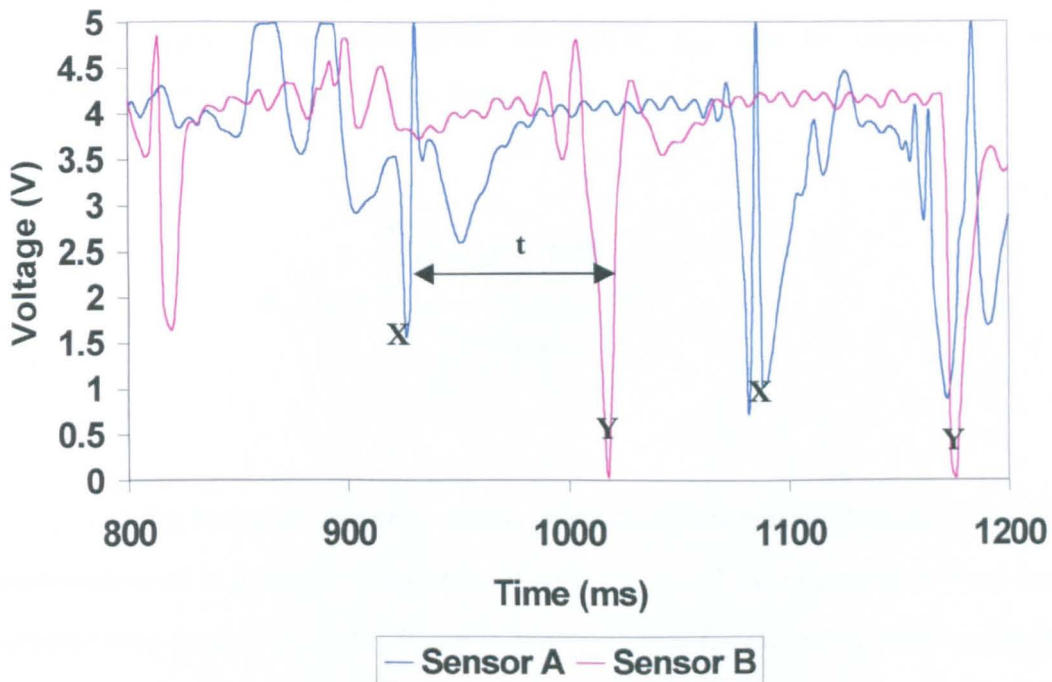


Figure 7.8: Plot showing manual method for individual wave celerity measurement.

The plot is a superimposition of a sample of the upper (Sensor A) and lower (Sensor B) sensor voltage signals on a shared time axis. Visual inspection and thickness measurement of falling liquid films indicates that disturbance wave structure is essentially fixed, unless contact with another wave is made. Therefore, individual disturbance waves can be distinguished from their similar influence on the sensor outputs as they cross the light paths. Figure 7.8 shows where two disturbance waves, X & Y, have been highlighted from the sensor outputs. The figure also demonstrates how measurement of the time taken (t) for the disturbance wave to pass between the sensors can be achieved. As the distance between the sensors (x) is known, the celerity (u) of the individual disturbance wave can be calculated from:

$$u = \frac{x}{t} \quad (7.2)$$

For an averaged local disturbance wave celerity measurement, a cross-correlation technique was applied. As previously indicated in Chapter 6, cross-correlation is the standard analysis technique applied for wave celerity determination from a paired probe output. In review, a cross-correlation coefficient, R_{12} , can be computed over a statistically significant amount of time from:

$$R_{12}(\tau) = \frac{\int_0^T f_1(t)f_2(t + \tau)dt}{\int_0^T f_1^2(t)dt} \quad (7.3)$$

where; $f_1(t)$ is the measured quantity at one point as a function of time, $f_2(t + \tau)$ is the quantity measured at a downstream point at time $t + \tau$, and the averaging is done over a sufficiently long time T such that $R_{12}(\tau)$ is constant with T . The most likely transit time of the disturbance wave will then be given when $R_{12}(\tau)$ reaches a maximum (Figure 6.8).

For this study, the cross-correlation was performed automatically by the development of a Microsoft Excel, Visual Basic macro. The tasks of the macro program were as follows:

- (i) For each of the sensor outputs, the maximum and minimum values were obtained and data converted relative to these values (i.e. 0 (min) – 1 (max)).
- (ii) Within a spreadsheet, the two relative sensor outputs were cross-correlated at 2ms intervals for a maximum time shift of 500ms.
- (iii) The cross-correlation coefficient, R_{12} , was evaluated for each proposed transit time. As the signals from the sensors were not identical, the denominator of Equation 7.3 was determined from the geometric mean value obtained from both sensor outputs. Additionally, as all two thousand five hundred data points for each output were utilised in the correlation, the coefficient value was scaled to compensate for the diminishing number of data points available as the time shift increases.
- (iv) Finally, the coefficient values representative of each time shift were plotted graphically to visually identify the maximum coefficient value, and thus the most likely disturbance wave transit time. An example of such a plot is given in Figure 7.9.

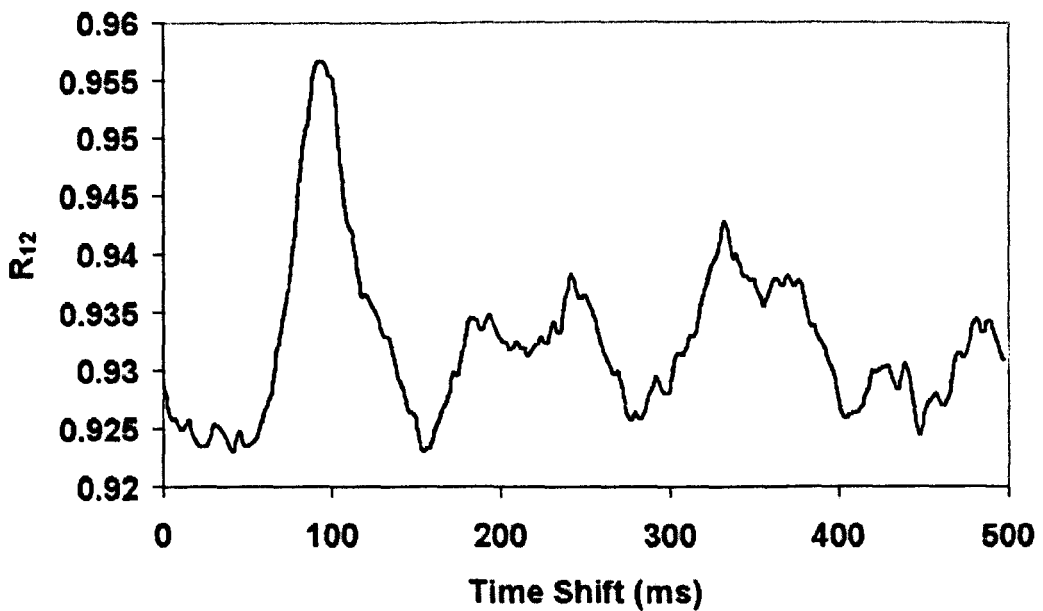


Figure 7.9: Cross-correlation coefficients plot to determine most likely disturbance wave transit time.

The figure clearly shows a maximum coefficient value is reached at a time shift of approximately 100ms, and therefore, this value would be recorded as the disturbance wave transit time between the sensors. It is noteworthy how favourably this compares with the analysis of a small segment of the data that is plotted in Figure 7.8, suggesting a high level of wave periodicity under this flow condition. The range of coefficient values displayed in Figure 7.9 (~0.92 - 0.96) are representative of the high values of correlation and limited coefficient range obtained throughout the study. This is likely a result of the periodic, impulse type data (illustrated in Figure 7.7) that was received by the sensors during the study.

As previously mentioned at the beginning of this section, it was hoped that the temporal data obtained could be suitably calibrated to give localised film thickness data. It was believed that a relationship between sensor output and film thickness could be determined utilising the wedge shaped calibration cell applied in the calibration of LAIT. For the calibration to have been accurate, the light emitted from the lens lamp arrangements must be kept constant at both the calibration stage and during measurement. However, the following practical difficulties prevented this:

- (i) Although the lamp outputs could be controlled individually, both lamps obtained their power from the same supply. As a consequence each lamp's light output was influenced by even small deviations of current input or light output intensity of the other lamp.
- (ii) There was a significant variation in the quality of lens bulbs utilised. Under measurement conditions, the lifetime of the bulbs ranged from as little as a few minutes up to several hours. When a bulb was replaced, subtle manipulation of the orientation of the lens of the new bulb was required to achieve the desired output to the receiver. Additionally, during a bulb replacement it was noticed that there was often a significant variation in the light output between bulbs at constant current conditions, making current adjustments necessary.
- (iii) The output from a lamp could vary significantly over its lifetime. This was tested by setting up the data acquisition equipment to record the output every few minutes from a single lamp over the entire lifetime of a

bulb. This suggested small deviations occurred during the majority of the lifetime of a bulb with a rapid decline in output during the last few minutes of life.

Clearly, using individual power supplies to the lamps could have easily rectified problem (i), however, the problems (ii) and (ii) could not be resolved to any satisfaction without utilising alternative light sources.

A further difficulty that prevented simple calibration of the output into film thickness data was the effect of light refraction/reflection effects caused by the relatively high angular slopes of the disturbance waves. As previously discussed, it is this author’s belief that these effects are responsible for the spurious readings obtained around the disturbance wave signals, and compensation for them is not trivial.

7.4 COMPARISON OF THE TWO TECHNIQUES

The application of two different celerity measurement techniques during the course of this study provided an opportunity for direct comparison of the results obtained from both techniques.

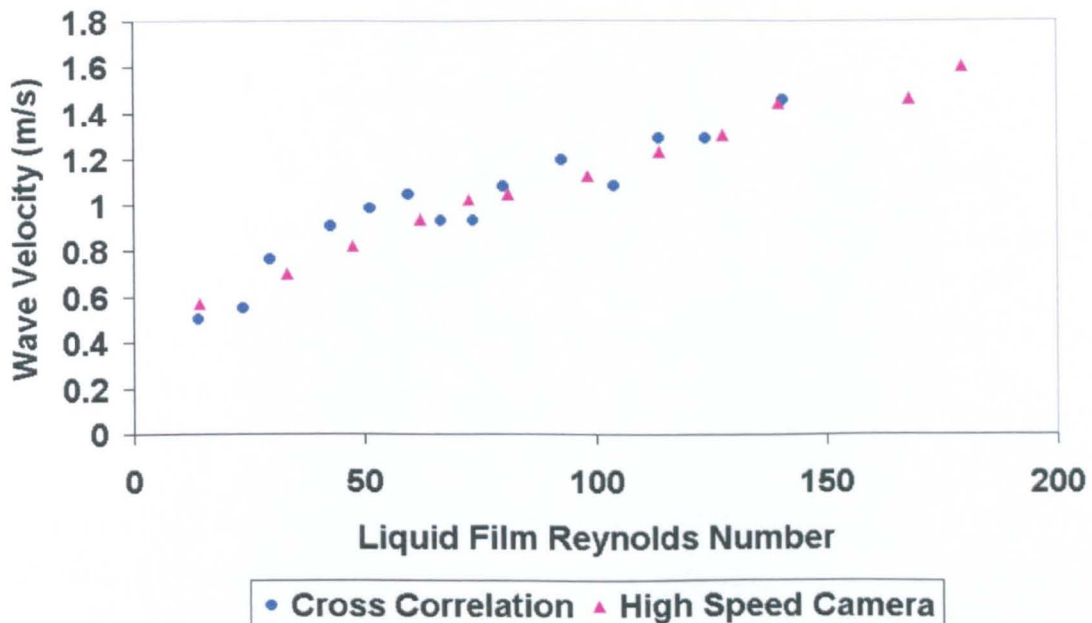


Figure 7.10: Comparison of results obtained from the two measurement techniques for dodecylbenzene/air system under comparable flow conditions. (Air velocity ~ 5m/s)

Figure 7.10 is provided to illustrate the generally close agreement achieved between the photographic and light absorption based techniques under comparable flow conditions, instilling confidence in the validity of the cross-correlation analysis of the wave celerity data obtained using the light absorption technique.

Chapter 8

RESULTS

Air-Water - Comparison with the Literature

8.1 INTRODUCTION

The purpose of this chapter is to summarise the experimental results obtained for wavy, vertical water films in both free falling and co-current air systems. The data were primarily collected as a means of validation of the techniques employed in this study by comparison with the considerable data available for these air-water systems in the literature.

Literature shows that a popular form to express liquid flow conditions is by utilising a dimensionless liquid film Reynolds Number, Re_L . However, literature also demonstrates that two forms of this dimensionless group have been implemented in previous studies. They are:

$$(i) \quad Re_L = \frac{\Gamma}{\mu} \quad (8.1)$$

$$(ii) \quad Re_L = \frac{4\Gamma}{\mu} \quad (8.2)$$

where, Γ is the liquid mass flowrate per unit perimeter (kg/m s) and μ is the dynamic liquid viscosity (kg/m s).

There seems to be no particular benefit from the use of one form of this dimensionless group over the other. Therefore, for consistency, expression (i) (equation 8.1) was utilised throughout this study. The main reasoning behind this decision was that Equation 1 was the version implemented in the study by Clegg (1969) from which much of the current work was initially developed.

The spatial film thickness data presented in this section were taken from images of a region 150mm wide (entire width of test section) by 300mm high that begins approximately 1500mm below the liquid entry weir. Each pixel image represents an area of the film of 0.36 mm^2 (0.6 mm by 0.6 mm) with 125,000 pixels representing the entire spatial area of film. The disturbance wave celerity data were exclusively obtained with a high-speed video camera approximately 1.6 and 1.7 metres below the inlet weir, utilising the direct photographic measurement technique detailed in Chapter 7

Air flowrates in the co-current studies are presented in terms of superficial velocity (m/s).

A complete summary of the air-water experimental results obtained is provided in tabular form in Appendix C.

8.2 WATER

8.2.1 Experimental Flow Conditions

The range of experimental flow conditions employed for the investigation of water films is summarised in Table 8.1

Table 8.1: Range of experimental flow conditions employed for the investigation of water films.

Liquid Flowrate per Wetted Perimeter, Γ (kg/m s)	0.11 - 0.89
Air Velocity (m/s)	0 - 33.0*

(* Air velocities above 17.4 m/s were possible during wave celerity measurements only)

Partial wetting of the glass viewing plate dictated the maximum air and water flowrates achievable. The minimum measurable liquid flowrate was limited by incomplete wetting of the flow plate. Additionally, these difficulties prevented measurement of the entire liquid flow range at the higher air velocities and vice versa. A detailed review of the experimental difficulties encountered, which gave rise to these flow limitations, is provided in Chapter 2 (Section 2.3.5). After the removal of a small number of blemished images, a range of fifty-four different flow conditions produced a total of one hundred and sixty three spatial images that were subsequently converted into spatial film thickness measurements.

It was not considered feasible or practical to present every possible parameter evaluated in this study to describe the interfacial characteristics of these films. Therefore, it is hoped that the selection of results displayed in this section, with parameters selected where comparison with the literature is possible, will not only validate the measurement techniques applied but also provide both visual and quantitative insight into the influence of air and liquid flow conditions on the interfacial characteristics of water films.

8.2.2 Flow Visualisation

Falling liquid film flow, with and without the presence of a co current downflow of air, produces complex three-dimensional interfacial flow structures that are impossible to completely describe empirically. The application of a rectangular test geometry and photographic nature of the film thickness technique employed provided an excellent opportunity to visualise the physical structure of the interface.

The flow structures obtained for the air-water two-phase system, over the range of flow conditions of this study, are summarised with the aid of Figures 8.1 to 8.4. These figures present sample film images at specific flow conditions to illustrate the dramatic influence of air and water flowrates on interfacial structure. The film images are presented with their corresponding spatial film thickness map to permit quantitative visualisation of the interface dimensions. The spatial maps were generated utilising commercial software (MATLAB) directly from the spatial film thickness data obtained from each image.

BEST COPY

AVAILABLE

Some text bound close to
the spine.

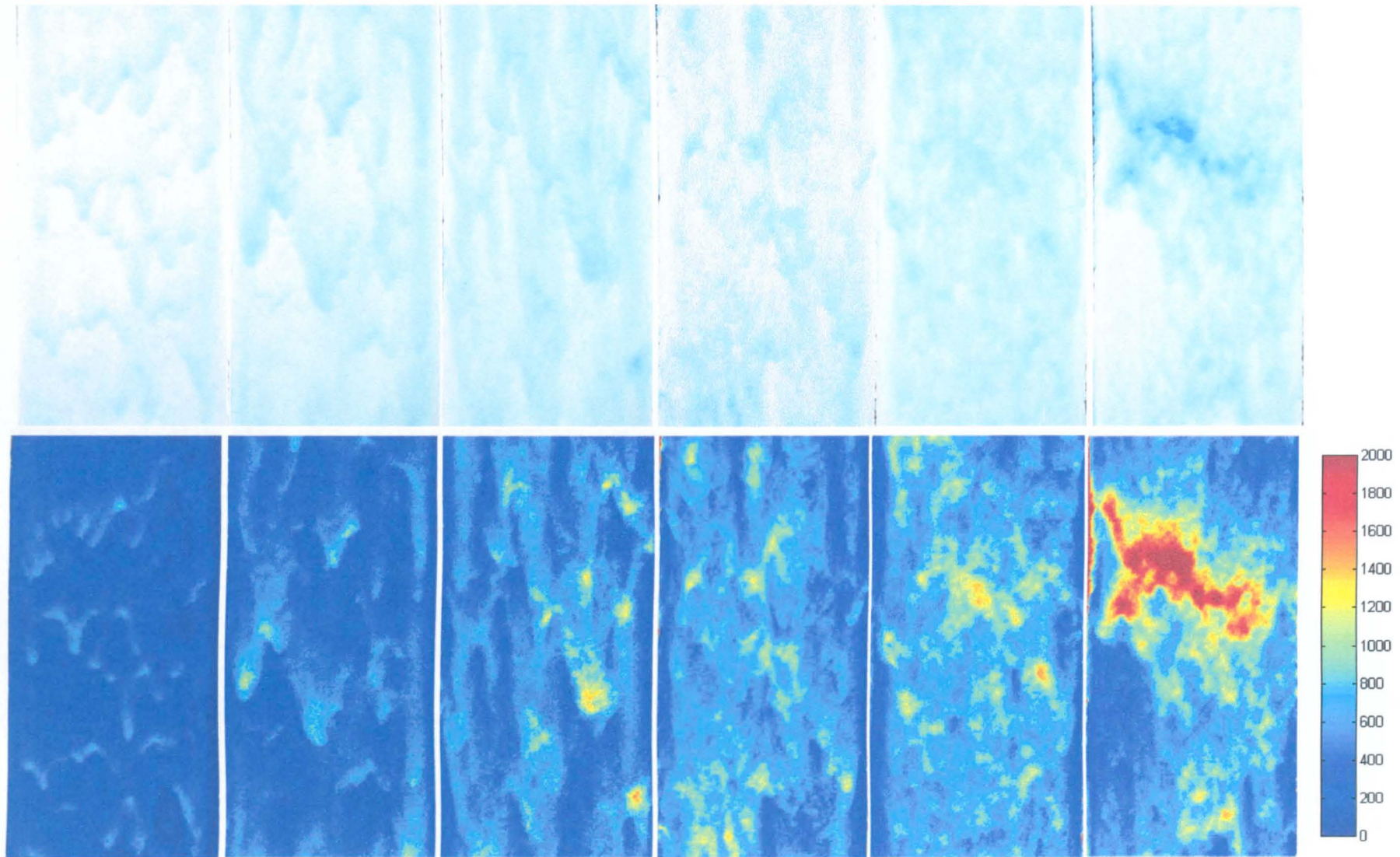


Figure 8.1: Film images and corresponding spatial film thickness maps for free falling water films with increasing liquid flowrate (left to right). Liquid flowrates 0.11, 0.23, 0.46, 0.57, 0.72 & 0.89 kg/m s. Legend in microns.

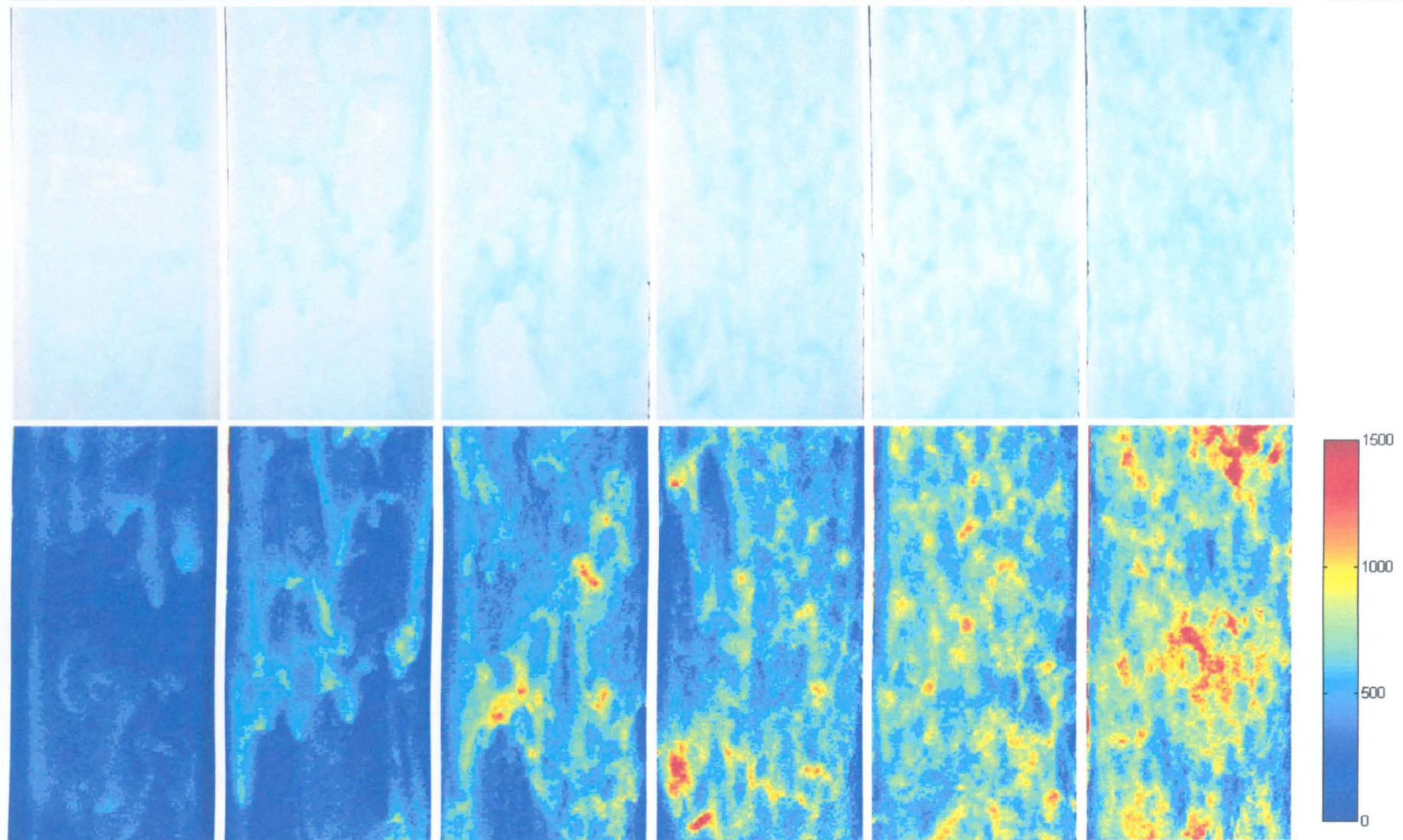


Figure 8.2: Film images and corresponding spatial film thickness maps for co-current air-water downflow at constant air velocity (7.4 m/s) with increasing liquid flowrate (left to right). Liquid flowrates 0.11, 0.23, 0.46, 0.57, 0.72 & 0.89 kg/m s. Legend in microns.

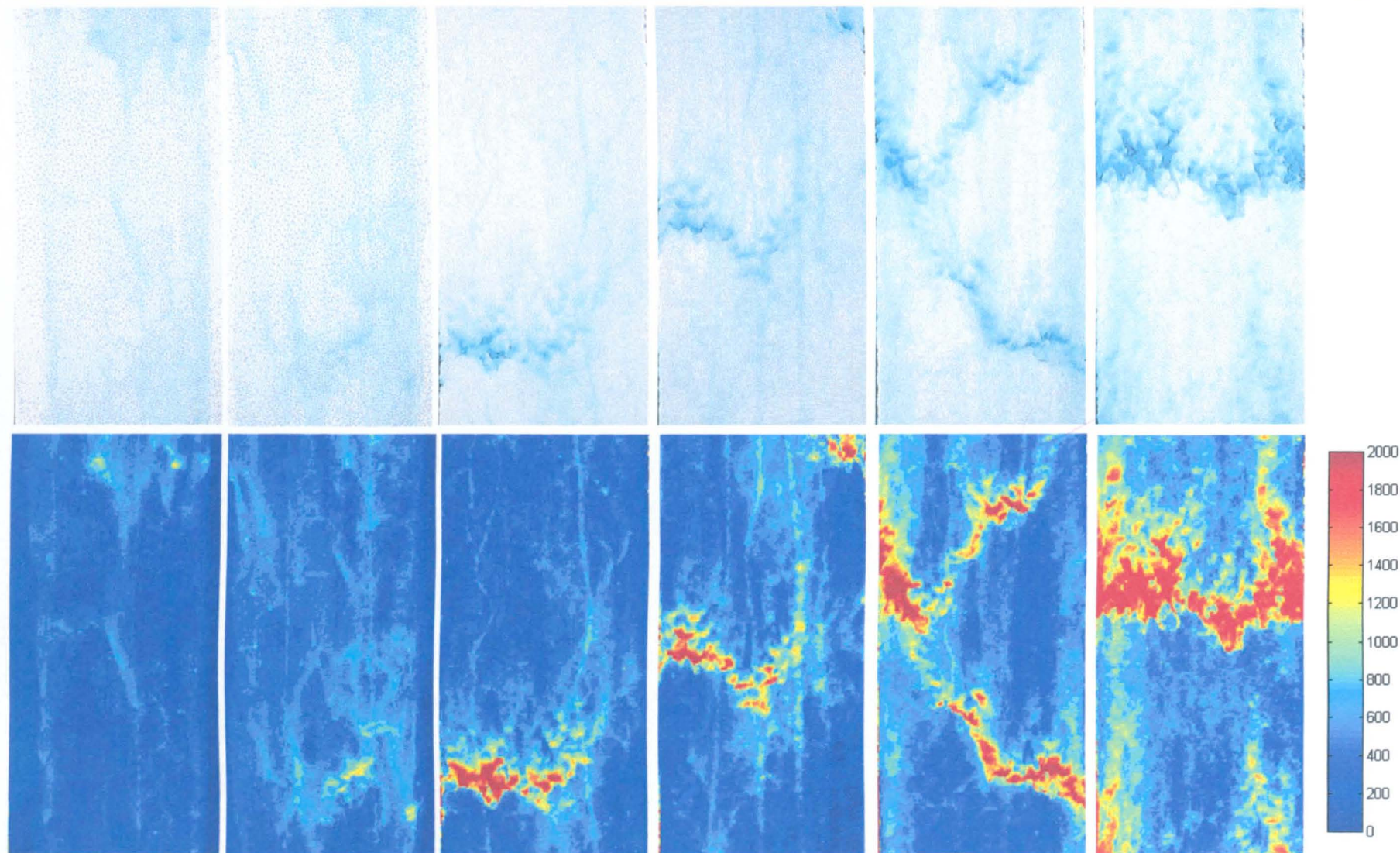


Figure 8.3: Film images and corresponding spatial film thickness maps for co-current air-water downflow at constant air velocity (15.2 m/s) with increasing liquid flowrate (left to right). Liquid flowrates 0.11, 0.23, 0.46, 0.57, 0.72 & 0.89 kg/m s. Legend in microns.

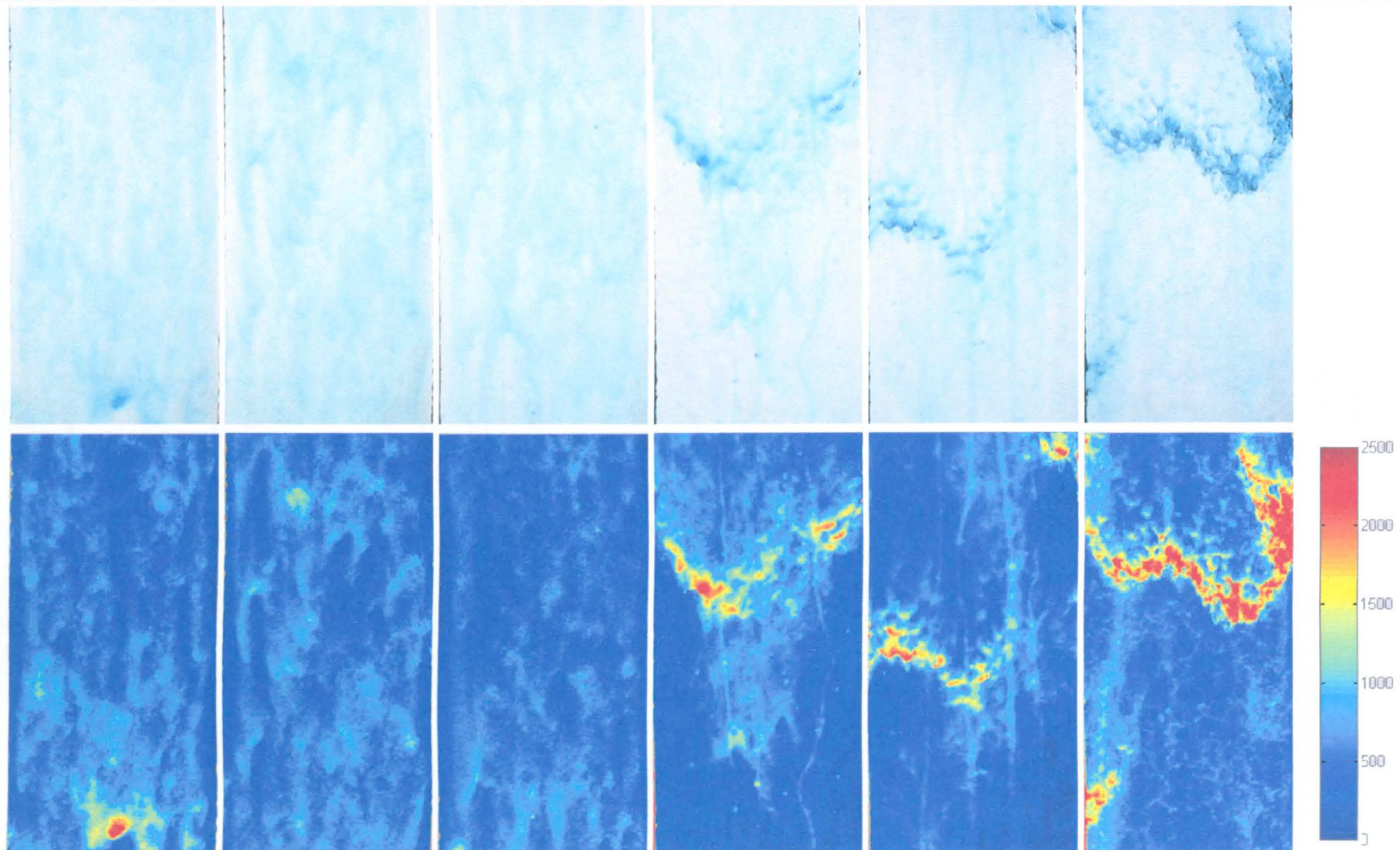


Figure 8.4: Film images and corresponding spatial film thickness maps for water falling films at constant liquid flowrate (0.57 kg/m s) with an increasing co-current downflow of air (left to right). Air flowrates 0, 4.9, 10.0, 12.5, 15.2 & 17.4 m/s. Legend in microns.

Figure 8.1 illustrates the influence of liquid flowrate on the interfacial structure of free falling water films. As the liquid flowrate is progressively increased the base substrate film becomes thicker, and the disturbance waves become taller, volumetrically larger and less frequent. This statement is confirmed from plots of the film thickness profiles of a centrally located strip of each of the six images, presented in Figure 8.5. Figure 8.5 shows that the profile of typical free falling disturbance waves consists of a steep wave front with a gentler trailing edge. These wave types are comparable to the 'gravity' type disturbance waves identified and discussed by Webb & Hewitt (1975), Andreussi (1980) and other workers at similar flow conditions.

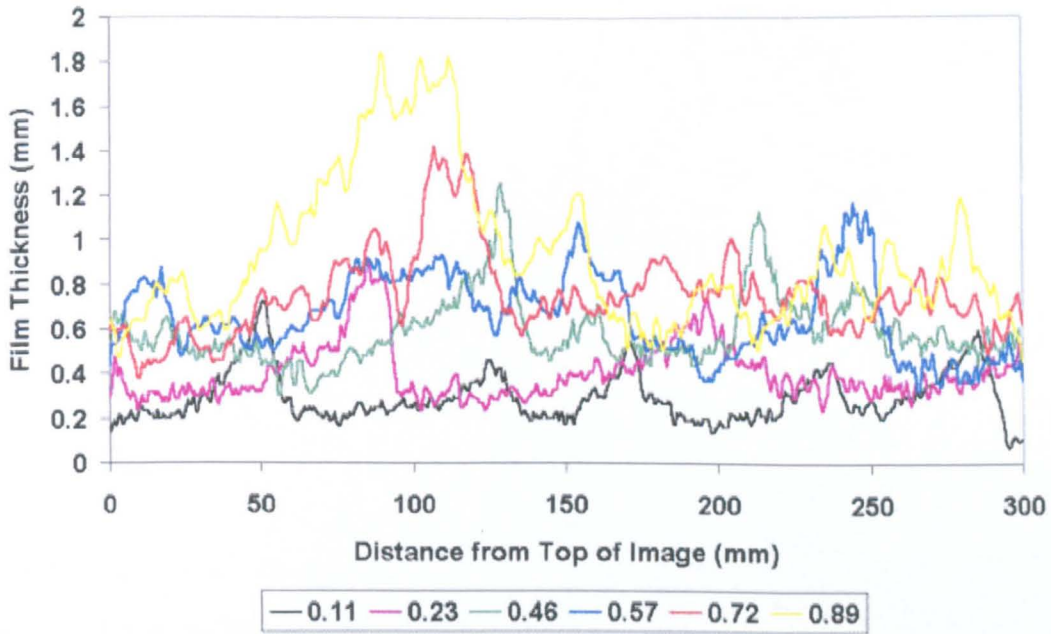


Figure 8.5: Film thickness profiles for a centrally located strip of the free falling images in Figure 8.1. Legend in kg/m s.

In a similar manner to Figure 8.1, Figures 8.2 and 8.3 illustrates the influence of liquid flowrate on the interfacial structure of falling films in the presence of a co-current downflow of air (7.4 and 15.2 m/s, respectively).

Figure 8.2 suggests that even the addition of a relatively low flowrate of air dramatically alters the physical structure of the interface. There is still the increase in base substrate height associated with increasing liquid flowrate, however, plots of the film thickness

profiles of a central strip of each of the six images, presented in Figure 8.6, confirm that the disturbance amplitudes have been dampened and their trailing edge profile has become more acute. Visual observation of these waves within the test section also showed them to be more periodic and frequent than their free falling counterparts.

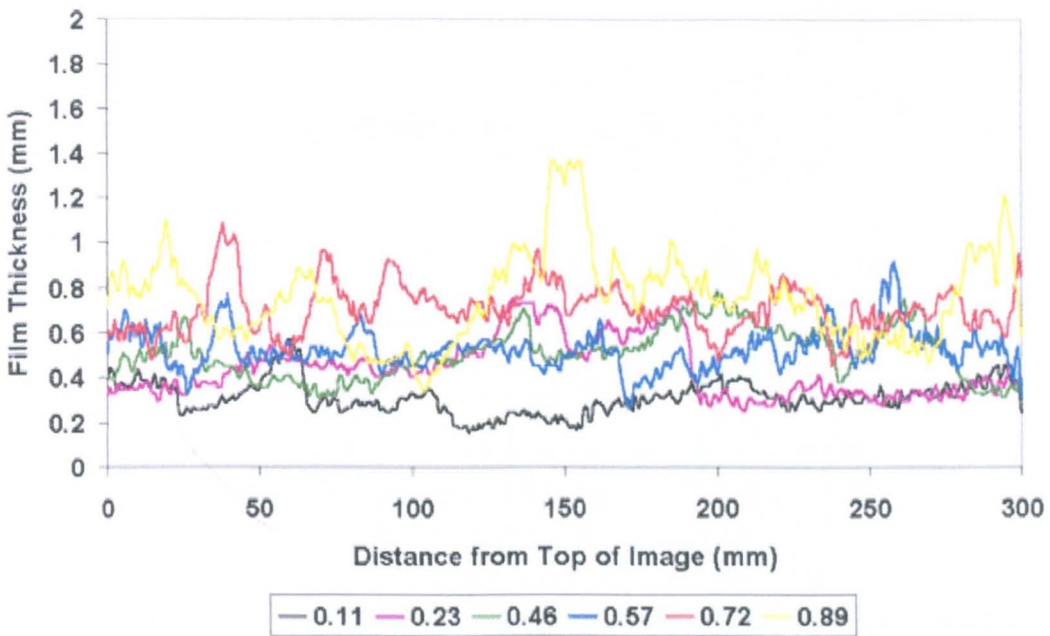


Figure 8.6: Film thickness profiles for a centrally located strip of the falling film images in Figure 8.2. Legend in kg/m s.

Figure 8.3 demonstrates that at the higher end of the air flowrates investigated there is a return to the development of large disturbance wave structures at the largest liquid flowrates. However, plots of the film thickness profiles of a centrally located strip of each of these six images, presented in Figure 8.7, illustrates that the wave profiles markedly differ from those encountered in free falling films. The waves at the intermediate liquid flowrates are generally taller than their free falling counterparts but they reach a similar maximum height at the largest liquid flowrates. They exhibit a less ordered shape that often appears to have multiple peaks. Additionally, they do not appear to have the long trailing edge associated with free falling disturbance waves. The trailing edge of these gas sheared disturbance waves appears almost as steep as the leading edge. These wave types are analogous to the ‘regular’ type disturbance waves considered by Webb & Hewitt (1975) and Andreussi (1980).

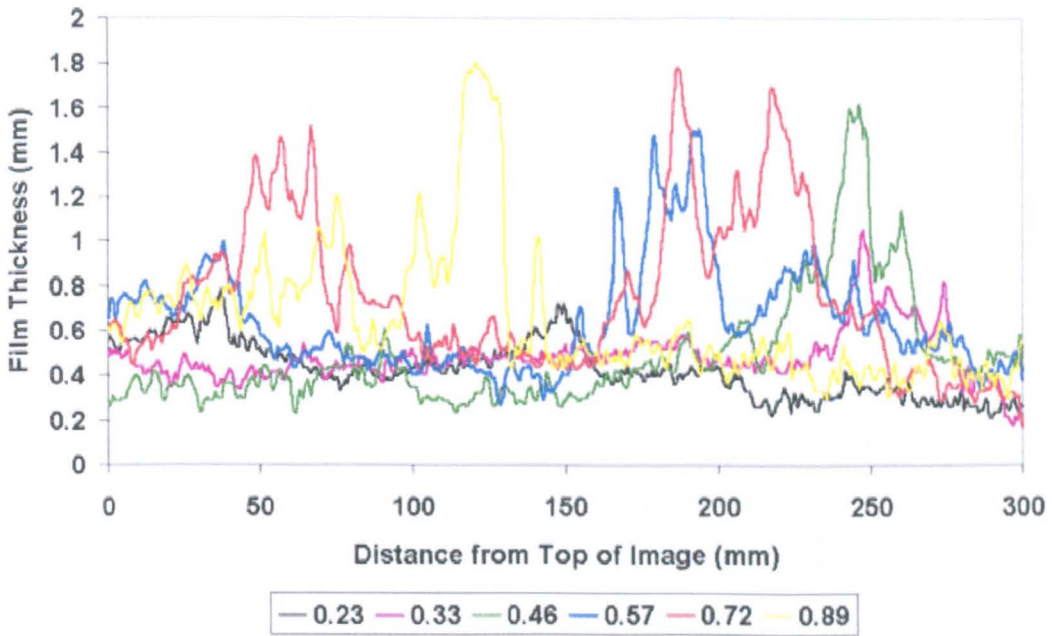


Figure 8.7: Film thickness profiles for a centrally located strip of the falling film images in Figure 8.3. Legend in kg/m s.

Clearly, the influence of a dynamic air stream on film interfacial structure is dramatic, and Figure 8.4 is provided to further demonstrate this by considering the effects on a constant liquid flowrate. With the aid of the film thickness profiles presented in Figure 8.8, it is possible to see the transformation of the interfacial structure from ‘gravity’ type to ‘regular’ type disturbances. As the airflow is introduced and steadily increased, it is interesting to note the dampening of the disturbances to the point where there is almost a complete lack of significant disturbances present (ten metres per second air flow condition). This is observed in all three images and at this flow condition and is a general trend for all but the highest liquid flowrates investigated at this air flowrate, where large disturbance structures are also present.

Further increases in the air velocity above ten metres per second; result in the development of the large, steep disturbances profiled in Figure 8.8. Figure 8.8 also demonstrates the slight compression of the base substrate film that occurs from the introduction of the airflow.

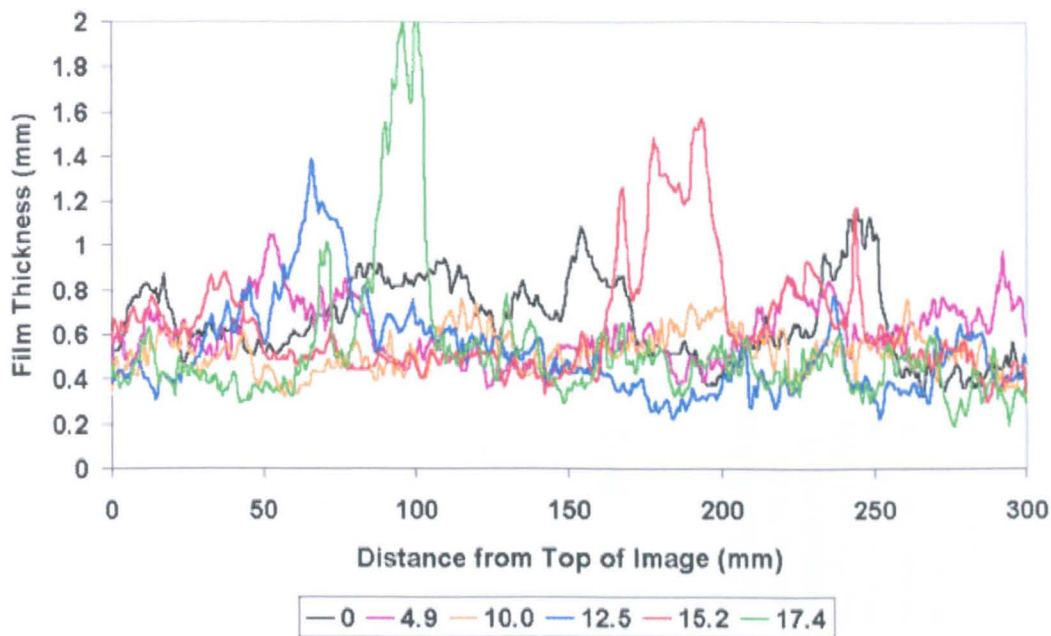


Figure 8.8: Film thickness profiles for a centrally located strip of the falling film images in Figure 8.4. Legend in m/s.

8.2.3 Mean Film Thickness

The mean thickness of the film is the simplest parameter to calculate from the spatial data, as it only involves averaging the thickness values over the entire region.

8.2.3.1 Free Falling Films

Figure 8.9 presents the average (*i.e.* averaged over the three images at each flow condition) of the mean film thickness values obtained for free falling water films over the range of liquid flowrates investigated in the current study, and plots these values with the results from all comparable studies found in the literature. The liquid flowrates are presented in terms of the dimensionless liquid film Reynolds number, defined in Equation 8.1. The similarity of the current data with the majority of previous studies is encouraging, and the data collectively suggests that mean film thickness is the same for vertical flat plates and for flow outside or inside a vertical pipe. The only major discrepancy highlighted from the figure is the data given by Chu (1973), whose mean measurements are significantly lower than the majority of the other data. It has been suggested by Karapantsios *et al.* (1989) that this apparent measurement error may be attributed to a lack of sensitivity of the conductance probes utilised by Chu.

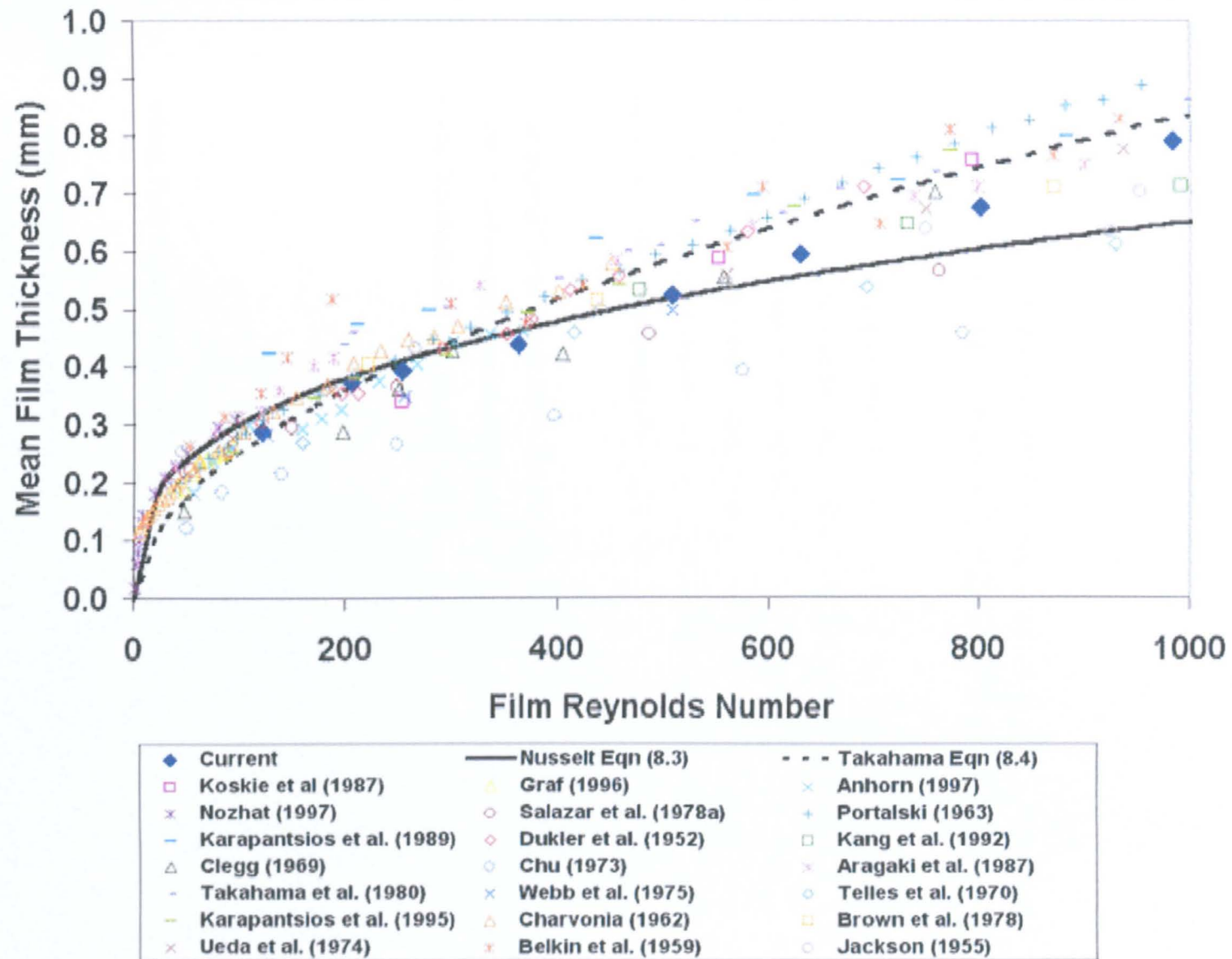


Figure 8.9: Comparison between current study and literature of free falling film mean film thickness values.

The solid line in Figure 8.9 is the theoretical prediction of mean film thickness, h , of Nusselt (1916) for a smooth laminar film with no gas shear, given by:

$$h = \left[\frac{3\mu \Gamma}{\rho^2 g} \right]^{\frac{1}{3}} \quad (8.3)$$

where, Γ is the flowrate per wetted perimeter (kg/ms), μ and ρ are the liquid viscosity (kg/ms) and density (kg/m³) respectively, and g is acceleration due to gravity (m/s²).

Figure 8.9 would suggest that in general, the Nusselt Equation tends to slightly over-predict film thickness at low liquid film Reynolds numbers (0-400) and under-predict, with increasing severity, film thickness at higher values (400+). Takahama & Kato (1980) also identified this critical value for Reynolds number, and it is no coincidence that this value agrees closely with the initial development point of the larger gravity type disturbance structures profiled in Figure 8.5

The dashed line in Figure 8.9 is the empirical prediction suggested by Takahama & Kato (1980) based on their own thickness measurements of free falling films. In this case, the mean film thickness, h , is predicted by:

$$h = 0.473 \left(\frac{\mu^2}{\rho^2 g} \right)^{\frac{1}{3}} \text{Re}^{0.526} \quad (8.4)$$

where, Re is liquid film Reynolds number (Eqn. 8.1).

It is clear from the figure that the equation of Takahama & Kato has a closer agreement with both the bulk of the available literature data and data from the current study than the theoretical prediction of Nusselt (1916). If the database of measurement points for this empirical equation is extended to include the measurements of the other studies

from the literature (approximately two hundred measurement points), the following predictive equation (in the format of Takahama & Kato) is obtained:

$$h = 0.91 \left(\frac{\mu^2}{\rho^2 g} \right)^{\frac{1}{3}} \text{Re}^{0.42} \quad (8.5)$$

Comparison of the mean measurement data for the water falling films investigated in this study with this new predictive equation (Figure 8.10), shows close correlation and suggests that global measurement accuracy of LAIT is comparable with other established measurement techniques.

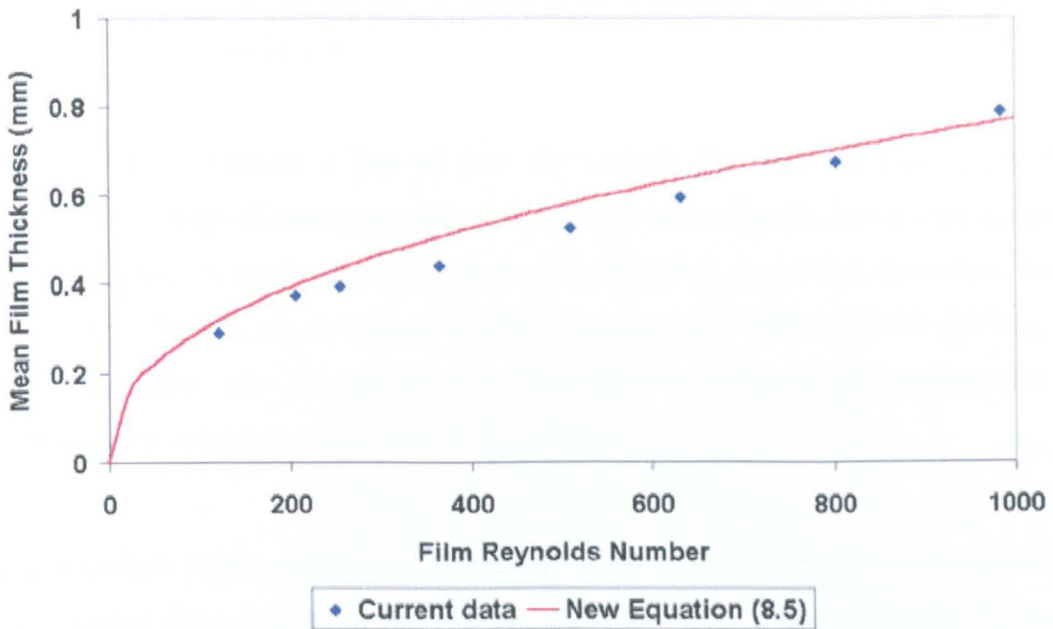


Figure 8.10: Comparison of current mean film thickness data for falling water films with Equation 8.5.

8.2.3.2 Falling Water Films with a Co-current Airflow

The influence of co-current airflows on mean water film thickness is presented in Figure 8.11.

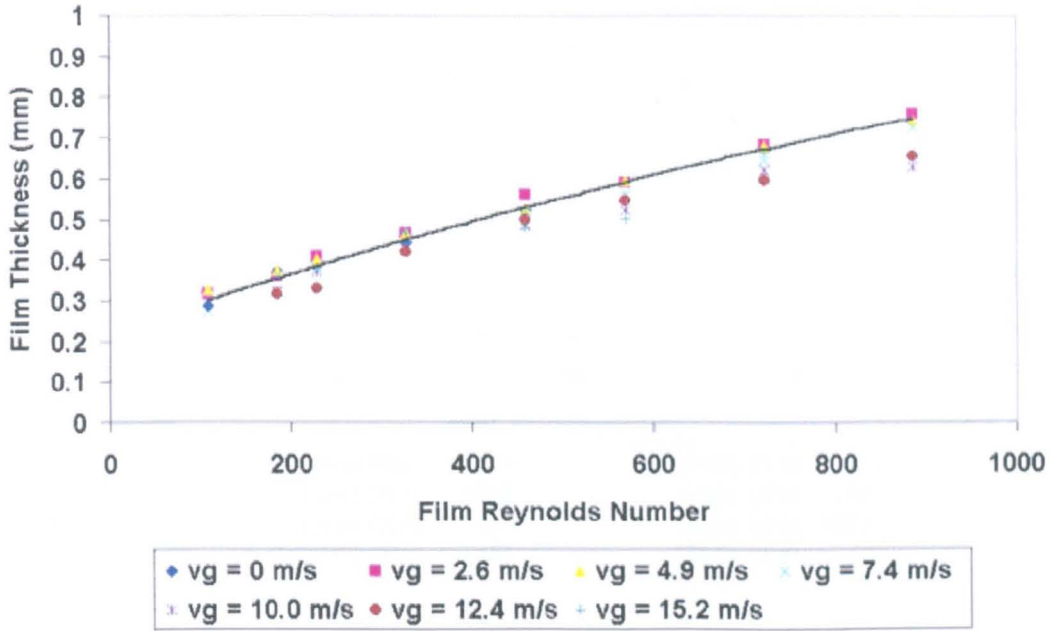


Figure 8.11: The influence of a co-current airflow on mean water film thickness.

The solid line represents a line of best fit through the data for free falling films ($v_g=0\text{m/s}$) and helps illustrate the slight reduction in mean film thickness with increasing airflow velocity. A similar trend is reported by all other co-current downflow studies (e.g. Brown (1978), Ueda & Tanaka (1974), Thwaites *et al.* (1976), Webb (1970b), and Charvonja (1962)). The decrease in mean film thickness can simply be attributed to the overall acceleration of the liquid film by the airflow.

For comparison purposes, Figure 8.12 presents a sample of the mean film thickness data for co-current downflow from the current study and from a study by Ueda & Tanaka (1974) at similar flow conditions.

Clearly, the figure illustrates a close agreement between the studies. However, this is not the case when attempting a similar comparison with the data from the study by Webb (1970b). Although there is good agreement at the lower liquid film Reynolds numbers, at higher values the mean film thickness data of Webb is markedly lower. The reasons for this disagreement are unclear.

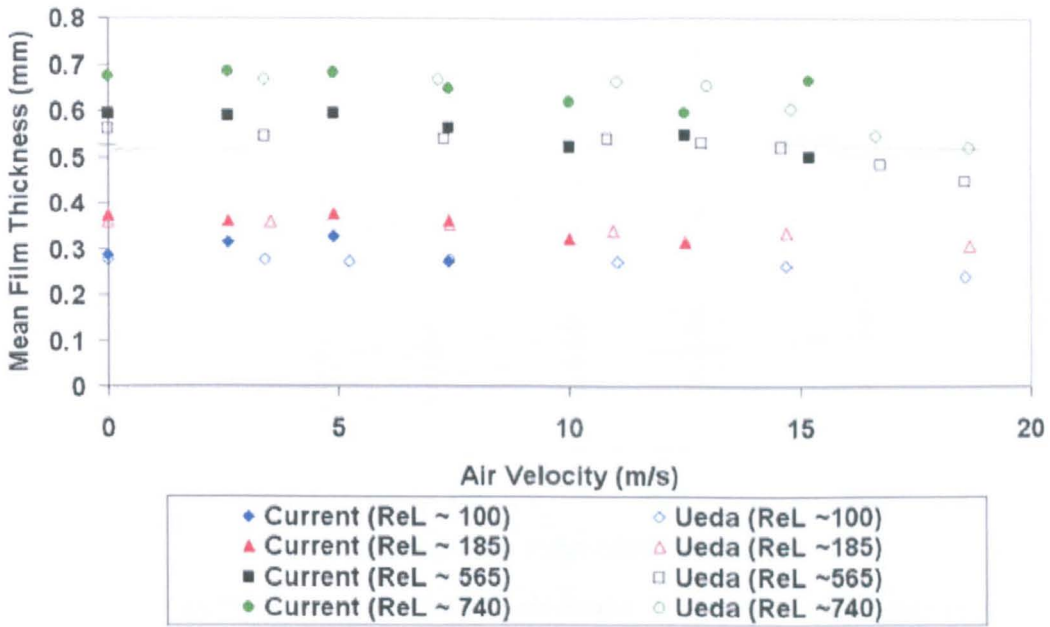


Figure 8.12: Comparison of a sample of the current study’s mean film thickness data for co-current downflow with the study by Ueda & Tanaka (1974).

8.2.4 Maximum & Minimum Film Thickness

The number of possible definitions of these parameters complicates comparison of the maximum and minimum film thickness values obtained with the values given in the literature. This is illustrated by Figure 8.13, which presents the possible film thickness measurement parameters, utilising LAIT, for the free falling water film data of the current study. The mean film, mean disturbance wave and mean substrate height are included for reference, which leaves two possible alternative definitions of the both the maximum and minimum film thickness value.

The maximum-recorded film thickness points are simply the largest values obtained from the analysis of each of the three film images at each flow condition. The high degree of scatter for these points suggest that the data from a single spatial image is insufficient to characterise this value for a given film flow. The maximum disturbance height data were obtained for each film image by averaging all the maximum values of the packets of disturbance data identified by the algorithm described in detail in Chapter 5. These values are significantly lower than the maximum recorded and the scatter has been significantly removed.

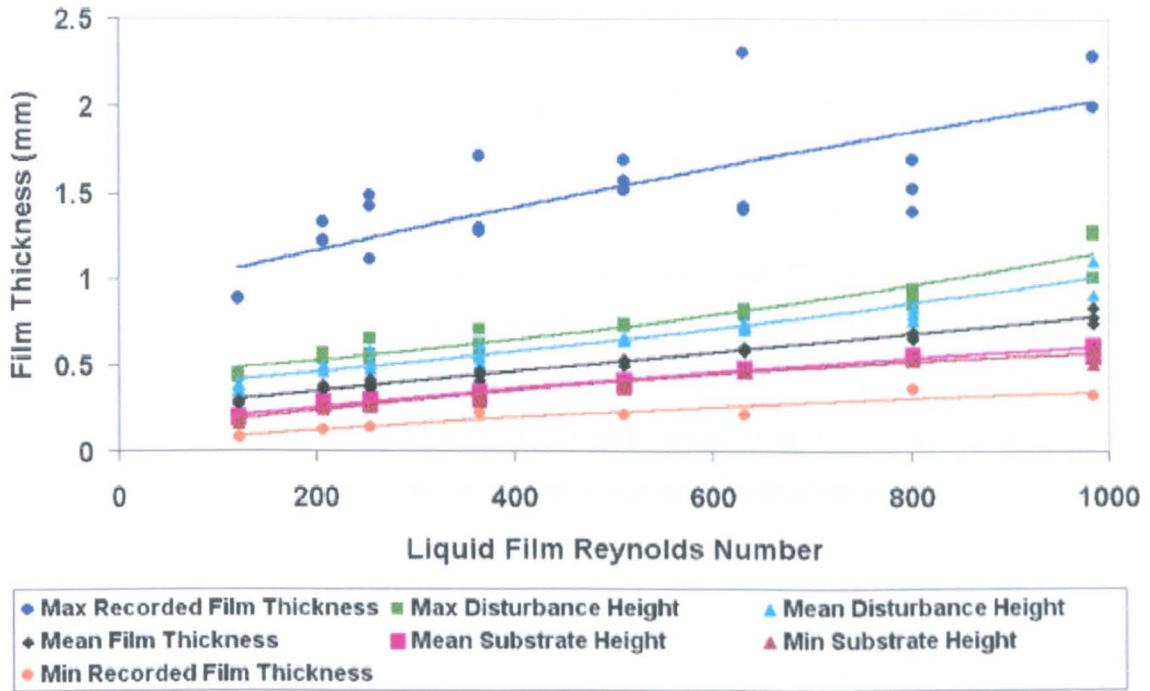


Figure 8.13: Illustration of the possible film thickness measurement parameters utilising LAIT. Data presented is for free falling films of current study.

If the data (averaged over the three images at each flow condition) from the two alternative definitions of maximum film thickness presented above are compared with data from the literature (Figure 8.14) it becomes evident that previous studies have not been consistent in their definition of maximum film thickness.

Figure 8.14 demonstrates that the data from the literature can be loosely categorised into two regions, that each contain data from the one of the alternative definitions. Study of the reports from the studies which lie in the upper data region confirms that they utilised the extreme film thickness value obtained. The spread of the data in this upper region must partly be due to the sampling time utilised. Obviously, probability dictates that a longer sampling time provides the opportunity for more extreme film behaviour in such a chaotic system as falling films. It is also not surprising that our extreme maximum film thickness values are generally the lowest, as they are obtained from the spatial ‘snapshot’ at three instances in time, whereas the other data in this region is obtained from several seconds of film thickness probe output. The procedure for determination of the maximum thickness data for the literature studies in the lower region is less clear. The study of Aragaki *et al.* (1987) reports utilising the average maximum value obtained from

four, two-second samples of probe output. Chu (1973) applied his interface characterisation method, described in Chapter 5, and it is assumed he utilised an average of the maximum heights of the waves determined from his probe output. No information could be found on the procedure applied by Telles & Dukler (1970), however, the location of their maximum data would suggest that some averaging has taken place. As expected, the current data is slightly lower than the other studies in this region, as the averaging is based on packets of disturbance data strips (see Chapter 5). For a truer measurement of maximum (disturbance) height the algorithm requires adaptation to consider all the data contained within each individual wave.

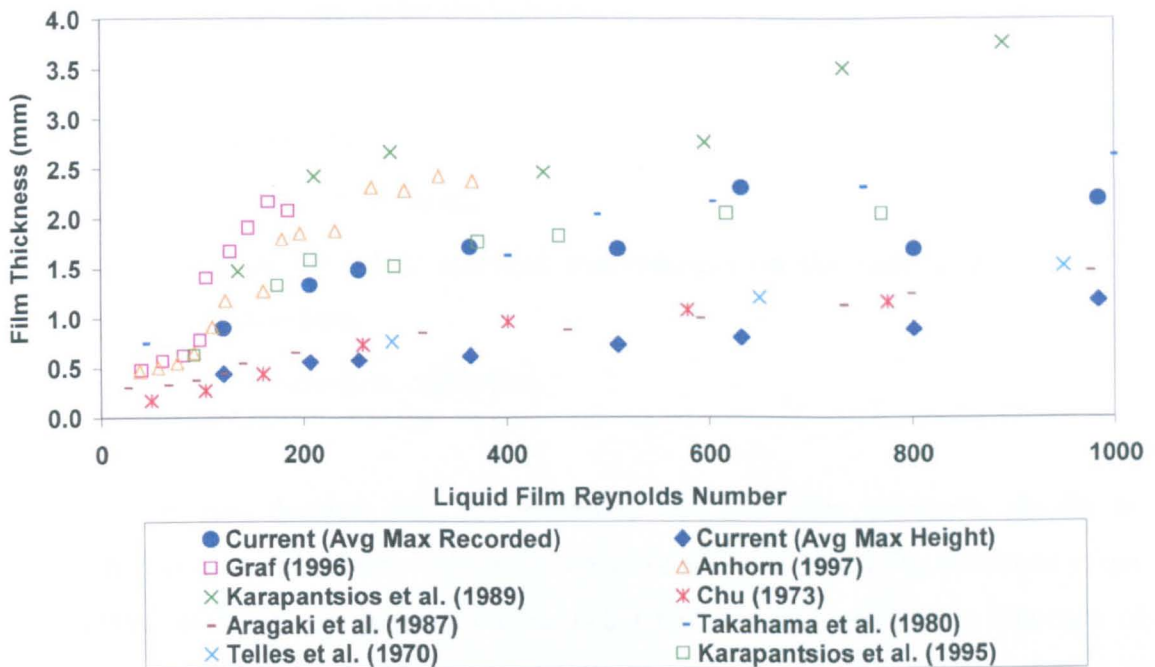


Figure 8.14: Comparison of current data with literature for maximum film thickness for free falling films.

The significant difference in values for the two Karapantsios studies in Figure 8.14 highlights another phenomenon, the influence of longitudinal distance from the entry point on maximum film thickness. Studies by Takahama & Kato (1980) and Karapantsios & Karabelas (1995) have investigated the longitudinal flow characteristics of wavy falling films, and identified a strong dependence of maximum film thickness on the distance from the film entry point. Fortunately, the majority of the literature film thickness data available is taken at a comparable distance from the entry point to the

current study (1.5 - 2.0 metres). The data from Karapantsios *et al.* (1989) and Karapantsios & Karabelas (1995) is from a longitudinal distance of 2.5 metres and 1.7 metres from the film entry point, respectively, and this helps explain the differences obtained from application of virtually identical techniques.

For minimum film thickness, Figure 8.13 also offers two alternative definitions. The minimum substrate height was the average minimum height of all the substrate strips obtained through the analysis detailed in Chapter 5. The minimum recorded film thickness was more difficult to obtain than its maximum counterpart, as small numbers of erroneous points ensured that the recorded minimum value was often zero. These erroneous points could usually be attributed to:

- (i) edge effects,
- (ii) light reflection issues,
- (iii) specks of lightly coloured contaminants on the viewing glass plate or camera lens,
- (iv) minor errors in calibration.

Therefore, it was decided that the minimum recorded film thickness should be determined as the point where only one percent of the entire spatial film thickness values were lower, with the one percent criteria being included to remove any influence of erroneous points. If the data (again averaged over the three images at each flow condition) from the two alternative definitions of minimum film thickness are compared with data from the literature (Figure 8.15), it becomes evident that previous studies have been more consistent with their definition.

Figure 8.15 clearly demonstrates that the minimum recorded thickness values obtained in the current investigation are comparable with the majority of other studies. Only Aragaki *et al.* (1987) report the application of averaging in their determination, and this is reflected in their data being significantly higher than other studies and closer to our averaged minimum values.

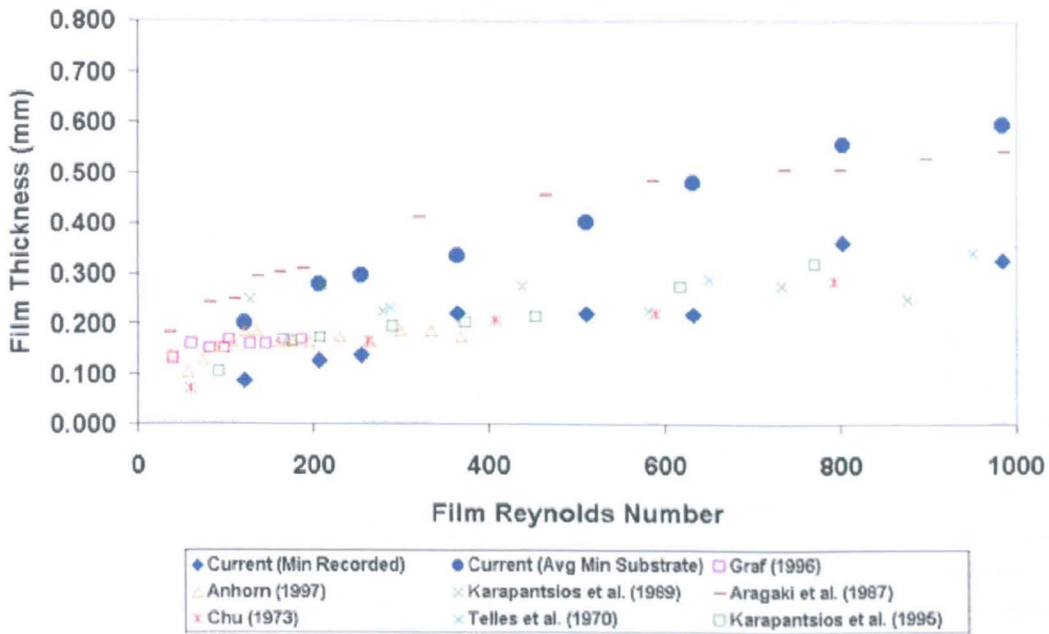


Figure 8.15: Comparison of current data with literature for minimum film thickness for free falling films.

8.2.5 Disturbance Wave Characteristics

The characterisation of the interface into disturbance wave and substrate film regions by the approach detailed in Chapter 5, allows the characteristics of the disturbance wave to be studied independently.

8.2.5.1 Maximum Disturbance Wave Height

Figure 8.16 is provided to illustrate the influence of a co-current downflow of air on the averaged maximum disturbance height for a variety of falling liquid film flows.

As might be expected, Figure 8.16 demonstrates there is an almost proportional increase in maximum disturbance wave height with increasing liquid flow, with factor of three increase in recorded heights over the range of liquid flowrates investigated. Of particular interest is the tendency for maximum disturbance wave height to initially fall under the influence of a co-current air stream to a critical value (7–10m/s), and then, at the higher liquid flowrates, to begin to rapidly increase as the air velocity is increased beyond this value. This coincides directly with the transition of the disturbance wave structure from

gravity to regular type wave structure, which can be observed at these flow conditions (see Section 8.2.3).

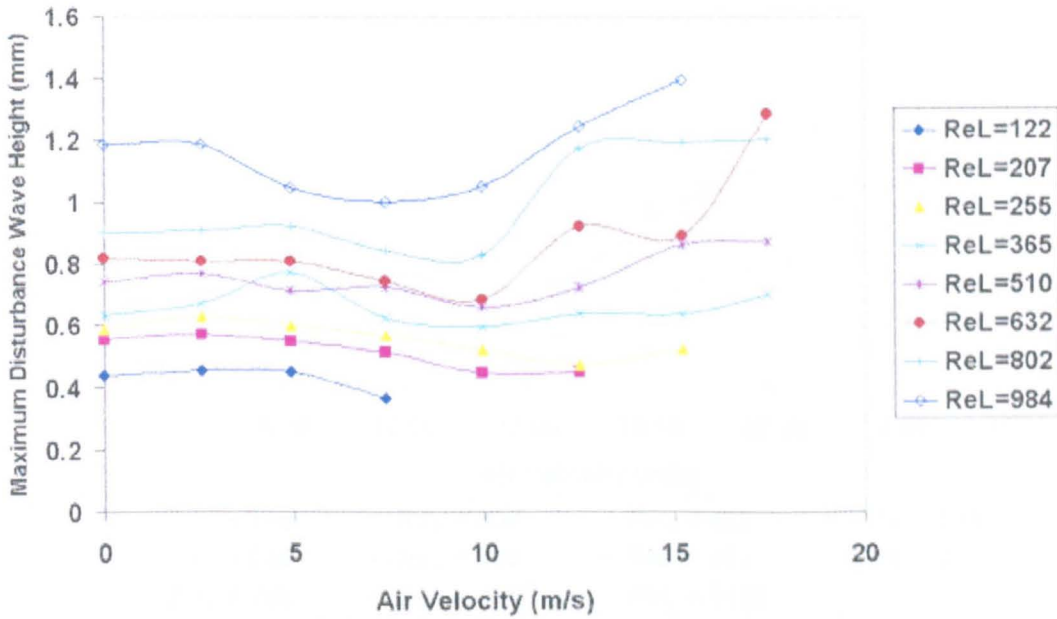


Figure 8.16: Influence of a co-current downflow of air on the averaged maximum disturbance height for a variety of falling liquid film flows.

8.2.5.2 Disturbance Wave Celerity

Figure 8.17 presents the influence of a co-current downflow of air on disturbance wave celerity for the falling water film flows investigated in the current study.

The figure suggests that the transition between gravity and regular wave structure type also has a significant influence on disturbance wave celerity. Unfortunately, an error in the calibration of the air orifice plate prevented measurements at lower co-current airflows within the time allocated with the high-speed video equipment. However, the wave celerity measurements of free falling films would suggest that a gradual, linear increase in wave celerity up to the wave structure transition point is likely. At velocities just below and above the transition there appears to be a region of virtually no growth. This is apparently followed by a rapid increase in wave celerity as the air velocity is increased beyond the transition region. Figure 8.17 also suggests that the rate of water

flow has little impact on wave celerity; with only a minor proportional increase in celerity being attributed to increasing film flowrate over the region of flowrates investigated.

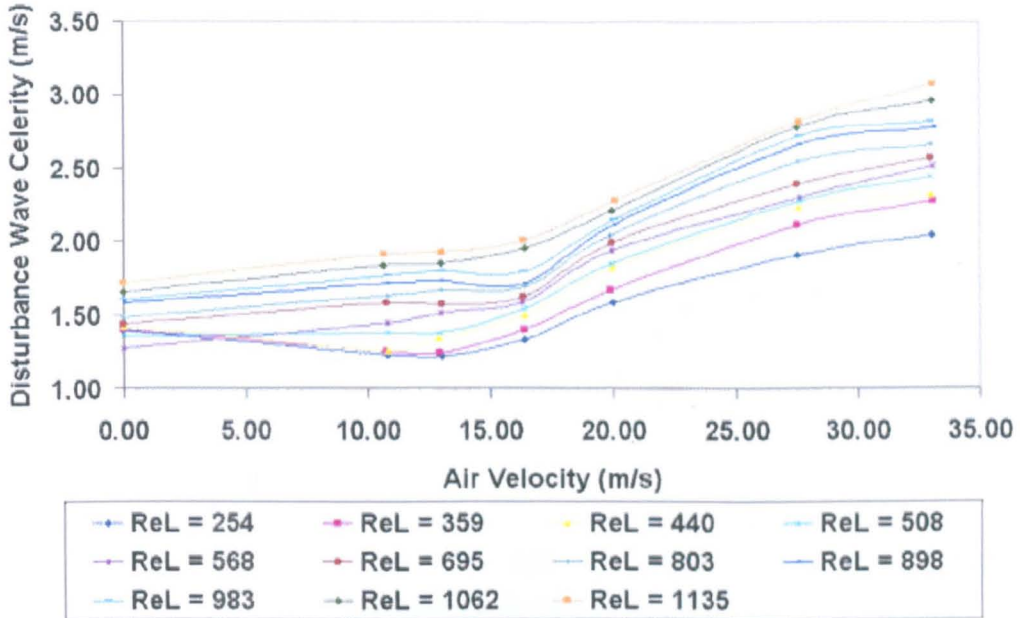


Figure 8.17: Influence of a co-current downflow of air on disturbance wave celerity for the falling water film flows investigated in the current study.

Figure 8.18 provides comparison of the current wave celerity measurements with a sample of the available literature.

Figure 8.18 illustrates the general agreement in measurement trends for the current study with the literature. However, the figure further suggests that the current technique has a tendency to record lower wave celerity values, with the differences being particularly evident at higher airflows. This is certainly partly due to the subjectivity required by the human operator in choosing individual waves during the analysis process. This author attempted to randomly select waves of all sizes and from all regions of the film plate, and this usually resulted in a diverse range of wave celerity measurements being recorded at each experimental run. As only six to ten waves were sampled to represent each flow it is possible that slower, less representative waves were disproportionally recorded. This could result in a tendency for under prediction of the average wave celerity for that flow.

Cross-correlation based techniques, utilised in the other studies in Figure 8.17, do not suffer from these subjectivity difficulties.

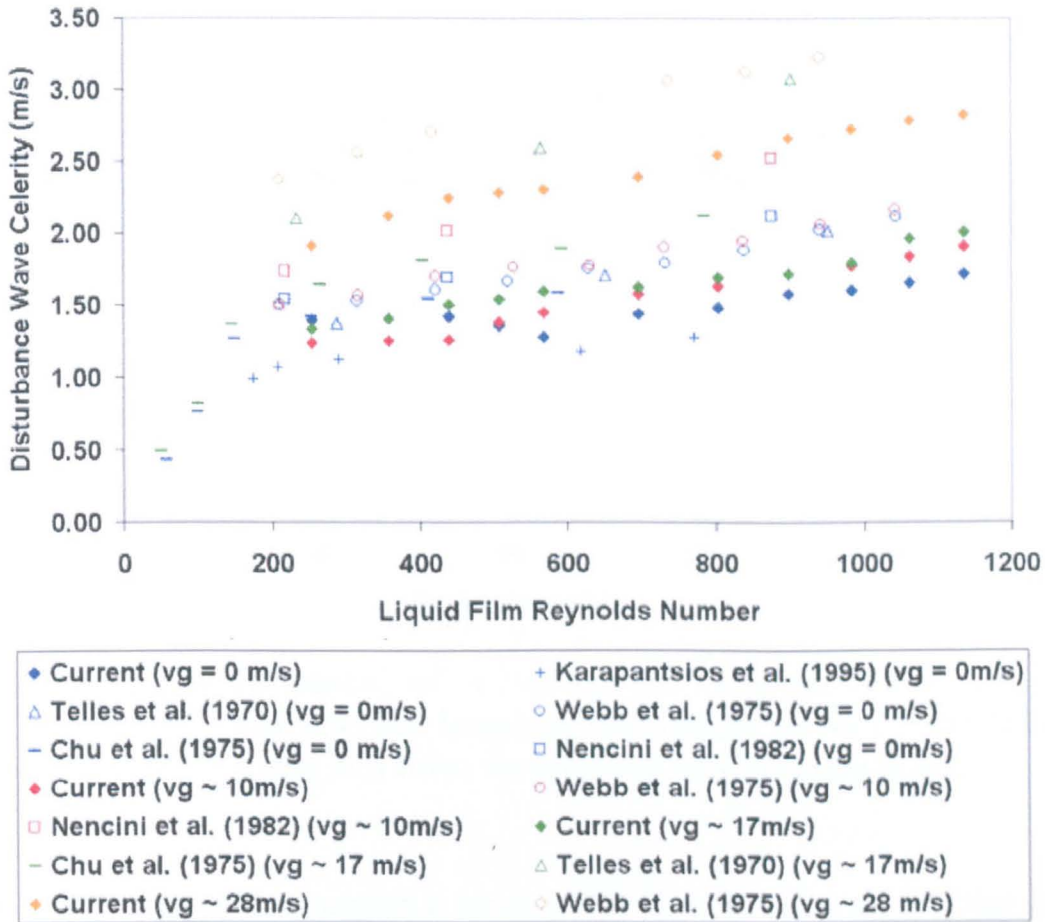


Figure 8.18: Comparison of the current wave celerity measurements with a sample of the available literature.

8.2.5.3 Characteristic Length of Disturbance Waves

Figure 8.19 presents the influence of a co-current downflow of air on characteristic longitudinal length of disturbance waves for the falling water film flows investigated in the current study.

The Figure illustrates quite clearly the effect that the disturbance wave transition that occurs around at the central region of the air velocities investigated has on longitudinal wave shape. There is the strong suggestion that after a steady decline in longitudinal

wavelength as the air velocity is applied and increased towards the transition; the wave length reaches a minimum during this transition.

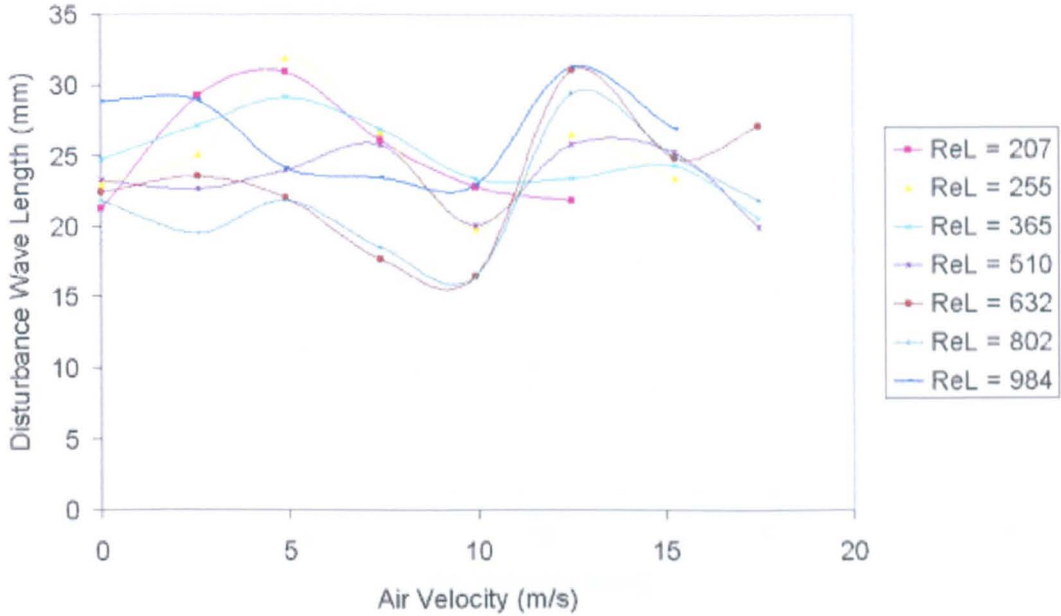


Figure 8.19: Influence of a co-current downflow of air on characteristic length of disturbance waves for the falling water film flows investigated in the current study.

The behaviour above the transition is less clear, however, the figure suggests that at the higher water loads the minimum is rapidly followed by a peak in wave length before a return to a decline in length as the airflow is increased higher.

Due to a lack of available data, comparison with the literature was limited to the study by Nencini & Andreussi (1982) on disturbance wave behaviour in two-phase downflow. Figure 8.20 presents a plot of comparable samples of both studies measurements of the characteristic longitudinal lengths of waves. The most dramatic feature of Figure 8.20 is the difference in scale between the current results and those of Nencini & Andreussi, and this can be attributed to the different forms of analysis. Nencini & Andreussi only considered the lengths of the largest disturbance waves, whereas the current analysis takes an average of the strips of all disturbance structures travelling on the interface. For it to be possible to determine the longitudinal length of the larger waves only, it would be necessary to consider the disturbance wave as a whole in the spatial analysis. It is

interesting to note that at relatively high liquid and air flows, where the larger disturbance waves dominate the disturbance region of the interface, the current study values rapidly approach the values from Nencini & Andreussi.

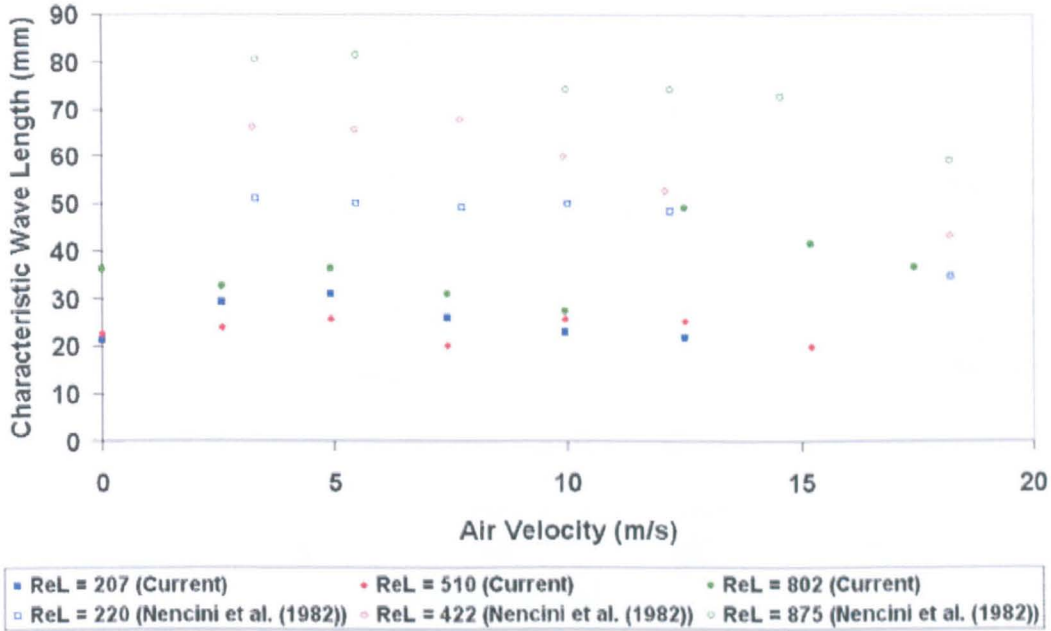


Figure 8.20: Comparison of characteristic lengths with results reported by Nencini & Andreussi (1982).

8.2.6 Base Substrate Film Characteristics

The characterisation of the interface into disturbance wave and substrate film regions by the approach detailed in Chapter 5, allows the characteristics of the base substrate film to be studied independently.

8.2.6.1 Mean Substrate Thickness

Figure 8.21 presents the influence of a co-current downflow of air on mean substrate thickness for the falling water film flows investigated in the current study.

The figure demonstrates the almost proportional increase in substrate height with increasing liquid load, with a factor of three increase over the range of liquid conditions investigated. The figure also demonstrates the slight compression of the substrate in the

presence of a co-current flow of air. Values at the higher liquid Reynolds numbers suggest that the transition between disturbance wave regimes also has a significant effect on substrate height.

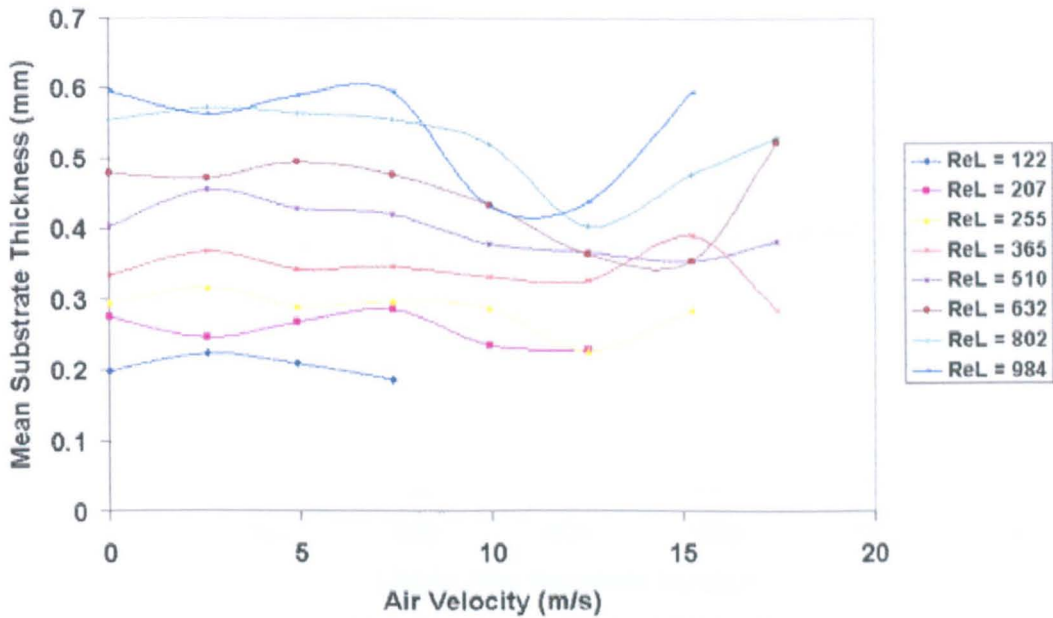


Figure 8.21: Influence of a co-current downflow of air on mean substrate thickness for the falling water film flows investigated in the current study.

8.2.6.2 Ratio of Mean Substrate Height to Maximum Disturbance Height

Aragaki *et al.* (1987) report, in their study of free falling water films on a vertical tube, that they observed an interesting phenomenon related to the ratio of the thickness of the substrate layer to the maximum film thickness (*i.e.* maximum height of the disturbances). They observed that this ratio fell rapidly at very low Reynolds numbers until, at $ReL \sim 170$, the value suddenly became constant at approximately 0.5, and remained constant at this value until $ReL \sim 800$, where it started to fall slowly. They attributed this phenomenon to a change in wave shape that they observed around $ReL \sim 200$. As the current study Reynolds number range is limited to between approximately two hundred and a thousand, it is only possible to investigate whether the constant ratio region was observed in the current results, and Figure 8.22 presents this comparison between studies. It is clear from the figure that although there is general agreement between studies in the value of the ratio, the current data demonstrates a gentle increase in ratio

over the supposed constant Reynolds region. However, there is some evidence that the fall in ratio observed by Aragaki and his co-workers above the constant region can also be observed in the final data point of the current work.

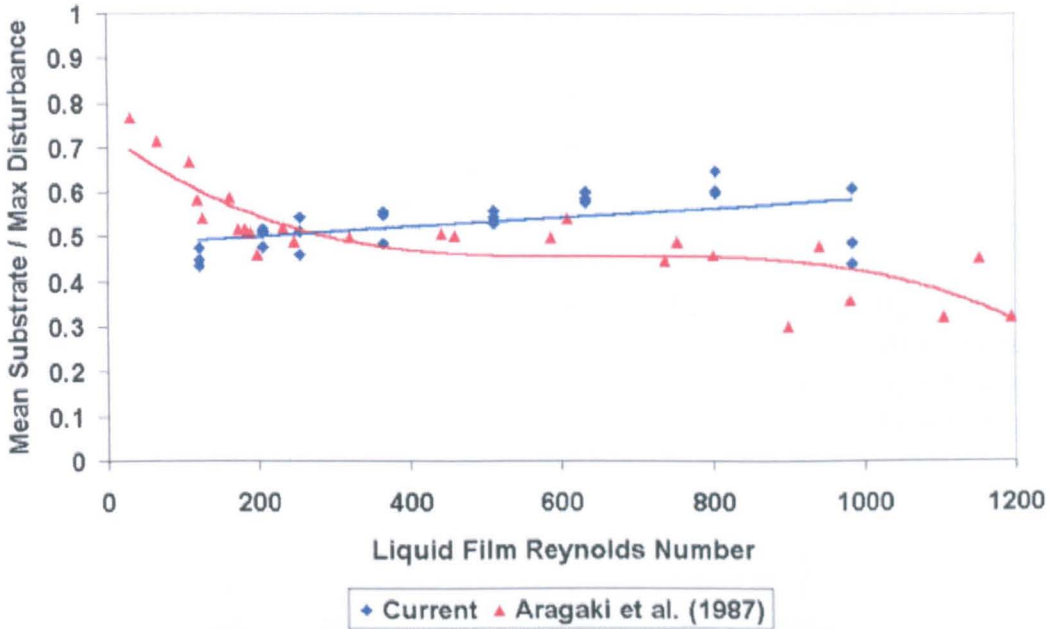


Figure 8.22: Comparison between studies of ratio of substrate height to maximum disturbance/film height.

If the examination of this ratio is extended to include the data from co-current flow conditions, presented in Figure 8.23, it is interesting to note once more the dramatic effect that transition between wave structure types has on the interfacial characteristics of the film.

The figure illustrates that the trend for free falling films is continued until the transition region, and that after the transition to ‘regular’ type disturbances the trend is reversed. This is a direct result of:

- (i) The dominance of the large ‘regular’ type disturbances in the determination of the maximum disturbance height (*i.e.* the majority of the disturbance strips used in the calculation of the maximum height are material from these structures).

- (ii) Whereas 'gravity' type disturbances exhibit a three dimensional structure, large 'regular' type disturbances show signs of a development of a more two dimensional structure (see Figure 8.3), which results in an almost constant maximum height over the strips of data used in the calculation of the maximum height.

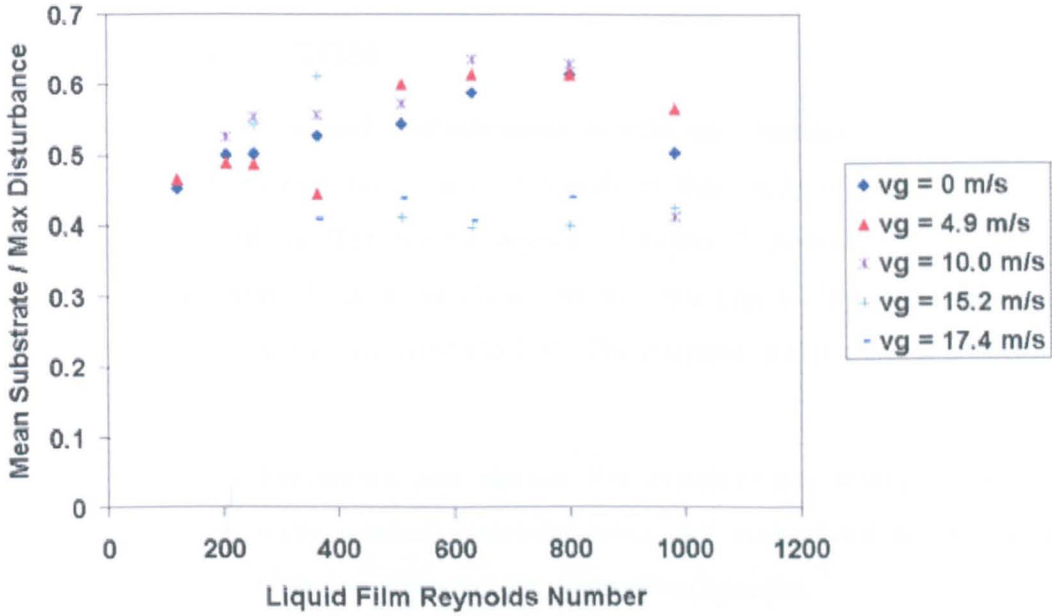


Figure 8.23: Influence of a co-current downflow of air on the ratio of mean substrate height to maximum disturbance height.

Chapter 9

RESULTS

Air-Organics: The Study of Hydrodynamic Conditions in Falling Film Reactors

9.1 INTRODUCTION

For the study of physical and hydrodynamic conditions encountered in falling film reactors it is important that the choice of liquids in this study reflected the physical properties of actual falling film reactor liquids. Chapter 2 (Section 2.4) provides an account of the reasoning behind the choice of the two organic liquids utilised in the study, dodecylbenzene and ethoxylated alcohol. The purpose of this chapter is two-fold:

- (i) Summarise and discuss the experimental results obtained for wavy, vertical dodecylbenzene and ethoxylated alcohol films in both free falling and co-current air systems.
- (ii) Investigate the influence of the physical properties of the liquids on film interfacial characteristics by comparison of a sample of the results obtained at similar flow conditions using water, dodecylbenzene and ethoxylated alcohol.

Criterion (ii) was made possible by utilising an identical measurement location for both the organic liquids and water (*i.e.* all data presented in this chapter is taken from images of a 150mm wide by 300mm high region that begins approximately 1500mm below the liquid entry weir). Each pixel image represents an area of the film of 0.36 mm² with 125,000 pixels required to represent the entire spatial area of film. As with the water data, a complete summary of the experimental results obtained with both organic liquids is provided in tabular form in Appendix C. Expression of the flow conditions is consistent with the methods used and described in Chapter 8. Physical properties for the organic liquids are available in Appendix A, and summarised for standard operating conditions in Table 2.1.

9.2 DODECYLBENZENE

9.2.1 Experimental Flow Conditions

The range of experimental flow conditions employed for dodecylbenzene films is summarised in Table 9.1

Table 9.1: Range of experimental flow conditions employed for dodecylbenzene films.

Liquid Flowrate per Wetted Perimeter, Γ (kg/m s)	0.09 - 0.99
Air Velocity (m/s)	0 - 14.7

Partial wetting of the glass viewing plate dictated the maximum air and liquid flowrates achievable. The minimum liquid flowrate studied was limited by flow measurement sensitivity and a desire to keep consistent with the flow conditions utilised in the study of water films. Difficulties associated with wetting of the viewing glass plate prevented measurement of the entire liquid flow range at the higher air velocities and vice versa. A detailed review of the experimental difficulties encountered, which gave rise to these flow limitations, is provided in Chapter 2 (Section 2.3.5).

A range of eighty-six differing flow conditions produced a total of two hundred and fifty eight spatial images that were subsequently converted into spatial film thickness measurements. The same eighty-six flow conditions were utilised in disturbance wave celerity measurements. It was not considered feasible or practical to present every possible parameter evaluated in this study to describe the interfacial characteristics of dodecylbenzene films, therefore, it is hoped that the selection of results displayed in this section will provide both visual and quantitative insight into the influence of air and liquid flow conditions on the interfacial characteristics of dodecylbenzene films.

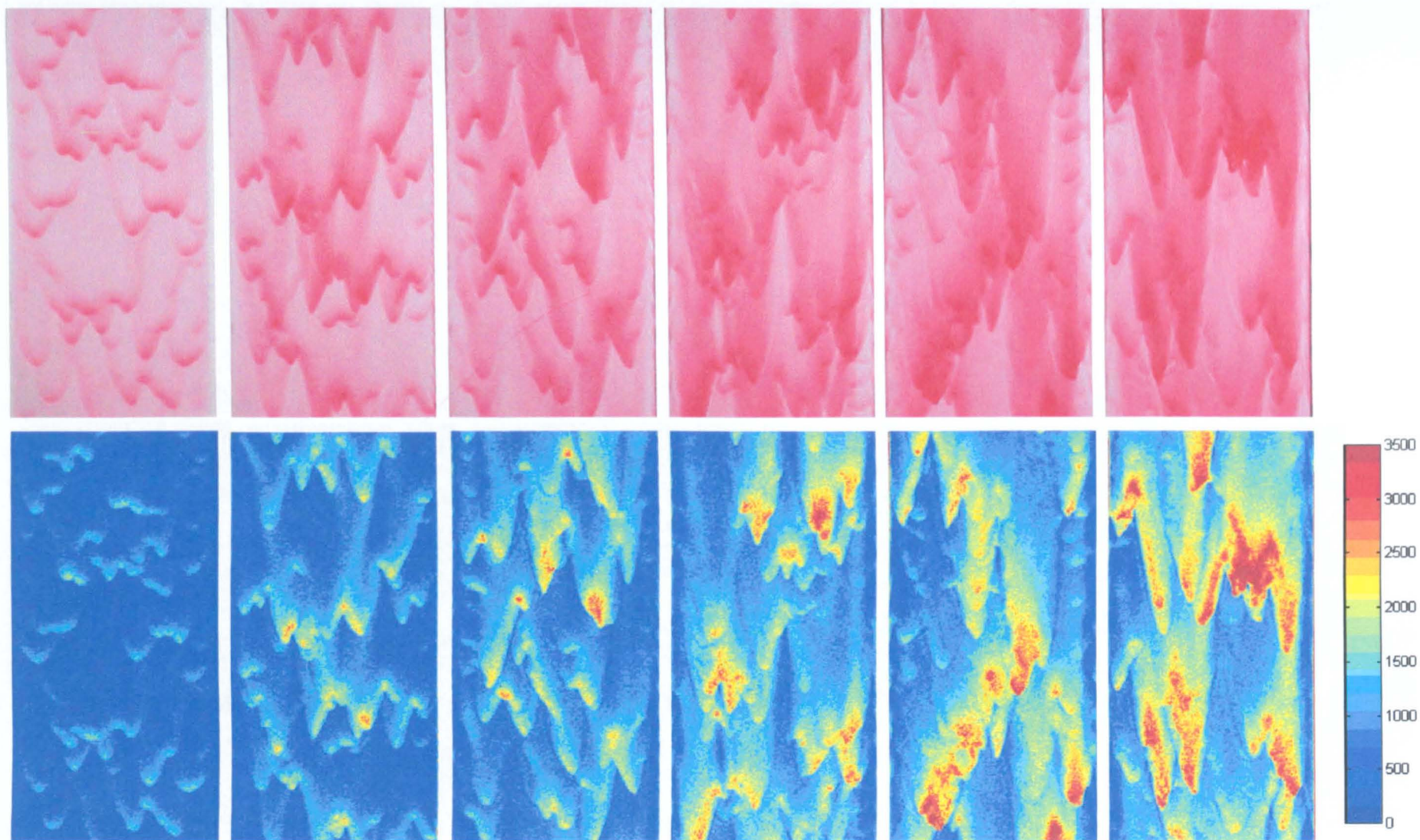


Figure 9.1: Film images and corresponding spatial film thickness maps for free falling dodecylbenzene films with increasing liquid flowrate (left to right). Liquid flowrates 0.09, 0.27, 0.47, 0.67, 0.80 & 0.99 kg/m s. Legend in microns.

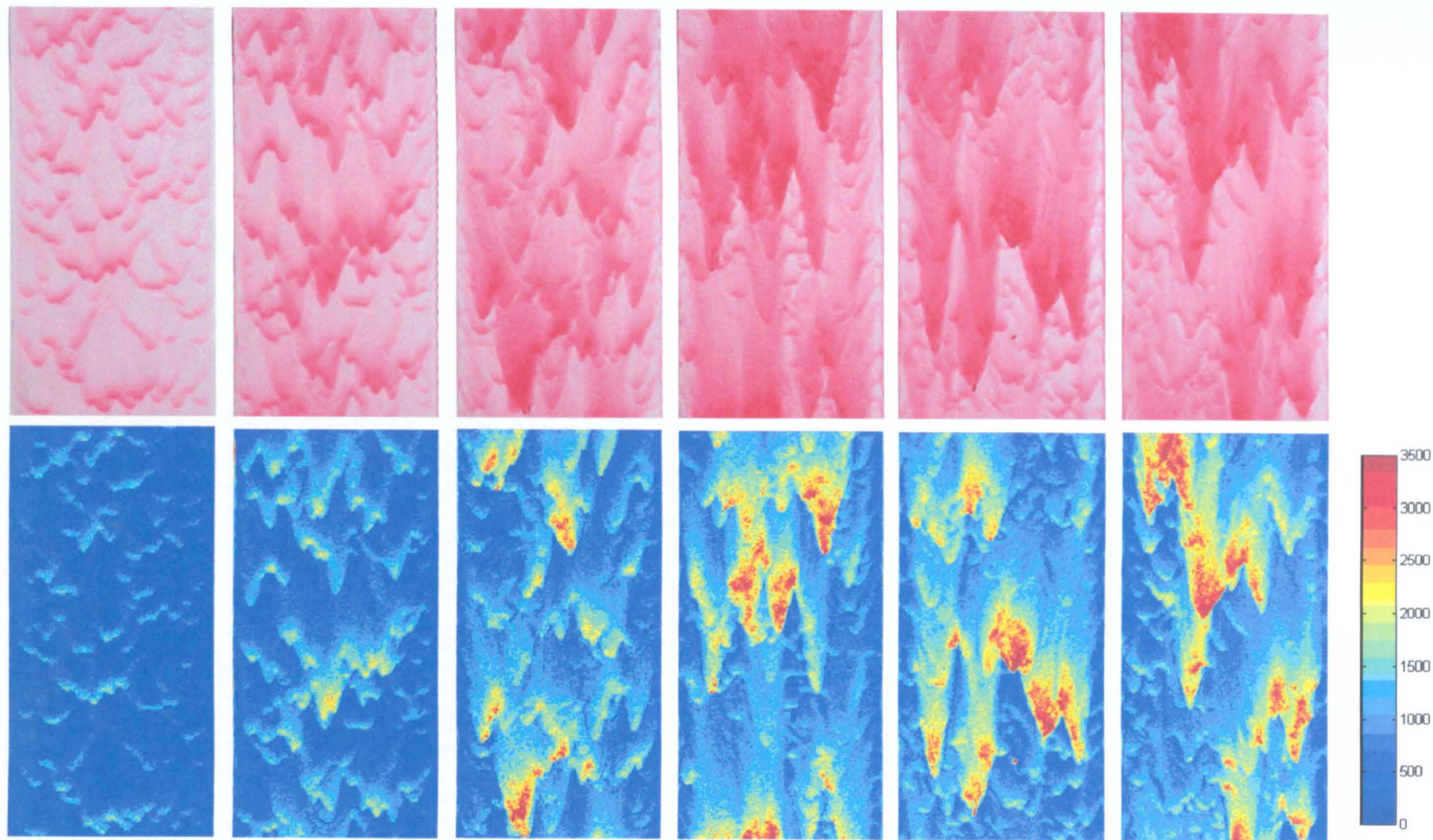


Figure 9.2: Film images and corresponding spatial film thickness maps for co-current air-dodecylbenzene downflow at constant air velocity (7.3 m/s) with increasing liquid flowrate (left to right). Liquid flowrates 0.09, 0.27, 0.47, 0.67, 0.80 & 0.99 kg/m s. Legend in microns.

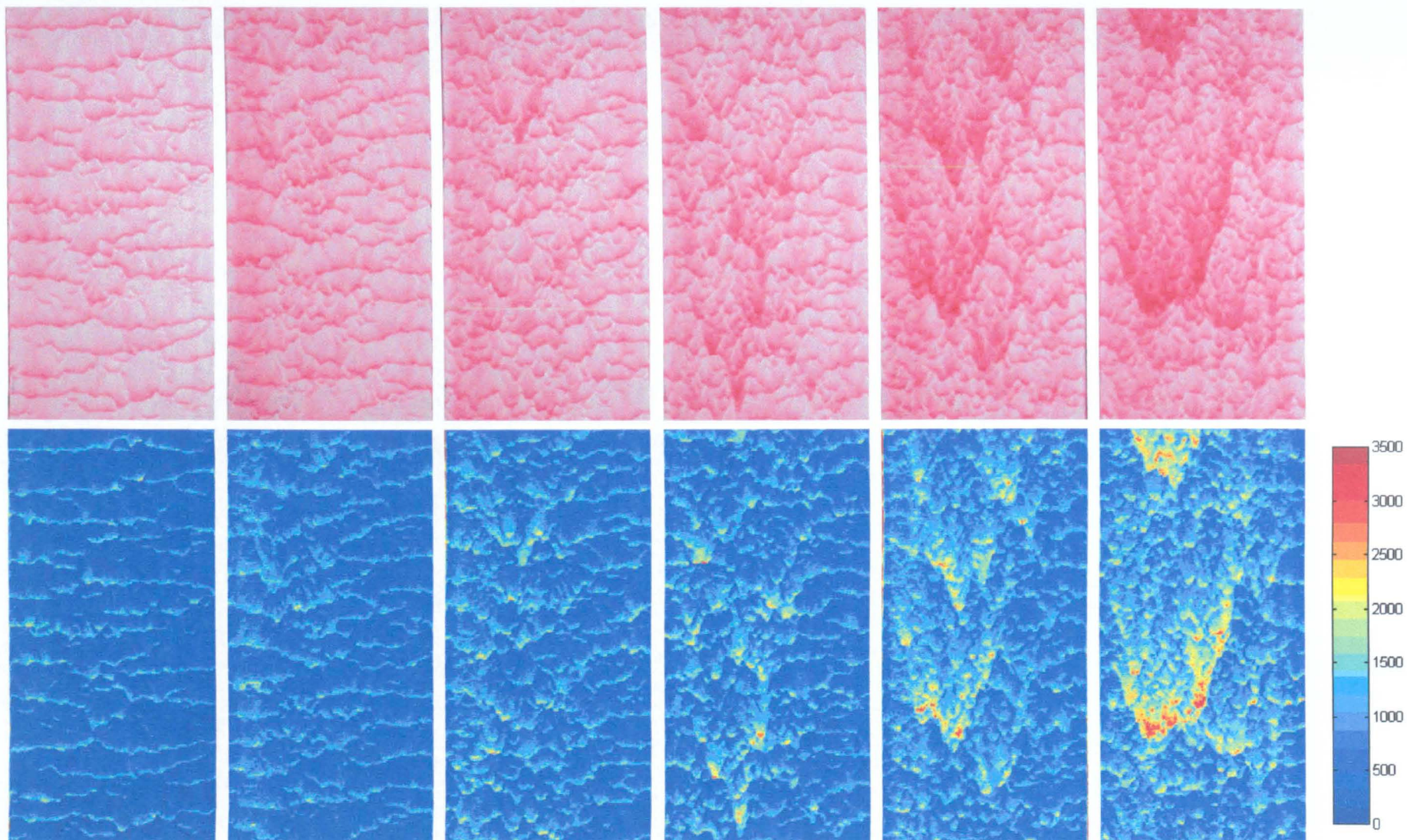


Figure 9.3: Film images and corresponding spatial film thickness maps for co-current air-dodecylbenzene downflow at constant air velocity (14.7 m/s) with increasing liquid flowrate (left to right). Liquid flowrates 0.15, 0.19, 0.27, 0.33, 0.43 & 0.52 kg/m s. Legend in microns.

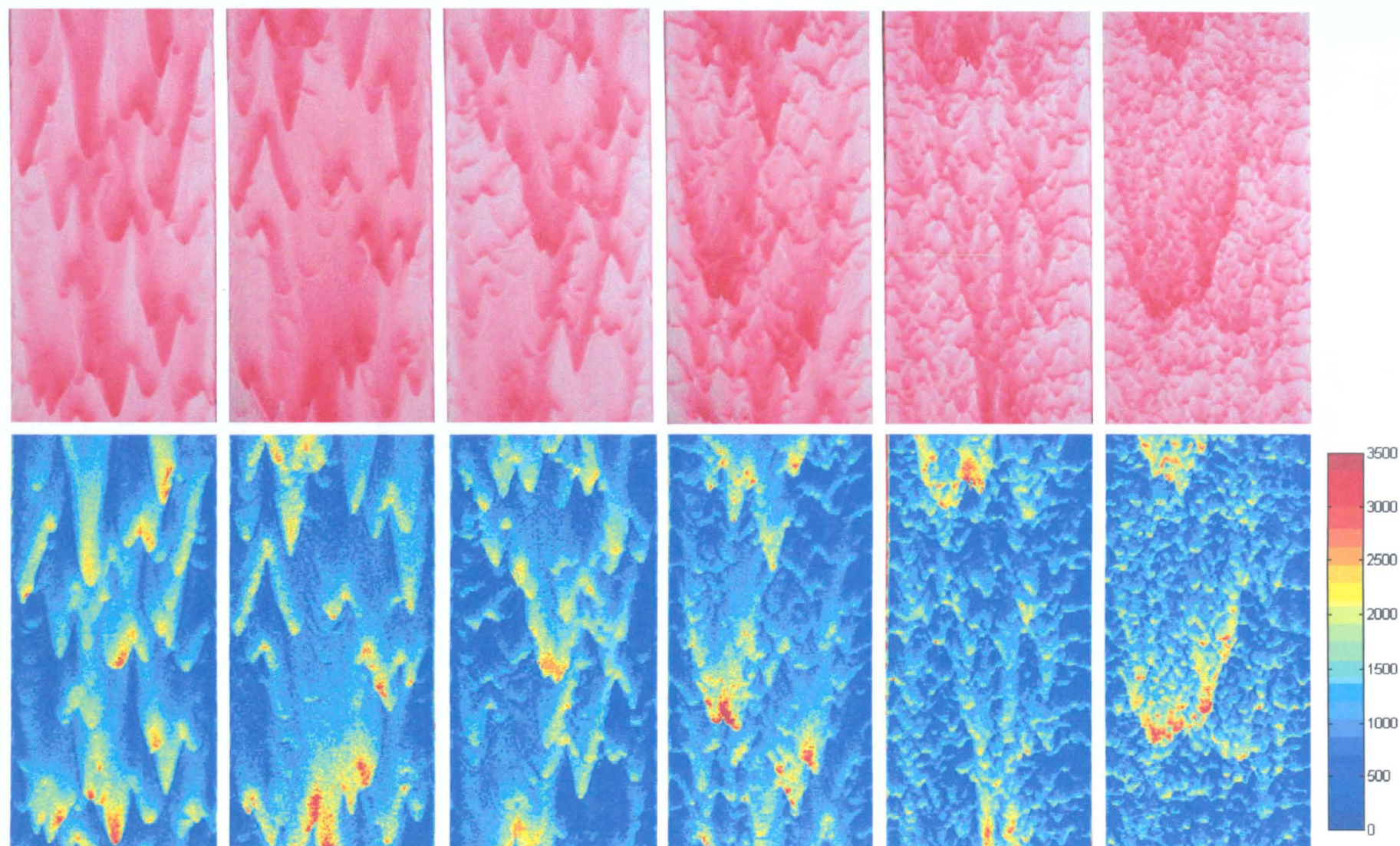


Figure 9.4 Film images and corresponding spatial film thickness maps for dodecylbenzene falling films at constant liquid flowrate (0.52 kg/m s) with an increasing co-current downflow of air (left to right). Air flowrates 0, 5.2, 7.3, 9.7, 12.2 & 14.7 m/s. Legend in microns.

9.2.2 Flow Visualisation

As with the water data, the application of a rectangular test geometry and photographic nature of the film thickness technique employed provided an excellent opportunity to visualise the physical structure of the dodecylbenzene film interface. The flow structures obtained for the air-dodecylbenzene two-phase system over the range of flow conditions of this study are summarised with the aid of Figures 9.1 to 9.4. These figures present sample film images at specific flow conditions to illustrate the dramatic influence of air and liquid flowrates on interfacial structure. The film images are presented with their corresponding spatial film thickness map to permit quantitative visualisation of the interface dimensions. The spatial maps were generated utilising commercial software (MATLAB) directly from the spatial film thickness data obtained from each image. Liquid flowrates are presented in terms of Γ , the flowrate per wetted perimeter (kg/m s), to simplify comparison of the spatial images with their corresponding spatial images for water and ethoxylated alcohol films.

Figure 9.1 illustrates the influence of liquid flowrate on the interfacial structure of free falling dodecylbenzene films. In a similar manner to the water films visualised in Chapter 8, as the liquid flowrate is progressively increased the base substrate film becomes thicker, and the disturbance waves become taller, volumetrically larger and less frequent. This observation is substantiated by plots of the film thickness profiles of a centrally located strip of each of the six images, presented in Figure 9.5. Figure 9.5 shows the profile of typical free falling dodecylbenzene disturbance waves to be similar to water based disturbances, comprising of a steep wave front with a gentler trailing edge. Therefore, it is reasonable to consider these wave types to be analogous to the 'gravity' type disturbance waves discussed in the previous chapter.

Figures 9.2 and 9.3 illustrate the influence of liquid flowrate on the interfacial structure of falling films in the presence of a co-current downflow of air (7.3 and 14.7 m/s, respectively).

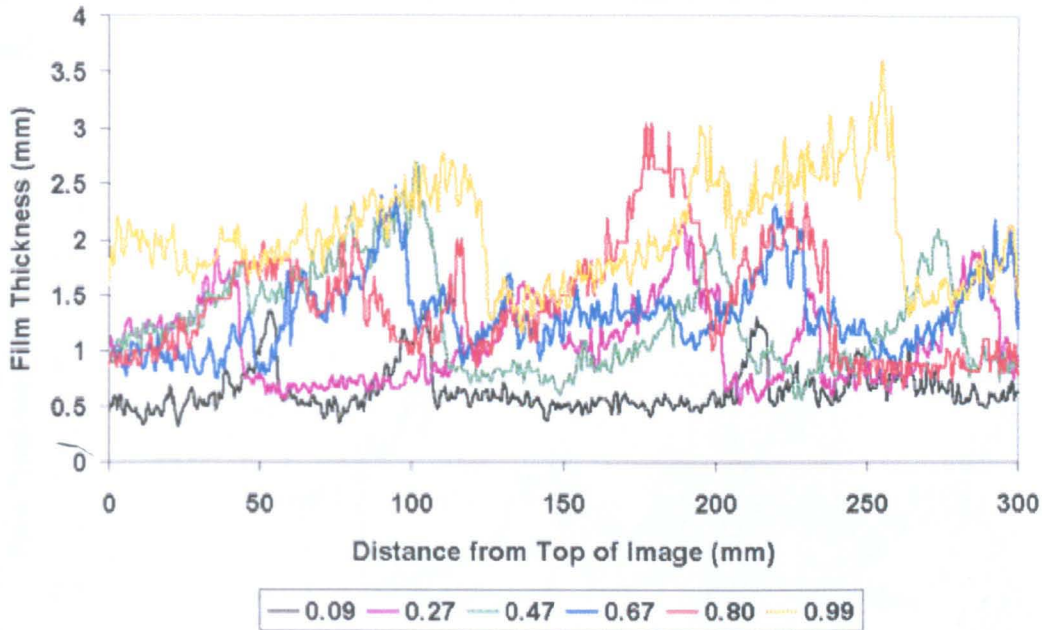


Figure 9.5: Film thickness profiles for a centrally located strip of the free falling images in Figure 9.1. Legend in kg/m s .

Figure 9.2 demonstrates that the addition of a relatively low flowrate of air does indeed have a considerable influence on the physical structure of the interface. Comparison of the interfacial characteristics of the very largest flow structures in Figures 9.1 and 9.2 suggests that for a number of these structures there is a slight increase in wave height and acuteness of the trailing wave edge associated with the addition of a dynamic airflow. This partial change in large wave shape is easier to visualise when a comparison is made of the film thickness profiles of the images in Figure 9.2, presented in Figure 9.6, with their free falling counterparts in Figure 9.5. This suggests to this author that these differences in wave shape are analogous to the transition of the interface from ‘gravity’ to ‘regular’ wave type disturbances encountered in water films at similar flow conditions.

However, Figure 9.2 also demonstrates the development of a new type of small wave on the interface; a shorter, volumetrically smaller wave with steep leading and trailing edges. This new wave structure is particularly evident at lower liquid loads, where it can be seen to be a natural development in wave structure on the free falling waves by the interaction of the dynamic airflow (compare 0.09kg/m s wave profiles in Figures 9.5 & 9.6). Interestingly, these small wave structures can also be seen to co-exist with the larger disturbances at higher liquid loads. Visual observation of these waves within the test

section showed them to be slower than, and virtually independent of, the larger disturbances.

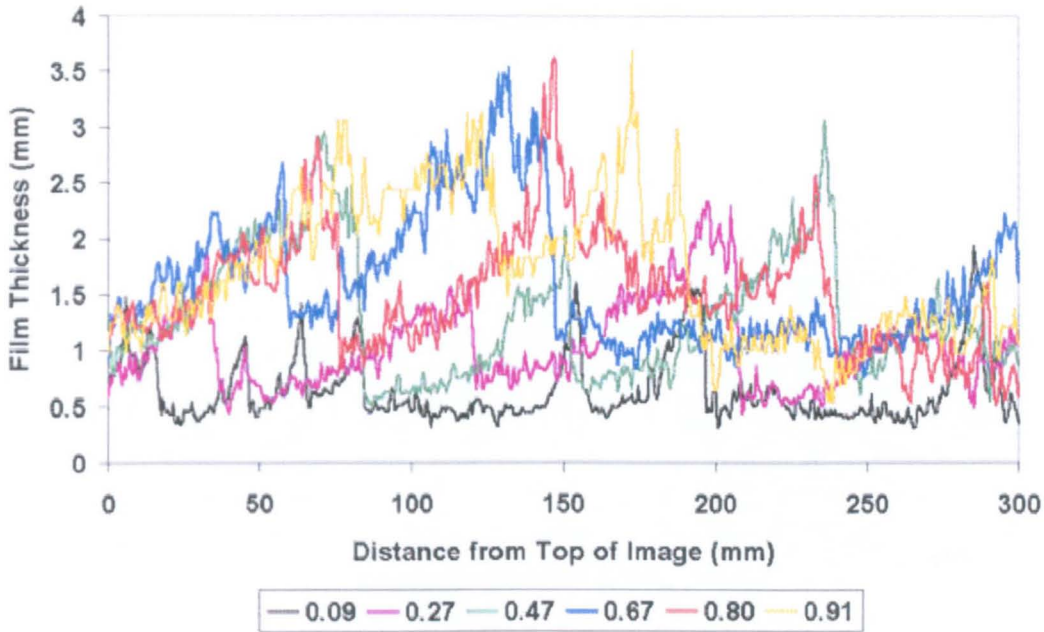


Figure 9.6: Film thickness profiles for a centrally located strip of the falling film images in Figure 9.2. Legend in kg/m s.

Figure 9.3 demonstrates the domination of the dodecylbenzene film interface, at the higher end of the air flowrates investigated, by a further development in the smaller wave structures discussed in the previous paragraph. Under these flow conditions the waves expanded horizontally, to cover virtually the entire width of the test section, and form a ‘ripple’ like disturbance structure. The increase in the frequency and periodicity of these rippled structures is clearly evident from the images. Figure 9.7, the wave profiles of centrally located strips for a selection of the images in Figure 9.3, illustrates the profile of these small waves and also demonstrates how liquid flowrate appears to have little effect on their height and shape.

At the higher liquid flowrates, where this wave structure cannot support all of the liquid flow, a further type of disturbance structure is also present. These disturbance structures exhibit the less ordered shape, with multiple peaks, and steep wave edges that are associated with the ‘regular’ type wave structures observed in water films at similar flow conditions. Visual observation of the interfacial flow structure within the test section at

these higher liquid flowrates revealed that the faster moving ‘regular’ type waves sweep through the smaller ripple structures, leaving a disturbed wake which gradually reforms into the original ripple structure.

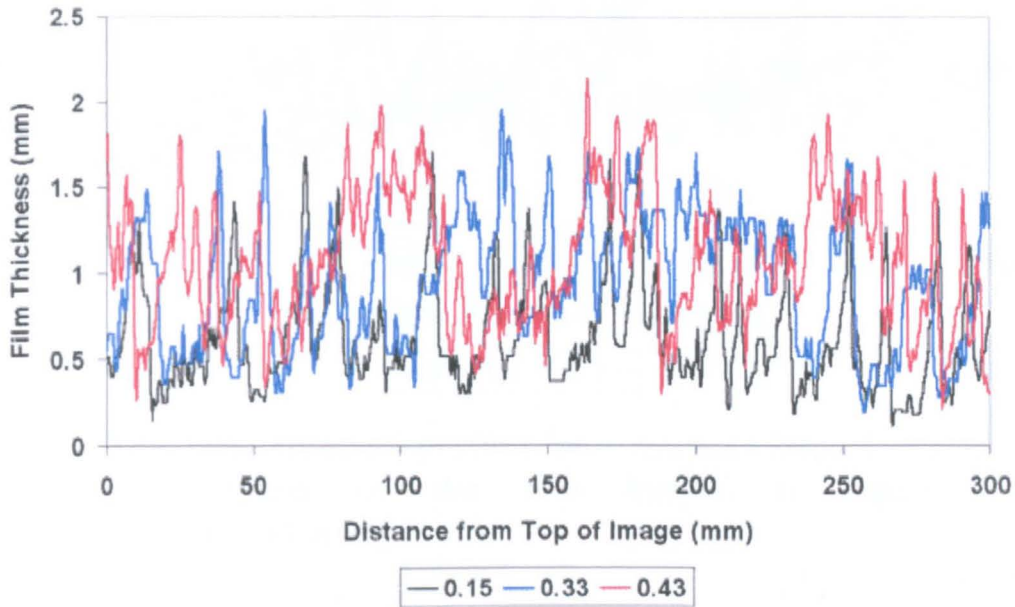


Figure 9.7: Film thickness profiles for a centrally located strip of a selection of the falling film images in Figure 9.3. Legend in kg/m s.

As with water films, it is clear that the influence of a dynamic air stream on film interfacial structure is dramatic. Figure 9.4, and a selection of the corresponding film thickness profiles from this figure (Figure 9.8), are provided to further demonstrate the transition between the interfacial wave structures described above by considering the effects of an increasing dynamic airflow on a constant liquid flowrate. It is clear from Figure 9.4 that the transition between gravity and ‘regular’ disturbance wave structures occurs somewhere near the ten metres per second air flowrate region, and this corresponds closely to the transition point observed in the water films presented in Chapter 8. The development of the large, steep, often multiple peaked ‘regular’ disturbance waves after this transition region is illustrated in the corresponding film thickness profile of Figure 9.8. Figure 9.8 also suggests there is continued compression of the base substrate film as the air velocity is further increased.

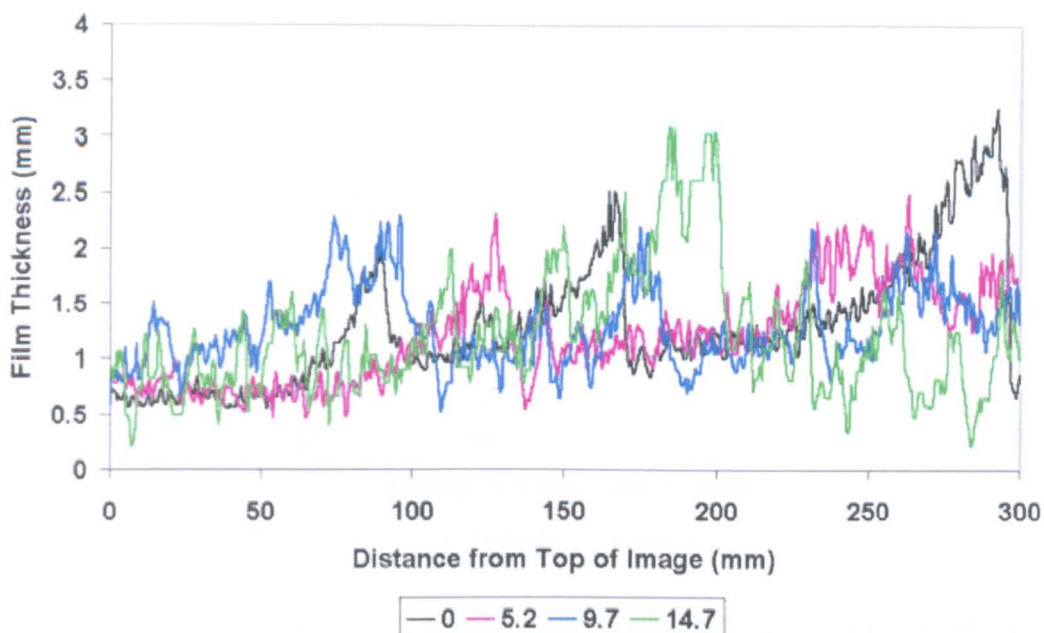


Figure 9.8: Film thickness profiles for a centrally located strip of a selection of the film images in Figure 9.4. Legend in m/s.

9.2.3 Mean Film Thickness

The mean thickness of the film is calculated from averaging the thickness values over the entire spatial measurement region.

9.2.3.1 Free Falling Films

Figure 9.9 presents a comparison of the mean film thickness values obtained for free falling dodecylbenzene films over the range of liquid flowrates investigated with the prediction of Nusselt (1916) defined in Equation 8.3. It illustrates the generally close agreement between the current data and Nusselt. It is evident from the figure that Nusselt gives a slight over-prediction for Reynolds values less than about one hundred. Above this value the current data suggests the reverse is true, with Nusselt under-predicting with increasing error as the liquid film Reynolds number is increased. This is identical to the trend observed in water films (see Figure 8.9). However, for water films the crossover region was observed around a Reynolds value of four hundred. Interestingly, if volumetric flow is considered rather than liquid film Reynolds number, there is much closer agreement on the crossover point.

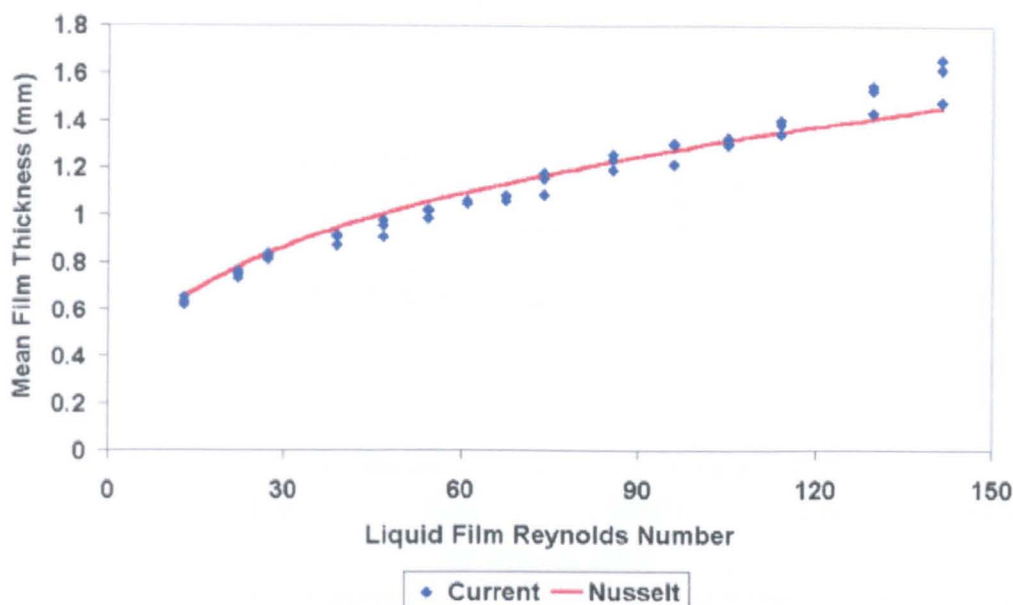


Figure 9.9: Comparison of mean film thickness values obtained for free falling dodecylbenzene films over the range of liquid flowrates investigated with the prediction of Nusselt (1916).

9.2.3.2 Falling Films with a Co-current Airflow

The influence of a co-current airflow on the mean dodecylbenzene film thickness is presented in Figure 9.10.

As would be expected, Figure 9.10 shows a steady increase in mean film thickness being associated with increases in liquid flowrate, with the mean film thickness increasing almost two and a half times over the range of liquid flows investigated. The figure also illustrates the slight reduction in mean film thickness associated with an increasing airflow that can be attributed to the overall acceleration of the film. It is interesting to note that where the disturbance wave shape transition is visually observed to begin ($\sim 5 - 7.5\text{m/s}$, see Figure 9.4), and in particular the onset of the development of the small amplitude 'ripple' like disturbances, at several of the liquid flowrates investigated the largest single drop in mean film thickness is recorded. With the limited data above the transition region, the figure suggests that mean film thickness remains virtually constant or even possibly rises at the lower liquid flowrates. A possible explanation for this trend at the lower liquid flowrates must be the domination of the interface by the small, slower moving rippled disturbances.

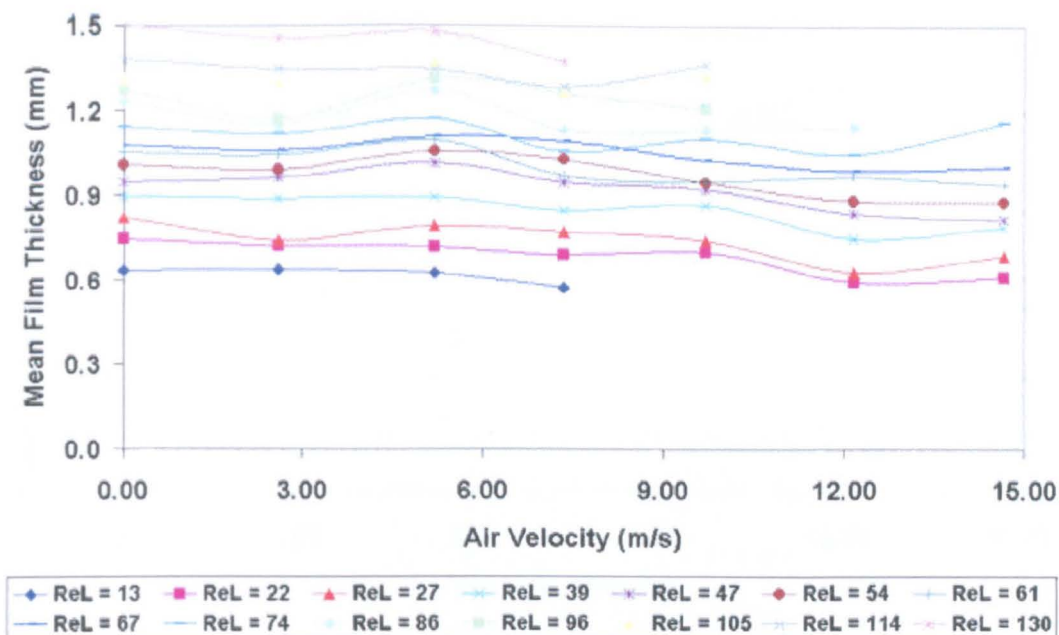


Figure 9.10: Influence of co-current airflow on mean dodecylbenzene film thickness.

9.2.4 Disturbance Wave Characteristics

The characterisation of the interface into disturbance wave and substrate film regions by the approach detailed in Chapter 5 allows the characteristics of the disturbance wave to be studied independently.

9.2.4.1 Mean Disturbance Wave Amplitude

The influence of flow conditions on the mean dodecylbenzene disturbance wave amplitude is presented in Figure 9.11. The mean disturbance wave amplitude was given by:

$$h_{\max} = \left(\frac{h_{\min} + h'_{\min}}{2} \right) \quad (9.1)$$

where, h_{\max} is the mean maximum height of the disturbance waves, h_{\min} is the mean minimum height at the front of the disturbance waves and h'_{\min} is the mean minimum height at the back of the disturbance waves.

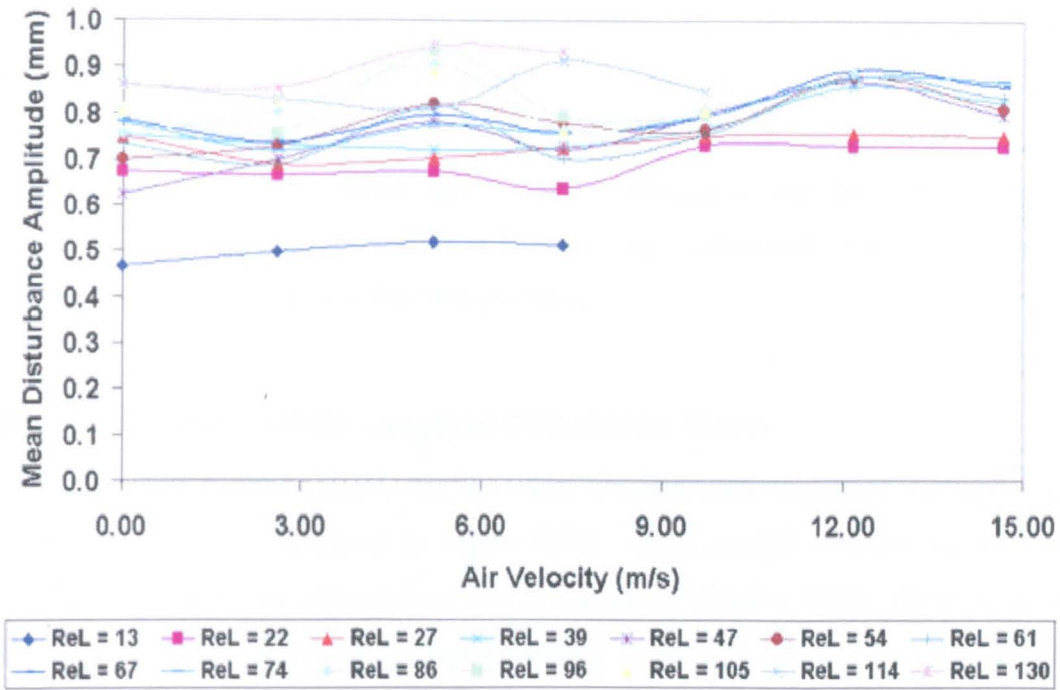


Figure 9.11: Influence of flow conditions on mean dodecylbenzene disturbance wave amplitude.

At air flowrates below the observed onset of wave structure transition (0-5 m/s), Figure 9.11 highlights a relatively clear relationship between increases in liquid loading and increases in the mean amplitude of dodecylbenzene ‘gravity’ type disturbance wave structures. At the higher air flowrates investigated, where the transition to ‘ripple’ and ‘regular’ type disturbance wave structures appears complete, the data appears to cluster into two distinct groupings. This is certainly related to the calculation method of this parameter; with the disturbance amplitude value plotted being a mean amplitude value for all disturbances on the interface. This results in the large number of small developed and semi-developed disturbance ripples that are particularly evident at these flow conditions, dominating the calculation of the mean amplitude value. Therefore, the clustering of the data into two groups at the higher air flowrates would be a result of the data being split between liquid films with and without large ‘regular’ disturbance waves present (see Figure 9.3).

A further point worth discussing from the figure is the data representing the lowest liquid film Reynolds number presented ($Re_L=13$) which is substantially lower than the rest of the recorded data. This implies that the disturbance structures at this flow

condition have significantly lower amplitudes, and this is confirmed by visual observation (see extreme left hand image and spatial map in Figure 9.1). A possible explanation for this disparity is that the disturbance structures at this relatively low liquid film Reynolds number are not fully developed ‘gravity’ wave structures, but pre-cursor structures developed during the transition from a laminar film. Obviously, further investigation would be necessary to confirm this interpretation.

9.2.4.2 Mean Characteristic Length of Disturbance Waves

The influence of flow conditions on the mean characteristic length of dodecylbenzene disturbance waves is presented in Figure 9.12. In a similar manner to the trends observed for the mean disturbance wave amplitude (Figure 9.11), there is a clear relationship between increases in liquid loading leading to steady increases in mean characteristic length of the disturbance waves at air flowrates below the wave structure transition region (with a two and a half fold increase over the flowrates investigated); and above the transition region the data appears to also cluster into two groupings with the same flowrate split.

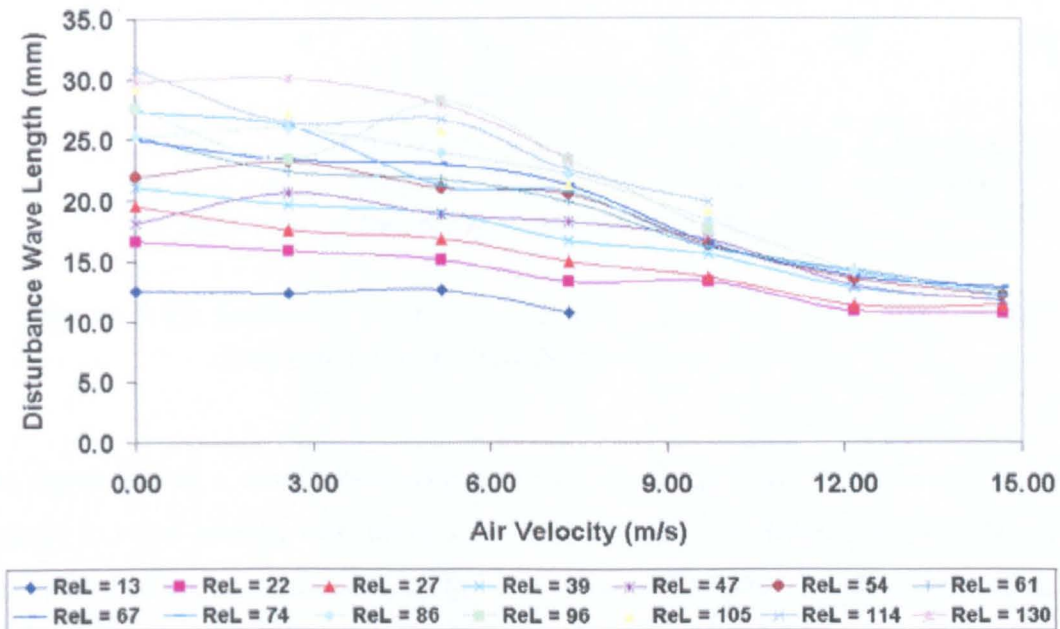


Figure 9.12: Influence of flow conditions on the mean characteristic length of dodecylbenzene disturbance waves.

Where Figures 9.12 and 9.11 differ is that in Figure 9.12 there is also a clear relationship between air flowrate and characteristic length, with the mean length value being reduced by twenty percent at low liquid flows and over fifty percent in the case of the higher liquid flows as the ‘gravity’ type disturbance structures are transformed in ‘regular’ and ‘ripple’ type disturbance structures.

9.2.4.3 Disturbance Wave Celerity

The influence of flow conditions on the mean dodecylbenzene disturbance wave celerity is presented in Figure 9.13.

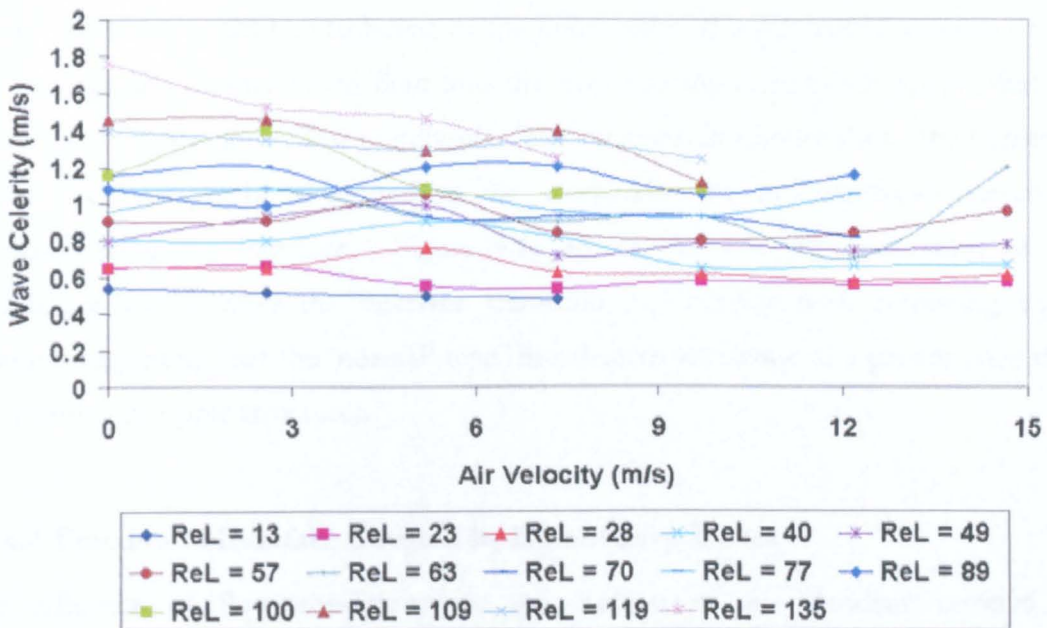


Figure 9.13: Influence of co-current airflow on the mean dodecylbenzene disturbance wave celerity.

The figure shows a clear relationship between increasing liquid flowrate and a steady increase in wave celerity, with up to a two and half fold increase in celerity values over the liquid flowrate measurement range. The effect of a co-current downflow of air on disturbance wave celerity is less clear. For the smallest dodecylbenzene flows there is little recorded effect. For the intermediate dodecylbenzene flows investigated the figure tentatively suggests that a slight increase in wave celerity can be expected up to air velocities approaching the onset of the transition of disturbance structures (~ 5m/s).

Here, the trend is reversed, with celerity values now beginning to fall, and the wave celerity appears to continue this fall until the wave shape transition is completed ($\sim 10\text{m/s}$). The limited data above this region suggests that a steady increase in wave celerity can then be expected as the air flowrate is further increased, which is consistent with the results obtained for water films (see Figure 8.17). The trend for the largest dodecylbenzene flowrates investigated is similar to the intermediate flows, however, there is no evidence to suggest any significant increases in wave celerity below the transition point.

The trends described in the paragraph above are consistent with visual observation of the changes in interfacial structure. The decreases in wave celerity during the ‘gravity’ to ‘ripple’ transition could be attributed to the conversion of a substantial portion of the ‘gravity’ type disturbance-based fluid into the slow moving disturbance ripples that are observed to form at these flow conditions. The increases in celerity above the transition region could simply be attributed to the acceleration of all disturbance structures travelling along the interface. Figure 9.13 shows the rate of acceleration of the disturbance waves, after the interface transition, to increase with increasing liquid flowrate, suggesting that the ‘normal’ type disturbances accelerate at a greater pace than the disturbance ripple structures.

9.2.4.4 Fraction of Interface Covered by Disturbance Waves

The influence of flow conditions on the fraction of the interface covered by dodecylbenzene disturbance waves is presented in Figure 9.14.

This parameter was simply determined from the ratio of the number of points categorised as disturbance region points over the total number of spatial measurement points, and as such, is a measure of the ‘roughness’ of the interface.

The influence of liquid flowrate on surface coverage of the disturbance waves appears small and proportional, with a typical increase of five percent in fractional coverage over the liquid flowrates measurement range.

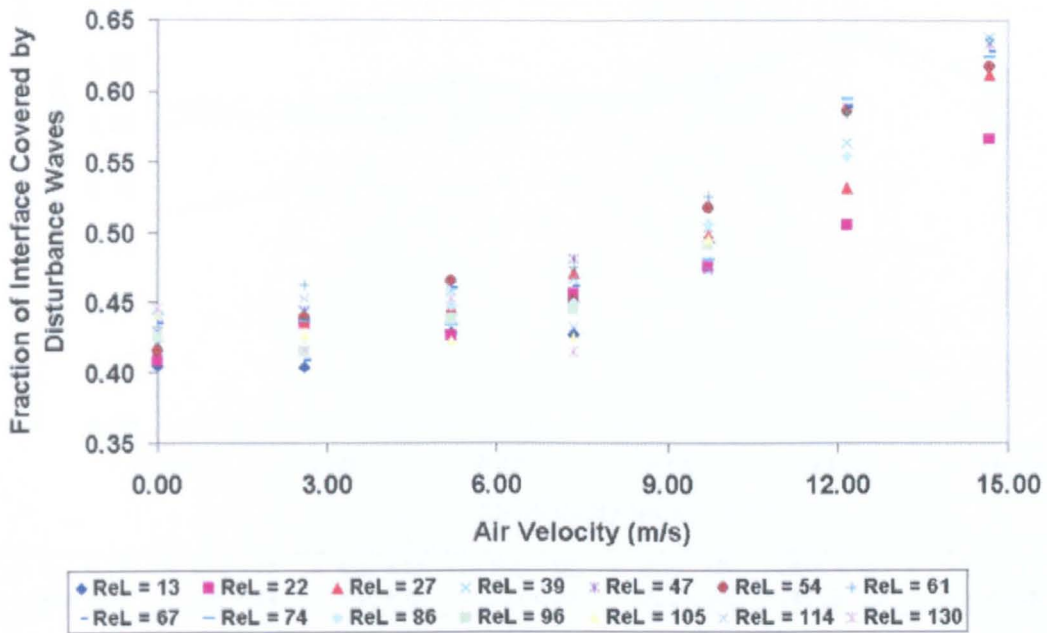


Figure 9.14: Influence of flow conditions on the fraction of the interface covered by dodecylbenzene disturbance waves.

For the influence of a dynamic co-current air flow on fractional coverage, Figure 9.14 shows that the transition between ‘gravity’ and ‘regular’ disturbance wave regimes is once more clearly marked by a change in the trend of the data. The figure suggests that below the transition region ($\sim 0\text{--}5\text{m/s}$) there is only a slight increase in interface coverage associated with increasing air flowrate. However, during and after transition the gradient of this increase in coverage becomes significantly steeper. These trends are confirmed by visual observation (see Figure 9.4), with the disturbed area of the interface growing rapidly, particularly with the onset and expansion of the disturbance ripples.

9.2.4.5 Liquid Hold-up Fraction Contained in Disturbance Waves

The influence of flow conditions on the liquid hold-up fraction of the film contained in dodecylbenzene disturbance waves is presented in Figure 9.15.

The data was obtained during the categorisation of the interface (Chapter 5) by application of Equation 5.1.

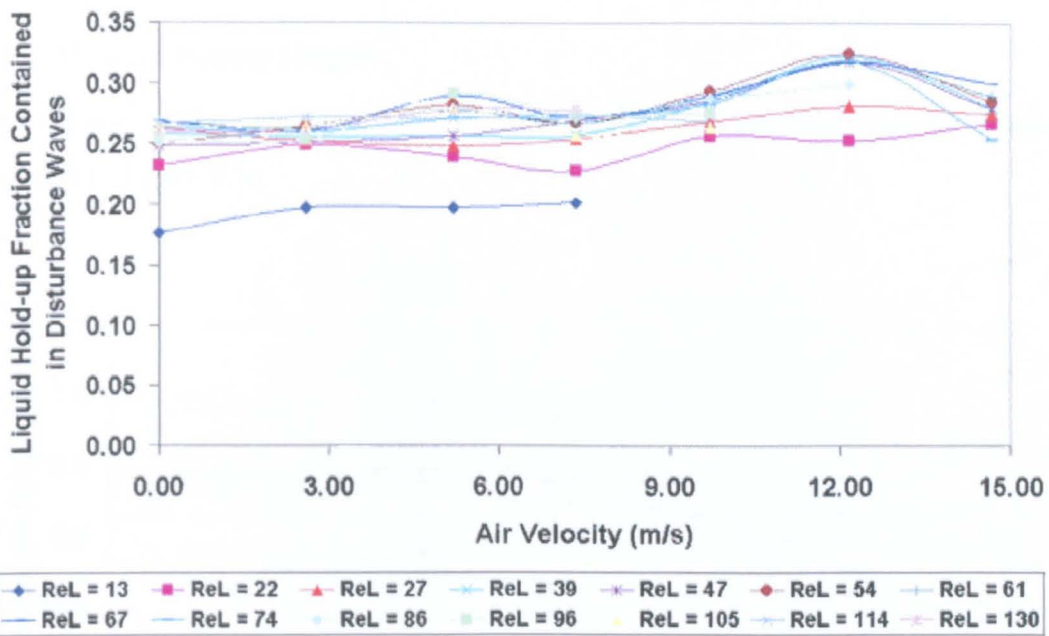


Figure 9.15: Influence of flow conditions on the liquid hold-up fraction of the film contained in dodecylbenzene disturbance waves.

The figure highlights the trend for a slight increase in hold-up fraction within the disturbance waves as air flowrate is increased. A similar trend is observed for the effect of liquid flowrate on hold-up fraction. However, significant increases in hold-up fraction appear to only occur over the lower liquid flowrates, with the values for the intermediate and higher liquid flows effectively constant. This is another example of the data being sub-divided by the presence or absence of the larger disturbance structures. The influence of the transition between wave regimes on this parameter is difficult to interpret. The significantly lower values recorded for the lowest liquid Reynolds number ($Re_L=13$) again highlights the possibility that the make-up of the interfacial structure at this flowrate is not fully consistent with the other flowrates studied.

9.2.5 Base Substrate Film Characteristics

The characterisation of the interface into disturbance wave and substrate film regions by the approach detailed in Chapter 5, allows the characteristics of the base substrate film to be studied independently.

9.2.5.1 Mean Substrate Height

The influence of flow conditions on the mean dodecylbenzene base substrate height is presented in Figure 9.16.

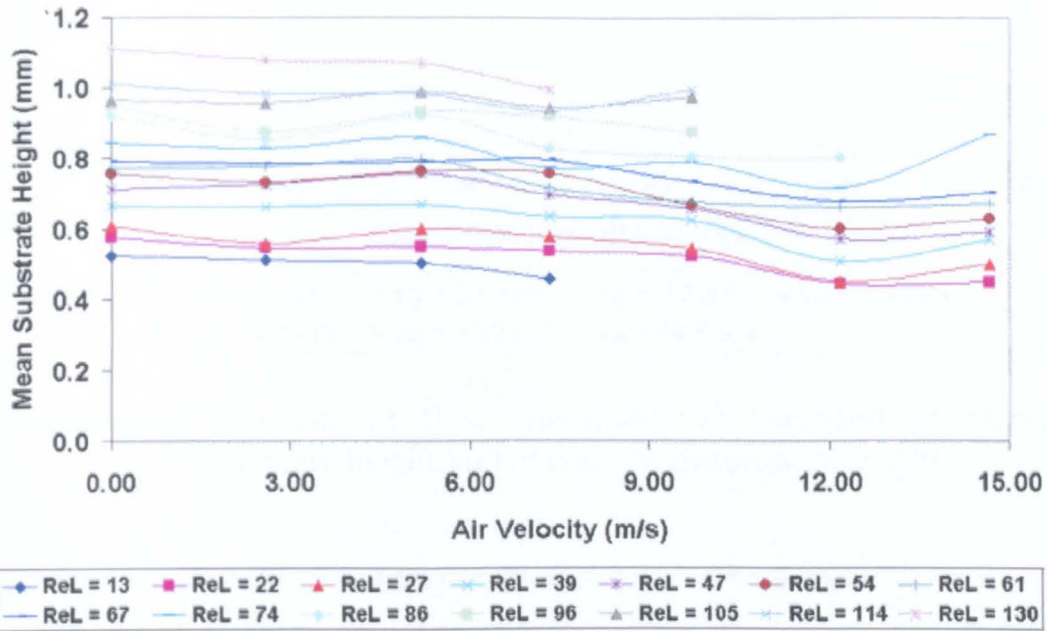


Figure 9.16: Influence of flow conditions on the mean dodecylbenzene base substrate height.

The figure demonstrates a steady increase in substrate height with increasing liquid load, with mean substrate height increasing by a factor of around two over the measurement range. The figure also demonstrates the slight compression of the substrate in the presence of a co-current flow of air. Where values are available at the highest measured air flowrate there is the suggestion that the mean base substrate film height then begins to rise. This may possibly be due to the algorithm utilised in the categorisation of the film structures being unable to distinguish between the substrate and the very smallest disturbances generated by action of the co-current airflow on the film interface.

9.2.5.2 Ratio of Mean Substrate Height and Maximum Disturbance Height

The influence of flow conditions on the ratio of mean substrate height and maximum disturbance height is presented in Figure 9.17.

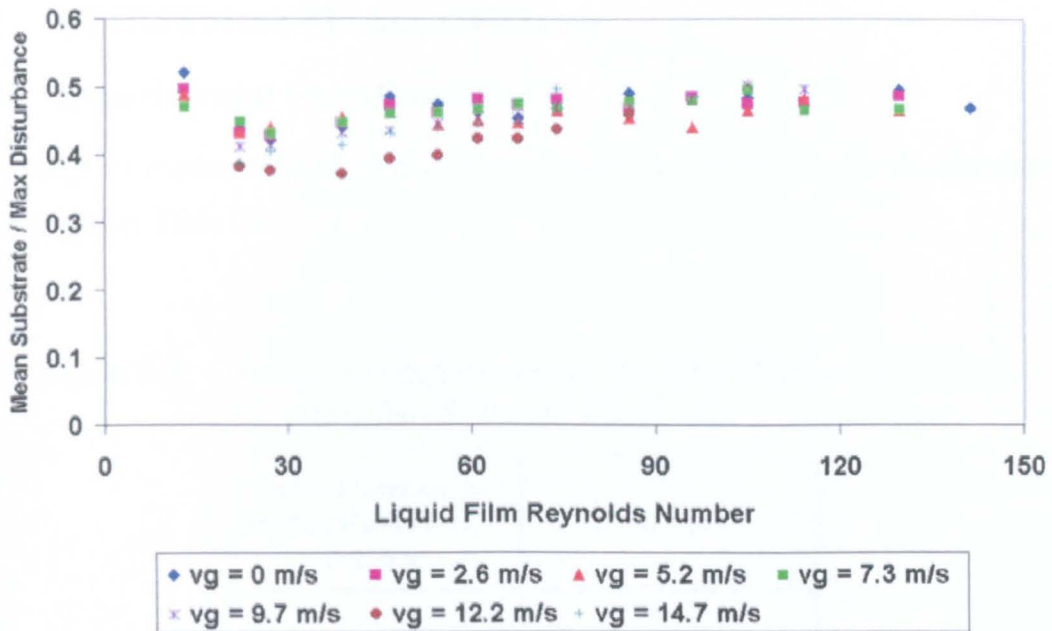


Figure: 9.17 Influence of flow conditions on the ratio of mean substrate height and maximum disturbance height.

Comparison in volumetric flow terms of this figure with the equivalent figure for water films (Figure 8.23) highlights several differences. There is no longer the clear division in trends between air flowrates above and below the wave structure transition region. This is probably due to the dampening influence on the averaged maximum disturbance height of the small amplitude disturbance ripples that are encountered in dodecylbenzene films but not present in water films at comparable flow conditions. The steady increase in the ratio with increasing liquid Reynolds number observed in water films across the entire measurement range is not repeated in Figure 9.17. The trend is replaced in Figure 9.17 by an initial drop, followed by a slight increase over a limited liquid Reynolds number range ($Re_L \sim 30-60$), before reaching a constant value at a ratio value around 0.45. In many ways the data in Figure 9.17 more closely resembles the trend of Aragaki *et al.* (1987) presented in Figure 8.22.

9.3 ETHOXYLATED ALCOHOL

9.3.1 Experimental Flow Conditions

The range of experimental flow conditions employed for ethoxylated alcohol films is summarised in Table 9.2

Table 9.2: Range of experimental flow conditions employed for ethoxylated alcohol films.

Liquid Flowrate per Wetted Perimeter, Γ (kg/m s)	0.09 - 0.76
Air Velocity (m/s)	0 - 12.5

Partial wetting of the glass viewing plate dictated the maximum air and liquid flowrates achievable. The minimum liquid flowrate studied was limited by flow measurement sensitivity and a desire to keep consistent with the flow conditions utilised in the study of water films. Difficulties associated with wetting of the viewing glass plate prevented measurement of the entire liquid flow range at the higher air velocities and vice versa. A detailed review of the experimental difficulties encountered, which gave rise to these flow limitations, is provided in Chapter 2 (Section 2.3.5). A range of thirty-six differing flow conditions produced a total of one hundred and eight spatial images that were subsequently converted into spatial film thickness measurements. Forty-two similar flow conditions were utilised in disturbance wave celerity measurements.

As with the other liquids studied, it was considered not feasible or practical to present every possible parameter evaluated in this study to describe the interfacial characteristics of these films, therefore, it is hoped that the selection of results displayed in this section will provide both visual and quantitative insight into the influence of air and liquid flow conditions on the interfacial characteristics of ethoxylated alcohol films.

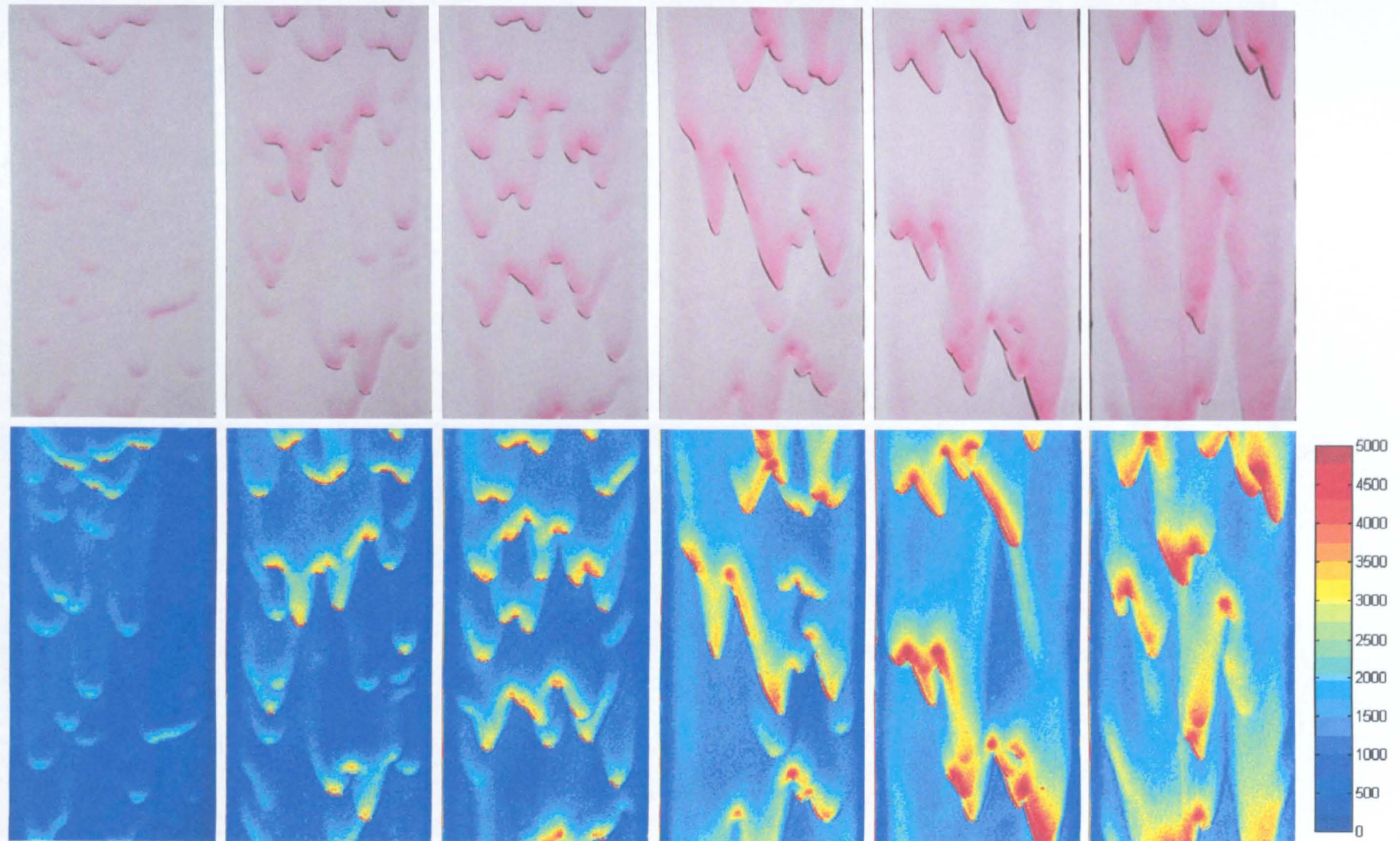


Figure 9.18: Film images and corresponding spatial film thickness maps for free falling ethoxylated alcohol films with increasing liquid flowrate (left to right). Liquid flowrates 0.09, 0.20, 0.28, 0.49, 0.62 & 0.76 kg/m s. Legend in microns.

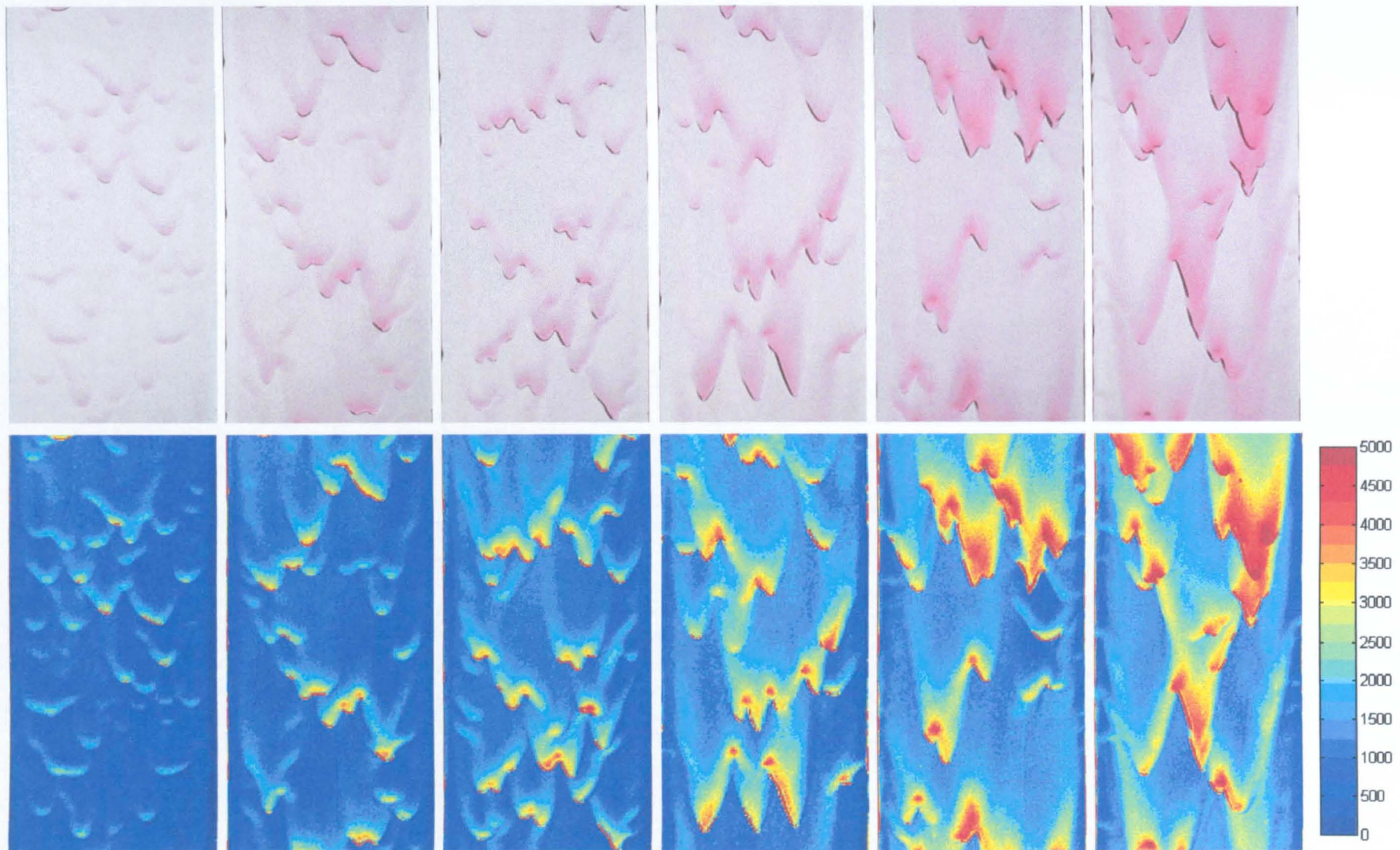


Figure 9.19: Film images and corresponding spatial film thickness maps for co-current air-ethoxylated alcohol downflow at constant air velocity (4.9 m/s) with increasing liquid flowrate (left to right). Liquid flowrates 0.09, 0.20, 0.28, 0.49, 0.62 & 0.76 kg/m s. Legend in microns.

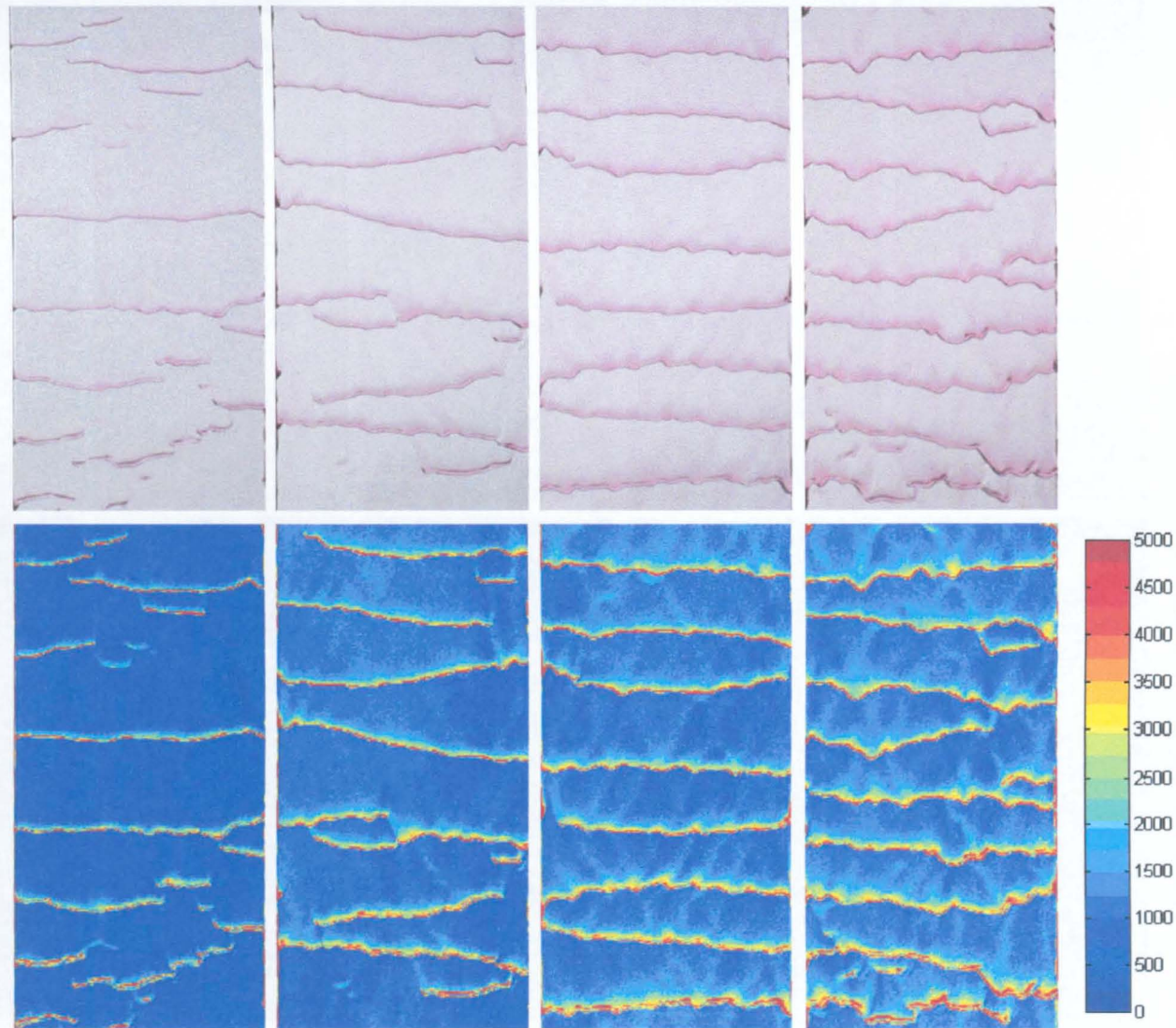


Figure 9.20: Film images and corresponding spatial film thickness maps for co-current air-ethoxylated alcohol downflow at constant air velocity (10.0 m/s) with increasing liquid flowrate (left to right). Liquid flowrates 0.09, 0.16, 0.20, & 0.28 kg/m s. Legend in microns.

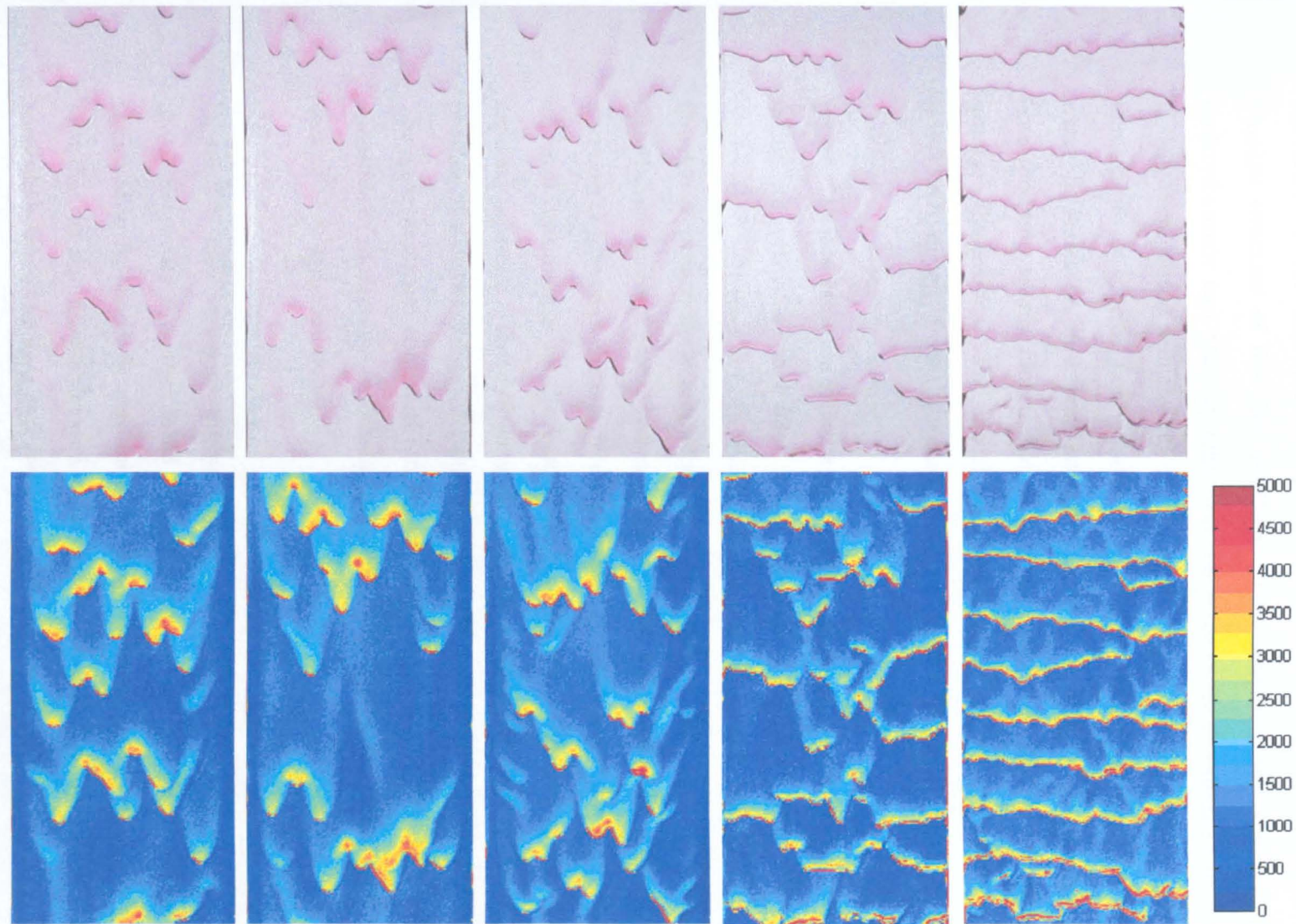


Figure 9.21: Film images and corresponding spatial film thickness maps for ethoxylated alcohol falling films at constant liquid flowrate (0.28 kg/m s) with an increasing co-current downflow of air (left to right). Air flowrates 0, 2.6, 4.9, 7.4 & 10.0 m/s. Legend in microns.

9.3.2 Flow Visualisation

Once again, the application of a rectangular test geometry and photographic nature of the film thickness technique employed provided an excellent opportunity to visualise the physical structure of the film interface. The flow structures obtained for the air-dodecylbenzene two-phase system, over the range of flow conditions of this study, are visually summarised with the aid of Figures 9.18 to 9.22. These figures present sample film images at specific flow conditions to illustrate the dramatic influence of air and water flowrates on interfacial structure. The film images are presented with their corresponding spatial film thickness map to permit quantitative visualisation of the interface dimensions. The spatial maps were generated utilising commercial software (MATLAB) directly from the spatial film thickness data obtained from each image.

Figure 9.18 illustrates the influence of liquid flowrate on the interfacial structure of free falling ethoxylated alcohol films. It is clear from the figure that a similar trend is observed to that seen in both water and dodecylbenzene free falling films, *i.e.* as liquid flowrate is progressively increased the base substrate film becomes thicker, and the disturbance waves become taller, volumetrically larger and less frequent. Another noteworthy feature of the interface highlighted by this figure is the almost complete lack of small disturbances on the base substrate, creating a mirror like smoothness to the exposed substrate. These observations are substantiated by plots of the film thickness profiles of a centrally located strip of each of the six images, presented in Figure 9.22. The wave structures consist of the steep wave fronts with a gentler trailing edge that are indicative of the 'gravity' type disturbances encountered for the other liquids of this study under free falling conditions.

Figure 9.22 also highlights the particular difficulties experienced in obtaining reliable wave shape data for ethoxylated alcohol films, as the total light exclusion problems discussed in Appendix B were most frequently observed under this flow regime. It is clear that the algorithm developed to combat this problem was not successful in all cases, particularly when the light excluded region was greater than one pixel thick, leaving the leading edge of some of the waves distorted.

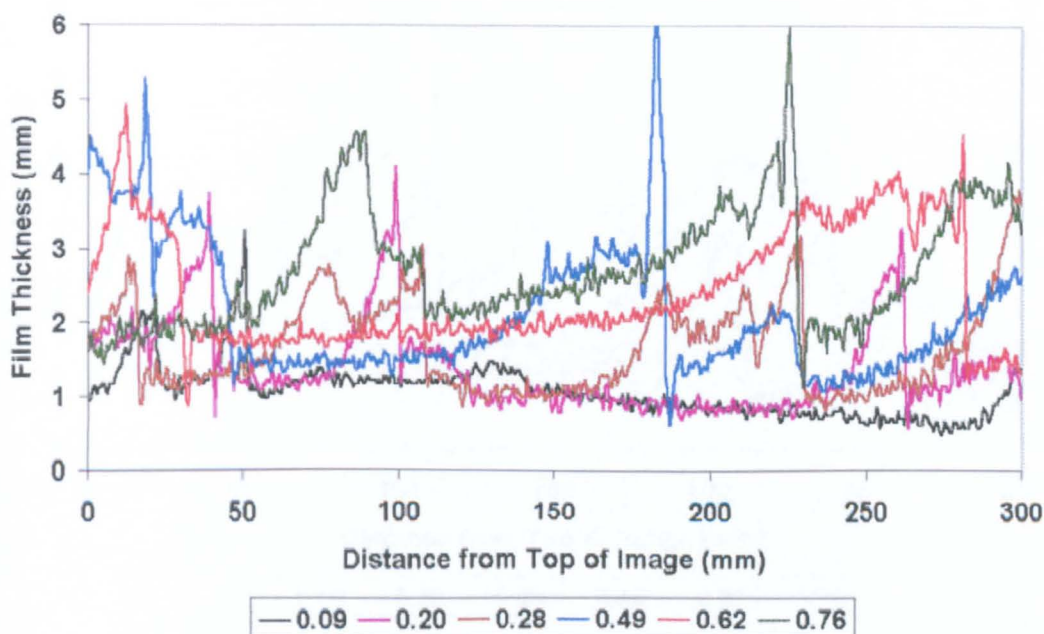


Figure 9.22: Film thickness profiles for a centrally located strip of the free falling images in Figure 9.18.
Legend in kg/m s.

Figures 9.19 and 9.20 illustrate the influence of liquid flowrate on the interfacial structure of ethoxylated alcohol falling films in the presence of a co-current downflow of air (4.9 and 10.0 m/s, respectively). Visual comparison of the co-current flow in Figure 9.19 with the free falling films at identical flow conditions in Figure 9.18, suggests that the action of the co-current downflow of air has little influence on the physical structure of the interface. However, examination of typical film thickness profiles for the images in Figure 9.19, presented in Figure 9.23, indicates that some shortening of the wave trailing edge has been experienced.

Figure 9.20 demonstrates the complete transformation of the interface that finishes close to the highest air flowrates that could be investigated. All liquid flows showed the transition of the large chaotic disturbance wave structures into thin, ripple like disturbances that spanned the entire test section width. These ripples are clearly analogous to the disturbance ripples encountered for dodecylbenzene films at similar flow conditions; however, the ethoxylated alcohol ripples are more coherent and have much larger amplitudes. The structure of these rippled disturbance waves can be more clearly seen through examination of some typical film thickness profiles of the spatial images presented in Figure 9.24.

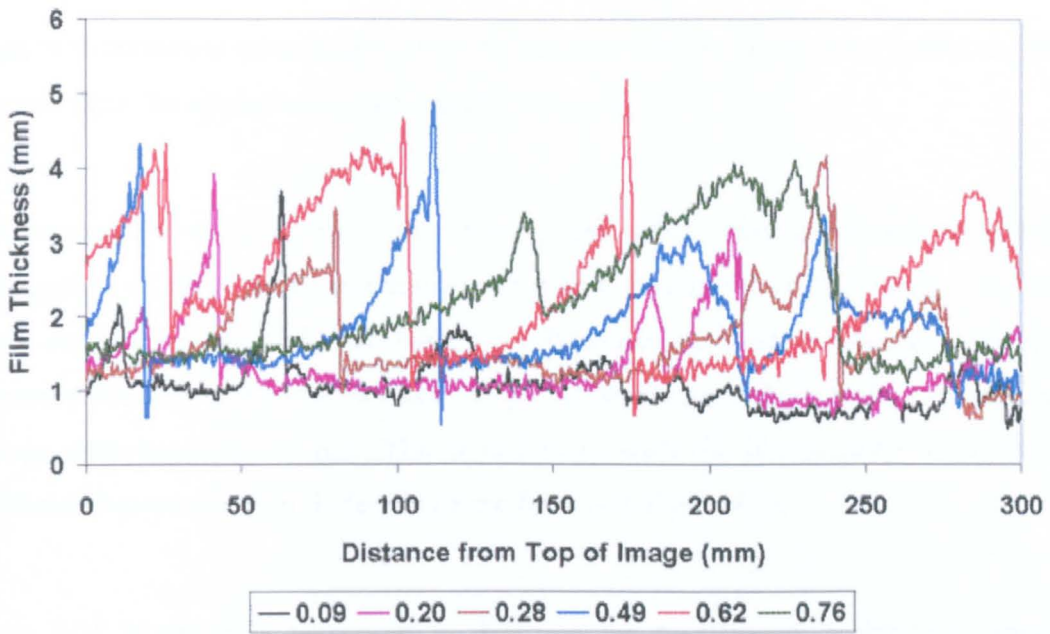


Figure 9.23: Film thickness profiles for a centrally located strip of the falling film images in Figure 9.19. Legend in kg/m s

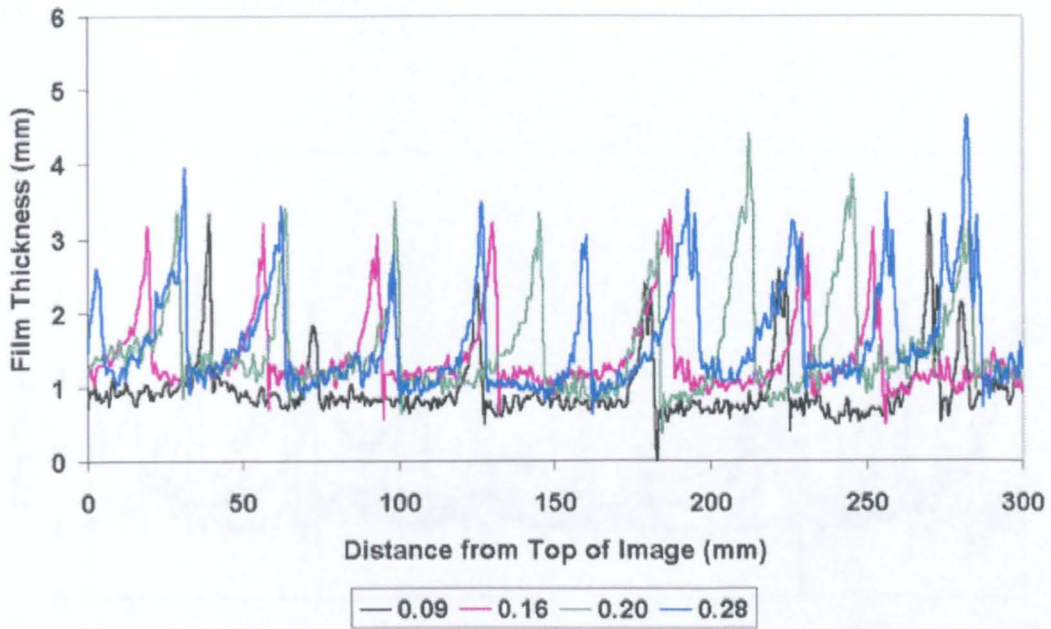


Figure 9.24: Film thickness profiles for a centrally located strip of the film images in Figure 9.20. Legend in kg/m s.

Figure 9.24 illustrates that there is some wave growth associated with increasing liquid loading. Although the ripple amplitudes appear relatively constant over the measurement

range, with increased wave height offset by increased height of the base substrate, there are clear signs the ripples are volumetrically 'fatted'.

Unfortunately, severe wetting of the viewing test section plate prevented quantitative investigation of these ripple phenomena at higher liquid and air flowrates. However, visual observation showed that higher air flowrates resulted in increases in ripple frequency and higher liquid flows saw the partial break-up of these ripples by the onset of large disturbance structures. This is consistent with the observations made for the interfacial characteristics in dodecylbenzene films (see Figure 9.3).

Figure 9.21 is primarily presented to illustrate the mechanism behind the dramatic changes in interfacial structure associated with the action of a co-current downflow of air on the film. The figure shows that the development of the ripple structures from the 'gravity' type disturbances is simply a gradual re-distribution of the fluid on the interface, which can also be observed by examination of typical film thickness profiles for the images, presented in Figure 9.25.

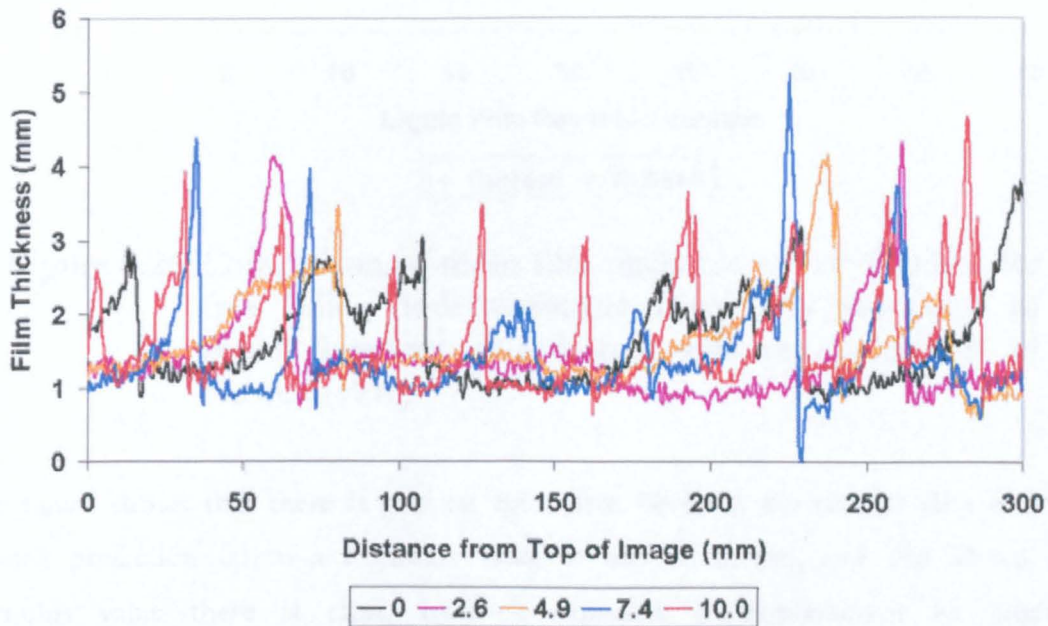


Figure 9.25: Film thickness profiles for a centrally located strip of the film images in Figure 8.4. Legend in m/s.

9.3.3 Mean Film Thickness

As stated previously, the mean film thickness is simply calculated from averaging the thickness values over the entire spatial measurement region.

9.3.3.1 Free Falling Films

Figure 9.26 presents a comparison of the mean film thickness values obtained for free falling ethoxylated alcohol films over the range of liquid flowrates investigated with the prediction of Nusselt (1916) defined in Equation 8.3.

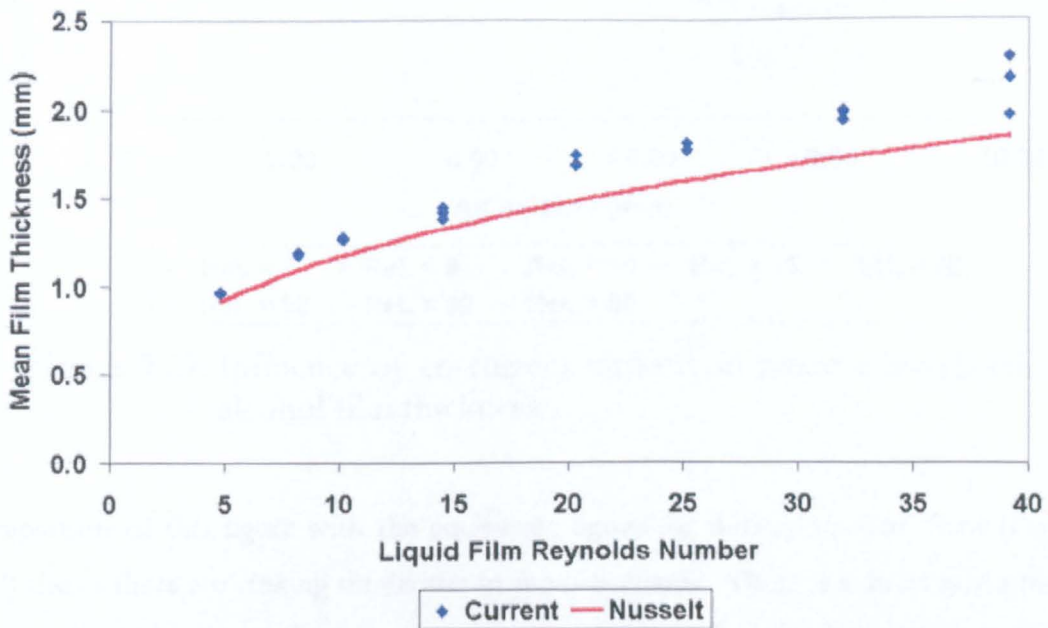


Figure 9.26: Comparison of mean film thickness values obtained for free falling dodecylbenzene films over the range of liquid flowrates investigated with the prediction of Nusselt (1916).

The figure shows that there is a close agreement between the current data and the Nusselt prediction up to a Reynolds value of around fifteen, and that above this Reynolds value there is clear, relatively constant under-prediction by Nusselt. Interestingly, this change in trend occurs, in volumetric flow terms, close to the crossover point identified in both water and dodecylbenzene free falling films.

9.3.3.2 Falling Films with a Co-current Airflow

The influence of a co-current airflow on the mean ethoxylated alcohol film thickness is presented in Figure 9.27.

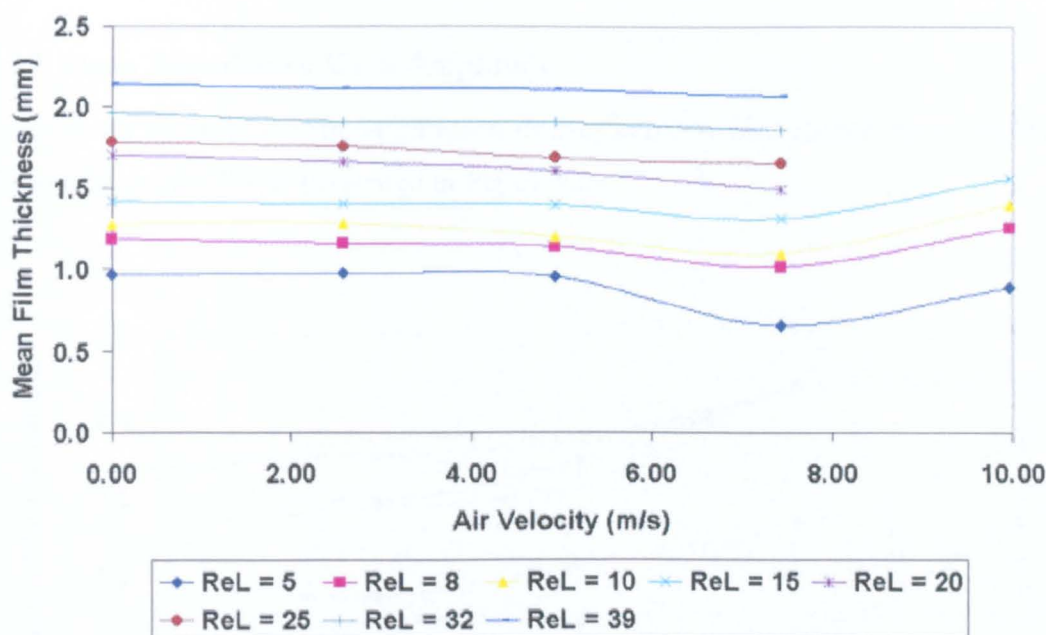


Figure 9.27: Influence of co-current airflow on mean ethoxylated alcohol film thickness.

Comparison of this figure with the equivalent figure for dodecylbenzene films (Figure 9.10) shows there are striking similarities in the data trends. There is a direct relationship between liquid loading and mean thickness once more, with over a two fold increase in mean film thickness recorded over the liquid flowrate measurement range. Examination of the influence of dynamic co-current airflows highlights again a steady drop in mean film thickness that marks the onset of the transition of the disturbance region into the disturbance ripple structures. The drop is most pronounced in the data for the lowest Reynolds number, and this is probably a result of the volumetric significance of the ripple structures at lower liquid flowrates. The drop is followed by a rise in mean thickness value at air flowrates where the transformation visually appears to have been completed (see Figure 9.20). However, the drop in value appears to occur at slightly a lower air flowrate value for ethoxylated alcohol films, which suggests the transition in disturbance wave structures begins earlier in ethoxylated alcohol films.

9.3.4 Disturbance Wave Characteristics

The characterisation of the interface into disturbance wave and substrate film regions by the approach detailed in Chapter 5 allows the characteristics of the ethoxylated alcohol disturbance waves to be studied independently.

9.3.4.1 Mean Disturbance Wave Amplitude

The influence of flow conditions on mean dodecylbenzene disturbance wave amplitude, defined in Equation 9.1, is presented in Figure 9.28.

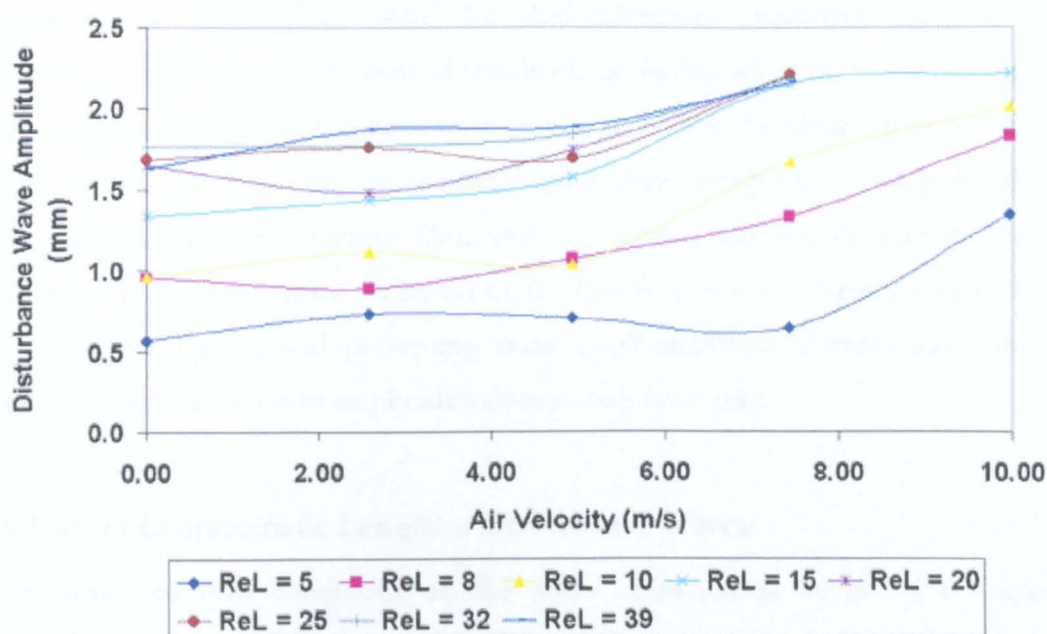


Figure 9.28: Influence of co-current airflow on mean ethoxylated alcohol disturbance wave amplitude.

Figure 9.28 once more highlights a clear relationship between liquid loading and mean disturbance wave amplitude, with over a threefold increase in wave amplitude recorded over the liquid flowrate measurement range. However, clustering of the data at the higher liquid Reynolds numbers suggests the relationship is not a proportional one, with the majority of wave amplitude growth occurring over the lower liquid film Reynolds numbers.

For the relationship between air flowrate and mean amplitude, the available data suggests that the onset of the wave structure transition results in a rapid increase in disturbance wave amplitude, and is consistent with the observations recorded for dodecylbenzene films. It must be noted that the rapid increase in mean amplitude values is not a result of the disturbance ripples being significantly higher than the 'gravity' structures they are formed from, as this is patently untrue, but a result of the two-dimensional wave structure of the ripples. Where the algorithm utilised identifies that 'gravity' structures have a range of maximum values along their horizontal width, it identifies a virtually constant maximum height along the horizontal width of the disturbance ripple structures.

Comparison of Figure 9.28 with the dodecylbenzene equivalent (Figure 9.11) demonstrates that although the general trends of the figures are similar, the influence of flow conditions on mean disturbance wave amplitude is more pronounced in ethoxylated alcohol films. This more pronounced relationship must surely be at least partly due to the smoothness of the substrate film, with the virtual absence of minor interface disturbances making the characterisation of the interface into substrate and disturbance regions less ambiguous, and preventing these small amplitude disturbances having a significant influence on mean amplitude values during averaging.

9.3.4.2 Mean Characteristic Length of Disturbance Waves

The influence of flow conditions on the mean characteristic length of ethoxylated alcohol disturbance waves is presented in Figure 9.29.

Figure 9.29 illustrates the clear relationship between increases in mean length and increased liquid loading, with over a twofold maximum increase in mean length of the waves recorded over the liquid flowrate measurement range. This relationship appears to be continued both during and after the transition from the 'gravity' type structures to the two-dimensional ripple structures, and is a result of the observed 'fattening' of the ripples (see Figures 9.20 and 9.24). The relationship between air velocity and mean length value shows the expected drop in length associated with the conversion of the gravity structures into the significantly thinner ripple structures, with in some cases the disturbance ripples being almost half the mean length of the 'gravity' type structures they are created from.

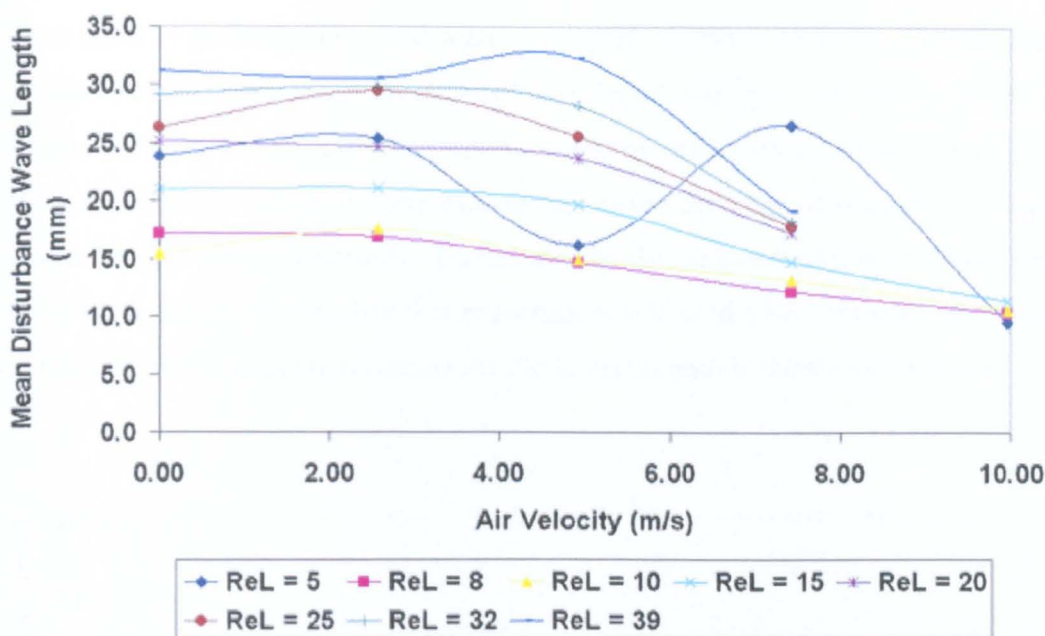


Figure 9.29: Influence of flow conditions on the mean characteristic length of ethoxylated alcohol disturbance waves.

The only major discrepancy within Figure 9.29 is observed for the data for the lowest Reynolds number ($ReL=5$), which does not follow the trends established by the other data. Visual observation of the flow structures at this flow condition suggest that the mean lengths should be lower than recorded, suggesting this discrepancy is the result of film categorisation difficulties during the analysis.

9.3.4.3 Disturbance Wave Celerity

The influence of co-current airflow on the mean dodecylbenzene disturbance wave celerity is presented in Figure 9.30.

The figure shows a clear relationship between increasing liquid flowrate and increased mean wave celerity, with as much as four fold increase in wave celerity over the liquid flowrate measurement range. As with the dodecylbenzene data, the effect of a co-current downflow of air on disturbance wave celerity is less clear, however, there is evidence to suggest the importance of the transition of the interfacial structure on recorded values. For Reynolds numbers less than around twenty there is little recorded effect until an air velocity of around seven metres per second is reached, and transition of the disturbance structures is visually apparent (see Figure 9.20). From this point the mean wave celerity

for these flows is gradually increased with increasingly dynamic airflows. For the higher liquid film Reynolds numbers investigated the figure suggests that the onset of the transition results in a significant decrease in mean recorded wave celerity values. This could be explained by a loss of wave momentum when the larger disturbance structures transform into the ripple structures. Unfortunately, data is not available for these higher liquid flows to determine whether this reduction is followed after transition is complete (circa 10 m/s) by the increase recorded for the lower Reynolds number film flows.

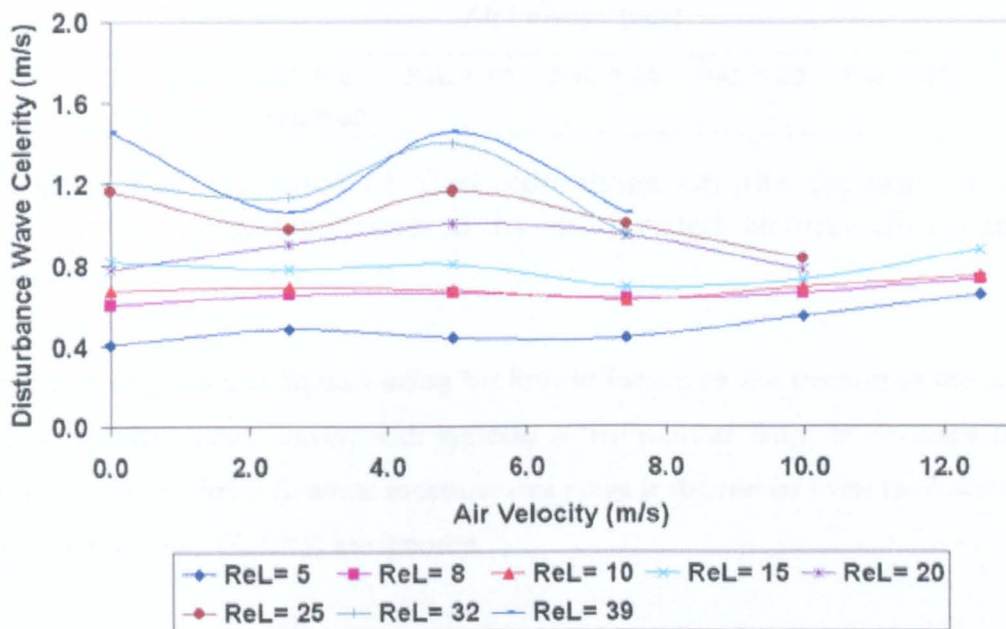


Figure 9.30: Influence of flow conditions on the mean ethoxylated alcohol disturbance wave celerity.

9.3.4.4 Fraction of Interface Covered by Disturbance Waves

The influence of flow conditions on the fraction of the interface covered by ethoxylated alcohol disturbance waves is presented in Figure 9.31.

As explained previously in the dodecylbenzene section of this chapter, this parameter was simply determined from the ratio of the number of points categorised as disturbance region points over the total number of spatial measurement points.

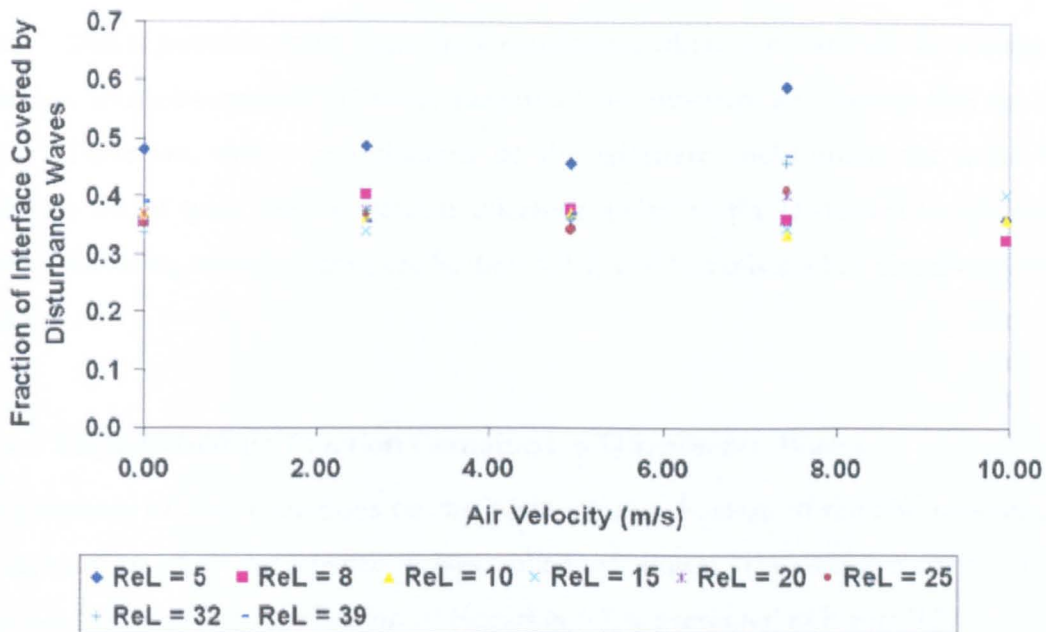


Figure 9.31: Influence of flow conditions on the fraction of the interface covered by ethoxylated alcohol disturbance waves.

Figure 9.31 suggests that liquid loading has little influence on the fraction of the interface covered by disturbance waves, with typically a five percent range in coverage fraction recorded over the liquid flowrate measurement range if the results from the lowest liquid film Reynolds value ($ReL=5$) are ignored.

What is particularly interesting about Figure 9.31 is that it does not show the markedly clear change in data trends witnessed for dodecylbenzene films (see Figure 9.14). The relatively constant values obtained for most of the liquid flows investigated are evidence of there being little change in film surface roughness by the interaction of a dynamic co-current airflow, however, the limited data in the transition region for the higher liquid flows studied suggests that increases in surface roughness are likely for these flows if the air velocity measurement range could be extended.

As with the mean characteristic length of the disturbance waves, the values for the lowest flow studied ($ReL = 5$) are significantly different (*i.e.* significantly higher) from those recorded for other liquid film flows. When these results for this liquid film Reynolds number are compared with their respective spatial images it is clear that the algorithm must be attributing significant proportions of the base substrate film to the disturbance

waves. This is possible under these flow conditions, where the substrate dominates the interface, and subsequently the mean heights of the substrate and overall film are very close. Therefore, minor perturbations of the substrate could attain the mean film thickness height (plus the ten percent tolerance added to the algorithm to attempt to prevent this categorisation error, see Section 5.2.4) and be registered as disturbance wave material.

9.3.4.5 Liquid Hold-up Fraction Contained in Disturbance Waves

The influence of flow conditions on the liquid hold-up fraction of the film contained in ethoxylated alcohol disturbance waves, obtained during the categorisation of the interface (Chapter 5) by application of Equation 5.1, is presented in Figure 9.32.

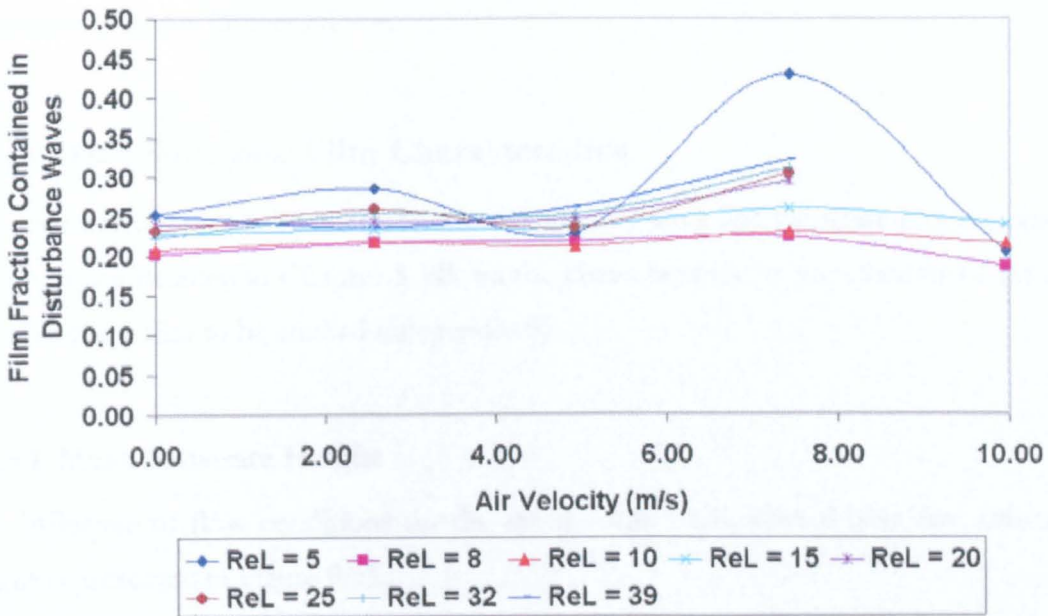


Figure 9.32: Influence of flow conditions on the liquid hold-up fraction of the film contained in ethoxylated alcohol disturbance waves.

Figure 9.32 highlights a clear, although small, relationship between the fraction of the film held-up in ethoxylated alcohol disturbance waves, with typically a five percent increase in hold-up fraction recorded over the liquid flowrate measurement range.

Examination of the influence of air flowrate on hold-up fraction highlights that the transition of the disturbance structures on the interface appears to have a noticeable effect on hold-up fraction. For air flowrates below the transition the figure identifies little influence of the airflow. During the transition of the wave structures (circa air flowrate of 5–9m/s) the figure identifies a slight increase in disturbance film fraction that is particularly evident in the data for the larger liquid film Reynolds numbers investigated. Where data is available after the transition is complete (10m/s) the figure suggests that any gains in disturbance film fraction have been lost, and this is consistent with the observation that the transition in ethoxylated alcohol films is merely a re-organisation of existing disturbance material.

Once again there appears to be inconsistency associated with the data for the lowest liquid film Reynolds number ($Re_L = 5$) that is caused by errors in the categorisation of the interface at this flow condition.

9.3.5 Base Substrate Film Characteristics

The characterisation of the interface into disturbance wave and substrate film regions by the approach detailed in Chapter 5, allows the characteristics of the ethoxylated alcohol base substrate film to be studied independently.

9.3.5.1 Mean Substrate Height

The influence of flow conditions on the mean ethoxylated alcohol base film substrate height is presented in Figure 9.33.

In a similar fashion to the results recorded in dodecylbenzene films, at the lower air flowrates investigated the figure demonstrates the steady increase in substrate height (typically over two fold over liquid flowrate measurement range) with increasing liquid load, and the slight compression of the substrate in the presence of a co-current flow of air. As with both water and dodecylbenzene films (see Figures 8.21 and 9.16), at the highest measured air flowrate there is the suggestion that the mean base substrate film height has risen with any previous losses more than recovered. This can be explained by

the categorisation of much of the trailing material from the wake of the disturbance ripples (see Figure 9.21) as substrate material.

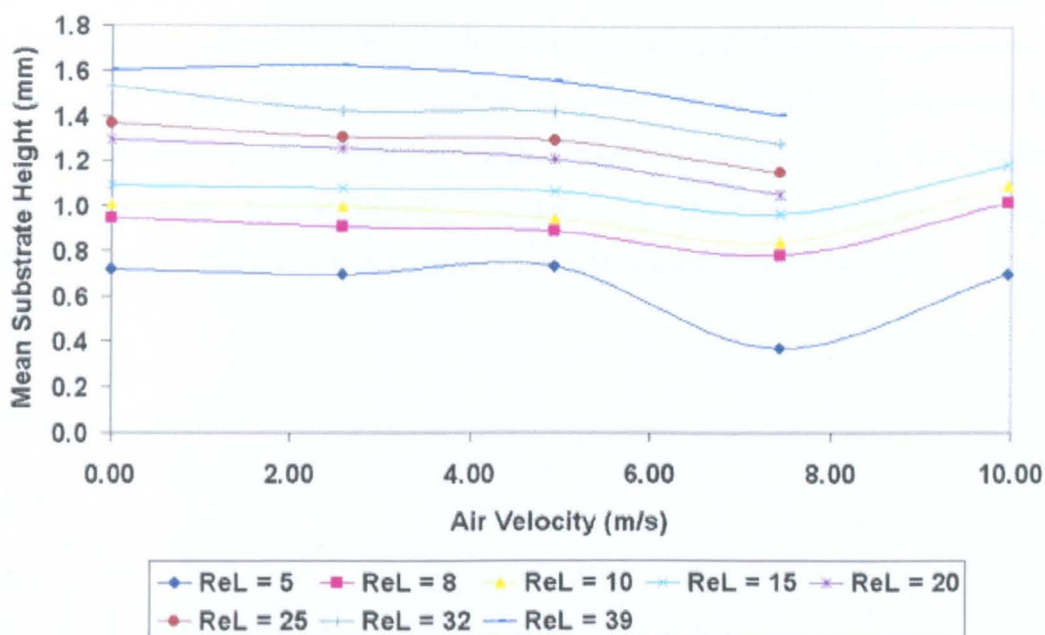


Figure 9.33: Influence of flow conditions on the mean ethoxylated alcohol base film substrate height.

9.3.5.2 Ratio of Mean Substrate Height and Maximum Disturbance Height

The influence of flow conditions on the ratio of mean substrate height and maximum disturbance height is presented in Figure 9.34.

Figure 9.34 demonstrates that although all air velocities investigated show a similar trend, the ratio values for the air flows that coincide with the transition of the interface structure ($v_g = 7.4$ & 10.0 m/s) are offset significantly lower than the data representing airflows below the transition region. The offset is particularly prevalent at the lower and intermediate liquid film Reynolds numbers studied, with the data converging at the higher liquid loadings. All but the highest air flowrate investigated show a marked drop in ratio value as liquid film Reynolds numbers are increased to about thirteen. Above this value the ratio is effectively constant in the presence of ‘gravity’ wave type disturbance structures. This drop can be explained by re-examination of the flow images presented in Figures 9.18 and 9.19. It is clear from those flow images that the ‘gravity’

type structures are not all fully developed into their long trailing edge structures until the third image from the left, with that image corresponding to the value of thirteen identified above as the upper limit of the drop in ratio. This would also explain why the drop is not recorded at the highest air flowrate, as Figure 9.20 shows that the transition has been completed at this air velocity and only rippled disturbance structures are present. The suggestion then is that this drop in ratio highlights another interfacial structure transition, that from a purely laminar flow to a gravity induced wavy structure, not dissimilar to the drop identified by Aragaki *et al.* (1987) in water films (see Figure 8.23) that was also attributed to a transition from laminar to wavy flow regime.

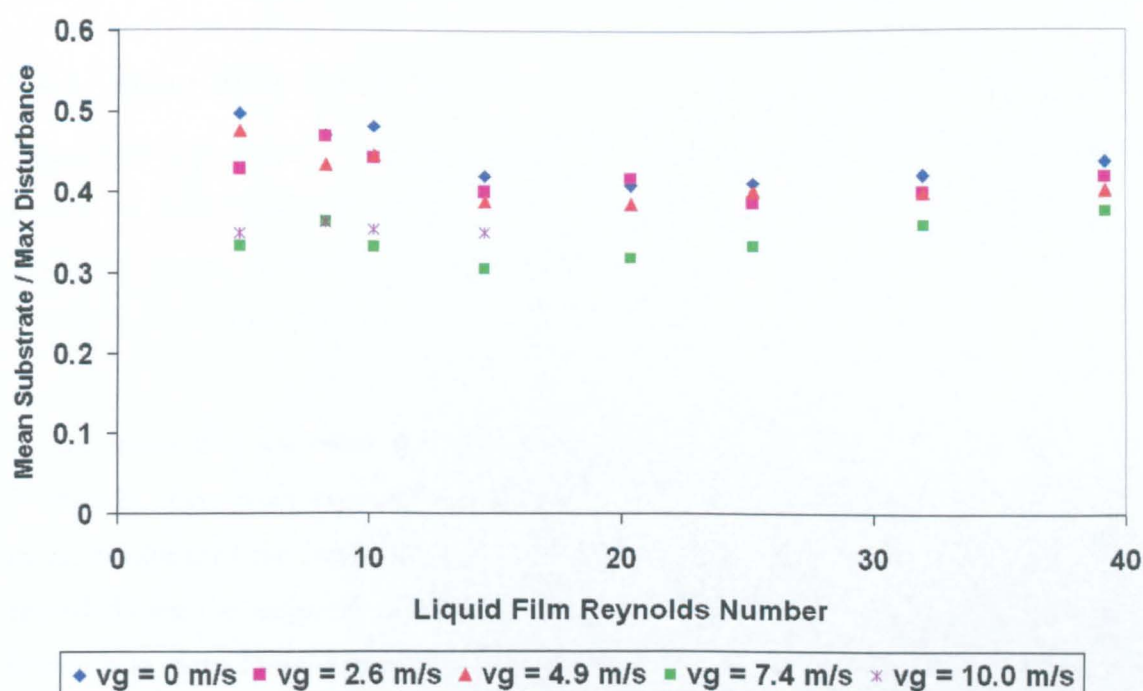


Figure: 9.34 Influence of flow conditions on the ratio of mean ethoxylated alcohol substrate height and maximum disturbance height.

9.4 HYDRODYNAMIC EFFECTS OF PHYSICAL PROPERTIES ON INTERFACIAL STRUCTURE

As stated in the introduction to this chapter, the purpose of this section is to summarise some of the hydrodynamic effects of the physical properties of the three investigated liquids on the interfacial characteristics of falling films, by direct comparison of selected data obtained at virtually identical flow conditions and measurement location.

The most important physical property related to interfacial structure must surely be viscosity, which is a measure of the resistance offered by the fluid to deformation by a shear stress (as defined by Perry & Green (1984)). Table 2.1 shows that water, dodecylbenzene and ethoxylated cover a large viscosity range (approximately 1, 7, and 20 kg/m s respectively at 20°C). However, differences in interfacial structure between the three liquids cannot be attributed solely to viscous effects, due to significant differences in surface tension between the organic liquids studied and water.

To simplify comparison between the three liquids, liquid flowrates are expressed in terms of Γ , the flowrate per wetted perimeter (kg/m s), which is not viscosity dependent.

9.4.1 Mean Film Thickness

Figure 9.35 is provided to demonstrate the effects of the physical properties of the three liquids on their mean film thickness. The figure is a comparison plot of mean film thickness versus co-current downflow air velocity at three virtually identical liquid volumetric flow conditions.

As the mean film thickness data generally follows the trend of the Nusselt predictor (Eqn. 8.3), there is an expected clear relationship between the liquid viscosity and the mean thickness of the film, with almost a factor of four increase in mean film thickness recorded over the range of viscosities investigated. The figure visually suggests that the increases in mean film thickness associated with increased liquid loading become larger as the viscosity of the fluid increases. However, when the percentage rises in mean thickness from the lowest to the highest liquid flowrate in the figure are evaluated, the differences are seen to be less significant (water ~ 50% increase, dodecylbenzene & ethoxylated alcohol ~ 60-70% increase). The relatively uniform spacing of the three liquid flowrates displayed in the figure suggests that the rate of increase in mean thickness with increased liquid flowrate is not constant, with the differences in thickness between the lower and middle point much greater than for the middle and upper point. The figure also again demonstrates the slight compression of the interface height observed in all three liquids with the addition of a co-current downflow of air.

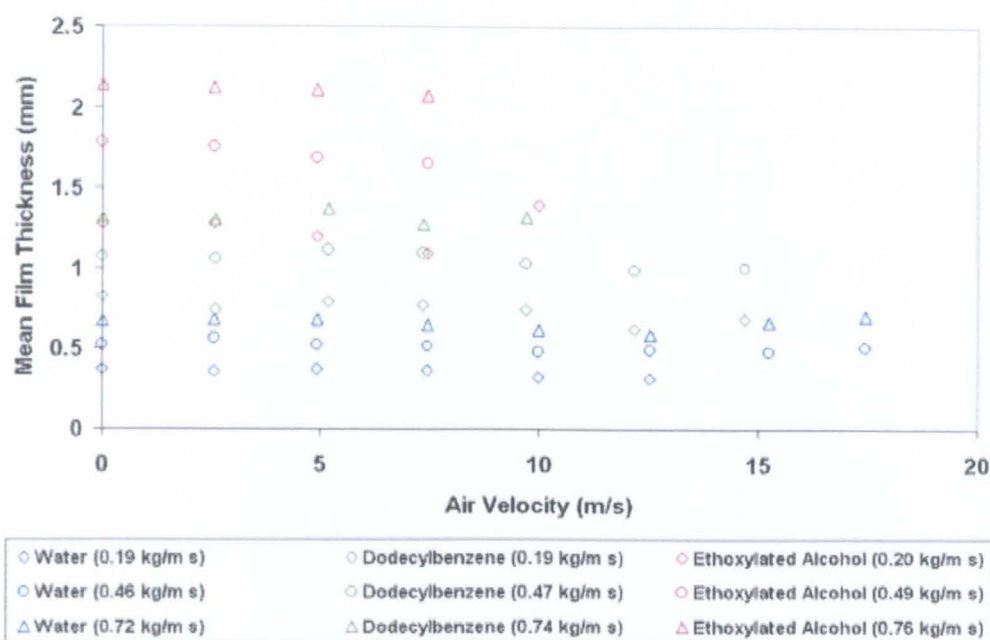


Figure 9.35: Comparison plot for the three liquids of mean film thickness versus co-current downflow air velocity at three virtually identical liquid volumetric flow conditions.

9.4.2 Disturbance Wave Characteristics

9.4.2.1 Mean Disturbance Wave Height

The mean disturbance wave height was simply evaluated for the images at each flow condition by the averaging of all the spatial film thickness points characterised as belonging to disturbance wave structures. Figure 9.36 demonstrates the effects of the physical properties of the three liquids on the mean height of their disturbance wave structures, by presenting a comparison plot of mean disturbance wave height versus co-current downflow air velocity at three virtually identical liquid volumetric flow conditions.

As with the mean thickness of the film, there is a clear relationship between the liquid viscosity and the mean height of the disturbance wave structures, with a similar factor of four increase in mean disturbance wave height observed over the viscous range investigated. The percentage rises in disturbance height associated with increases in liquid loading are consistent with those identified for mean film thickness, as is the trend for mean disturbance wave height increases with liquid flowrate.

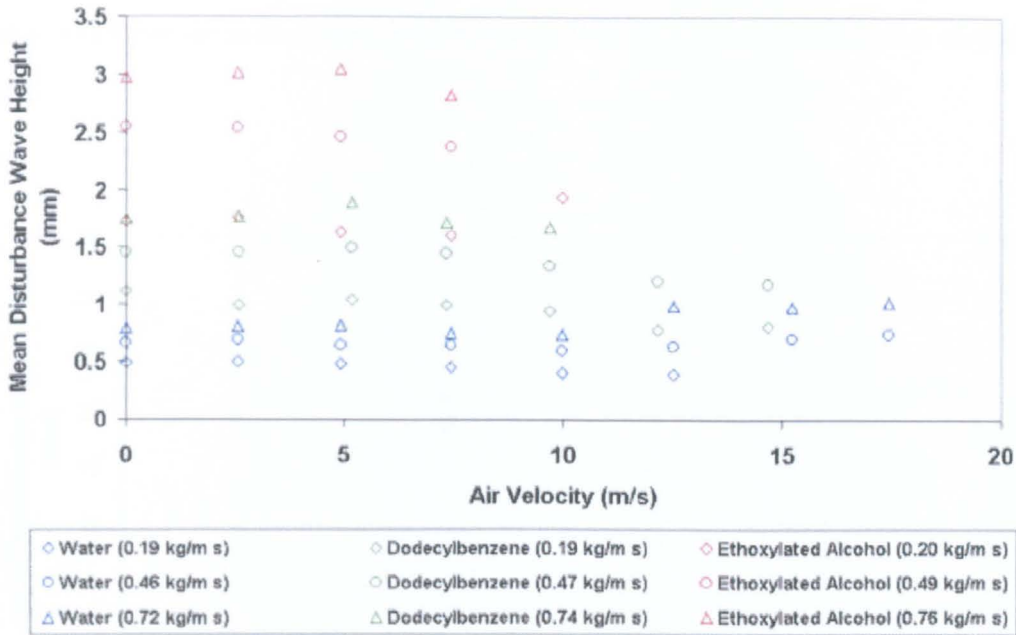


Figure 9.36: Comparison plot for the three liquids of mean disturbance wave height versus co-current downflow air velocity at three virtually identical liquid volumetric flow conditions.

9.4.2.2 Mean Characteristic Length of Disturbance Waves

Figure 9.37 demonstrates the effects of the physical properties of the three liquids on the mean characteristic length of the disturbance wave structures, by presenting a comparison plot of mean disturbance wave height versus co-current downflow air velocity at three virtually identical liquid volumetric flow conditions.

The figure highlights some important differences in hydrodynamic behaviour of the three liquids, particularly during and after the transition of interfacial disturbance wave structures by the action of a sufficiently dynamic airflow, that is observed in all three liquids.

At air flowrates below this transition the organic liquids display a trend for the characteristic length of the disturbance waves to rise with increased liquid loading. This is consistent with the development of volumetrically larger disturbance waves as the volume of film travelling liquid is increased. Interestingly, this trend is reversed with the data for water films. Visual observation (see Figure 8.1) shows some evidence of the increasing development of numerous smaller amplitude disturbance waves structures as

water film flowrate is increased, which would lead to a reduction in mean characteristic length.

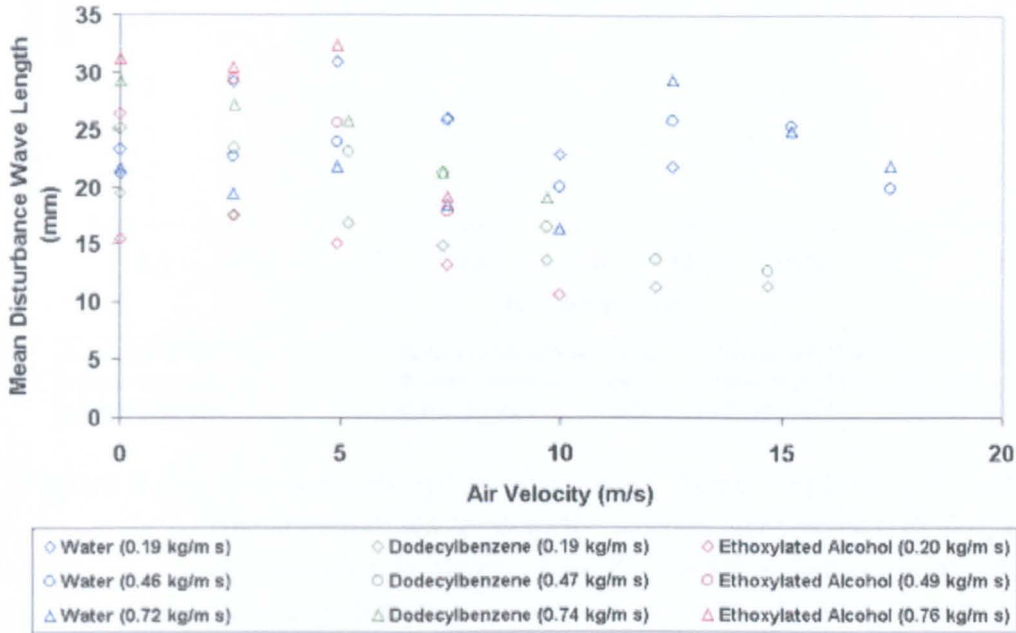


Figure 9.37: Comparison plot for the three liquids of mean disturbance wave length versus co-current downflow air velocity at three virtually identical liquid volumetric flow conditions.

For air flowrates during and above the region of transition, the data for the organics and water diverges. The mean characteristic length for the organic liquid disturbance waves continues to fall rapidly until the development of the disturbance ripple like structures has been completed (see Figures 9.4 & 9.21). However, the mean characteristic length of the water disturbance waves shows a significant rise in value, a result of the development of the large ‘regular’ type disturbances, which are present the flow images at these flow conditions (see Figures 8.3 & 8.4).

9.4.2.3 Mean Disturbance Wave Celerity

Figure 9.38 demonstrates the effects of the physical properties of the three liquids on the mean disturbance wave celerity, by presenting a comparison plot of mean disturbance wave celerity versus co-current downflow air velocity at three virtually identical liquid volumetric flow conditions.

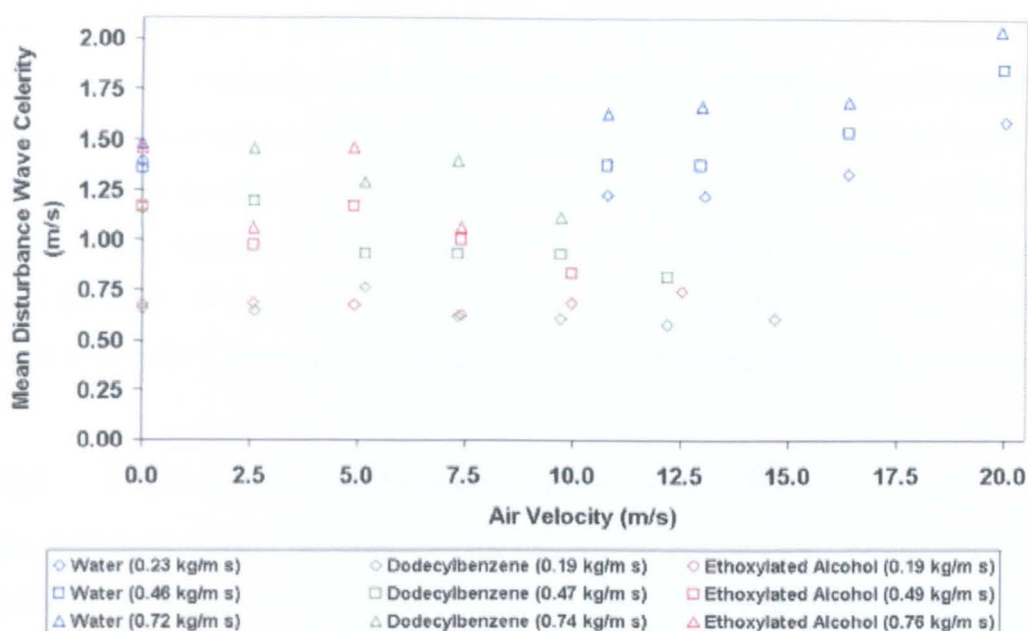


Figure 9.38: Comparison plot for the three liquids of mean disturbance wave celerity versus co-current downflow air velocity at three virtually identical liquid volumetric flow conditions.

Figure 9.38 highlights a clear relationship between increased liquid loading and increases in disturbance wave celerity for all three liquids. However, the figure also highlights differences in hydrodynamic behaviour between the organic liquids and water brought about by the transition of the interfacial structure.

At air flowrates below the transition, the figure implies that the organic disturbance wave celerity is effectively constant. Unfortunately, the lack of water data in this region (see Section 8.2.6.2 for explanation) prevents any comment on hydrodynamic behaviour.

During the transition of the interfacial structure the intermediate and highest organic flowrates show evidence of fall in mean disturbance wave celerity, brought on by the development of the slower moving ripple structures. The lowest organic flowrates show little evidence of this fall, remaining effectively constant over the entire measurement range, and this must be due to the lack of the larger gravity/regular disturbance structures at these low liquid loadings. Again, the lack of water data in this region prevents any comment on hydrodynamic behaviour.

Above the transition a gradual acceleration of the water disturbance waves can be observed. The limited organic data above their respective transitions would suggest that there is some acceleration of the rippled structures, however, the differences in wave celerity between the relatively slower rippled organic liquid wave structures and the large, faster travelling water based disturbances is almost a factor of two where comparable data is available. If it was possible to extend the data for the organic liquids it is not unrealistic to believe that these differences in celerity values would increase substantially.

9.4.2.4 Fraction of Interface Covered by Disturbance Waves

Figure 9.39 demonstrates the effects of the physical properties of the three liquids on the fraction of the interface covered by disturbance waves, by presenting a comparison plot of this fraction versus co-current downflow air velocity at three virtually identical liquid volumetric flow conditions.

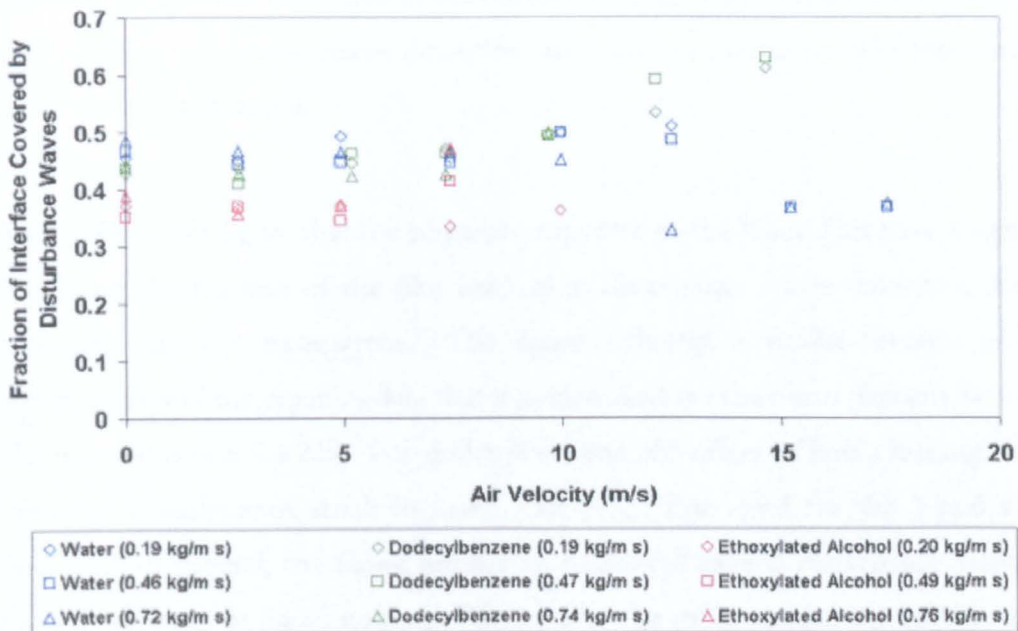


Figure 9.39: Comparison plot for the three liquids of the fraction of interface covered by disturbance waves versus co-current downflow air velocity at three virtually identical liquid volumetric flow conditions.

As stated previously, the parameter is simply calculated from the ratio of the number of points categorised as disturbance region points over the total number of spatial measurement points, and subsequently is a measure of the surface 'roughness' of the interface.

The figure highlights the 'smoothing' of the base substrate film that is observed with application of more viscous flows. The apparent drop in disturbance wave coverage in water films identified above ten metres per second is a direct result of the capture of only a single large disturbance structure in each of these images, suggesting that the spatial measurement area utilised in this study is not sufficiently large enough for film characterisation at these flow conditions.

9.4.2.5 Liquid Hold-up Fraction Contained in Disturbance Waves

Figure 9.40 demonstrates the effects of the physical properties of the three liquids on the liquid hold-up fraction contained in disturbance waves, by presenting a comparison plot of this fraction versus co-current downflow air velocity at three virtually identical liquid volumetric flow conditions.

It is clear from this figure that the physical properties of the liquid film have a significant influence on the fraction of the film held-up in disturbance waves, however, the exact relationships are not transparent. The figure indicates a similar reversal in trends between water and the organics data that was identified for the mean characteristic length of the waves (Section 9.4.2.2). For dodecylbenzene, the effect of liquid loading on hold-up fraction is sufficiently small to make analysis of this trend for this liquid virtually impossible. In general, the figure implies that dodecylbenzene disturbance waves have the largest capacity of liquid hold-up, followed by the more viscous ethoxylated alcohol waves and then the less viscous water waves. The significance of this order is not clear.

What is clear from all three liquids is that the onset of the structure transition of the disturbed interface results in a rise in disturbance wave hold-up fraction, with the suggestion of a closer agreement in hold-up fraction between the liquids once the transition has been completed.

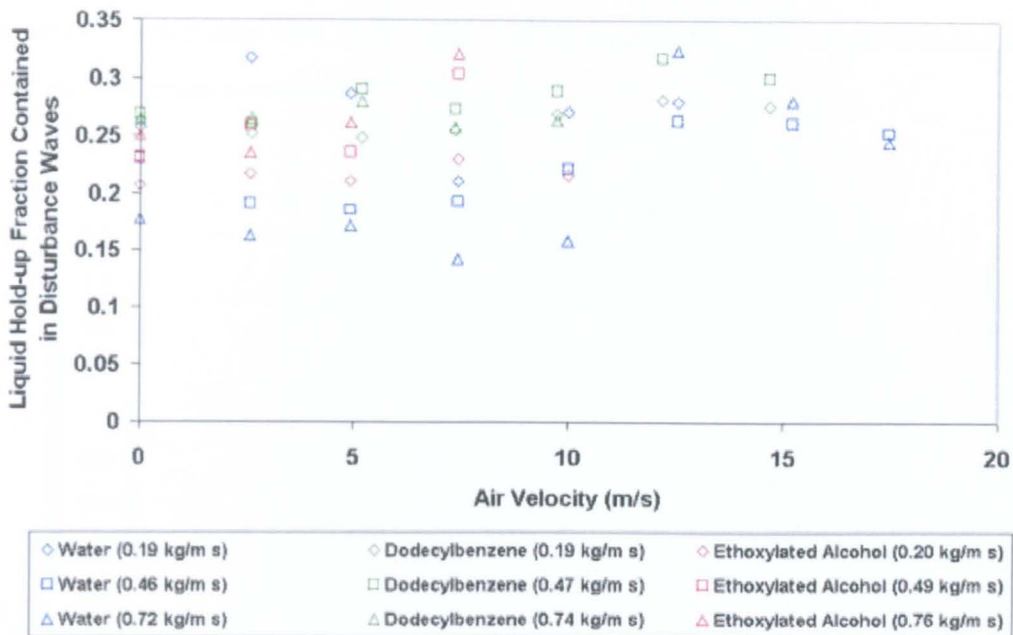


Figure 9.40: Comparison plot for the three liquids of the liquid hold-up fraction of the film contained in disturbance waves versus co-current downflow air velocity at three virtually identical liquid volumetric flow conditions.

9.4.3 Base Substrate Film Characteristics

9.4.3.1 Mean Substrate Height

Figure 9.41 demonstrates the effects of the physical properties of the three liquids on the mean disturbance wave celerity, by presenting a comparison plot of mean disturbance wave celerity versus co-current downflow air velocity at three virtually identical liquid volumetric flow conditions.

As with both the mean thickness of the film and mean height of the disturbance waves, there is a clear relationship between the liquid viscosity and the mean substrate height, and Figure 9.41 identifies a similar range in recorded mean substrate height values over the viscous range investigated. Interestingly, the percentage increase in substrate height associated with increases in liquid loading is significantly different between the organic and water films. There is a sixty percent increase recorded for ethoxylated alcohol and dodecylbenzene between the lowest and highest flowrates displayed on the figure, whereas the increase in water films is closer to one hundred percent. Each of the liquids record a slight compression of the substrate height at the onset of the transition of the

disturbance structures with some evidence to suggest that this height loss is recovered after the transition is complete.

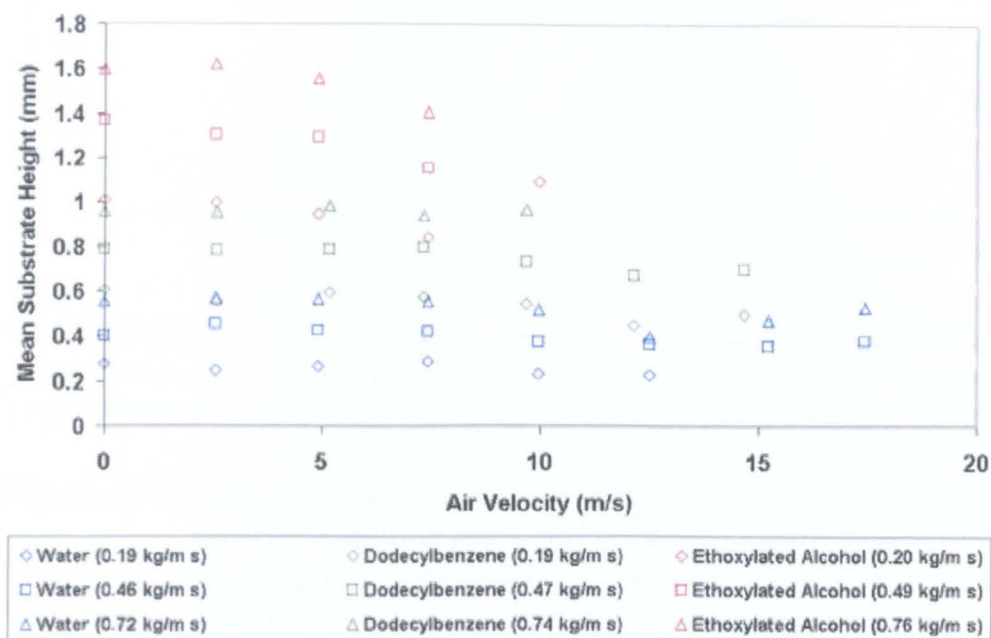


Figure 9.41: Comparison plot for the three liquids of the mean base film substrate height versus co-current downflow air velocity at three virtually identical liquid volumetric flow conditions.

9.4.3.2 Ratio of Mean Substrate Height and Maximum Disturbance Height

Figure 9.42 demonstrates the effects of the physical properties of the three liquids on the ratio of mean substrate height and maximum disturbance height, by presenting a comparison plot of this ratio versus co-current downflow air velocity at three virtually identical liquid volumetric flow conditions.

It is evident from the figure there is a clear relationship between the physical properties of the film and the value of this ratio parameter. The ratio is a measure of the disturbance wave amplitude of the corresponding liquid and identifies the link between viscosity and development of taller disturbance structures.

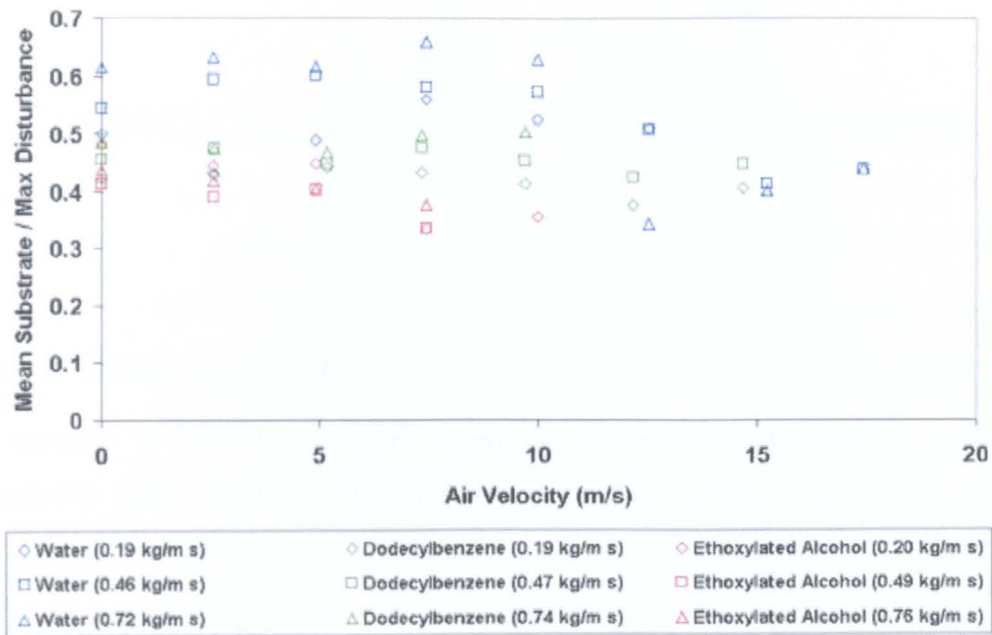


Figure 9.42: Comparison plot for the three liquids of the ratio of mean substrate height and maximum disturbance height versus co-current downflow air velocity at three virtually identical liquid volumetric flow conditions.

Chapter 10

CONCLUSIONS AND RECOMMENDATIONS

10.1 INTRODUCTION

The purpose of this chapter is to summarise the main achievements of the work presented in this thesis and to suggest recommendations for future work.

10.2 CONCLUSIONS

The main objective of this study was the better understanding through experimental study of the interfacial characteristics of liquid falling films in the presence of a co current down flow of air, with emphasis on the physical and hydrodynamic conditions encountered in current falling film reactor technology, so that the information obtained can be implemented in the enhancement of falling film reactor modelling. It is believed that this objective has been met, with the study providing a comprehensive set of data on the hydrodynamic structure of the interface for both water and actual sulphonation feed stocks as the liquid phase. The following conclusions can be drawn from the study:

- (i) The Light Absorption Imaging Technique (LAIT) developed for film thickness measurements in this study has been shown to have the potential to give unparallel spatial information on the interfacial structure of falling liquid films. It has also been shown that the accuracy of the technique is on a par with more established film thickness measurement techniques. The two inherent limitations of the technique are the necessity for application on a flat surface, therefore excluding application on tubular geometries, and an inability to obtain measurement data, due to total light exclusion from the spatial image, at high (roughly greater than forty-five degrees) interface contact angles. The light exclusion problem has been shown to be a refraction-based phenomenon, and is comparable to the measurement difficulties at more modest interface

contact angles (around four to nine degrees) associated with ultrasonic film thickness measurement techniques (see Section 3.3.6). An attempt has been made, with limited success; to correct the measurement data in light excluded regions. The major experimental difficulty that was identified during the application of LAIT was the establishment of uniform lighting conditions. It was discovered that uniform lighting conditions were not possible with the equipment available; therefore, a method was developed to automatically correct the measurement data for deviations in background light intensity.

- (ii) The cross-correlation of the output signal from two light sources has been shown to be a simple yet effective method for disturbance wave celerity measurements. Accuracy of the technique was shown to be comparable to manual time-of-flight measurement of the celerity of disturbance waves, using the images from a high-speed video camera. However, the extension of the technique to localised quantitative film thickness measurements was found to be not viable with the resources available.
- (iii) It has been demonstrated that it is possible to describe the film as a base substrate with relatively faster disturbance waves travelling along this. A computer algorithm based technique has been developed for categorisation of the spatial film data obtained by LAIT into substrate and disturbance wave regions. Visual inspection of the resulting categorisation of the measurement data suggest the algorithm is quite effective, and that accurate globally averaged characteristics of the interfacial structure are obtained.
- (iv) The dramatic influence of both flow conditions and physical properties on interfacial characteristics has been demonstrated. In particular, a transition of the disturbance wave structures in falling water films due to the influence of a co-current airflow, reported by other workers (*e.g.* Webb & Hewitt (1975)), has been identified at comparable flow conditions (*i.e.* ~ 10 m/s). Similar transitions have been identified in both the more viscous organic liquid films at slightly lower air velocities (*i.e.* 5-8 m/s).

- (v) Differences in the disturbance wave structure have been identified between the organic and water films after the interfacial transition highlighted in (iv). Although both water and organic films consist of large three-dimensional 'regular' type disturbances at the higher liquid flowrates investigated, the organic films also develop relatively slower moving, large two-dimensional 'ripple' type structures that dominate the interface at the liquid flowrates investigated.

10.3 RECOMMENDATIONS FOR FUTURE WORK

The major recommendation for the continuation of this work is to find appropriate means to incorporate the relevant hydrodynamic data collected from this study into the enhancement of falling film reactor models. Possible approaches range from the simple substitution into current models of empirical equations, which define the interfacial characteristics, to the development of a new model. If recent work by Pols (1998) in developing a model which successfully predicts the shape of the large-amplitude disturbance waves (example given in Figure 10.1) can be combined with the hydrodynamic data collected in this study, it opens the possibility to develop a completely new type of reactor model capable of predicting gas-liquid interfacial mass transfer, and the equally important mixing and mass transfer within the film, with minimal recourse to empirical correlations. Another new approach being considered is to model the complex two-phase system within the falling film reactor through the application of Computational Fluid Dynamics (CFD), using predicted interface boundary conditions that have validated by detailed experimental measurements.

A disappointing feature of the flow facility was the limitation of the investigation to moderate co-current airflows (approximately ten and 20 metres per second for the organics and water respectively) and restricted liquid flowrates at the these moderate air flowrates, due predominantly to the wetting problems on the viewing glass plate that are reviewed in Section 2.3.5. It is recommended that effort be made into extending the air and liquid flow range, particularly for the organic liquids studied, both so that hydrodynamic data is available for air higher flow conditions encountered in falling film reactors (15-90 m/s) and that the structure of the interface after disturbance wave transition in the organic films can be more thoroughly examined. To achieve this air

flowrate extension in a rectangular geometry it is likely that alternative fluid introduction and test section dimensions are necessary. A possible alternative is to transfer the investigation to a tubular geometry, where literature shows that these higher air flowrates have been comfortably attained. This would require the adaptation of the spatial film thickness measurement technique discussed in the next paragraph

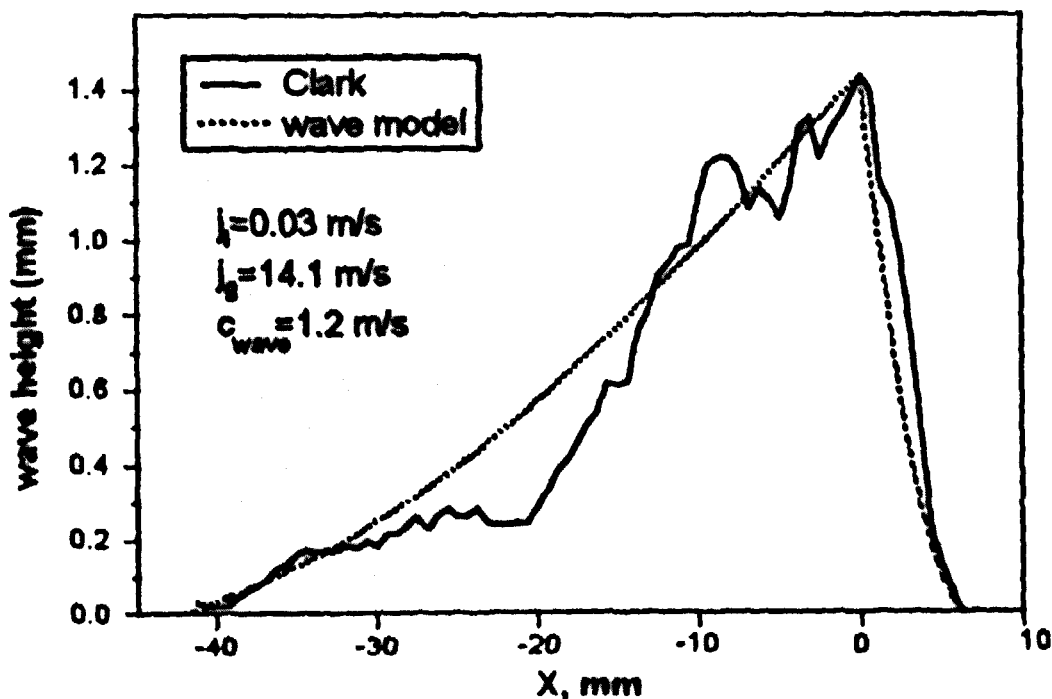


Figure 10.1: Comparison of Pols (1998) prediction of wave structure with data from the current study. (Taken from Pols *et al.* (1998).

A disadvantage of the spatial film thickness measurement technique developed in this study (*i.e.* LAIT) is that it is restricted by optical requirements to a flat plate. This is a disadvantage as literature shows that film thickness measurements are predominately required/investigated in tubular geometries. A possible method of extending the application of this spatial technique to tubular geometries would be to investigate the feasibility of incorporating the image analysis aspects of the technique to another optical measurement method, where measurements in tubular geometries are possible. Of the film thickness measurement techniques that have been applied previously in a tubular geometry, the pigment luminance method of Ohba & Nagae (1993) (reviewed in Section 3.5.4) appears to be the best suited to adaptation.

By this own author's admission the analysis of the spatial film thickness data obtained using LAIT (CHAPTER 5) has several potential areas of improvement. These include:

- (i) The development of a more sophisticated means to correct for the regions of total light exclusion from the image that are caused by the optical phenomenon detailed in Appendix B. It is considered also pertinent that some effort should be made to compare the interfacial structure predicted by any correction method with interfacial data obtained using a technique not afflicted by this phenomenon, to ensure corrections are valid.
- (ii) Investigate algorithmic approaches to provide analysis on individual disturbance wave structures. The approach utilised in this study of analysing 'strips' of the disturbance wave data appears quite effective at providing globally averaged information on disturbance wave structure, however, is not suited to providing information on individual disturbance structures. The potential advantages of having access to individual disturbance wave structure information is that the range of disturbance waves sizes and shapes present on the film can easily be analysed, and where multiple wave types are present, their relative importance in hydrodynamic behaviour can be assessed. The development of an algorithm to analyse the disturbance data as individual structures is non-trivialised by the necessity of complex path-finding routines.

The selection of results in Chapter 9 demonstrates how the physical properties (in particular the viscosity and surface tension) of the liquid film have a dramatic influence on its interfacial characteristics. Although this study has highlighted the general trends in the relationship of physical properties and film structure there are obvious benefits to be gained in a comprehensive study. It would be particularly advantageous to study the influence of viscosity and surface tension independently. For the influence of viscosity, a range of sugar solutions, which have a relatively constant surface tension, could be utilised. For surface tension effects the results from the sugar solution study could be compared with similar viscosity organics. Extension of the liquid film viscosity range would also have the added benefit of allowing the interfacial characteristics of

sulphonation products, significantly more viscous than the sulphonation feedstocks investigated in this study, to be simulated. It would be also of interest to study the influence of temperature on interfacial structure as a considerable temperature gradient, and thus physical property range, can be expected within a falling film reactor. A temperature gradient will exist both through the falling film, from the film-gas interface to column wall, and longitudinally down the reactor column.

BIBLIOGRAPHY

- Alekseenko, S. V., Nakoryakov, V. E. and Pokusaev, B. G., (1985a), "Wave formation on vertical falling liquid films," *International Journal of Multiphase Flow*, Vol. 11, No. 5, pp 607-627.
- Alekseenko, S. V., Nakoryakov, V. E. and Pokusaev, B. G., (1985b), "Wave formation on vertical falling liquid films," *AIChE Journal*, Vol. 31, No. 9, pp 1446-1460.
- Alekseenko, S. V., Nakoryakov, V. E. and Pokusaev, B. G., (1994), "Wave Flow of Liquid Films", *Begeell House*, New York, USA.
- Ambrosini, W., Forgione, N., Oriolo, F. and Vigni, P., (1996), "Characterization of a falling film for heat and mass transfer experiments," *2nd European Thermal-Sciences and 14th UIT National Heat Transfer Conference*, Roma, Italy, May 29-31.
- Ambrosini, W., Anhorn, I., Forgione, N., Oriolo, F. and Vigni, P., (1998), "Surface characteristics of a water film falling down a flat plate in the laminar-wavy regime," *Third International Conference on Multiphase Flow, ICMF'98*, Lyon, France, June 8-12.
- Amenitskii, A. N., Rinkevichyus, B. S. and Fabrikant, V. A., (1969), "Laser measurement of the velocity distribution in a film of liquid," *High Temperature*, Vol. 1, pp 974-975.
- Anderson, G. H. and Hills, P. D., (1974), "Two-phase annular flow in tube bends," Symposium on multi-phase flow systems, Strathclyde, Scotland, *I. Chem. E. Symp. Ser.*, No. 38, Paper J1.
- Andreussi, P., (1980), "The onset of droplet entrainment in annular downward flows," *Canadian Journal of Chemical Engineering*, Vol. 58, pp 267-270.
- Anhorn, I., (1997), "Statistical characterisation of a wavy falling film for heat and mass transfer experiments," *University of Pisa Internal Report*, Report No. DCMN NT 315(97).
- Aragaki, T., Nakayama, S., Suzuki, M., and Toyama, S., (1987), "Characteristics of a falling liquid on a vertical tube," *International Chemical Engineering*, Vol. 27, No. 2, pp 326-333.
- Arnold, C. R. and Hewitt, G. F., (1967), "Further developments in the photography of two-phase gas-liquid flow," *UKAEA*, Report No. AERE-R 5318.
- Asali, J. C., Hanratty, T. J., and Andreussi, P., (1985), "Interfacial drag and film height for vertical annular flow," *American Institute for Chemical Engineers Journal*, Vol. 31, No. 6, pp 895-902.
- Atkinson, B. and Caruthers, P. A., (1965), "Velocity profile measurements in liquid films," *Trans. Instn Chem. Engrs*, Vol. 43, pp T33-T39.

- Azzopardi, B. J., (1977), "Interaction between a falling liquid film and a gas stream," *Ph.D. Thesis*, University of Exeter.
- Azzopardi, B. J., (1978), "Consideration of the fluorescence film thickness technique," *Oxford University Engineering Laboratory*, Report 1229/78.
- Azzopardi, B. J., Fryer, P. J. and Freeman, G., (1979), "The frequency of disturbance waves in annular two phase flow," *UKAEA*, Report No. AERE-R 9347.
- Belkin, H. H., Macleod, A. A., Monrad, C. C. and Rothfus, R. R., (1959), "Turbulent liquid flow down vertical walls," *A.I.Ch.E. Journal*, Vol. 5, No. 2, pp 245-248.
- Benn, D. N., (1972), "An experimental capacitance liquid film thickness monitor. Operating instructions and circuit details," *UKAEA*, Report No. AERE-R 7155.
- Bennett, J. A. R. and Thornton, J. D., (1961), "Data on the vertical flow of air-water mixtures in the annular and dispersed flow regions. Part I: Preliminary study," *Transactions of the Institution of Chemical Engineers*, Vol. 39, pp 101-112.
- Bezrodnyy, M. K. and Antoshko, Yu., (1992), "An acoustic method for measuring the thickness of a flowing film," *Fluid Mechanics Research*, Vol. 21, No. 3, pp 1-5.
- Brown, R. C., Andreussi, P. and Zanelli, S., (1978), "The use of wire probes for the measurement of liquid film thickness in annular gas-liquid flows," *Canadian Journal of Chemical Engineering*, Vol. 56, pp 754-757.
- Butterworth, D., (1972), "Air-water annular flow in a horizontal tube," *Progress in Heat and Mass Transfer*, Vol. 6, pp 235-251.
- Butterworth, D. and Pulling, D. J., (1973), "RS95: Film flow and film thickness measurements for horizontal, annular, air-water flow," *UKAEA*, Report No. AERE-R 7576.
- Cassagrande, I., (1962), "Researches on adiabatic two-phase flow", *Energia Nucleare (Milan)*, Vol. 9, pp 148-159.
- Chang, J. S., Ichikawa, Y. and Irons, G. A., (1982), "Flow regime characterization and liquid film thickness measurement in horizontal gas-liquid two-phase flow by an ultrasonic method," *Measurements in Polyphase Flow*, Vol. 7, pp 7-12.
- Charvonia, D. A., (1961), "An experimental investigation of the mean liquid film thickness and the characteristics of the interfacial surface in annular, two-phase flow," *Paper presented at the Winter Annual Meeting of the ASME*, New York, Nov. 26 – Dec. 1st.
- Chu, K. J., (1973), "Statistical characterisation and modelling of wavy liquid films in vertical two-phase flow," *Ph.D. Thesis*, University of Houston.
- Chu, K. J. and Dukler, A. E., (1974), "Statistical characteristics of thin, wavy films. Part II: Studies on the substrate and its wave structure," *American Institute of Chemical Engineering Journal*, Vol. 20, No. 4, pp 695-706.

BIBLIOGRAPHY

- Chu, K. J. and Dukler, A. E., (1975), "Statistical characteristics of thin, wavy films. Part III: Structure of the large waves and their resistances to gas flow," *American Institute of Chemical Engineering Journal*, Vol. 20, No. 4, pp 695-706.
- Chun, M. H., Park, J. R. and Lee, S., (1984), "Parametric effects on the liquid-film thickness measurement by an ultrasonic method," *Transactions of the American Nuclear Society*, Vol. 46, pp 849-850.
- Clark, W.W., Hills, J.H, and Azzopardi, B. J. (1998), "The interfacial characteristics of falling film reactors," *IchemE Research Event*, Newcastle.
- Clark, W.W., Hills, J.H, and Azzopardi, B. J. (1999), "Spatial film thickness measurements in falling films in a co-current airflow using a novel adaptation of the light absorption technique," *2nd International Symposium on two-phase flow modelling and experimentation*, Pisa, May 1999.
- Clegg, A. J., (1969), "Studies of film flow on wetted wall columns," *Ph.D. Thesis*, University of Surrey, Guildford, Surrey.
- Collier, J. G. and Hewitt, G. F., (1961), "Data on the vertical flow of air-water mixtures in the annular and dispersed flow regions. Part II: Film thickness and entrainment data and analysis of pressure drop measurements," *Transactions of the Institution of Chemical Engineers*, Vol. 39, pp 127-136.
- Collier, J. G. and Hewitt, G. F., (1964), "Film thickness measurements," *UKAEA*, Report No. AERE-R 4684.
- Coney, M. W. E., (1973), "The theory and application of conductance probes for the measurement of liquid film thickness in two-phase flow," *Journal of Physics E: Scientific instruments*, Vol. 6, pp 903-910.
- Coney, J. E. R., El-Shafei, E. A. M., and Sheppard, C. G. W., (1989), "A dual laser beam method for wavy thickness measurement," *Optics and Lasers in Engineering*, Vol. 11, pp 1-14.
- Cook, R. A. and Clark, R. H., (1971), "The experimental determination of velocity profiles in smooth falling liquid films," *The Canadian Journal of Chemical Engineering*, Vol. 49, pp 412-416.
- Craik, A. D. D., (1966), "Wind generated waves in thin liquid films," *Fluid Mechanics*, Vol. 26, No. 2, pp 369-392.
- Cravarolo, L., Hassid, A. and Villani, S., (1961), "A beta-ray attenuation method for density measurements of liquid-gas mixtures in adiabatic flow," *Energia Nucleare*, Vol. 8, No. 12, pp 751-757.
- Crozier, J. A., Hewitt, G. F. and Lovegrove, P. C., (1961), "Density and surface tension measurements on aqueous solutions of water-soluble nigrosine used in film thickness measurements," *UKAEA*, Report No. AERE-M 877.

BIBLIOGRAPHY

- Dallman, J. C., (1981), "Application of ultrasonics to the measurement of thin liquid films," *Transactions of the American Nuclear Society*, Vol. 39, pp 1039-1041.
- Davis, E. J., Van Ouwerkerk, M. and Venkatesh, S., (1979), "An analysis of the falling film gas-liquid reactor," *Chemical Engineering Science*, Vol. 34., pp 539-550.
- Dicoi, O., and Canavas, C., (1993). *German Patent DE 41 28 827 A 1*.
- Douglas, P., (1988), "Photosensitive materials for use in velocity profile measurements in the water phase of air-water systems and in single phase liquid systems," *UKAEA*, Report No. AERE R-13638.
- Driscoll, D. I., Schmitt, R. L. and Stevenson, W. H., (1992), "Thin flowing liquid film thickness measurement by laser induced fluorescence," *Journal of Fluids Engineering*, Vol. 114, pp 107-112.
- Dukler, A. E. and Bergelin, O. P., (1952), "Characteristics of flow in falling liquid films," *Chemical Engineering Progress*, Vol. 48, No. 11, pp 557-563.
- Dunn, S. G. and Smith, J. W., (1971), "Turbulent momentum transfer in rough pipes," *Chemical Engineering Science*, Vol. 26, pp 685-692.
- Elkins, R. E., Jackman, G. R., Johnson, R. R. and Lindgren, E. R., (1977), "Evaluation of stereoscopic trace particle records of turbulent flow fields," *Review of Scientific Instruments*, Vol. 48, No. 7., pp738-746.
- Elsäßer, A., Samenfink, W., Ebner, J., Dullenkopf, K. and Wittig, S., (1997), "Dynamics of shear-driven liquid films," *7th International conference on Laser Anemometry, Advances & Applications*, Karlsruhe, Germany.
- Elsäßer, A., Samenfink, W., Ebner, J., Dullenkopf, K. and Wittig, S., (1998), "Effect of variable liquid properties on the flow structure within shear-driven wall films," *9th International Symposium on Laser Application to Fluid Mechanics*, Lisbon, Portugal.
- El-Sayed, El-Ayouty, D. I., and Stepanek, J. B., (1983), "Use of microwaves in the measurements of frequencies and amplitudes in liquid hold-up fluctuations," *International Journal of Multiphase Flow*, Vol. 9, No. 1, pp 49-72.
- Enos, R.D. and Douglas, P., (1989a), "Screening of potential water soluble photochromic dyes for use in flow visualisation studies," *UKAEA*, Report No. AERE R-13638.
- Enos, R.D. and Douglas, P., (1989b), "Characterisation and application of a photochromic triarylmethane dye sulphite as a tracer in the visualisation of water flows," *UKAEA*, Report No. AERE R-13480.
- Fogwell, T. W., (1986), "Window materials for use with flow visualization techniques," *UKAEA*, Report No. AERE R-12313.

BIBLIOGRAPHY

- Frantisak, F. Palade de Iribarne, A., Smith, J. W. and Hummel, R. L., (1969), "Nondisturbing tracer technique for quantitative measurements in turbulent flow," *Ind. Engng Chem. Fundamentals*, Vol.8, No.1, pp160-167.
- Fujita, H. and Katoh, K., (1985), "Falling water films over a ring attached to a vertical cylinder (wave characteristics measured by capacitance method)," *Bulletin of the Japanese Society of Mechanical Engineers*, Vol. 28, No. 241, pp 1401-1408.
- Fujita, H., Katoh, K. and Takahama, H., (1986), "Falling water films on a vertical cylinder with a downward step," *International Journal of Engineering Science*, Vol.24, No. 8, pp 1405-1418.
- Fukano, T., Sekoguchi, K. and Nishikawa, K., (1971), "Characteristics of static pressure fluctuations in upward air-water two-phase flow," *Technology Report of Kyushu University*, Vol. 44, No. 4, pp 594-601.
- Fukano, T., (1998), "Measurement of time varying thickness of liquid film flowing with high speed gas flow by a constant electric current method," *Nuclear Engineering and Design*, Vol. 184, pp 363-377.
- Gill, L.E., Hewitt, G. F. and Hitchon, J. W., (1962), "Sampling probe studies of the gas core in annular two phase flow: Part I. The effect of length on phase and velocity distribution", *UKAEA*, Report No. AERE-R 3954.
- Gill, L.E., Hewitt, G. F. and Lacey, P. M. C., (1963), "Sampling probe studies of the gas core in annular two phase flow: Part II. Studies of the effect of phase flow rates on phase and velocity distribution", *UKAEA*, Report No. AERE-R 3955.
- Gill, L. E., Hewitt, G. F. and Roberts, D. N., (1969), "Studies on the behaviour of disturbance waves in annular flow in a long vertical tube," *UKAEA*, Report No. AERE-R 6012.
- Gimbutis, G., (1988), "Heat transfer in gravitational flow of liquid film" (in Russian), *Vilnyus, Moksas*, pp 232.
- Graf, H., (1996), "Measurement of falling water film thickness," *University of Pisa Internal Report*, Report No. DCMN NT 292(96).
- Grimley, S. S., (1945), "Liquid flow conditions in packed towers," *Trans. Inst. Chem. Engrs.*, Vol. 23, pp 228-235.
- Gutiérrez-González, J., Mans-Teixidó, C. and Costa-López, J., (1988), "Improved mathematical model for a falling film sulfonation reactor," *Ind. Eng. Chem. Res.*, Vol. 27, pp 1701-1707.
- Hagiwara, Y., Miwada, T., Suzuki, K. and Sato, T., (1984), "A study on liquid film flow characteristics in annular two-phase flow," *Proceedings of Multi-phase flow and Heat Transfer 3*, April 18-20, Miami Beach, Florida, pp 249-263.

BIBLIOGRAPHY

- Hall Taylor, N., Hewitt, G. F. and Lacey, P. M. C., (1963), "The motion and frequency of large disturbance waves in annular two-phase flow of air-water mixtures," *Chemical Engineering Science*, Vol. 18, pp 537-552.
- Hewitt, G. F., King, I. and Lovegrove, P. C., (1961), "Holdup and pressure drop measurements in the two-phase annular flow of air-water mixtures," *UKAEA*, Report No. AERE-R 3764.
- Hewitt, G. F. and Lovegrove, P. C., (1962), "The application of the light absorption technique to continuous film thickness recording in annular two-phase flow," *UKAEA*, Report No. AERE-R 3953.
- Hewitt, G. F., King, R. D. and Lovegrove, P. C., (1962), "Techniques for liquid film and pressure drop studies in annular two-phase flow," *UKAEA*, Report No. AERE-R 3921.
- Hewitt, G. F. and Lovegrove, P. C., (1963), "Comparative film thickness and holdup measurements in vertical annular flow," *UKAEA*, Report No. AERE-M 1203.
- Hewitt, G. F., Lovegrove, P. C. and Nicholls, B., (1964), "Film thickness measurement using a fluorescence technique. Part I: Description of the method," *UKAEA*, Report No. AERE-R 4478.
- Hewitt, G. F., (1966), "Improvements in or relating to liquid film thickness measurements," *British Patent*, Specification No. 1051641.
- Hewitt, G. F. and Lovegrove, P. C., (1969), "Frequency and velocity measurements of disturbance waves in annular two-phase flow," *UKAEA*, Report No. AERE-R 4304.
- Hewitt, G. F. and Nicholls, B., (1969), "Film thickness measurement in annular two-phase flow using a fluorescence spectrometer technique. Part II: Studies of the shape of disturbance waves," *UKAEA*, Report No. AERE-R 4506.
- Hewitt, G. F., (1978), "Measurement of Two Phase Flow Parameters," *Academic Press*, London.
- Hewitt, G. F., (1982), "Measurement Techniques," In *Handbook of Multiphase Systems* (Edited by Hetsroni, G.), Chapter. 10., Hemisphere, Washington, DC.
- Ho, F. C. K. and Hummel, R. L., (1970), "Average velocity distributions within falling films," *Chemical Engineering Science*, Vol. 25, pp. 1225-1237.
- Hsu, Y. Y., Simoneau, R. J., Simon, F. F. and Graham, R. W., (1969), "Photographic and other optical techniques for studying two-phase flow," *11th Natl ASME/AICHE Heat Transfer Conf., Two-Phase Flow Instrumentation*, pp.1.
- Hughmark, G. A., Pressburg, B. S., (1961), "Holdup and pressure drop with gas-liquid flow in a vertical pipe," *A.I.Ch.E. Journal*, Vol.7, No.4, pp 677-682.

- Humphrey, J. A. C., Smith, J. W., Davey, B. and Hummel, R. L., (1974), "Light-induced disturbances in photochromic flow visualization," *Chemical Engineering Science*, Vol. 29, pp 308-312.
- Hurlburt, E. T. and Newell, T. A., (1996), "Optical measurement of liquid film thickness and wave velocity in liquid film flows," *Experiments in fluids*, Vol. 21, pp 357-362.
- Irons, F. E., (1995), "An interferometric measurement of the wall thickness of a cylindrical glass tube with application to a draining film," *Meas. Sci. Technol.*, Vol. 6, 1356-1361.
- Ishigai, S., Nakanishi, S., Koizumi, T. and Oyabu, Z., (1972), "Hydrodynamics and heat transfer of vertical falling liquid films. (Part 1, Classification of flow regimes)," *Bulletin of the JSME*, Vol. 15, No. 83, pp 594-602.
- Ito, R. and Tomura, K., (1979), "Velocity profile in "calming zone" of falling liquid films on inclined plates," *Journal of Chemical Engineering of Japan*, Vol. 12, No. 1, pp 10-13.
- Jackson, M. L., (1955), "Liquid films in viscous flow," *American Institute of Chemical Engineering Journal*, Vol. 1, No. 2, pp 231-240.
- Johnson, G. R. and Crynes, B. L., (1974), "Modelling of a Thin-Film Sulfonation Reactor," *Ind. Eng. Chem., Process Des. Develop.*, Vol. 13, No. 1., pp 6-15.
- Johnson, M. F. G., Schulter, R. A. and Bankoff, S. G., (1997), "Fluorescent imaging system for global measurement of liquid film thickness and dynamic contact angle in free surface flows," *Review of Scientific Instruments*, Vol. 68, No. 11, pp 4097-4102.
- Jones, L. O. and Whitaker, S., (1966), "An experimental study of falling liquid films," *American Institute of Chemical Engineering Journal*, Vol. 12, No. 3, pp 525-529.
- Kamei, S. and Oishi, S., (1954), "Hold-up in a wetted wall tower," *Chemical Engineering (Japan)*, Vol. 18, pp 545-555.
- Kamei, T. and Serizawa, A., (1998), "Two dimensional local instantaneous measurement of liquid film thickness around simulated nuclear fuel rod using ultrasonic transmission technique," *Japan-UK Mini-Seminar*, October 8-9th, Kumatori, Japan.
- Kang, H. C. and Kim, M. H., (1992a), "The development of a flush-wire probe and calibration technique for measuring liquid film thickness," *International Journal of Multiphase Flow*, Vol. 19, No. 3, pp 423-437.
- Kang, H. C. and Kim, M. H., (1992b), "Measurement of three-dimensional wave form and interfacial area in an air-water stratified flow," *Nuclear Engineering and Design*, Vol. 136, pp 347-360.
- Kapitsa, P. L. and Kapitsa, S. P., (1949), "Wave flow of thin layers of viscous fluid," *Zhurn.Eksp.Teor.Fiz*, Vol. 19, No. 2, pp 105-120.

BIBLIOGRAPHY

- Karapantsios, T. D., Paras, S. V. and Karabelas, A. J., (1989), "Statistical characteristics of free falling films at high reynolds numbers," *International Journal of Multiphase Flow*, Vol. 15, No. 1, pp 1-21.
- Karapantsios, T. D. and Karabelas, A. J., (1990), "Surface characteristics of roll waves on free falling films," *International Journal of Multiphase Flow*, Vol. 16, No. 5, pp 835-852.
- Karapantsios, T. D. and Karabelas, A. J., (1995), "Longitudinal characteristics of wavy falling films," *International Journal of Multiphase Flow*, Vol. 21, No. 1, pp 119-127.
- Karimi, G. and Kawaji, M., (1996), "A study of hydrodynamic characteristics of non-conductive falling films in counter-current annular flow," *31st National Heat Transfer Conference*, Houston, Texas, USA, HTD- Vol. 326, pp 205-221.
- Kawaji, M., Ahmad, W., DeJesus, J. M., Sutharshan, B., Lorencez, C. and Ojha, M., (1993), "Flow visualization of two-phase flows using photochromic dye activation method," *Nuclear Engineering and Design*, Vol.141, pp 343-355.
- Keeley, A. M., Waters, N. D., Cummins, P. G., Rennie, G. and Staples, E. J., (1989), "Draining thin films- part 2 laser measurements of film thickness and velocity profile," *Journal of Non-Newtonian Fluid Mechanics*, Vol. 32, pp 79-94.
- Keska, J. K. and Fernando, R. D., (1992), "An experimental study of liquid film thickness measurements in a two-phase flow," *AIChE Symposium Series*, Vol. 88, No. 288, pp 34-43.
- Kirillov, P. L., Smogalev, I. P., Suvorov, M. Ya., Shumsky, R. V. and Stein, Yu. Yu., (1978), "Investigation of steam-water flow characteristics at high pressures," *Proceedings of the 6th International Heat Transfer Conference*, Vol. 1, pp 315-320.
- Kondo, Y., Mori, K., Yagishta, T. and Nakabo, A., (1999), "Effect of liquid viscosity on wave behaviour in gas-liquid two-phase flow," *Proceedings of the 5th ASME/JSME Joint Thermal Engineering Conference*, March 15-19th, San Diego, California, USA.
- Koskie, J. E. Mudawar, I. and Tiederman, W. G., (1989), "Parallel-wire probes for the measurement of thick liquid films," *International Journal of Multiphase Flow*, Vol. 15, No. 4, pp 521-530.
- Kulov, N. N., Maksimov, V. V., Maljusov, V. A. and Zhavoronkov, N. M., (1979), "Pressure drop, mean film thickness and entrainment in downward two-phase flow," *The Chemical Engineering Journal*, Vol. 18, pp 183-188.
- Kvurt, Yu. P., Kholpanov, L. P., Malyusov, V. A. and Zhavoronkov, N. M., (1981), "Influence of the alternating-current on the results of measurement of the thickness of liquid films by the conductivity method," *Journal of Applied Chemistry in the USSR*, Vol. 54, No. 5, pp 872-876.
- Lacey, C. E., Sheintuch, M. and Dukler, A. E., (1991), "Methods of deterministic chaos applied to the flow of thin wavy films," *AIChE Journal*, Vol. 37, No. 4, pp 481-489.

- Lacey, C. E. and Dukler, A. E., (1994), "Flooding in vertical tubes-I: Experimental studies of the entry region," *International Journal of Multiphase Flow*, Vol. 20, No. 2, pp 219-233.
- Laurinat, J. E., Hanratty, T. J., Dallman, J. C., (1984), "Pressure drop and film height measurements for annular gas-liquid flow," *International Journal of Multiphase Flow*, Vol. 10, No. 3, pp 341-356.
- Leskovar, B., Sun, R. K., Kolbe, W. F. and Turko, B., (1979), "Measurement of the thickness of liquid film by means of the capacitance method," *Prepared for the Electric Power Research Institute*, Research project 1379-1, Report No. NP-1212.
- Lilleleht, L. U. and Hanratty, T. J., (1961), "Measurement of interfacial structure for co-current air-water flow," *Journal of Fluid Mechanics*, Vol. 11, No. 1, pp 65-81.
- Lyu, T. H. and Mudawar, I., (1991), "Statistical investigation of the relationship between interfacial waviness and sensible heat transfer to a falling liquid film," *International Journal of Heat and Mass Transfer*, Vol. 34, No. 6, pp 1451-1464.
- Martin, C. J. and Whalley, P. B., (1983), "Wall shear stress measurements in annular two-phase flow," *International conference on the physical modelling of multiphase flow, Coventry, England, April 19-21*, pp 283-300.
- Martin, C. J., (1984), "The non intrusive measurement of wall shear stress and velocity profiles in vertical annular two phase flow," *American Society of Mechanical Engineers, Heat Transfer Division (Publication) HTD*, Vol. 31, pp 47-54.
- Miya, M. Y., Woodmansee, D. E., Hanratty, T. J., (1971), "A model for roll waves in gas-liquid flow," *Chemical Engineering Science*, Vol. 26, pp 1915-1931.
- Mudawar, I. and Houpt, R. A., (1993a), "Measurement of mass and momentum transport in wavy-laminar falling liquid films," *International Journal of Heat and Mass Transfer*, Vol. 36, No. 17, pp 4151-4162.
- Mudawar, I. and Houpt, R. A., (1993b), "Mass and momentum transport in smooth falling liquid films laminarized at relatively high Reynolds numbers," *International Journal of Heat and Mass Transfer*, Vol. 36, No. 14, pp 3437-3448.
- Murav'ev, M. Yu., Vashak, F. and Kulov, N. N., (1984), "Determination of the instantaneous thickness of a falling liquid film with a microelectrode," *Theoretical Foundations of Chemical Engineering*, Vol. 17, No. 6, pp 511-515.
- Nakoryakov, V. E., Pokusaev, B. G. and Alekseenko, S. V., (1976), "Stationary two-dimensional rolling waves on a vertical film of fluid," *Inzhenerno-Fizicheskii Zhurnal*, Vol. 30, No. 5, pp 780-785.
- Nakoryakov, V. E., Pokusaev, B. G., Alekseenko, S. V. and Orlov, V. V., (1977), "Instantaneous velocity profile in a wavy liquid film," *Journal of Engineering Physics*, Vol. 33, No. 5, pp 1012-1016.

- Nash, B. A. and Freeman, G., (1980), "Film thickness measurements for flow rates below wave inception," *UKAEA, Report No. AERE-M 3131*.
- Nedderman, R. M., (1961), "The use of stereoscopic photography for the measurement of velocities in liquids," *Chemical Engineering Science*, Vol. 16, pp 113-119.
- Nedderman, R. M. and Shearer, C. J., (1963), "The motion and frequency of large disturbance waves in annular two-phase flow of air-water mixtures," *Chemical Engineering Science*, Vol. 18, pp 661-670.
- Nencini, F. and Andreussi, P., (1982), "Studies of the behaviour of disturbance waves in annular two-phase flow," *The Canadian Journal of Chemical Engineering*, Vol. 60, pp 459-465.
- Nosoko, T., Yoshimura, P.N., Nagata, T., and Oyakawa, K., (1996), "Characteristics of two-dimensional waves on a falling liquid film," *Chemical Engineering Science*, Vol. 51, No. 5, pp 725-732.
- Nozhat, W. M., (1997), "Measurement of liquid-film thickness by laser interferometry," *Applied Optics*, Vol. 36, No. 30, pp 7864-7869.
- Nusselt, N., (1916), "Die oberflächenkondensation der wasserdampfes," *Zeit. Ver. D. Ing.*, Vol. 60, pp 541-569.
- Ohba, K., Origuchi, T. and Shimanaka, Y., (1984), "Multi-fiber optic liquid film sensor. I," *Proceedings of the 4th Sensor Symposium*, pp 33-37.
- Ohba, K., Origuchi, T. and Takada, H., (1985), "Multi-fiber optic liquid film sensor. II," *Proceedings of the 5th Sensor Symposium*, pp 63-67.
- Ohba, K. and Origuchi, T., (1985), "Multi-fiber optic liquid film sensor for measurement of two-phase annular and stratified flow," *International Symposium of Fluid Control and Measurement, Tokyo, Japan*, pp 1085-1094.
- Ohba, K., Takada, H., Kawakami, N. and Nagae, K., (1992), "Twin fiber optic liquid film sensor for simultaneous measurement of local film thickness and velocity in two-phase annular flow," *The 6th International Symposium for the Application of Laser Techniques to Fluid Mechanics*, Lisbon, Portugal, Vol. 39, No. 1, pp 1-6.
- Ohba, K. and Nagae, K., (1993), "Characteristics and behaviour of the interfacial wave on the liquid film in a vertically upward air-water two-phase annular flow," *Nuclear Engineering and Design*, Vol. 141, pp 17-25.
- Ohba, K., Naimi, F., Morimoto, T., Nakamura, K., (1996), "Dynamic interaction between ripple, ring and disturbance waves in vertically upward air-water annular flow," *Proceedings of the Japan - U.S. Seminar on Two-Phase Flow Dynamics*, July 15-20, Fukuoka, Japan.

- Okada, O. and Fujita, H., (1992), "Behaviour of liquid films in high velocity annular mist flow in a vertical pipe," *Proceedings of the 2nd JSME-KSME thermal engineering conference*, October 19-21, No.2, pp 249-254.
- Oldengarm, J. van Kricken, A. H. and van der Klooster, H. W., (1975), "Velocity profile measurements in a liquid film flow using the laser doppler technique," *Journal of Physics E: Scientific Instruments*, Vol.8, No. 3, pp 203-205.
- Ozgu, M. R., Chen J. C., and Eberhardt, N., (1973), "A capacitance method for measurement of film thickness in two-phase flow," *Review of Scientific Instruments*, Vol. 44, No. 12, pp 1714-1716.
- Pearlman, M. D., (1963), "Dynamic calibration of wave probes," *Department of Naval Architecture and Marine Engineering*, University of M. I. T.
- Perry, R. H. and Green, D., (1984), "Perry's chemical engineers' handbook," *McGraw-Hill International Editions*.
- Pols, R. M., (1998), "Waves in separated two-phase flow", *Ph.D. Thesis*, University of Nottingham.
- Pols, R. M., Hibberd, S. and Azzopardi, B. J., (1998), "Discontinuous wave solutions in stratified and annular two-phase flows," *The Third International Conference on Multiphase Flow*, Lyon, France, June 8-12.
- Popovich, A. T. and Hummel, R.L., (1967), "A new method for non-disturbing turbulent flow measurements very close to the wall," *Chemical Engineering Science*, Vol. 22, pp 21-25.
- Portalski, S., (1963), "Studies of falling liquid film flow," *Chemical Engineering Science*, Vol. 18, pp 787-804.
- Portalski, S. and Clegg, A. J., (1971)," Interfacial area increase in rippled film flow on wetted wall columns," *Chemical Engineering Science*, Vol. 26, pp 773-784.
- Portalski, S. and Clegg, A. J., (1972), "An experimental study of wave inception on falling liquid films," *Chemical Engineering Science*, Vol. 27, pp 1257-1265.
- Portalski, S., (1973), "Phase velocities on liquid films flowing on a smooth vertical plate," *AIChE Journal*, Vol. 19, No. 6, pp 1244-1246.
- Root, L. F. and Kaufman, I., (1992), "Noncontacting low-cost instrument for film thickness measurement," *IEEE Transactions on Instrumentation and Measurement*, Vol. 41, No. 6, pp 1014-1019.
- Roskamp, H., Elsäßer, A., Samenfink, W., Meisl, J., Willmann, M. and Wittig, S., (1998), "An enhanced model for predicting the heat transfer to wavy shear-driven liquid wall films," *Third International Conference on Multiphase Flow, ICMF'98*, Lyon, France, June 8-12, 1998.

- Roy, R. P., Ku, J., Kaufman, I. and Shukla, J., (1986), "Microwave method for measurement of liquid film thickness in gas-liquid flow," *Review of Scientific Instruments*, Vol. 57, No. 5, pp 952-956.
- Salazar, R. P. and Marschall, E., (1975), "Thickness measurement in liquid film flow by laser scattering," *Review of Scientific Instruments*, Vol.46, No. 11, pp 1539-1541.
- Salazar, R. P. and Marschall, E., (1978a), "Time-average local thickness measurement in falling liquid film flow," *International Journal of Multiphase Flow*, Vol. 4, pp 405-412.
- Salazar, R. P. and Marschall, E., (1978b), "Statistical properties of the thickness of a falling liquid film," *Acta Mechanica*, Vol. 29, pp 239-255.
- Samenfink, W., Elsässer, A., Wittig, S., and Dullenkopf, K., (1996), "Internal transport mechanisms of shear-driven liquid films," 8th *International Symposium on Laser Application to Fluid Mechanics*, Lisbon, Portugal, 1998.
- Schmitt, R. L., Stevenson, W. H. and Simmons, H. C., (1982), "Optical measurement of liquid film thickness," *Laser Institute of America (LIA)*, Vol. 33, pp 31-35.
- Schwanbom, E. A., Braun, D., Hamann, E. and Hiby, J. W., (1971), "A double-ray technique for the investigation of liquid boundary layers," *Int. J. Heat. Mass. Transfer*, Vol. 14, pp 998-1001.
- Sekoguchi, K., Takeishi, M. and Ishimatsu, T., (1985), "Interfacial structure in vertical upward annular flow," *PhysicoChemical Hydrodynamics*, Vol. 6., No. 1-2, pp 239-255.
- Sekoguchi, K. and Takeishi, M., (1989), "Interfacial structures in upward huge wave flow and annular flow regimes," *International Journal of Multiphase Flow*, Vol. 15, No. 3, pp 295-305.
- Sekoguchi, K. and Mori, K., (1997), "New development of experimental study on interfacial structure in gas-liquid two-phase flow," *Experimental Heat Transfer, Fluid Mechanics and Thermodynamics*, Edizioni ETS, pp 1177-1187.
- Semena, M. G. and Mel'nichuk, G. A., (1978), "Mean-velocity distributions in a falling film," *Fluid mechanics-Soviet Research*, Vol.7, No.5, pp 145-151.
- Serizawa, A., Kamei, T., Nagane, K., Takahashi, T. and Kawara, Z., (1994), "Non-intrusive measurement of dynamic behaviour of a liquid film," *Proceedings of the German-Japanese Symposium on Multiphase Flow*, Karlsruhe, Germany, pp 63-73.
- Shedd, T. A. and Newell, T. A., (1998), "Automated optical liquid film thickness measurement method," *Review of Scientific Instruments*, Vol. 69, No. 12, pp 4205-4213.
- Solesio, J. N., Flamand, J. C. and Delhaye, J. M., (1978), "Liquid film thickness measurements by means of an x-ray absorption technique," Taken from *Topics in heat transfer and two phase flow*, Author: Bankoff, S. G., pp 193-198.

- Stainthorp, F. P. and Allen, J. M., (1965), "The development of ripples on the surface of a liquid film flowing inside a vertical tube," *Transactions of the Institution of Chemical Engineers*, Vol. 43, ppT85-T91.
- Stainthorp, F. P. and Batt, R. S. W., (1967), "The effect of co-current and counter-current air flow on the wave properties of falling liquid films," *Transactions of the Institution of Chemical Engineers*, Vol. 45, ppT372-T382.
- Starkovich, V. S., (1980), "Ultrasonic liquid film thickness measurements," *Transactions of the American Nuclear Society*, Vol.35, pp 640-641.
- Strumolo, G. S., Ziehl, W. and Dukler, A. E., (1985), "Measurements of a vertical falling film using laser doppler velocimetry," *2nd International Conference on multi-phase flow, London, England, 19-21 June, Paper G3*.
- Sun, R. K., Kolbe, W. F., Leskovar, B. and Turko, B., (1982), "Measurement of thickness of thin water film in two-phase flow by a capacitance method," *IEEE Transactions on Nuclear Science*, Vol. 29, No. 1, pp 688-694.
- Sutharshan, B., Kawaji, M. and Ousaka, A., (1995), "Measurement of circumferential and axial liquid film velocities in horizontal annular flow," *Int. J. Multiphase Flow*, Vol. 21, No. 2, pp 193-206.
- Swanson, R. W., (1966), "Characteristics of the gas-liquid interface in two phase annular flow," *Ph.D. Thesis*, University of Delaware, Delaware.
- Tailby, S. R., and Portalski, S., (1960), "The hydrodynamics of liquid films flowing on a vertical surface", *Trans. Instn Chem. Engrs*, Vol.38, pp 324-330.
- Takahama, H. and Kato, S., (1980), "Longitudinal flow characteristics of vertically falling liquid films without concurrent gas flow," *International Journal of Multiphase Flow*, Vol.6, pp 203-215.
- Takahama, H., Okada, O., Fujita, H. and Mizuno, A., (1983), "Study on annular mist flow in pipe (2nd report, Behaviour of water film in the non-equilibrium region of downward annular mist flow with low water flow rate)," *Bulletin of the Japanese Society of Mechanical Engineers*, Vol. 26, No. 222, pp 2091-2099
- Talens, F. I., Hreczuch, W., Bekierz, G. and Szymanowski, J., (1998), "Ethoxylation of alcohols in falling film reactors," *Journal of Dispersion Science*, Vol. 19, No. 4, pp 423-433.
- Talens, F. I., (1999), "The modelling of falling film chemical reactors," *Chemical Engineering Science*, Vol. 54, pp 1871-1881.
- Telles, A. S. and Dukler, A. E., (1970), "Statistical characteristics of thin, vertical, wavy, liquid films," *Industrial Engineering Chemistry Fundamentals*, Vol. 9, No. 3, pp 412-421.
- Than, C. F., Tee., K. C., Low, K. S. and Tso, C. P., (1993), "Optical measurement of slope, thickness and velocity in liquid film flow," *Smart Materials and Structures*, Vol. 2., pp 13-21.

BIBLIOGRAPHY

- Thomas, W. C. and Rice, J. C., (1973), "Application of the hydrogen-bubble technique for velocity measurements in thin liquid films," *American Society of Chemical Engineers, Journal of Applied Mechanics*, Vol. 95, pp 321-325.
- Thwaites, G. R., (1973), "Drag reduction in single- and two-phase flow," *Ph.D. Thesis*, University of Cambridge.
- Thwaites, G.R., Kulov, N. N., and Nedderman, R. M., (1976), "Liquid film properties in two-phase annular flow," *Chemical Engineering Science*, Vol. 31, pp. 481-486.
- Ueda, T. and Tanaka, T., (1974), "Studies of liquid film flow in two-phase annular and annular-mist flow regions (Part 1, downflow in a vertical tube)," *Bulletin of the JSME*, Vol.17, No.107, pp 603-613.
- Ueda, T. and Tanaka, T., (1975), "Measurements of velocity, temperature and velocity fluctuation distributions in falling liquid films", *International Journal of Multiphase Flow*, Vol.2, pp 261-272.
- Unterberg, W., (1961), "Studies of liquid film flow and evaporation with reference to saline water distillations," *Internal Report*, Report No. N 61-26, University of California, Department of Engineering, Los Angeles, USA.
- Wallis, G. G., (1969), "One Dimensional Two-Phase Flow", *McGraw Hill Book Company*, New York, USA.
- Wasden, F. K. and Dukler, A. E., (1989), "Insights into the hydrodynamics of free falling wavy films," *AIChE Journal*, Vol. 35, No. 2, pp 187-195.
- Wasden, F. K. and Dukler, A. E., (1992), "An experimental study of mass transfer from a wall into a wavy falling film," *Chemical Engineering Science*, Vol. 47, No. 17, pp 4323-4331.
- Webb, D., (1970a), "Studies of the characteristics of downward annular two-phase flow: Part I: The effect of length," *UKAEA*, Report No. AERE-R 6426.
- Webb, D., (1970b), "Studies of the characteristics of downward annular two-phase flow: Part II: Description of experimental apparatus and its calibration," *UKAEA*, Report No. AERE-R 6426.
- Webb, D., (1970c), "Studies of the characteristics of downward annular two-phase flow: Part III: Measurements off entrainment rate, pressure gradient, probability distribution of film thickness and disturbance wave inception," *UKAEA*, Report No. AERE-R 6426.
- Webb, D. R. and Hewitt, G. F., (1975), "Downwards co-current annular flow," *International Journal of Multiphase Flow*, Vol. 2, pp 35-49.
- Whalley, P. B., Hewitt, G. F. and Hutchinson, P., (1973), "Experimental wave and entrainment measurements in vertical annular two-phase flow," *UKAEA*, Report No. AERE-R 7521.

BIBLIOGRAPHY

- Wilkes, J. O. and Nedderman, R. M., (1962), "The measurement of velocities in thin films of liquid," *Chemical Engineering Science*, Vol. 17, pp 177-187.
- Wittig, S., Himmelsbach, J., Noll, B., Feld, D. J. and Samenfink, W., (1992), "Motion and evaporation of shear-driven liquid films in turbulent gases," *ASME-Journal of Engineering for Gas Turbines and Power*, Vol. 114, pp. 395-400.
- Wolf, A., Jayanti, S. and Hewitt, G. F., (1996), " On the nature of ephemeral waves in vertical annular flow," *International Journal of Multiphase Flow*, Vol. 22, No. 2, pp 325-333.
- Yablounik, R. M. and Khaimov, V. A., (1972), "Application of the electric contact method in measuring the thickness of thin fluid films," *Heat Transfer - Soviet Research*, Vol. 4, No. 3, pp 70-75.
- Yih, S. and Hsu, T., (1985), "Gas absorption into wavy and turbulent non-newtonian falling liquid films in a wetted-wall column," *Chemical engineering communications*, Vol. 34, No. 1-6, pp 65-76.
- Yu, S. C. M. and Tso, C. P., (1995), "Simulation of fiber optic sensors in determination of thin liquid film thicknesses," *Advances in Engineering Software*, Vol. 22, pp 55-62.
- Zabaras, G., Dukler, A. E. and Moalem-Maron, D., (1986), "Vertical upward co-current gas-liquid annular flow," *American Institute of Chemical Engineers Journal*, Vol. 32, No. 5, pp 829-843.

Appendix A

DETERMINATION OF LIQUID PHYSICAL PROPERTIES

This appendix presents a detailed description of the methodology for acquisition of the physical properties (*i.e.* density, viscosity, surface tension) of the fluids utilised in this study. The majority of the well established physical properties of water were acquired straight from literature sources.

This author would like to once more acknowledge our gratitude to Unilever Plc. for their provision of the organic liquids utilised in this study.

A.1 DENSITY

The density of the organic liquids was obtained by simply weighing the liquid required to completely fill a known volume, in this case a 50cm³ density flask. A number of measurements were taken for each fluid at 20°C, with the results presented in Table A.1.

Table A.1: Density values at 20°C.

	Dodecylbenzene	Ethoxylated Alcohol
Density (kg/m ³)	830	860

A.2 VISCOSITY

The viscosity of the organic liquids, over the range of experimental temperatures observed in this study, were obtained through measurement with a dial viscometer (Brookfield, Model-LVT).

Figure A.1 summarises the results graphically. The lines represent the equations suggested by Talens (1999) in a recently published study on the modelling of falling film chemical reactors.

Figure A.1 clearly shows that good agreement between the current study and Talens (1999) was obtained for dodecylbenzene. However, for ethoxylated lauryl alcohol an approximately 10% higher viscosity value was measured than suggested by Talens (1999). Correspondence by this author with Dr. F. Talens highlighted that this apparent measurement discrepancy was most likely due to the use of differing grades of ethoxylate, as the exact blend of carbon groups used in the synthesis is manufacturer specific

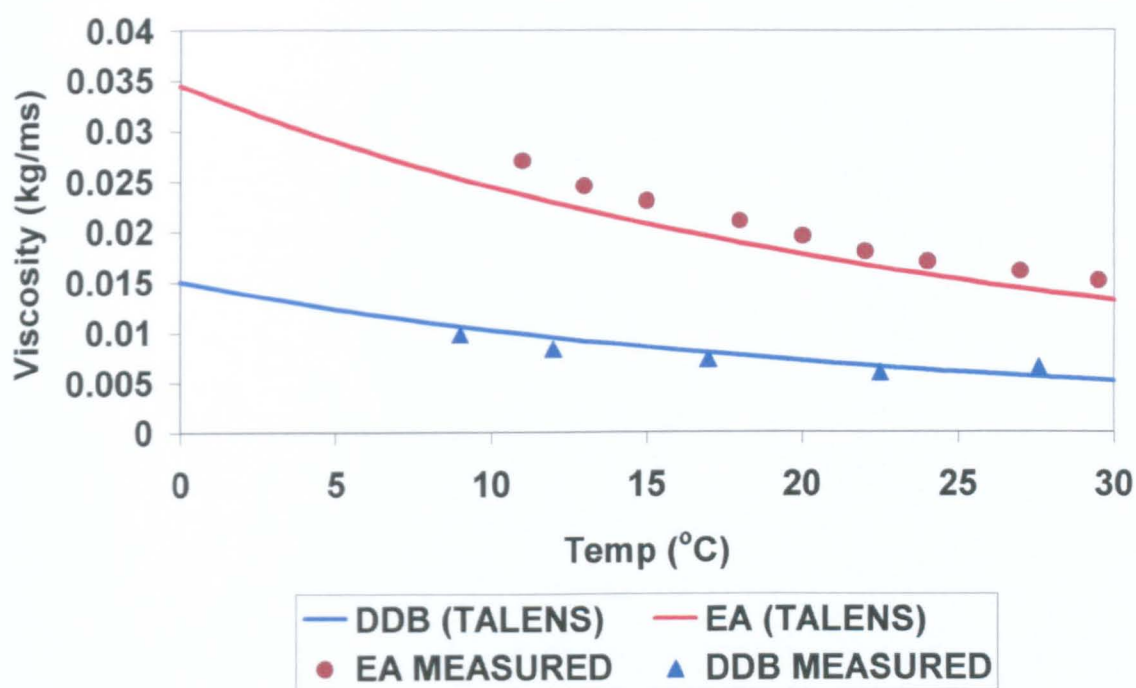


Figure A.1: Comparison of measured viscosity and suggested values of Talens (1999) versus temperature.

A.3 SURFACE TENSION

Surface tension properties of the organic liquids at room temperature were acquired using the torsion balance (White Electrical Instrument Co. Ltd., Model-OS).

A number of readings were made for each fluid, with the mean values obtained presented in Table A.2. Both dyed and un-dyed fluids were measured to determine the influence of the dye on surface activity. Table A.2 shows that little measurable difference

Appendix A: Determination of Liquid Physical Properties

was observed between respective dyed and un-dyed fluid at the dye concentrations utilised in this study.

Table A.2: Liquid Surface Tension at 20°C.

	Water	Dodecylbenzene	Ethoxylated Alcohol
Un-Dyed	0.072	0.0310	0.0325
Dyed	0.071	0.0315	0.0325

Appendix B

OPTICAL EFFECTS

B.1 INTRODUCTION

The purpose of this appendix is to review the number of investigations undertaken into potential limitations of the light absorption film thickness measurement technique employed in the current work due to optical phenomena.

The first section of this appendix examines the conditions required for the total exclusion of light to occur from a point or region of film image. The second section to this appendix attempts to quantify the error identified by Clegg (1969), and discussed in the review of his technique in Section 3.5.1, associated with the application of a lighting arrangement where the light source and camera are behind and in front of the falling film respectively.

B.2 LIGHT EXCLUSION FROM THE IMAGE

It became apparent from examination of the film images obtained during the course of the current work that for certain flow conditions a number of the wave-substrate boundaries were represented on the film image by points totally devoid of colour/light. (*e.g.* Figure B.1)

The mechanism identified as the probable cause of this phenomenon was that the angle between the air-liquid interface and the vertical was sufficiently large to prevent light refraction into the film. Determination of the exact interface contact angle conditions required is possible with the aid of simple trigonometrically based analysis of the standard photographic arrangement, which is shown schematically for reference in Figure B.2.

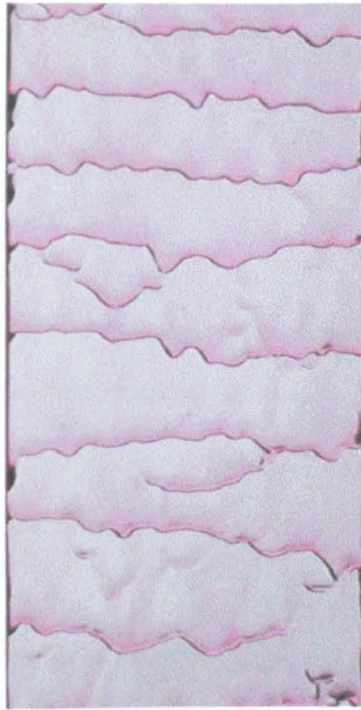


Figure B.1: Film image displaying total exclusion of light at much of the leading edge wave-substrate boundaries.

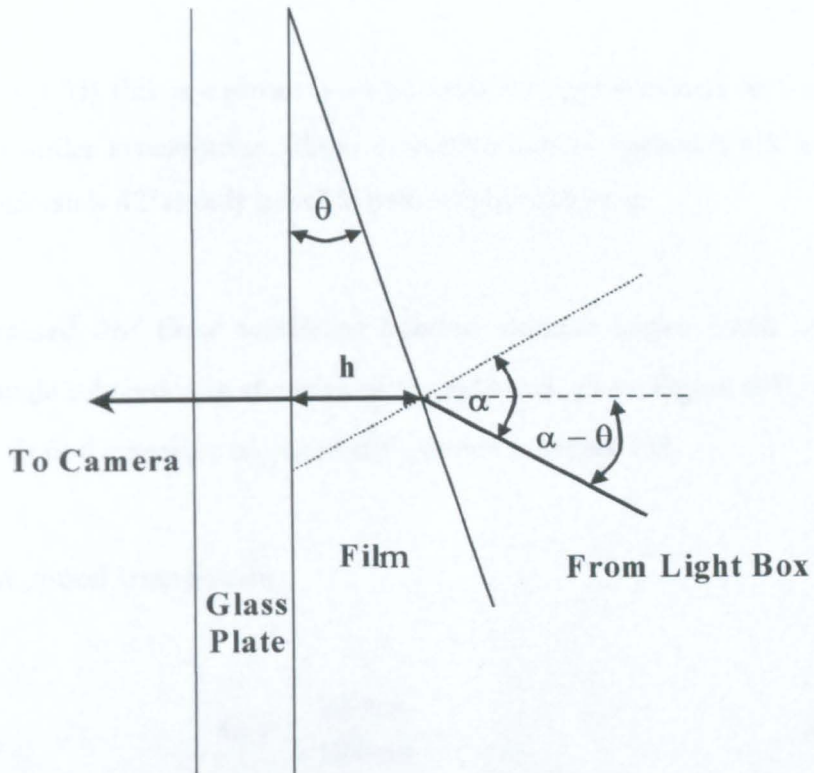


Figure B.2: Trigonometrically based analysis of the standard photographic arrangement.

From Figure B.2, Snell's law of refraction dictates:

$$\frac{\text{Sin}\alpha}{\text{Sin}\theta} = \mu \quad (\text{B.1})$$

where, α is the angle of incidence to the film, θ the angle of refraction (equivalent to the interface contact angle) and μ is the refractive index.

If $\alpha \geq 90^\circ$, no light can enter the film.

Therefore, the maximum interface contact angle θ_{max} to allow light entry can be determined from:

$$\theta_{\text{max}} = \text{Sin}^{-1}\left(\frac{1}{\mu}\right) \quad (\text{B.2})$$

For water ($\mu = 1.33$) this is equivalent to an angle of approximately 49° , and for the organic liquids under investigation whose refractive indices approach 1.5, a maximum angle of approximately 42° is only possible before light exclusion.

It was also realised that these maximum interface contact angles could be restricted further if the angle subtended by the edge of the light box, γ (see Figure B.3), was smaller than the angle from the horizontal plane ($\alpha-\theta$) shown in Figure B.2.

For the current optical arrangement:

$$\tan \gamma = \frac{500\text{mm}}{600\text{mm}} \quad (\text{B.3})$$

$$\therefore \gamma = 39.8^\circ.$$

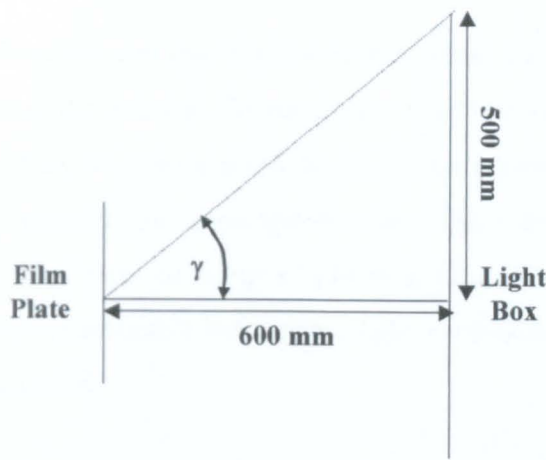


Figure B.3: Schematic of the angle subtended by the edge of the light box.

Utilising Snell's Law of refraction, it is possible to calculate values for $(\alpha - \theta)$ at a given interface contact angle (θ) up to the maximum allowable contact angle (θ_{max}) to determine whether the angle subtended by the edge of the light box (γ) is ever surpassed. The results of these calculations, applicable to the photographic arrangement and liquids utilised in the current study, are presented graphically in Figure B.4.

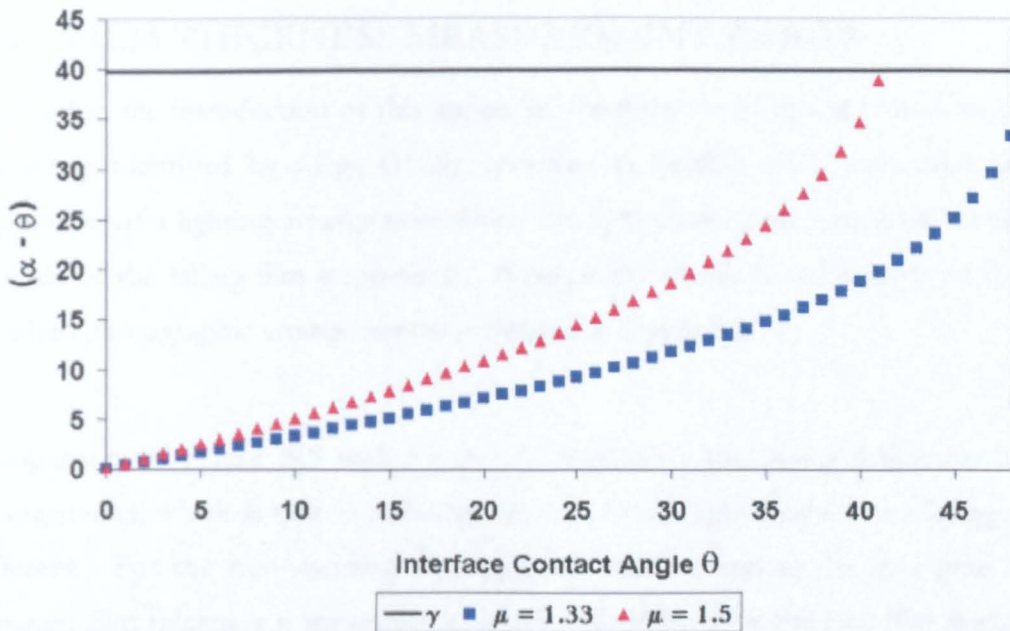


Figure B.4: Graphical summary of the influence of the angle subtended by the edge of the light box on maximum allowable interface contact angle.

Figure B.4 clearly demonstrates that for the current study the photographic arrangement does not further limit the measurable maximum interface contact angle for the liquid films investigated. This was more good fortune than judgement, as this phenomenon was not considered prior to the investigation. By simply doubling the distance of the light box from the film plate or using a light box source half the size, the maximum interface contact angle measurable before total light exclusion would be between 5 and 8 degrees lower than quoted.

As the film substrate is essentially flat, interface contact angles as high as those quoted could only be obtainable with the slopes associated with disturbance wave structure. The current work would tend to indicate that high enough interface angles are possible under certain flow conditions, however, they are limited to wave-substrate boundaries particularly at the leading edge of the disturbance wave. Fortunately, when this phenomenon occurs only a minute fraction (typically less than 0.1 %) of the film image is affected and has a negligible influence on global measurement parameters. However, correction is necessary to prevent distortion of wave profiles and heights. The method of correction employed in this study is detailed in Chapter 5.

B.3 FILM THICKNESS MEASUREMENT ERROR

As stated in the introduction of this appendix, the purpose of this section is to quantify the errors identified by Clegg (1969), reviewed in Section 3.5.1, associated with the application of a lighting arrangement where the light source and camera are behind and in front of the falling film respectively. A trigonometrically based analysis of this non-standard photographic arrangement is presented in Figure B.5.

Comparison of Figure B.5 with Figure B.2 highlights the major difference between arrangements, which is that the absorption path of the light through the falling film, is different. For the non-standard photographic arrangement shown in Figure B.5, an apparent film thickness is measured, z , which will differ from the true film thickness, y , dependent on the interface contact angle, θ , and the refraction angle, α .

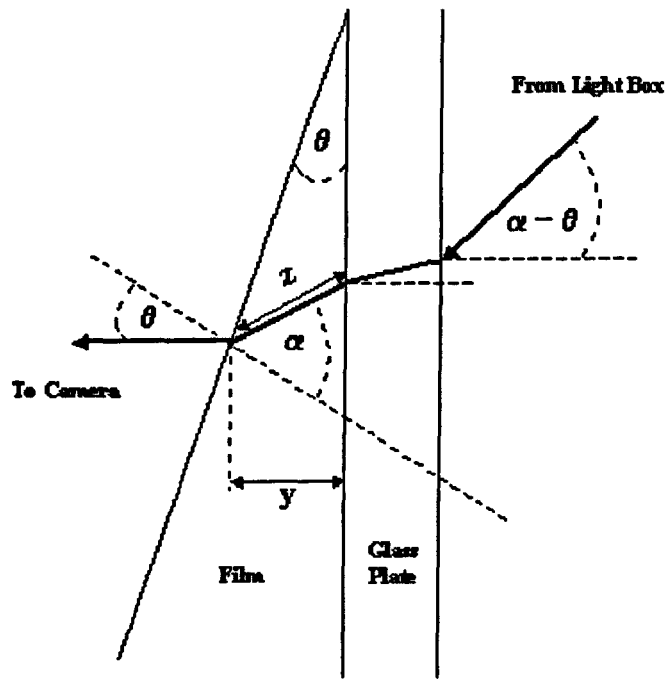


Figure B.5: Trigonometrically based analysis of the non-standard photographic arrangement.

Trigonometry gives the exact relationship between apparent and true film thickness measurement as:

$$\frac{y}{z} = \cos(\alpha - \theta) \quad (\text{B.4})$$

Expansion of the R.H.S gives:

$$\frac{y}{z} = \cos\alpha \cos\theta + \sin\alpha \sin\theta \quad (\text{B.5})$$

By application of Snell's Law of Refraction (Eqn. B.1):

$$\frac{y}{z} = \cos\theta \sqrt{1 - \mu^2 \sin^2\theta} + \mu \sin^2\theta \quad (\text{B.6})$$

Therefore, by application of Eqn. B.6, the relationship between y/z (measurement error) and interface contact angle θ can easily be determined for any given physical conditions. Figure B.6 shows this relationship graphically for two refractive indices representative of the current study.

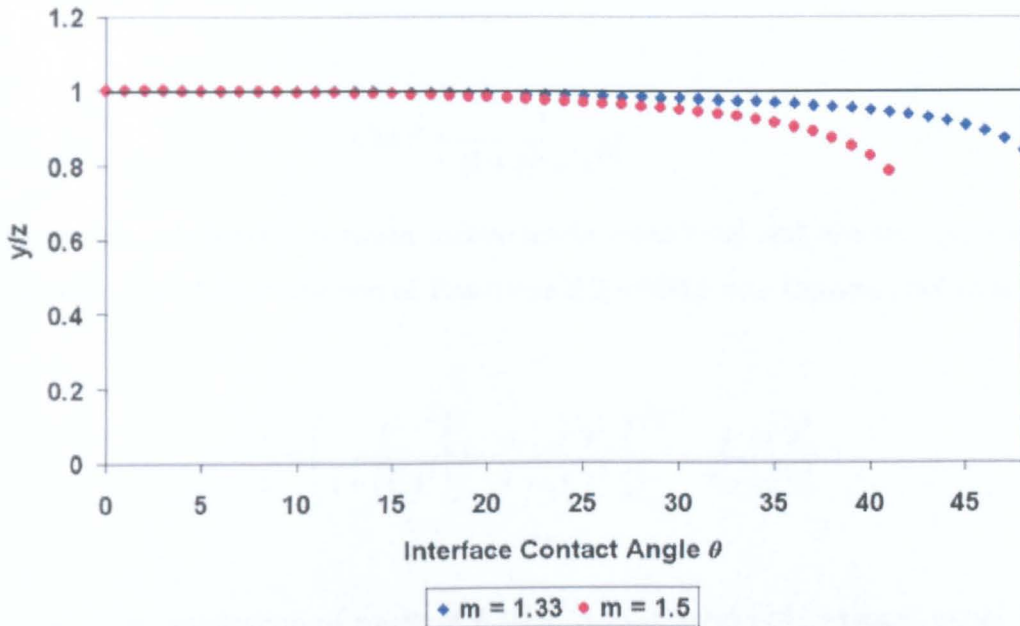


Figure B.6: Measurement error (y/z) as a function of interface contact angle (θ).

The figure clearly demonstrates that measurement error is negligible, irrespective of liquid film refractive index, except at interface contact angles approaching the maximum allowable contact angle, where over-prediction of the film thickness can be as large as twenty percent. The maximum allowable interface contact angles, θ_{\max} , are identical to the values determined in the previous section.

To correct actual film thickness values it is simpler to work in terms of interface gradients rather than contact angles. The relationship between interface gradient, y' , and contact angle is:

$$\tan\theta = y' \quad \text{B.7}$$

Therefore:

$$\sin\theta = \frac{y'}{(1+(y')^2)^{0.5}} \quad \text{B.8}$$

And similarly:

$$\cos\theta = \frac{1}{(1+(y')^2)^{0.5}} \quad \text{B.9}$$

Therefore, the relationship between measurement error (y/z) and interface gradient (y') can be determined by substitution of Equations B.8 and B.9 into Equation B.6 to give:

$$\frac{y}{z} = \left(\frac{1}{1+(y')^2} \left[1 - \frac{\mu^2 (y')^2}{1+(y')^2} \right] \right)^{0.5} + \frac{\mu (y')^2}{1+(y')^2} \quad \text{B.10}$$

However, direct application of equation B.10 to correct measured/apparent values (z) to true values (y) is complicated by the fact that the interface gradient data available relates to the apparent data and not the real data required by Equation B.10. Therefore, an iteration-based method was developed to correct the measurement error by estimation of the true gradient values from the measurement data. The method consisted of the following steps:

- (i) Take the first estimate $Y(1)_i = Z_i$ (*i.e.* the measured value) at all points i .
- (ii) Calculate the gradient y'_i at each point from:

$$\frac{Y(1)_{i+1} - Y(1)_{i-1}}{2\delta} \quad \text{B.11}$$

where, δ is the vertical distance between two points.

- (iii) Substitute gradient y'_i into equation B.10 to calculate y_i/z_i .

- (iv) Obtain new estimate $Y(2)_i = (y_i/z_i) \times Z_i$.
- (v) Iterate from step (ii) until no further change in $Y(n)_i$.

Naturally, for the large number of data points generated from the spatial images in this study a calculation of this type is best suited to a computer based solution. Application of the method on sample data from this study suggested that a small number (1-3) of iterations are necessary before solution. Figure B.7 presents a graphical comparison of a sample of raw and corrected data taken from a longitudinal strip of a air/dodecylbenzene film image.

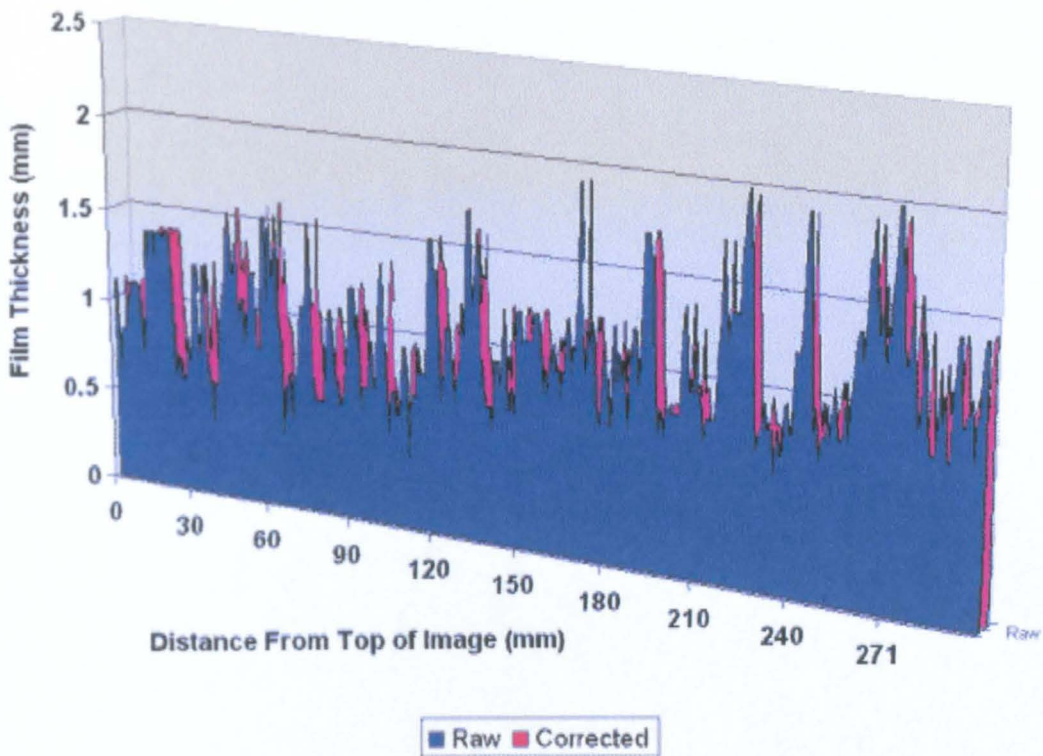


Figure B.7: Comparison plot of a sample of raw and corrected film thickness data after application of the correction for light arrangement induced measurement error.

It is clear from Figure B.7 that any measurement error is negligible, with both film thickness values and interface shape remaining consistent. Therefore, it was concluded that correction of the dodecylbenzene data taken using this lighting arrangement was unnecessary.

Appendix C

SUMMARY OF MEASUREMENT DATA

C.1 INTRODUCTION

The purpose of this appendix is to provide a summary of the spatial film thickness and wave celerity data obtained for the three investigated liquids. For ease of reference, the summaries are presented for each liquid in turn in tabular form.

C.2 WATER

C.2.1 Data from Spatial Film Thickness Measurements

Run No.	Liquid Flowrate (l/min)	Liquid Flowrate (kg/ms)	Liquid Film Reynolds Number	Air Mass Flowrate (kg/s)	Air Velocity (m/s)	Mean Film Thickness (mm)	Mean Disturbance Height (mm)	Mean Disturbance Wave Min Start (mm)	Mean Disturbance Wave Max (mm)	Mean Disturbance Wave Finish (mm)	Mean Disturbance Wave Cell Number	Mean Disturbance Wave Length (mm)	Mean Substrate Height (mm)	Mean Substrate Min Value (mm)	Mean Substrate Max Value (mm)	Mean Substrate Cell Number	Mean Substrate Length (mm)	Number of Disturbance Wavelets	% Area Covered By Disturbance Waves	% Area Covered By Substrate	% Volume Contained in Disturbance Waves
1	1	0.11	122	0.000	0.0	0.288	0.363	0.259	0.439	0.238	40	24.3	0.208	0.192	0.285	39	23.3	1487	50.59%	49.41%	27.42%
2	1	0.11	122	0.000	0.0	0.296	0.391	0.262	0.453	0.259	38	22.6	0.197	0.169	0.302	40	23.6	1611	50.88%	49.12%	33.35%
3	1	0.11	122	0.000	0.0	0.28	0.368	0.245	0.431	0.220	34	20.2	0.193	0.169	0.284	32	19.1	1848	52.28%	47.72%	30.81%
4	1.7	0.19	207	0.000	0.0	0.395	0.504	0.367	0.573	0.338	34	20.5	0.291	0.274	0.403	44	26.4	1532	44.07%	55.93%	24.38%
5	1.7	0.19	207	0.000	0.0	0.395	0.486	0.335	0.537	0.311	38	22.6	0.277	0.246	0.376	41	24.8	1480	46.78%	53.22%	24.10%
6	1.7	0.19	207	0.000	0.0	0.368	0.493	0.334	0.561	0.312	34	20.5	0.262	0.246	0.390	42	24.9	1595	45.72%	54.28%	26.70%
7	2.1	0.23	266	0.000	0.0	0.369	0.482	0.337	0.539	0.320	34	20.3	0.275	0.254	0.386	41	24.3	1601	45.43%	54.57%	25.49%
8	2.1	0.23	266	0.000	0.0	0.415	0.592	0.399	0.665	0.397	46	27.2	0.300	0.266	0.435	66	39.6	1066	40.65%	59.35%	27.62%
9	2.1	0.23	266	0.000	0.0	0.398	0.507	0.369	0.567	0.370	36	21.3	0.308	0.267	0.415	46	27.3	1522	45.31%	54.69%	22.65%
10	3	0.33	366	0.000	0.0	0.443	0.552	0.418	0.629	0.405	47	28.2	0.350	0.330	0.456	53	31.9	1165	45.95%	54.05%	20.95%
11	3	0.33	366	0.000	0.0	0.408	0.516	0.369	0.580	0.360	36	21.3	0.307	0.293	0.420	40	23.8	1617	48.21%	51.79%	24.63%
12	3	0.33	366	0.000	0.0	0.47	0.625	0.456	0.711	0.424	41	24.8	0.344	0.336	0.493	54	32.3	1294	45.00%	55.00%	26.90%
13	4.2	0.46	610	0.000	0.0	0.504	0.649	0.478	0.731	0.468	45	27.1	0.386	0.371	0.523	54	32.5	1186	44.95%	55.05%	23.45%
14	4.2	0.46	610	0.000	0.0	0.537	0.668	0.504	0.745	0.509	33	19.7	0.417	0.411	0.558	40	24.0	1727	47.58%	52.42%	22.24%
15	4.2	0.46	610	0.000	0.0	0.531	0.668	0.498	0.747	0.487	38	23.0	0.406	0.401	0.553	41	24.8	1480	47.69%	52.31%	23.53%
16	5.2	0.57	632	0.000	0.0	0.583	0.710	0.580	0.794	0.541	42	26.4	0.485	0.469	0.601	44	26.7	1369	48.33%	51.67%	20.31%
17	5.2	0.57	632	0.000	0.0	0.6	0.733	0.576	0.832	0.583	41	24.5	0.481	0.471	0.630	44	26.4	1362	47.44%	52.56%	19.92%
18	5.2	0.57	632	0.000	0.0	0.603	0.756	0.573	0.818	0.567	29	17.2	0.480	0.473	0.628	40	24.1	1770	42.69%	57.31%	19.76%
19	6.6	0.72	802	0.000	0.0	0.696	0.837	0.663	0.950	0.666	44	26.5	0.567	0.560	0.722	49	29.5	1293	47.32%	52.68%	18.59%
20	6.6	0.72	802	0.000	0.0	0.67	0.799	0.649	0.906	0.621	38	22.7	0.546	0.531	0.689	36	22.9	1641	49.07%	50.93%	18.53%
21	6.6	0.72	802	0.000	0.0	0.658	0.769	0.623	0.855	0.629	27	16.0	0.553	0.534	0.689	29	17.6	2173	48.66%	51.34%	15.97%
22	8.1	0.89	984	0.000	0.0	0.78	1.110	0.730	1.262	0.691	61	36.5	0.553	0.612	0.784	70	42.0	799	40.81%	59.19%	29.14%
23	8.1	0.89	984	0.000	0.0	0.837	1.104	0.803	1.279	0.757	53	31.9	0.623	0.664	0.856	61	36.7	993	44.42%	55.58%	25.53%
24	8.1	0.89	984	0.000	0.0	0.748	0.913	0.724	1.010	0.744	30	18.1	0.613	0.603	0.790	39	23.2	1770	44.89%	55.11%	18.00%

Run No.	Liquid Flowrate (l/min)	Liquid Flowrate (kg/ms)	Liquid Film Reynolds Number	Air Mass Flowrate (kg/s)	Air Velocity (m/s)	Mean Film Thickness (mm)	Mean Disturbance Height (mm)	Mean Disturbance Wave Min Start (mm)	Mean Disturbance Wave Max Finish (mm)	Mean Disturbance Wave Cell Number	Mean Disturbance Wave Length (mm)	Mean Substrate Height (mm)	Mean Substrate Min Value (mm)	Mean Substrate Max Value (mm)	Mean Substrate Cell Number	Mean Substrate Length (mm)	Number of Disturbance Wavelets	% Area Covered By Disturbance Waves	% Area Covered By Substrate	% Volume Contained in Disturbance Waves	
25	1	0.11	122	0.006	2.6	0.297	0.376	0.273	0.444	0.265	49	29.4	0.209	0.219	0.302	43	25.6	1296	62.96%	47.05%	29.60%
26	1	0.11	122	0.006	2.6	0.317	0.411	0.307	0.463	0.296	43	25.6	0.226	0.244	0.335	46	27.8	1366	48.96%	61.04%	28.57%
27	1	0.11	122	0.006	2.6	0.335	0.421	0.308	0.466	0.311	45	26.9	0.237	0.248	0.347	41	24.6	1420	63.41%	46.59%	29.33%
28	1.7	0.19	207	0.006	2.6	0.347	0.447	0.356	0.506	0.324	47	26.3	0.257	0.274	0.363	55	33.2	1199	47.48%	52.52%	26.00%
29	1.7	0.19	207	0.006	2.6	0.384	0.510	0.374	0.573	0.347	48	28.7	0.290	0.276	0.396	69	35.2	1117	44.97%	55.03%	26.94%
30	1.7	0.19	207	0.006	2.6	0.35	0.549	0.321	0.634	0.349	51	30.5	0.202	0.226	0.360	61	40.6	996	42.61%	57.39%	42.24%
31	2.1	0.23	255	0.006	2.6	0.431	0.694	0.420	0.682	0.433	50	29.8	0.336	0.318	0.452	88	52.7	895	36.90%	63.10%	22.09%
32	2.1	0.23	255	0.006	2.6	0.404	0.513	0.389	0.599	0.355	43	25.7	0.311	0.292	0.419	51	30.6	1261	46.13%	53.87%	23.07%
33	2.1	0.23	255	0.006	2.6	0.393	0.533	0.379	0.596	0.346	33	19.7	0.301	0.271	0.407	62	31.1	1448	39.87%	60.13%	23.54%
34	3	0.33	365	0.006	2.6	0.47	0.642	0.466	0.736	0.477	53	31.5	0.369	0.351	0.489	86	51.4	836	36.92%	63.08%	21.44%
35	3	0.33	365	0.006	2.6	0.474	0.690	0.457	0.664	0.456	46	29.1	0.373	0.369	0.496	57	34.4	1145	46.65%	53.35%	21.36%
36	3	0.33	365	0.006	2.6	0.451	0.566	0.436	0.621	0.424	35	20.7	0.359	0.344	0.479	45	27.0	1540	44.73%	55.27%	20.53%
37	4.2	0.46	510	0.006	2.6	0.593	0.711	0.575	0.787	0.571	35	21.0	0.493	0.483	0.613	50	29.9	1402	41.26%	58.74%	15.43%
38	4.2	0.46	510	0.006	2.6	0.541	0.665	0.524	0.737	0.490	46	27.4	0.431	0.424	0.559	50	29.9	1225	47.05%	52.95%	20.35%
39	4.2	0.46	510	0.006	2.6	0.562	0.710	0.537	0.773	0.514	33	19.5	0.441	0.425	0.585	39	23.3	1642	44.95%	55.05%	21.52%
40	5.2	0.57	632	0.006	2.6	0.577	0.712	0.592	0.795	0.545	44	26.3	0.461	0.469	0.602	51	30.7	1253	46.15%	53.85%	20.07%
41	5.2	0.57	632	0.006	2.6	0.599	0.729	0.582	0.832	0.554	42	25.5	0.470	0.482	0.620	41	24.7	1393	49.70%	50.30%	21.49%
42	5.2	0.57	632	0.006	2.6	0.596	0.710	0.571	0.786	0.560	31	18.8	0.491	0.493	0.624	32	19.3	1914	60.41%	49.59%	19.37%
43	6.6	0.72	802	0.006	2.6	0.691	0.807	0.669	0.907	0.673	31	18.5	0.602	0.567	0.725	42	25.0	1677	43.43%	56.57%	12.88%
44	6.6	0.72	802	0.006	2.6	0.695	0.809	0.653	0.912	0.661	37	22.0	0.556	0.555	0.710	35	21.2	1654	60.89%	49.11%	18.80%
45	6.6	0.72	802	0.006	2.6	0.677	0.815	0.670	0.901	0.642	30	18.1	0.560	0.553	0.713	37	22.1	1809	45.74%	54.26%	17.23%
46	8.1	0.89	984	0.006	2.6	0.752	0.906	0.719	1.105	0.757	60	29.9	0.578	0.538	0.779	71	42.7	1015	42.45%	57.55%	23.14%
47	8.1	0.89	984	0.006	2.6	0.793	1.057	0.841	1.245	0.749	52	31.0	0.590	0.560	0.800	76	45.6	951	41.35%	58.65%	24.86%
48	8.1	0.89	984	0.006	2.6	0.747	1.096	0.729	1.205	0.727	43	25.7	0.520	0.532	0.780	68	40.7	1093	39.35%	60.65%	30.45%
51	1	0.11	122	0.012	4.9	0.328	0.413	0.310	0.461	0.302	77	46.0	0.210	0.235	0.331	49	29.4	904	68.28%	41.72%	36.07%
52	1.7	0.19	207	0.012	4.9	0.38	0.486	0.371	0.544	0.369	50	29.9	0.279	0.298	0.396	49	29.2	1171	49.05%	50.95%	26.72%
53	1.7	0.19	207	0.012	4.9	0.36	0.473	0.349	0.547	0.342	61	36.4	0.248	0.269	0.370	60	36.2	971	49.47%	50.53%	30.92%
54	1.7	0.19	207	0.012	4.9	0.386	0.500	0.361	0.555	0.361	44	26.6	0.277	0.291	0.399	46	27.5	1313	48.30%	51.70%	28.25%
55	2.1	0.23	255	0.012	4.9	0.413	0.547	0.419	0.609	0.375	51	30.3	0.297	0.302	0.424	69	35.2	1091	46.31%	53.69%	28.03%
56	2.1	0.23	255	0.012	4.9	0.395	0.515	0.356	0.579	0.367	58	35.0	0.289	0.294	0.409	62	37.4	955	46.32%	53.68%	26.79%
57	2.1	0.23	255	0.012	4.9	0.404	0.539	0.379	0.602	0.374	50	30.3	0.286	0.286	0.417	56	33.9	1105	46.84%	53.16%	29.33%
58	3	0.33	365	0.012	4.9	0.453	0.623	0.452	0.710	0.437	46	27.9	0.346	0.346	0.470	78	46.6	987	36.56%	61.44%	23.58%
59	3	0.33	365	0.012	4.9	0.471	0.688	0.467	0.756	0.445	52	31.0	0.360	0.351	0.489	83	49.5	861	37.34%	62.66%	23.62%
60	3	0.33	365	0.012	4.9	0.474	0.687	0.475	0.843	0.450	48	26.6	0.320	0.339	0.492	76	45.6	1043	41.82%	58.18%	32.36%
61	4.2	0.46	510	0.012	4.9	0.513	0.646	0.503	0.710	0.487	44	26.4	0.417	0.412	0.541	55	33.0	1131	41.76%	58.24%	18.54%
62	4.2	0.46	510	0.012	4.9	0.533	0.639	0.519	0.706	0.501	41	24.4	0.443	0.433	0.559	47	27.9	1953	46.17%	53.83%	16.98%
63	4.2	0.46	510	0.012	4.9	0.531	0.666	0.520	0.724	0.503	35	21.1	0.425	0.424	0.555	45	26.8	1568	46.04%	53.96%	20.03%
64	5.2	0.57	632	0.012	4.9	0.575	0.705	0.574	0.775	0.545	38	22.6	0.484	0.460	0.602	56	33.6	1300	41.14%	58.86%	15.81%
65	5.2	0.57	632	0.012	4.9	0.629	0.757	0.605	0.875	0.589	44	26.3	0.515	0.494	0.651	49	29.6	1273	46.93%	53.07%	18.05%
66	5.2	0.57	632	0.012	4.9	0.595	0.689	0.553	0.763	0.548	28	17.1	0.495	0.469	0.613	31	18.8	2051	49.07%	50.93%	17.11%
67	6.6	0.72	802	0.012	4.9	0.694	0.820	0.666	0.915	0.667	36	21.8	0.598	0.552	0.727	43	25.5	1493	45.67%	54.33%	15.27%
68	6.6	0.72	802	0.012	4.9	0.697	0.819	0.662	0.944	0.652	40	24.0	0.583	0.564	0.723	42	24.9	1434	48.19%	51.81%	16.32%
69	6.6	0.72	802	0.012	4.9	0.655	0.810	0.635	0.896	0.633	33	19.6	0.524	0.516	0.692	44	25.5	1666	45.71%	54.29%	19.96%
70	8.1	0.89	984	0.012	4.9	0.721	0.963	0.700	1.054	0.683	45	27.1	0.546	0.545	0.754	57	34.0	1108	42.06%	57.94%	24.33%
71	8.1	0.89	984	0.012	4.9	0.75	0.911	0.721	1.050	0.701	44	26.3	0.604	0.575	0.774	48	28.7	1287	47.47%	52.53%	19.43%
72	8.1	0.89	984	0.012	4.9	0.761	0.952	0.721	1.027	0.722	32	18.9	0.621	0.609	0.795	44	26.2	1594	42.22%	57.78%	18.36%

Run No.	Liquid Flowrate (l/min)	Liquid Flowrate (kg/ms)	Liquid Film Reynolds Number	Air Mass Flowrate (kg/s)	Air Velocity (m/s)	Mean Film Thickness (mm)	Mean Disturbance Height (mm)	Mean Disturbance Wave Min Start (mm)	Mean Disturbance Wave Max Finish (mm)	Mean Disturbance Wave Cell Number	Mean Disturbance Wave Length (mm)	Mean Substrate Height (mm)	Mean Substrate Min Value (mm)	Mean Substrate Max Value (mm)	Mean Substrate Cell Number	Mean Substrate Length (mm)	Number of Disturbance Wavelets	% Area Covered By Disturbance Waves	% Area Covered By Substrate	% Volume Contained in Disturbance Waves	
74	1	0.11	122	0.018	7.4	0.285	0.344	0.277	0.382	0.261	53	31.8	0.208	0.226	0.298	44	26.2	1263	66.18%	43.82%	26.81%
75	1	0.11	122	0.018	7.4	0.259	0.318	0.232	0.361	0.232	40	23.7	0.154	0.207	0.269	27	16.0	1863	61.89%	38.11%	36.80%
76	1.7	0.19	207	0.018	7.4	0.371	0.462	0.365	0.526	0.344	44	26.2	0.304	0.276	0.386	57	34.4	1148	42.07%	67.93%	17.92%
77	1.7	0.19	207	0.018	7.4	0.346	0.437	0.328	0.481	0.308	52	31.0	0.264	0.246	0.357	64	32.1	1082	46.97%	63.03%	23.49%
78	1.7	0.19	207	0.018	7.4	0.368	0.456	0.368	0.526	0.337	36	21.0	0.298	0.288	0.386	43	25.6	1612	47.43%	62.57%	21.65%
79	2.1	0.23	265	0.018	7.4	0.403	0.520	0.390	0.601	0.365	42	25.1	0.321	0.296	0.415	58	34.6	1169	41.14%	68.86%	20.31%
80	2.1	0.23	265	0.018	7.4	0.377	0.478	0.372	0.549	0.343	54	32.5	0.302	0.274	0.396	73	44.0	930	42.39%	67.61%	19.79%
81	2.1	0.23	265	0.018	7.4	0.356	0.491	0.338	0.541	0.320	37	22.3	0.266	0.264	0.376	69	35.2	1280	39.97%	60.03%	25.26%
83	3	0.33	365	0.018	7.4	0.443	0.549	0.429	0.633	0.414	47	28.0	0.359	0.328	0.487	56	33.8	1121	43.99%	66.01%	18.87%
84	3	0.33	365	0.018	7.4	0.43	0.543	0.419	0.611	0.392	43	26.6	0.332	0.317	0.452	48	28.7	1291	46.35%	63.65%	22.74%
85	4.2	0.46	510	0.018	7.4	0.523	0.657	0.513	0.740	0.495	45	26.8	0.412	0.395	0.544	53	31.7	1208	45.31%	64.69%	21.23%
86	4.2	0.46	510	0.018	7.4	0.518	0.639	0.505	0.726	0.491	45	27.2	0.426	0.413	0.541	55	33.2	1133	43.15%	66.85%	17.74%
87	4.2	0.46	510	0.018	7.4	0.518	0.633	0.495	0.702	0.478	39	23.4	0.420	0.401	0.541	46	27.2	1399	45.89%	64.11%	18.87%
88	5.2	0.57	632	0.018	7.4	0.595	0.666	0.552	0.724	0.539	29	17.7	0.490	0.472	0.596	36	21.7	1799	44.55%	65.45%	13.25%
89	5.2	0.57	632	0.018	7.4	0.595	0.688	0.544	0.769	0.529	31	18.6	0.463	0.447	0.596	38	22.8	1740	45.36%	64.64%	18.06%
90	5.2	0.57	632	0.018	7.4	0.561	0.661	0.537	0.735	0.527	27	16.5	0.474	0.464	0.590	32	19.5	2015	46.54%	63.46%	15.51%
91	6.6	0.72	802	0.018	7.4	0.646	0.753	0.614	0.842	0.623	31	18.7	0.551	0.522	0.673	36	21.4	1802	47.31%	62.69%	14.79%
92	6.6	0.72	802	0.018	7.4	0.635	0.732	0.617	0.829	0.613	34	20.3	0.549	0.526	0.688	40	24.3	1646	46.91%	63.09%	13.52%
93	6.6	0.72	802	0.018	7.4	0.66	0.775	0.631	0.866	0.632	27	16.3	0.585	0.536	0.695	35	20.9	1986	45.42%	64.58%	14.45%
94	8.1	0.89	984	0.018	7.4	0.704	0.874	0.712	0.961	0.686	40	23.9	0.662	0.649	0.732	49	29.2	1355	45.41%	64.59%	20.13%
95	8.1	0.89	984	0.018	7.4	0.74	0.914	0.694	1.095	0.724	46	27.4	0.603	0.580	0.767	58	35.0	1145	43.90%	66.10%	18.45%
96	8.1	0.89	984	0.018	7.4	0.739	0.860	0.730	0.996	0.700	32	18.9	0.619	0.680	0.773	42	25.4	1667	44.24%	66.76%	16.22%
104	1.7	0.19	207	0.024	10.0	0.336	0.420	0.323	0.458	0.313	33	19.7	0.255	0.268	0.358	37	22.4	1782	49.21%	60.79%	24.17%
105	1.7	0.19	207	0.024	10.0	0.304	0.395	0.288	0.444	0.284	48	29.0	0.212	0.233	0.313	53	31.9	1233	60.09%	49.91%	30.15%
106	1.7	0.19	207	0.024	10.0	0.326	0.413	0.306	0.442	0.298	33	19.7	0.238	0.269	0.343	34	20.6	1818	60.20%	49.80%	26.95%
107	2.1	0.23	265	0.024	10.0	0.339	0.450	0.322	0.600	0.302	35	21.2	0.252	0.255	0.358	49	29.2	1473	43.73%	66.27%	25.54%
108	2.1	0.23	265	0.024	10.0	0.385	0.499	0.378	0.642	0.355	32	19.4	0.302	0.300	0.409	48	28.7	1538	41.77%	68.23%	21.37%
109	2.1	0.23	265	0.024	10.0	0.386	0.490	0.367	0.610	0.367	31	18.8	0.305	0.312	0.409	41	24.7	1667	43.86%	66.14%	21.02%
110	3	0.33	365	0.024	10.0	0.443	0.561	0.428	0.612	0.411	37	22.1	0.356	0.345	0.464	48	28.6	1362	42.14%	67.86%	19.50%
111	3	0.33	365	0.024	10.0	0.422	0.528	0.405	0.680	0.386	35	20.9	0.326	0.332	0.438	42	25.1	1627	47.62%	62.38%	22.79%
112	3	0.33	365	0.024	10.0	0.421	0.543	0.408	0.591	0.395	45	26.9	0.310	0.331	0.445	53	32.0	1264	47.70%	62.30%	26.40%
113	4.2	0.46	510	0.024	10.0	0.47	0.581	0.443	0.644	0.440	35	21.3	0.361	0.379	0.491	38	23.0	1838	49.89%	60.31%	23.26%
114	4.2	0.46	510	0.024	10.0	0.516	0.625	0.492	0.694	0.485	31	18.4	0.412	0.418	0.538	34	20.6	1892	48.77%	61.23%	20.13%
115	4.2	0.46	510	0.024	10.0	0.47	0.576	0.448	0.641	0.442	34	20.4	0.361	0.377	0.493	36	21.9	1772	60.67%	49.33%	23.18%
116	5.2	0.57	632	0.024	10.0	0.522	0.611	0.496	0.675	0.489	29	17.4	0.434	0.422	0.546	30	18.0	2054	60.15%	49.85%	17.00%
117	5.2	0.57	632	0.024	10.0	0.524	0.614	0.495	0.672	0.488	26	15.8	0.439	0.419	0.546	30	17.7	2203	48.63%	61.37%	16.24%
118	5.2	0.57	632	0.024	10.0	0.524	0.635	0.492	0.702	0.503	27	16.2	0.428	0.409	0.554	35	20.8	2041	46.36%	63.64%	18.31%
119	6.6	0.72	802	0.024	10.0	0.619	0.734	0.590	0.818	0.596	26	15.9	0.522	0.502	0.650	34	20.5	2086	45.76%	64.24%	15.67%
120	6.6	0.72	802	0.024	10.0	0.614	0.729	0.577	0.819	0.584	26	15.6	0.513	0.483	0.643	32	19.3	2127	46.46%	63.54%	16.34%
121	6.6	0.72	802	0.024	10.0	0.627	0.757	0.599	0.845	0.589	30	17.8	0.528	0.486	0.656	39	23.4	1728	43.15%	66.85%	15.76%
122	8.1	0.89	984	0.024	10.0	0.611	0.814	0.581	0.928	0.573	38	22.9	0.437	0.465	0.640	46	27.9	1433	45.96%	64.04%	28.36%
123	8.1	0.89	984	0.024	10.0	0.642	1.028	0.713	1.094	0.593	32	19.2	0.457	0.420	0.662	75	45.2	1210	32.51%	67.49%	28.92%
124	8.1	0.89	984	0.024	10.0	0.636	0.976	0.588	1.121	0.578	44	26.7	0.403	0.420	0.650	80	35.9	1080	40.76%	69.25%	36.71%

Run No.	Liquid Flowrate (l/min)	Liquid Flowrate (kg/ms)	Liquid Film Reynolds Number	Air Mass Flowrate (kg/s)	Air Velocity (m/s)	Mean Film Thickness (mm)	Mean Disturbance Height (mm)	Mean Disturbance Wave Min Start (mm)	Mean Disturbance Wave Max Finish (mm)	Mean Disturbance Wave Min Cell Number	Mean Disturbance Wave Length (mm)	Mean Substrate Height (mm)	Mean Substrate Min Value (mm)	Mean Substrate Max Value (mm)	Mean Substrate Cell Number	Mean Substrate Length (mm)	Number of Disturbance Wavelets	% Area Covered By Disturbance Waves	% Area Covered By Substrate	% Volume Contained in Disturbance Waves	
125	1.7	0.19	207	0.030	12.5	0.34	0.419	0.326	0.468	0.309	33	19.9	0.276	0.269	0.354	40	23.7	1612	44.91%	55.09%	18.89%
126	1.7	0.19	207	0.030	12.5	0.297	0.396	0.262	0.457	0.258	45	27.3	0.196	0.207	0.306	41	24.6	1373	52.45%	47.55%	37.44%
127	1.7	0.19	207	0.030	12.5	0.312	0.362	0.279	0.427	0.278	31	18.3	0.226	0.244	0.325	28	16.5	2147	65.11%	44.89%	27.55%
128	2.1	0.23	255	0.030	12.5	0.333	0.426	0.310	0.466	0.296	49	29.4	0.237	0.244	0.341	47	28.2	1236	50.97%	49.03%	28.93%
129	2.1	0.23	255	0.030	12.5	0.33	0.418	0.319	0.478	0.293	47	26.0	0.232	0.241	0.337	41	24.8	1366	53.10%	46.90%	29.93%
130	2.1	0.23	255	0.030	12.5	0.33	0.427	0.293	0.472	0.266	37	22.3	0.213	0.240	0.336	33	20.0	1755	54.80%	45.20%	35.54%
131	3	0.33	365	0.030	12.5	0.423	0.577	0.403	0.643	0.379	41	24.5	0.302	0.438	0.686	39	39.4	1146	39.39%	60.61%	23.54%
132	3	0.33	365	0.030	12.5	0.455	0.611	0.437	0.696	0.414	36	23.0	0.358	0.326	0.474	56	33.5	1160	38.20%	61.80%	21.24%
133	3	0.33	365	0.030	12.5	0.381	0.518	0.359	0.571	0.341	38	22.6	0.295	0.269	0.393	57	34.1	1221	38.72%	61.28%	22.86%
134	4.2	0.46	510	0.030	12.5	0.493	0.630	0.469	0.702	0.461	48	26.0	0.357	0.377	0.507	47	28.0	1228	49.95%	50.05%	27.66%
135	4.2	0.46	510	0.030	12.5	0.498	0.601	0.450	0.699	0.448	41	24.5	0.382	0.372	0.507	43	25.6	1415	48.51%	51.49%	21.81%
136	4.2	0.46	510	0.030	12.5	0.515	0.690	0.476	0.769	0.472	40	23.9	0.363	0.378	0.535	47	28.1	1393	46.55%	53.45%	29.55%
137	5.2	0.57	632	0.030	12.5	0.563	0.794	0.517	1.015	0.484	67	40.0	0.367	0.367	0.562	67	40.1	816	45.75%	54.25%	34.70%
138	5.2	0.57	632	0.030	12.5	0.511	0.707	0.467	0.855	0.452	49	29.2	0.344	0.347	0.511	55	33.0	1125	45.98%	54.01%	32.57%
139	5.2	0.57	632	0.030	12.5	0.568	0.773	0.508	0.893	0.514	40	24.1	0.381	0.389	0.580	43	26.0	1413	47.78%	52.22%	32.98%
140	6.6	0.72	802	0.030	12.5	0.593	1.038	0.488	1.227	0.485	53	31.9	0.381	0.313	0.576	88	52.8	721	32.21%	67.79%	35.74%
141	6.6	0.72	802	0.030	12.5	0.598	0.952	0.542	1.120	0.510	45	27.0	0.425	0.382	0.607	78	46.8	870	32.89%	67.11%	28.99%
143	8.1	0.89	964	0.030	12.5	0.635	1.007	0.582	1.160	0.568	49	29.3	0.434	0.421	0.639	77	46.0	857	35.19%	64.81%	31.75%
144	8.1	0.89	964	0.030	12.5	0.651	1.070	0.575	1.226	0.553	53	31.8	0.438	0.406	0.649	84	50.5	758	33.76%	66.24%	32.77%
145	8.1	0.89	964	0.030	12.5	0.687	1.044	0.630	1.366	0.750	55	32.8	0.441	0.433	0.692	81	48.4	888	40.82%	59.18%	35.83%
146	2.1	0.23	255	0.036	15.2	0.377	0.461	0.379	0.502	0.356	36	21.9	0.300	0.314	0.397	42	25.1	1660	47.79%	52.21%	20.41%
147	2.1	0.23	255	0.036	15.2	0.4	0.506	0.401	0.558	0.370	40	23.8	0.303	0.320	0.419	46	27.9	1439	47.99%	52.01%	24.35%
148	2.1	0.23	255	0.036	15.2	0.364	0.464	0.346	0.513	0.333	41	24.6	0.253	0.290	0.379	39	23.6	1536	52.93%	47.07%	30.68%
149	3	0.33	365	0.036	15.2	0.493	0.593	0.474	0.667	0.464	46	27.7	0.395	0.400	0.509	50	30.3	1209	46.90%	53.10%	18.25%
150	3	0.33	365	0.036	15.2	0.482	0.690	0.477	0.653	0.458	36	21.3	0.408	0.399	0.508	49	29.3	1372	40.89%	59.11%	15.44%
151	3	0.33	365	0.036	15.2	0.44	0.534	0.419	0.594	0.410	40	24.1	0.368	0.349	0.457	49	29.4	1204	43.38%	56.62%	16.37%
152	4.2	0.46	510	0.036	15.2	0.5	0.796	0.525	0.994	0.442	45	26.7	0.372	0.329	0.513	89	53.2	889	33.30%	66.70%	25.58%
153	4.2	0.46	510	0.036	15.2	0.492	0.720	0.452	0.874	0.429	46	27.6	0.376	0.337	0.499	77	46.0	876	33.83%	66.17%	23.65%
154	4.2	0.46	510	0.036	15.2	0.447	0.627	0.406	0.717	0.391	36	21.6	0.317	0.310	0.461	52	31.0	1386	41.98%	58.02%	29.11%
155	5.2	0.57	632	0.036	15.2	0.512	0.727	0.501	0.914	0.445	51	30.7	0.358	0.337	0.519	68	40.7	971	41.74%	58.26%	30.08%
156	5.2	0.57	632	0.036	15.2	0.53	0.811	0.491	0.928	0.455	40	23.9	0.367	0.345	0.548	63	37.9	1101	36.83%	63.17%	30.86%
157	5.2	0.57	632	0.036	15.2	0.462	0.677	0.419	0.831	0.415	34	20.2	0.338	0.317	0.474	57	33.9	1294	36.57%	63.43%	26.83%
158	6.6	0.72	802	0.036	15.2	0.651	0.974	0.505	1.278	0.582	54	32.4	0.450	0.431	0.652	77	46.0	845	38.38%	61.62%	30.90%
159	6.6	0.72	802	0.036	15.2	0.625	0.886	0.581	0.987	0.576	31	18.8	0.482	0.465	0.643	55	32.8	1362	35.55%	64.45%	22.92%
160	6.6	0.72	802	0.036	15.2	0.718	1.103	0.657	1.309	0.627	40	23.7	0.501	0.452	0.723	65	39.0	1085	36.09%	63.91%	30.25%
161	8.1	0.89	964	0.036	15.2	0.795	1.236	0.742	1.397	0.707	46	27.5	0.574	0.561	0.806	80	48.0	857	33.35%	66.65%	27.77%
162	8.1	0.89	964	0.036	15.2	0.844	1.266	0.778	1.505	0.727	37	22.2	0.625	0.570	0.855	65	38.8	1097	34.13%	65.87%	25.92%
163	8.1	0.89	964	0.036	15.2	0.829	1.182	0.742	1.287	0.749	52	31.1	0.582	0.565	0.828	71	42.6	943	41.05%	58.94%	29.75%

Run No.	Liquid Flowrate (l/min)	Liquid Flowrate (kg/ms)	Liquid Film Reynolds Number	Air Mass Flowrate (kg/s)	Air Velocity (m/s)	Mean Film Thickness (mm)	Mean Disturbance Height (mm)	Mean Disturbance Wave Min Start (mm)	Mean Disturbance Wave Max (mm)	Mean Disturbance Wave Min Finish (mm)	Mean Disturbance Wave Cell Number	Mean Disturbance Wave Length (mm)	Mean Substrate Height (mm)	Mean Substrate Min Value (mm)	Mean Substrate Max Value (mm)	Mean Substrate Cell Number	Mean Substrate Length (mm)	Number of Disturbance Wavelets	% Area Covered By Disturbance Waves	% Area Covered By Substrate	% Volume Contained in Disturbance Waves
164	3	0.33	365	0.042	17.4	0.322	0.467	0.268	0.515	0.241	28	16.7	0.219	0.179	0.320	36	22.9	1869	43.52%	66.48%	32.17%
165	3	0.33	365	0.042	17.4	0.545	0.912	0.483	1.083	0.454	40	23.7	0.398	0.356	0.548	79	47.6	899	29.90%	70.10%	29.74%
166	3	0.33	365	0.042	17.4	0.349	0.454	0.315	0.605	0.305	36	21.2	0.251	0.249	0.363	41	24.7	1631	48.44%	61.56%	28.18%
167	4.2	0.46	510	0.042	17.4	0.481	0.748	0.432	0.891	0.421	35	21.2	0.346	0.325	0.495	67	40.1	1129	33.34%	66.66%	27.93%
168	4.2	0.46	510	0.042	17.4	0.5	0.663	0.471	0.787	0.451	33	20.1	0.384	0.374	0.518	47	28.5	1475	41.49%	58.51%	23.15%
169	4.2	0.46	510	0.042	17.4	0.555	0.811	0.514	0.941	0.483	31	16.5	0.417	0.362	0.569	54	32.5	1360	34.98%	65.02%	24.83%
170	5.2	0.57	632	0.042	17.4	0.783	1.107	0.670	1.338	0.661	60	30.1	0.545	0.512	0.756	70	41.8	920	38.76%	61.24%	28.55%
171	5.2	0.57	632	0.042	17.4	0.718	1.147	0.629	1.302	0.605	37	21.9	0.512	0.466	0.723	70	42.0	1057	32.46%	67.54%	28.70%
172	5.2	0.57	632	0.042	17.4	0.673	1.012	0.616	1.217	0.591	49	29.3	0.513	0.490	0.678	85	50.9	780	32.02%	67.98%	23.74%
173	6.6	0.72	802	0.042	17.4	0.721	1.043	0.665	1.243	0.640	45	27.0	0.543	0.509	0.733	72	43.0	943	35.63%	64.37%	24.71%
174	6.6	0.72	802	0.042	17.4	0.507	0.772	0.600	0.872	0.580	26	15.6	0.477	0.467	0.627	36	21.8	2035	44.34%	55.66%	21.55%
175	6.6	0.72	802	0.042	17.4	0.783	1.237	0.754	1.494	0.716	38	23.1	0.588	0.536	0.793	80	47.9	991	32.04%	67.96%	27.33%

C.2.2 Disturbance Wave Celerity Data

Run No.	Liquid Flowrate (l/min)	Liquid Flowrate (kg/m s)	Liquid Film Reynolds Number	Air Mass Flowrate (kg/s)	Air Velocity (m/s)	Mean Wave Celerity (m/s)
1	2.1	0.23	254	0.000	0.0	1.39
2	3.0	0.32	359	0.000	0.0	1.40
3	3.6	0.40	440	0.000	0.0	1.42
4	4.2	0.46	508	0.000	0.0	1.35
5	4.7	0.51	568	0.000	0.0	1.27
6	5.7	0.63	695	0.000	0.0	1.44
7	6.6	0.72	803	0.000	0.0	1.48
8	7.4	0.81	898	0.000	0.0	1.58
9	8.1	0.89	983	0.000	0.0	1.60
10	8.7	0.96	1062	0.000	0.0	1.66
11	9.3	1.02	1135	0.000	0.0	1.72

Run No.	Liquid Flowrate (l/min)	Liquid Flowrate (kg/m s)	Liquid Film Reynolds Number	Air Mass Flowrate (kg/s)	Air Velocity (m/s)	Mean Wave Celerity (m/s)
12	2.1	0.23	254	0.025	10.8	1.23
13	3.0	0.32	359	0.025	10.8	1.25
14	3.6	0.40	440	0.025	10.8	1.25
15	4.2	0.46	508	0.025	10.8	1.38
16	4.7	0.51	568	0.025	10.8	1.45
17	5.7	0.63	695	0.025	10.8	1.58
18	6.6	0.72	803	0.025	10.8	1.63
19	7.4	0.81	898	0.025	10.8	1.72
20	8.1	0.89	983	0.025	10.8	1.77
21	8.7	0.96	1062	0.025	10.8	1.84
22	9.3	1.02	1135	0.025	10.8	1.91

Run No.	Liquid Flowrate (l/min)	Liquid Flowrate (kg/m s)	Liquid Film Reynolds Number	Air Mass Flowrate (kg/s)	Air Velocity (m/s)	Mean Wave Celerity (m/s)
23	2.1	0.23	254	0.031	13.0	1.22
24	3.0	0.32	359	0.031	13.0	1.24
25	3.6	0.40	440	0.031	13.0	1.34
26	4.2	0.46	508	0.031	13.0	1.38
27	4.7	0.51	568	0.031	13.0	1.51
28	5.7	0.63	695	0.031	13.0	1.57
29	6.6	0.72	803	0.031	13.0	1.67
30	7.4	0.81	898	0.031	13.0	1.73
31	8.1	0.89	983	0.031	13.0	1.80
32	8.7	0.96	1062	0.031	13.0	1.85
33	9.3	1.02	1135	0.031	13.0	1.93

45	2.1	0.23	254	0.047	20.0	1.59
46	3.0	0.32	359	0.047	20.0	1.67
47	3.6	0.40	440	0.047	20.0	1.82
48	4.2	0.46	508	0.047	20.0	1.85
49	4.7	0.51	568	0.047	20.0	1.94
50	5.7	0.63	695	0.047	20.0	1.99
51	6.6	0.72	803	0.047	20.0	2.04
52	7.4	0.81	898	0.047	20.0	2.12
53	8.1	0.89	983	0.047	20.0	2.15
54	8.7	0.96	1062	0.047	20.0	2.21
55	9.3	1.02	1135	0.047	20.0	2.28

67	2.1	0.23	254	0.078	33.0	2.04
68	3.0	0.32	359	0.078	33.0	2.28
69	3.6	0.40	440	0.078	33.0	2.32
70	4.2	0.46	508	0.078	33.0	2.44
71	4.7	0.51	568	0.078	33.0	2.52
72	5.7	0.63	695	0.078	33.0	2.58
73	6.6	0.72	803	0.078	33.0	2.66
74	7.4	0.81	898	0.078	33.0	2.79
75	8.1	0.89	983	0.078	33.0	2.82
76	8.7	0.96	1062	0.078	33.0	2.96
77	9.3	1.02	1135	0.078	33.0	3.08

Run No.	Liquid Flowrate (l/min)	Liquid Flowrate (kg/m s)	Liquid Film Reynolds Number	Air Mass Flowrate (kg/s)	Air Velocity (m/s)	Mean Wave Celerity (m/s)
34	2.1	0.23	254	0.039	16.4	1.33
35	3.0	0.32	359	0.039	16.4	1.40
36	3.6	0.40	440	0.039	16.4	1.50
37	4.2	0.46	508	0.039	16.4	1.54
38	4.7	0.51	568	0.039	16.4	1.59
39	5.7	0.63	695	0.039	16.4	1.62
40	6.6	0.72	803	0.039	16.4	1.69
41	7.4	0.81	898	0.039	16.4	1.72
42	8.1	0.89	983	0.039	16.4	1.80
43	8.7	0.96	1062	0.039	16.4	1.96
44	9.3	1.02	1135	0.039	16.4	2.01

56	2.1	0.23	254	0.065	27.5	1.91
57	3.0	0.32	359	0.065	27.5	2.12
58	3.6	0.40	440	0.065	27.5	2.24
59	4.2	0.46	508	0.065	27.5	2.28
60	4.7	0.51	568	0.065	27.5	2.30
61	5.7	0.63	695	0.065	27.5	2.39
62	6.6	0.72	803	0.065	27.5	2.55
63	7.4	0.81	898	0.065	27.5	2.66
64	8.1	0.89	983	0.065	27.5	2.72
65	8.7	0.96	1062	0.065	27.5	2.79
66	9.3	1.02	1135	0.065	27.5	2.82

C.3 DODECYLBENZENE

C.3.1 Data from Spatial Film Thickness Measurements

Run No.	Liquid Flowrate (l/min)	Liquid Flowrate (kg/ms)	Liquid Film Reynolds Number	Air Mass Flowrate (kg/s)	Air Velocity (m/s)	Mean Film Thickness (mm)	Mean Disturbance Height (mm)	Mean Disturbance Wave Min Start (mm)	Mean Disturbance Wave Max Finish (mm)	Mean Disturbance Wave Cell Number	Mean Disturbance Wave Length (mm)	Mean Substrate Height (mm)	Mean Substrate Min Value (mm)	Mean Substrate Max Value (mm)	Mean Substrate Cell Number	Mean Substrate Length (mm)	Number of Disturbance Wavelets	% Area Covered By Disturbance Waves	% Area Covered By Substrate	% Volume Contained in Disturbance Waves	
1	1	0.09	13	0.000	0.0	0.819	0.764	0.521	0.976	0.497	21	12.9	0.513	0.431	0.642	29	17.6	2337	42.07%	57.93%	17.06%
2	1	0.09	13	0.000	0.0	0.833	0.793	0.552	0.978	0.525	20	11.9	0.521	0.452	0.654	29	17.3	2476	40.99%	59.01%	17.61%
3	1	0.09	13	0.000	0.0	0.864	0.846	0.585	1.056	0.537	21	12.8	0.534	0.454	0.680	34	20.4	2140	36.90%	61.90%	18.37%
6	1.7	0.15	22	0.000	0.0	0.732	0.997	0.522	1.365	0.556	33	19.5	0.543	0.450	0.734	43	25.6	1659	42.67%	57.33%	25.69%
7	1.7	0.15	22	0.000	0.0	0.766	1.01	0.695	1.276	0.651	24	14.6	0.604	0.535	0.790	37	22.2	1956	39.84%	60.16%	21.12%
8	1.7	0.15	22	0.000	0.0	0.752	1.007	0.682	1.296	0.628	26	15.7	0.691	0.505	0.771	39	23.5	1626	40.17%	59.83%	22.75%
11	2.1	0.19	27	0.000	0.0	0.811	1.1	0.689	1.501	0.583	38	22.6	0.692	0.480	0.803	46	27.5	1383	44.18%	55.82%	28.22%
12	2.1	0.19	27	0.000	0.0	0.826	1.116	0.765	1.409	0.675	30	18.3	0.616	0.549	0.844	43	26.1	1642	42.07%	57.93%	25.42%
13	2.1	0.19	27	0.000	0.0	0.835	1.132	0.765	1.410	0.672	29	17.4	0.624	0.555	0.849	41	24.8	1696	41.43%	58.57%	25.21%
16	3	0.27	39	0.000	0.0	0.916	1.232	0.811	1.635	0.683	42	26.3	0.669	0.551	0.917	50	29.8	1263	44.82%	55.18%	28.04%
17	3	0.27	39	0.000	0.0	0.907	1.227	0.835	1.495	0.760	34	20.6	0.69	0.604	0.935	50	29.9	1441	41.59%	58.42%	25.09%
19	3	0.27	39	0.000	0.0	0.971	1.197	0.789	1.427	0.701	29	17.3	0.669	0.580	0.899	44	26.3	1634	39.50%	60.50%	24.45%
21	3.6	0.33	47	0.000	0.0	0.909	1.21	0.868	1.370	0.795	29	17.1	0.691	0.641	0.943	42	24.9	1791	42.92%	57.08%	25.00%
22	3.6	0.33	47	0.000	0.0	0.956	1.257	0.882	1.503	0.803	32	18.9	0.732	0.649	0.995	44	26.3	1609	42.65%	57.35%	23.42%
23	3.6	0.33	47	0.000	0.0	0.979	1.313	0.908	1.526	0.792	30	18.3	0.723	0.651	0.992	41	24.4	1699	43.22%	56.78%	26.07%
26	4.2	0.39	54	0.000	0.0	1.019	1.403	0.933	1.629	0.836	40	24.2	0.726	0.638	1.031	51	30.9	1275	43.13%	56.87%	28.69%
27	4.2	0.39	54	0.000	0.0	1.023	1.393	0.968	1.607	0.857	36	21.6	0.785	0.695	1.058	52	31.4	1316	39.84%	60.16%	23.29%
28	4.2	0.39	54	0.000	0.0	0.989	1.309	0.936	1.543	0.851	33	19.9	0.758	0.703	1.032	45	27.3	1494	41.88%	58.12%	23.25%
31	4.7	0.43	61	0.000	0.0	1.051	1.396	0.939	1.699	0.829	46	27.7	0.789	0.672	1.088	54	32.2	1178	45.67%	54.33%	26.61%
32	4.7	0.43	61	0.000	0.0	1.06	1.414	1.004	1.637	0.879	41	24.8	0.768	0.702	1.084	54	32.4	1298	43.92%	56.08%	27.11%
33	4.7	0.43	61	0.000	0.0	1.064	1.482	0.950	1.675	0.928	39	23.5	0.781	0.715	1.092	59	35.5	1227	40.36%	59.64%	26.61%
36	5.2	0.47	67	0.000	0.0	1.067	1.45	0.982	1.840	0.955	50	30.0	0.771	0.693	1.097	57	34.4	1090	45.93%	54.07%	29.05%
37	5.2	0.47	67	0.000	0.0	1.054	1.449	1.024	1.674	0.915	39	22.6	0.615	0.756	1.122	50	30.2	1340	42.41%	57.59%	24.60%
38	5.2	0.47	67	0.000	0.0	1.062	1.45	1.010	1.681	0.989	38	22.5	0.773	0.724	1.091	52	30.9	1340	42.28%	57.72%	26.75%
41	5.7	0.52	74	0.000	0.0	1.062	1.411	0.987	1.725	0.905	47	25.4	0.808	0.725	1.119	55	33.0	1163	47.04%	52.96%	25.97%
42	5.7	0.52	74	0.000	0.0	1.18	1.626	1.143	1.860	0.985	46	27.7	0.865	0.833	1.212	64	39.3	1064	41.23%	58.77%	26.65%
43	5.7	0.52	74	0.000	0.0	1.159	1.546	1.097	1.804	0.986	43	25.9	0.852	0.770	1.182	52	31.4	1218	44.22%	55.78%	26.48%
46	6.6	0.60	86	0.000	0.0	1.26	1.698	1.133	1.993	1.049	52	31.1	0.921	0.828	1.289	61	36.8	1056	46.03%	53.97%	26.82%
47	6.6	0.60	86	0.000	0.0	1.194	1.654	1.163	1.786	1.086	42	25.0	0.898	0.860	1.295	55	32.9	1270	44.47%	55.53%	24.81%
49	6.6	0.60	86	0.000	0.0	1.236	1.629	1.177	1.837	1.109	33	19.8	0.944	0.920	1.289	48	29.5	1530	42.53%	57.47%	23.57%
51	7.4	0.67	96	0.000	0.0	1.213	1.656	1.102	2.008	1.022	59	35.1	0.895	0.780	1.247	81	48.3	938	41.23%	58.77%	26.20%
52	7.4	0.67	96	0.000	0.0	1.305	1.76	1.259	1.924	1.114	40	24.0	0.978	0.914	1.353	53	31.8	1242	41.77%	58.23%	25.03%
53	7.4	0.67	96	0.000	0.0	1.301	1.706	1.260	1.939	1.181	40	23.7	0.973	0.977	1.364	51	30.6	1345	44.67%	55.33%	25.24%
56	8.1	0.74	105	0.000	0.0	1.329	1.767	1.208	2.070	1.089	64	36.2	0.94	0.871	1.353	67	40.2	876	46.92%	53.08%	29.22%
57	8.1	0.74	105	0.000	0.0	1.299	1.698	1.260	1.860	1.194	38	23.0	0.994	0.969	1.372	51	30.4	1343	43.24%	56.76%	23.45%
58	8.1	0.74	105	0.000	0.0	1.31	1.798	1.270	2.050	1.122	44	26.6	0.957	0.910	1.354	61	36.4	1142	42.52%	57.48%	26.91%
61	8.8	0.80	114	0.000	0.0	1.385	1.834	1.265	2.250	1.152	72	43.1	0.968	0.888	1.397	76	45.4	798	48.16%	51.84%	30.11%
62	8.8	0.80	114	0.000	0.0	1.403	1.903	1.387	2.128	1.285	45	27.1	1.033	1.029	1.470	63	38.0	1120	42.54%	57.46%	26.38%
63	8.8	0.80	114	0.000	0.0	1.344	1.793	1.328	2.031	1.237	37	22.2	1.028	1.022	1.425	56	33.4	1346	41.89%	58.11%	23.53%
66	10	0.91	130	0.000	0.0	1.545	2.012	1.414	2.347	1.285	64	36.7	1.128	1.051	1.591	68	40.9	870	47.12%	52.88%	26.98%
67	10	0.91	130	0.000	0.0	1.433	1.926	1.383	2.132	1.277	39	23.5	1.08	1.065	1.501	55	33.0	1298	41.74%	58.26%	24.84%
68	10	0.91	130	0.000	0.0	1.528	2.026	1.499	2.236	1.419	45	27.2	1.123	1.184	1.607	60	36.2	1178	44.92%	55.08%	26.55%
71	10.9	0.99	141	0.000	0.0	1.668	2.195	1.513	2.632	1.384	62	37.4	1.186	1.120	1.691	66	39.6	901	47.16%	52.84%	26.36%
72	10.9	0.99	141	0.000	0.0	1.617	2.145	1.565	2.349	1.470	42	25.3	1.191	1.209	1.693	52	31.4	1261	44.73%	55.27%	26.39%
73	10.9	0.99	141	0.000	0.0	1.478	2.042	1.485	2.332	1.347	51	30.4	1.068	1.080	1.648	71	42.5	1004	42.70%	57.30%	28.43%

Run No.	Liquid Flowrate (l/min)	Liquid Flowrate (kg/min)	Liquid Film Reynolds Number	Air Mass Flowrate (kg/s)	Air Velocity (m/s)	Mean Film Thickness (mm)	Mean Disturbance Height (mm)	Mean Disturbance Wave Min Start (mm)	Mean Disturbance Wave Max (mm)	Mean Disturbance Wave Min Finish (mm)	Mean Disturbance Wave Cell Number	Mean Disturbance Wave Length (mm)	Mean Substrate Height (mm)	Mean Substrate Min Value (mm)	Mean Substrate Max Value (mm)	Mean Substrate Cell Number	Mean Substrate Length (mm)	Number of Disturbance Wavelets	% Area Covered By Disturbance Waves	% Area Covered By Substrate	% Volume Contained in Disturbance Waves
101	1	0.09	13	0.006	2.8	0.989	0.808	0.518	1.036	0.468	29	13.9	0.456	0.399	0.604	40	23.7	1945	37.76%	82.24%	22.57%
102	1	0.09	13	0.006	2.6	0.853	0.831	0.563	1.025	0.527	20	11.7	0.534	0.439	0.678	29	17.6	2439	39.98%	80.02%	18.19%
103	1	0.09	13	0.006	2.6	0.869	0.831	0.573	1.026	0.538	19	11.5	0.545	0.457	0.689	26	15.4	2704	43.38%	56.62%	18.54%
106	1.7	0.15	22	0.006	2.6	0.721	0.946	0.582	1.307	0.538	28	16.8	0.523	0.427	0.722	34	20.1	1979	46.51%	53.49%	27.41%
107	1.7	0.15	22	0.006	2.6	0.722	0.882	0.663	1.297	0.567	27	16.1	0.542	0.456	0.734	39	23.2	1622	41.00%	59.00%	24.89%
108	1.7	0.15	22	0.006	2.6	0.731	0.844	0.630	1.177	0.683	24	14.7	0.567	0.473	0.748	33	19.6	2112	43.48%	56.52%	22.42%
111	2.1	0.19	27	0.006	2.6	0.744	0.992	0.629	1.374	0.537	35	20.8	0.543	0.430	0.747	42	26.0	1634	44.78%	55.22%	27.02%
112	2.1	0.19	27	0.006	2.6	0.737	1.005	0.670	1.266	0.591	28	16.8	0.563	0.467	0.752	41	24.6	1734	40.79%	59.21%	25.02%
113	2.1	0.19	27	0.006	2.6	0.754	0.960	0.674	1.249	0.603	25	15.0	0.577	0.487	0.772	32	19.2	2161	45.37%	54.63%	23.63%
116	3	0.27	39	0.006	2.6	0.871	1.168	0.745	1.657	0.613	42	25.2	0.62	0.491	0.856	49	29.3	1298	45.01%	54.99%	28.62%
117	3	0.27	39	0.006	2.6	0.86	1.161	0.795	1.432	0.708	27	16.4	0.668	0.582	0.902	37	22.2	1670	43.05%	56.95%	24.12%
118	3	0.27	39	0.006	2.6	0.914	1.191	0.846	1.456	0.777	29	17.3	0.696	0.625	0.949	38	22.5	1617	44.00%	56.00%	23.63%
121	3.6	0.33	47	0.006	2.6	0.901	1.281	0.861	1.589	0.786	36	22.9	0.715	0.629	0.995	47	27.9	1466	46.94%	53.06%	27.08%
122	3.6	0.33	47	0.006	2.6	0.978	1.271	0.890	1.479	0.808	30	18.1	0.749	0.656	1.002	40	23.8	1723	43.79%	56.21%	23.37%
123	3.6	0.33	47	0.006	2.6	0.943	1.26	0.869	1.536	0.776	35	21.0	0.709	0.614	0.974	47	28.5	1447	42.49%	57.51%	24.83%
126	4.2	0.38	54	0.006	2.6	1.014	1.396	0.892	1.670	0.784	44	28.5	0.725	0.607	1.026	52	31.3	1217	45.15%	54.85%	28.54%
127	4.2	0.38	54	0.006	2.6	0.974	1.307	0.912	1.529	0.777	36	21.8	0.716	0.631	0.999	46	27.5	1427	43.59%	56.41%	26.45%
128	4.2	0.38	54	0.006	2.6	0.952	1.306	0.915	1.538	0.837	36	21.4	0.752	0.677	1.028	48	28.8	1437	43.15%	56.85%	24.19%
131	4.7	0.43	61	0.006	2.6	1.045	1.359	0.911	1.629	0.814	41	24.9	0.761	0.664	1.054	48	28.8	1360	47.42%	52.58%	27.14%
132	4.7	0.43	61	0.006	2.6	1.043	1.362	0.971	1.589	0.886	39	23.2	0.764	0.711	1.076	49	29.3	1392	45.17%	54.83%	26.76%
133	4.7	0.43	61	0.006	2.6	1.054	1.359	0.970	1.608	0.920	32	19.1	0.792	0.758	1.094	39	23.5	1726	46.21%	53.79%	24.85%
136	5.2	0.47	67	0.006	2.6	1.046	1.462	0.934	1.612	0.931	43	25.6	0.767	0.654	1.056	60	36.2	1121	40.21%	59.79%	26.72%
137	5.2	0.47	67	0.006	2.6	1.033	1.422	0.962	1.626	0.975	35	21.4	0.773	0.697	1.059	56	33.8	1337	40.14%	59.86%	25.22%
138	5.2	0.47	67	0.006	2.6	1.1	1.494	1.042	1.763	0.953	38	23.0	0.812	0.704	1.130	51	30.6	1312	42.27%	57.73%	26.21%
141	5.7	0.52	74	0.006	2.6	1.169	1.68	1.069	1.897	0.962	54	32.3	0.83	0.730	1.191	66	39.4	989	45.16%	54.84%	28.97%
142	5.7	0.52	74	0.006	2.6	1.079	1.399	1.019	1.696	0.972	36	21.7	0.833	0.785	1.126	48	26.8	1427	43.38%	56.62%	22.75%
143	5.7	0.52	74	0.006	2.6	1.107	1.496	1.042	1.666	0.914	41	24.5	0.819	0.744	1.142	54	32.3	1241	42.61%	57.39%	26.05%
146	6.6	0.60	95	0.006	2.6	1.185	1.556	1.069	1.862	0.915	53	32.0	0.841	0.746	1.195	56	33.8	1090	47.53%	52.47%	29.04%
147	6.6	0.60	95	0.006	2.6	1.156	1.612	1.111	1.897	0.976	43	25.7	0.867	0.783	1.210	63	37.6	1111	40.03%	59.97%	25.59%
149	6.6	0.60	95	0.006	2.6	1.099	1.496	1.043	1.655	0.941	34	20.2	0.845	0.765	1.143	51	30.8	1405	39.66%	60.34%	23.13%
151	7.4	0.67	96	0.006	2.6	1.148	1.596	1.017	1.772	0.886	45	25.7	0.852	0.728	1.156	61	36.6	1122	42.02%	57.98%	25.77%
152	7.4	0.67	96	0.006	2.6	1.19	1.596	1.136	1.758	1.041	39	22.7	0.906	0.849	1.244	56	33.6	1311	41.72%	58.28%	23.84%
153	7.4	0.67	96	0.006	2.6	1.175	1.625	1.107	1.866	1.063	35	20.8	0.865	0.867	1.229	54	32.7	1397	40.71%	59.29%	26.33%
156	8.1	0.74	105	0.006	2.8	1.223	1.866	1.109	1.925	0.947	52	30.9	0.882	0.773	1.231	65	38.8	1004	43.46%	56.54%	27.82%
157	8.1	0.74	105	0.006	2.8	1.302	1.751	1.261	2.013	1.238	38	22.9	0.981	0.946	1.371	56	33.5	1300	41.78%	58.22%	24.71%
158	8.1	0.74	105	0.006	2.6	1.378	1.875	1.320	2.100	1.236	46	27.9	1.007	0.991	1.421	62	36.9	1097	42.79%	57.21%	26.95%
161	8.8	0.80	114	0.006	2.6	1.317	1.756	1.245	2.090	1.057	50	30.1	0.939	0.844	1.338	59	36.6	1097	46.29%	53.71%	28.68%
162	8.8	0.80	114	0.006	2.6	1.33	1.773	1.267	1.994	1.187	44	26.6	0.95	0.952	1.373	56	33.6	1239	46.16%	53.84%	28.56%
163	8.8	0.80	114	0.006	2.6	1.39	1.838	1.330	2.063	1.213	37	22.5	1.049	1.015	1.448	49	29.6	1374	43.24%	56.76%	24.54%
166	10	0.91	130	0.006	2.6	1.43	1.898	1.305	2.166	1.262	70	41.8	1.036	1.002	1.464	76	45.8	789	46.24%	53.76%	27.55%
167	10	0.91	130	0.006	2.6	1.394	1.898	1.340	2.086	1.305	43	25.6	1.034	1.042	1.467	64	38.2	1146	41.03%	58.97%	25.32%
168	10	0.91	130	0.006	2.6	1.561	2.222	1.526	2.361	1.422	38	22.9	1.164	1.151	1.639	61	36.5	1172	37.65%	62.44%	25.46%

Run No.	Liquid Flowrate (l/min)	Liquid Flowrate (kg/lms)	Liquid Film Reynolds Number	Air Mass Flowrate (kg/s)	Air Velocity (m/s)	Mean Film Thickness (mm)	Mean Disturbance Height (mm)	Mean Disturbance Wave Min Start (mm)	Mean Disturbance Wave Max (mm)	Mean Disturbance Wave Min Finish (mm)	Mean Disturbance Wave Cell Number	Mean Disturbance Wave Length (mm)	Mean Substrate Height (mm)	Mean Substrate Min Value (mm)	Mean Substrate Max Value (mm)	Mean Substrate Cell Number	Mean Substrate Length (mm)	Number of Disturbance Wavelets	% Area Covered By Disturbance Waves	% Area Covered By Substrate	% Volume Contained in Disturbance Waves
201	1	0.09	19	0.012	5.2	0.804	0.75	0.486	1.031	0.453	26	15.8	0.471	0.390	0.603	29	17.4	2154	47.66%	52.42%	21.98%
202	1	0.09	19	0.012	5.2	0.82	0.792	0.525	1.021	0.482	19	11.3	0.502	0.405	0.639	28	16.8	2689	40.81%	59.19%	19.09%
203	1	0.09	19	0.012	5.2	0.851	0.828	0.565	1.022	0.526	18	10.9	0.532	0.441	0.666	28	16.7	2628	40.07%	59.93%	18.22%
205	1.7	0.15	22	0.012	5.2	0.895	0.845	0.606	1.319	0.539	29	17.6	0.511	0.413	0.684	39	18.1	1718	43.37%	57.63%	26.46%
207	1.7	0.15	22	0.012	5.2	0.745	0.863	0.648	1.254	0.577	24	14.3	0.576	0.477	0.753	30	18.1	2192	43.76%	56.25%	22.73%
208	1.7	0.15	22	0.012	5.2	0.719	0.946	0.632	1.216	0.598	22	13.4	0.566	0.464	0.740	32	19.5	2227	41.81%	58.19%	22.68%
211	2.1	0.19	27	0.012	5.2	0.794	1.041	0.672	1.419	0.568	33	19.7	0.595	0.471	0.794	38	23.0	1661	45.78%	54.22%	26.29%
212	2.1	0.19	27	0.012	5.2	0.801	1.046	0.710	1.333	0.621	26	15.1	0.614	0.506	0.817	33	19.9	2045	43.16%	56.85%	23.27%
213	2.1	0.19	27	0.012	5.2	0.788	1.031	0.700	1.300	0.619	26	15.8	0.592	0.509	0.803	33	19.9	2018	44.72%	55.28%	24.91%
215	3	0.27	39	0.012	5.2	0.904	1.196	0.767	1.536	0.651	39	23.1	0.643	0.527	0.893	42	25.1	1459	47.23%	52.77%	28.69%
217	3	0.27	39	0.012	5.2	0.892	1.139	0.815	1.442	0.707	27	16.3	0.679	0.580	0.911	33	19.6	2029	46.31%	53.69%	23.69%
219	3	0.27	39	0.012	5.2	0.9	1.177	0.809	1.423	0.730	29	17.3	0.692	0.586	0.919	37	22.2	1615	43.91%	56.09%	24.15%
221	3.6	0.33	47	0.012	5.2	1.002	1.309	0.863	1.644	0.736	37	22.1	0.745	0.600	1.021	43	25.8	1472	45.53%	54.47%	25.63%
222	3.6	0.33	47	0.012	5.2	1.037	1.382	0.939	1.674	0.828	31	18.4	0.755	0.646	1.098	38	23.0	1749	44.99%	55.01%	27.20%
223	3.6	0.33	47	0.012	5.2	1.014	1.355	0.915	1.583	0.836	27	16.0	0.769	0.677	1.049	39	23.5	1863	41.81%	58.19%	24.20%
226	4.2	0.38	54	0.012	5.2	1.05	1.354	0.889	1.731	0.772	41	24.7	0.739	0.618	1.052	40	23.9	1482	50.48%	49.52%	29.56%
227	4.2	0.38	54	0.012	5.2	1.07	1.413	0.963	1.673	0.889	33	19.8	0.78	0.696	1.096	39	23.3	1666	45.80%	54.20%	27.09%
228	4.2	0.38	54	0.012	5.2	1.066	1.458	0.957	1.730	0.886	31	18.6	0.767	0.696	1.099	43	25.6	1659	43.33%	56.67%	28.01%
231	4.7	0.43	61	0.012	5.2	1.142	1.536	1.017	1.903	0.896	47	28.1	0.806	0.671	1.152	53	32.1	1173	46.11%	53.89%	29.43%
232	4.7	0.43	61	0.012	5.2	1.124	1.504	1.024	1.776	0.936	36	21.5	0.788	0.733	1.148	42	24.9	1681	46.90%	53.10%	29.88%
233	4.7	0.43	61	0.012	5.2	1.038	1.384	0.938	1.599	0.860	26	15.7	0.789	0.703	1.076	38	22.6	1900	41.86%	58.15%	23.99%
236	5.2	0.47	67	0.012	5.2	1.11	1.489	1.023	1.806	0.901	42	25.1	0.789	0.686	1.146	52	31.2	1304	45.88%	54.12%	28.93%
237	5.2	0.47	67	0.012	5.2	1.12	1.493	1.017	1.752	0.914	37	22.1	0.762	0.702	1.143	41	24.9	1632	47.48%	52.52%	30.14%
238	5.2	0.47	67	0.012	5.2	1.11	1.49	1.012	1.736	0.943	37	21.9	0.801	0.734	1.143	46	27.6	1462	44.88%	55.12%	27.86%
241	5.7	0.52	74	0.012	5.2	1.141	1.589	1.107	1.871	0.948	43	25.7	0.793	0.736	1.176	56	33.4	1216	43.77%	56.23%	30.63%
242	5.7	0.52	74	0.012	5.2	1.21	1.645	1.143	1.891	1.050	36	21.5	0.894	0.859	1.252	51	30.6	1422	42.55%	57.45%	26.95%
243	5.7	0.52	74	0.012	5.2	1.174	1.536	1.077	1.741	1.026	27	16.2	0.891	0.847	1.220	37	22.0	1927	43.81%	56.19%	24.07%
245	6.6	0.60	86	0.012	5.2	1.214	1.596	1.111	1.900	0.928	47	28.4	0.967	0.754	1.231	49	28.5	1215	48.30%	51.70%	28.60%
247	6.6	0.60	86	0.012	5.2	1.352	1.844	1.273	2.062	1.154	37	22.1	0.984	0.925	1.406	49	25.4	1381	42.74%	57.26%	27.19%
249	6.6	0.60	86	0.012	5.2	1.254	1.725	1.133	2.013	1.045	36	21.4	0.91	0.833	1.299	45	27.1	1448	43.43%	56.57%	28.00%
251	7.4	0.67	96	0.012	5.2	1.314	1.771	1.184	2.154	1.087	56	33.4	0.947	0.831	1.342	67	40.5	952	44.47%	55.53%	27.89%
252	7.4	0.67	96	0.012	5.2	1.294	1.834	1.239	2.126	1.089	46	27.8	0.9	0.840	1.337	66	39.6	1093	42.21%	57.79%	30.47%
253	7.4	0.67	96	0.012	5.2	1.334	1.81	1.276	2.041	1.153	39	23.4	0.947	0.956	1.388	48	29.0	1368	44.81%	55.19%	28.99%
258	8.1	0.74	105	0.012	5.2	1.332	1.842	1.182	2.091	1.039	47	28.0	0.951	0.836	1.359	59	35.7	1090	42.81%	57.19%	28.64%
257	8.1	0.74	105	0.012	5.2	1.364	1.888	1.284	2.046	1.215	40	24.1	0.988	0.965	1.421	56	33.4	1240	41.78%	58.22%	27.57%
258	8.1	0.74	105	0.012	5.2	1.415	1.947	1.354	2.217	1.272	42	25.2	1.025	1.002	1.484	61	36.3	1197	42.30%	57.70%	27.56%
261	8.8	0.80	114	0.012	5.2	1.368	1.798	1.222	2.116	1.115	58	34.8	0.979	0.888	1.380	60	36.8	986	48.03%	51.97%	28.41%
262	8.8	0.80	114	0.012	5.2	1.364	1.804	1.301	2.013	1.215	36	21.6	1.003	0.963	1.421	46	27.7	1493	45.09%	54.91%	28.48%
263	8.8	0.80	114	0.012	5.2	1.311	1.73	1.276	1.957	1.190	40	23.7	0.963	0.962	1.364	54	32.3	1366	45.35%	54.65%	26.53%
266	10	0.91	130	0.012	5.2	1.568	2.052	1.410	2.396	1.278	63	37.8	1.078	1.009	1.572	62	37.1	930	49.27%	50.73%	30.80%
267	10	0.91	130	0.012	5.2	1.469	1.98	1.429	2.262	1.329	37	22.1	1.067	1.105	1.639	52	31.3	1420	44.02%	55.98%	27.36%
268	10	0.91	130	0.012	5.2	1.42	1.908	1.381	2.187	1.233	40	24.0	1.057	1.015	1.487	54	32.6	1267	42.61%	57.39%	26.66%

Run No.	Liquid Flowrate (l/min)	Liquid Flowrate (kg/lms)	Liquid Film Reynolds Number	Air Mass Flowrate (kg/s)	Air Velocity (m/s)	Mean Film Thickness (mm)	Mean Disturbance Height (mm)	Mean Disturbance Wave Min Start (mm)	Mean Disturbance Wave Max (mm)	Mean Disturbance Wave Min Finish (mm)	Mean Disturbance Wave Cell Number	Mean Disturbance Wave Length (mm)	Mean Substrate Height (mm)	Mean Substrate Min Value (mm)	Mean Substrate Max Value (mm)	Mean Substrate Cell Number	Mean Substrate Length (mm)	Number of Disturbance Wavelets	% Area Covered By Disturbance Waves	% Area Covered By Substrate	% Volume Contained in Disturbance Waves
301	1	0.09	13	0.018	7.3	0.58	0.712	0.468	0.963	0.424	19	11.3	0.448	0.364	0.688	26	15.6	2662	42.26%	57.74%	19.92%
302	1	0.09	13	0.018	7.3	0.576	0.738	0.464	1.001	0.430	19	11.1	0.451	0.362	0.680	24	14.4	2804	43.66%	56.34%	21.75%
303	1	0.09	13	0.018	7.3	0.589	0.739	0.461	0.960	0.461	16	9.7	0.478	0.389	0.608	23	13.6	3117	42.46%	57.54%	18.81%
306	1.7	0.15	22	0.018	7.3	0.662	0.837	0.540	1.190	0.471	26	15.2	0.501	0.404	0.654	27	16.2	2249	47.85%	52.15%	24.28%
307	1.7	0.15	22	0.018	7.3	0.685	0.899	0.593	1.157	0.532	21	12.3	0.54	0.440	0.688	29	16.9	2604	43.26%	56.75%	22.34%
308	1.7	0.15	22	0.018	7.3	0.722	0.909	0.621	1.217	0.552	20	12.1	0.563	0.466	0.732	26	14.8	2703	46.94%	53.06%	22.02%
311	2.1	0.19	27	0.018	7.3	0.751	0.964	0.622	1.368	0.514	27	16.4	0.561	0.436	0.729	29	17.7	2112	48.52%	51.48%	26.69%
312	2.1	0.19	27	0.018	7.3	0.781	1.008	0.671	1.326	0.571	24	14.3	0.58	0.454	0.777	27	16.2	2341	46.88%	53.12%	26.69%
313	2.1	0.19	27	0.018	7.3	0.79	1.013	0.692	1.314	0.590	23	13.9	0.6	0.496	0.796	27	16.4	2361	46.94%	53.06%	24.02%
316	3	0.27	39	0.018	7.3	0.917	1.043	0.664	1.406	0.546	30	18.2	0.598	0.470	0.600	31	18.7	1932	49.14%	50.86%	26.77%
317	3	0.27	39	0.018	7.3	0.954	1.126	0.749	1.409	0.651	27	16.5	0.631	0.529	0.657	35	20.7	1938	44.78%	55.22%	26.06%
318	3	0.27	39	0.018	7.3	0.964	1.136	0.773	1.416	0.689	26	15.4	0.667	0.564	0.699	30	17.9	2153	46.31%	53.69%	24.52%
321	3.6	0.33	47	0.018	7.3	0.965	1.223	0.804	1.570	0.700	34	20.2	0.677	0.571	0.934	34	20.4	1603	51.06%	48.94%	29.19%
322	3.6	0.33	47	0.018	7.3	0.93	1.207	0.825	1.431	0.713	30	18.7	0.691	0.593	0.940	34	20.2	1963	46.39%	53.61%	25.74%
323	3.6	0.33	47	0.018	7.3	0.97	1.256	0.872	1.518	0.799	30	17.7	0.719	0.625	0.988	34	20.5	1653	48.52%	51.48%	27.87%
326	4.2	0.38	54	0.018	7.3	1.065	1.387	0.869	1.890	0.777	39	25.6	0.761	0.651	1.039	39	23.5	1470	48.52%	51.48%	26.05%
327	4.2	0.38	54	0.018	7.3	1.015	1.361	0.934	1.816	0.789	31	18.7	0.752	0.625	1.036	43	25.9	1649	43.18%	56.82%	25.91%
328	4.2	0.38	54	0.018	7.3	1.028	1.376	0.921	1.815	0.792	32	19.1	0.753	0.648	1.047	41	24.4	1636	43.77%	56.23%	26.69%
331	4.7	0.43	61	0.018	7.3	0.956	1.228	0.840	1.538	0.711	37	22.4	0.672	0.578	0.954	38	22.6	1619	50.82%	49.18%	29.69%
332	4.7	0.43	61	0.018	7.3	1.008	1.343	0.924	1.602	0.792	34	20.1	0.736	0.647	1.027	43	26.8	1693	44.96%	55.04%	27.05%
333	4.7	0.43	61	0.018	7.3	0.959	1.215	0.873	1.434	0.788	28	16.9	0.733	0.656	0.989	33	19.5	1978	46.96%	53.04%	23.60%
336	5.2	0.47	67	0.018	7.3	1.116	1.454	0.983	1.704	0.831	40	23.8	0.823	0.701	1.115	45	26.7	1390	46.42%	53.58%	26.25%
337	5.2	0.47	67	0.018	7.3	1.063	1.454	1.006	1.681	0.860	32	19.1	0.787	0.710	1.104	39	23.2	1716	46.93%	53.07%	28.03%
338	5.2	0.47	67	0.018	7.3	1.079	1.421	0.964	1.649	0.841	34	20.6	0.782	0.691	1.092	41	24.5	1601	46.29%	53.71%	27.44%
341	5.7	0.52	74	0.018	7.3	1.057	1.376	0.925	1.660	0.823	38	22.7	0.773	0.669	1.066	43	28.0	1484	47.08%	52.92%	26.81%
342	5.7	0.52	74	0.018	7.3	1.097	1.467	0.985	1.666	0.829	36	21.5	0.781	0.667	1.110	42	26.5	1632	46.13%	53.87%	26.65%
343	5.7	0.52	74	0.018	7.3	1.027	1.399	0.961	1.697	0.817	30	17.8	0.761	0.674	1.051	43	25.7	1673	41.72%	58.28%	26.92%
346	6.6	0.60	86	0.018	7.3	1.151	1.482	1.041	1.726	0.925	41	24.8	0.847	0.757	1.173	46	27.6	1375	47.82%	52.18%	26.38%
347	6.6	0.60	86	0.018	7.3	1.167	1.548	1.070	1.749	0.931	34	20.4	0.84	0.742	1.186	41	24.5	1615	46.17%	53.83%	28.01%
349	6.6	0.60	86	0.018	7.3	1.092	1.525	0.994	1.703	0.804	36	21.2	0.794	0.667	1.096	48	28.9	1374	40.81%	59.19%	27.32%
351	7.4	0.67	96	0.018	7.3	1.219	1.611	1.062	1.898	0.963	47	28.3	0.865	0.732	1.218	53	32.1	1197	47.48%	52.52%	29.05%
352	7.4	0.67	96	0.018	7.3	1.266	1.729	1.190	1.931	1.134	33	19.8	0.936	0.814	1.324	45	26.9	1692	44.16%	55.84%	27.23%
353	7.4	0.67	96	0.018	7.3	1.269	1.752	1.211	1.905	1.127	36	21.7	0.954	0.837	1.341	51	30.5	1395	42.01%	57.99%	26.01%
366	8.1	0.74	105	0.018	7.3	1.262	1.769	1.179	1.921	1.054	41	24.5	0.939	0.815	1.308	56	33.8	1218	41.79%	58.21%	26.73%
367	8.1	0.74	105	0.018	7.3	1.251	1.698	1.169	1.886	1.086	33	19.7	0.927	0.872	1.290	42	26.2	1689	43.95%	56.05%	26.90%
368	8.1	0.74	105	0.018	7.3	1.263	1.72	1.200	1.887	1.150	33	19.8	0.967	0.861	1.331	46	27.5	1514	41.98%	58.02%	24.64%
361	8.8	0.80	114	0.018	7.3	1.433	2.001	1.378	2.427	1.075	50	29.9	1.026	0.940	1.452	74	44.3	998	41.81%	58.19%	28.44%
362	8.8	0.80	114	0.018	7.3	1.149	1.636	1.022	1.860	0.886	26	15.7	0.848	0.719	1.157	33	20.0	1992	43.84%	56.16%	26.21%
363	8.8	0.80	114	0.018	7.3	1.286	1.734	1.166	1.922	1.016	36	21.9	0.929	0.843	1.307	43	26.0	1446	44.94%	55.06%	27.76%
365	10	0.91	130	0.018	7.3	1.358	1.86	1.241	2.141	1.018	46	28.7	0.966	0.806	1.366	59	36.4	1091	43.80%	56.20%	28.93%
367	10	0.91	130	0.018	7.3	1.415	2.022	1.297	2.182	1.154	34	20.3	1.016	0.937	1.454	48	28.9	1386	38.68%	60.31%	28.25%
368	10	0.91	130	0.018	7.3	1.366	1.872	1.284	2.063	1.161	36	21.3	0.999	0.916	1.406	53	31.6	1373	40.92%	59.08%	26.36%

Run No.	Liquid Flowrate (l/min)	Liquid Flowrate (kg/ms)	Liquid Film Reynolds Number	Air Mass Flowrate (kg/s)	Air Velocity (m/s)	Mean Film Thickness (mm)	Mean Disturbance Height (mm)	Mean Disturbance Wave Min Start (mm)	Mean Disturbance Wave Max Finish (mm)	Mean Disturbance Wave Cell Number	Mean Disturbance Wave Length (mm)	Mean Substrate Height (mm)	Mean Substrate Min Value (mm)	Mean Substrate Max Value (mm)	Mean Substrate Cell Number	Mean Substrate Length (mm)	Number of Disturbance Wavelets	% Area Covered By Disturbance Waves	% Area Covered By Substrate	% Volume Contained In Disturbance Waves	
401	1.7	0.15	22	0.028	9.7	0.864	0.899	0.510	1.289	0.419	25	15.2	0.473	0.367	0.636	23	14.1	2454	52.07%	47.93%	28.70%
402	1.7	0.15	22	0.028	9.7	0.706	0.929	0.807	1.283	0.510	22	13.0	0.531	0.426	0.694	28	18.9	2420	43.97%	56.03%	24.79%
403	1.7	0.15	22	0.028	9.7	0.738	0.936	0.831	1.283	0.544	19	11.8	0.584	0.484	0.735	23	13.8	2880	46.82%	53.18%	23.60%
406	2.1	0.19	27	0.023	9.7	0.761	0.947	0.804	1.392	0.497	26	15.8	0.54	0.440	0.727	23	13.7	2455	54.24%	45.76%	29.01%
407	2.1	0.19	27	0.023	9.7	0.721	0.942	0.808	1.296	0.497	21	12.8	0.522	0.424	0.697	24	14.4	2661	47.54%	52.46%	27.69%
408	2.1	0.19	27	0.023	9.7	0.748	0.945	0.630	1.299	0.540	20	12.2	0.589	0.459	0.742	23	13.6	2783	47.86%	52.14%	23.96%
411	3	0.27	39	0.023	9.7	0.865	1.125	0.707	1.616	0.595	30	18.1	0.611	0.487	0.840	28	16.8	2100	53.26%	46.74%	30.93%
412	3	0.27	39	0.023	9.7	0.866	1.116	0.729	1.416	0.617	24	14.4	0.613	0.507	0.843	26	15.7	2403	48.33%	51.67%	28.40%
413	3	0.27	39	0.023	9.7	0.872	1.106	0.756	1.384	0.650	23	13.8	0.643	0.533	0.868	24	14.2	2657	49.38%	50.62%	26.22%
416	3.6	0.33	47	0.023	9.7	0.95	1.249	0.776	1.622	0.613	34	20.5	0.661	0.512	0.906	34	20.4	1743	50.05%	49.95%	31.50%
417	3.6	0.33	47	0.023	9.7	0.908	1.179	0.786	1.484	0.636	25	14.9	0.669	0.539	0.894	28	16.5	2282	47.77%	52.23%	27.35%
418	3.6	0.33	47	0.023	9.7	0.913	1.157	0.790	1.434	0.695	25	14.8	0.666	0.562	0.908	25	15.1	2412	50.12%	49.88%	26.84%
421	4.2	0.38	54	0.023	9.7	0.933	1.175	0.760	1.656	0.613	31	18.7	0.633	0.511	0.884	26	15.7	2105	56.26%	44.74%	32.10%
422	4.2	0.38	54	0.023	9.7	0.915	1.186	0.804	1.411	0.666	24	14.4	0.671	0.563	0.903	26	15.5	2438	49.31%	50.69%	26.68%
423	4.2	0.38	54	0.023	9.7	0.99	1.289	0.863	1.533	0.713	26	15.6	0.702	0.597	0.977	26	15.4	2320	50.79%	49.21%	29.09%
426	4.7	0.43	61	0.023	9.7	0.97	1.213	0.785	1.543	0.662	32	19.1	0.673	0.558	0.926	27	16.3	2053	55.01%	44.99%	30.63%
427	4.7	0.43	61	0.023	9.7	0.979	1.244	0.848	1.504	0.719	25	15.0	0.702	0.590	0.987	25	15.0	2420	51.01%	48.99%	28.24%
428	4.7	0.43	61	0.023	9.7	0.908	1.145	0.771	1.425	0.639	23	14.0	0.655	0.534	0.889	22	13.5	2540	51.85%	48.15%	27.87%
431	5.2	0.47	67	0.023	9.7	0.974	1.237	0.828	1.599	0.646	29	17.2	0.674	0.555	0.932	26	15.8	2214	53.33%	46.67%	30.63%
432	5.2	0.47	67	0.023	9.7	1.063	1.436	0.969	1.696	0.793	30	17.8	0.754	0.622	1.072	32	19.2	1841	48.26%	51.74%	30.39%
433	5.2	0.47	67	0.023	9.7	1.026	1.349	0.926	1.560	0.799	24	14.4	0.77	0.652	1.043	29	17.3	2274	45.86%	54.14%	25.63%
436	5.7	0.52	74	0.023	9.7	1.12	1.518	0.947	1.782	0.727	31	18.4	0.764	0.609	1.080	35	20.7	1638	47.31%	52.69%	31.85%
437	5.7	0.52	74	0.023	9.7	1.08	1.391	0.940	1.613	0.817	26	15.5	0.783	0.665	1.072	28	18.9	2248	48.88%	51.12%	27.51%
438	5.7	0.52	74	0.023	9.7	1.103	1.41	0.969	1.644	0.873	24	14.5	0.821	0.739	1.121	27	16.4	2389	47.99%	52.01%	25.83%
441	6.8	0.60	86	0.023	9.7	1.165	1.487	0.978	1.786	0.786	35	21.0	0.818	0.674	1.142	31	18.8	1788	52.10%	47.90%	30.01%
442	6.8	0.60	86	0.023	9.7	1.104	1.409	0.962	1.636	0.819	27	16.1	0.795	0.686	1.088	27	16.5	2223	50.26%	49.74%	27.95%
443	6.8	0.60	86	0.023	9.7	1.121	1.448	0.969	1.701	0.814	29	17.5	0.802	0.672	1.117	30	18.3	2010	49.37%	50.63%	28.45%
446	7.4	0.67	96	0.023	9.7	1.186	1.461	0.994	1.728	0.864	32	19.0	0.816	0.706	1.141	29	17.6	2034	54.24%	45.76%	30.01%
447	7.4	0.67	96	0.023	9.7	1.242	1.632	1.138	1.889	0.974	30	17.9	0.905	0.825	1.263	35	21.3	1852	46.38%	53.62%	27.15%
448	7.4	0.67	96	0.023	9.7	1.216	1.689	1.097	1.827	1.010	28	15.8	0.903	0.825	1.249	31	18.7	2148	47.02%	52.98%	25.75%
451	8.1	0.74	105	0.023	9.7	1.36	1.708	1.162	2.008	1.051	40	24.2	0.961	0.853	1.351	37	22.2	1555	52.73%	47.27%	29.57%
452	8.1	0.74	105	0.023	9.7	1.288	1.642	1.166	1.846	1.036	26	15.6	0.966	0.863	1.300	29	17.4	2212	48.48%	51.52%	25.82%
453	8.1	0.74	105	0.023	9.7	1.328	1.677	1.189	1.938	1.130	29	17.5	1.012	0.937	1.361	34	20.2	1938	47.53%	52.47%	23.80%
456	8.8	0.80	114	0.023	9.7	1.415	1.806	1.213	2.124	1.065	40	24.3	0.988	0.844	1.413	46	27.6	1360	46.91%	53.09%	29.46%
457	8.8	0.80	114	0.023	9.7	1.317	1.677	1.205	1.889	1.101	28	16.8	0.985	0.904	1.351	32	19.1	2042	47.94%	52.06%	25.19%
459	8.8	0.80	114	0.023	9.7	1.365	1.737	1.264	1.980	1.078	31	18.3	1.002	0.889	1.378	35	21.2	1673	48.07%	51.93%	26.08%

Run No.	Liquid Flowrate (l/min)	Liquid Flowrate (kg/ms)	Liquid Film Reynolds Number	Air Mass Flowrate (kg/s)	Air Velocity (m/s)	Mean Film Thickness (mm)	Mean Disturbance Height (mm)	Mean Disturbance Wave Min Start (mm)	Mean Disturbance Wave Max (mm)	Mean Disturbance Wave Min Finish (mm)	Mean Disturbance Wave Cell Length (mm)	Mean Disturbance Wave Length (mm)	Mean Substrate Height (mm)	Mean Substrate Min Value (mm)	Mean Substrate Max Value (mm)	Mean Substrate Cell Number	Mean Substrate Length (mm)	Number of Disturbance Wavelets	% Area Covered By Disturbance Waves	% Area Covered By Substrate	% Volume Contained in Disturbance Waves
501	1.7	0.15	22	0.029	12.2	0.575	0.714	0.418	1.225	0.344	22	13.0	0.409	0.309	0.545	19	11.3	2989	54.39%	45.61%	28.65%
902	1.7	0.15	22	0.029	12.2	0.599	0.752	0.480	1.196	0.421	16	9.8	0.453	0.388	0.587	18	10.9	3549	48.77%	51.23%	24.35%
903	1.7	0.15	22	0.029	12.2	0.612	0.761	0.506	1.121	0.430	16	9.8	0.472	0.375	0.611	18	10.7	3524	48.36%	51.64%	22.83%
906	2.1	0.19	27	0.029	12.2	0.507	0.73	0.421	1.217	0.326	22	13.3	0.396	0.295	0.545	17	10.4	3054	57.23%	42.77%	32.56%
907	2.1	0.19	27	0.029	12.2	0.537	0.813	0.501	1.226	0.410	18	10.6	0.469	0.369	0.611	18	10.8	3397	50.38%	49.62%	28.09%
908	2.1	0.19	27	0.029	12.2	0.66	0.804	0.538	1.157	0.468	17	10.0	0.503	0.413	0.654	16	9.9	3699	51.93%	48.07%	23.69%
511	3	0.27	39	0.029	12.2	0.714	0.884	0.495	1.391	0.369	26	14.8	0.466	0.333	0.644	17	10.1	2916	60.47%	39.53%	36.25%
512	3	0.27	39	0.029	12.2	0.752	0.953	0.604	1.398	0.456	20	12.0	0.514	0.399	0.709	17	10.1	3291	55.19%	44.81%	32.62%
513	3	0.27	39	0.029	12.2	0.768	0.957	0.626	1.331	0.508	19	11.7	0.554	0.438	0.742	18	10.6	3252	53.14%	46.86%	27.89%
516	3.6	0.33	47	0.029	12.2	0.836	1.002	0.611	1.492	0.452	25	14.9	0.554	0.425	0.756	15	9.2	3011	62.93%	37.07%	33.72%
517	3.6	0.33	47	0.029	12.2	0.839	1.042	0.675	1.434	0.515	20	11.8	0.579	0.455	0.794	16	9.7	3399	56.19%	43.81%	31.08%
519	3.6	0.33	47	0.029	12.2	0.935	1.026	0.664	1.417	0.533	20	12.2	0.579	0.455	0.791	16	9.7	3399	57.36%	42.64%	30.71%
521	4.2	0.38	54	0.029	12.2	0.953	1.042	0.619	1.506	0.496	27	16.1	0.549	0.439	0.779	17	10.1	2623	63.60%	36.40%	36.33%
522	4.2	0.38	54	0.029	12.2	0.969	1.07	0.696	1.445	0.553	20	11.7	0.607	0.495	0.817	16	9.5	3435	56.35%	43.65%	30.05%
523	4.2	0.38	54	0.029	12.2	0.918	1.143	0.747	1.533	0.584	21	12.8	0.635	0.504	0.869	19	10.7	3106	59.59%	44.32%	30.61%
526	4.7	0.43	61	0.029	12.2	0.99	1.204	0.727	1.641	0.559	28	16.7	0.641	0.500	0.900	19	10.8	2651	61.99%	38.01%	35.25%
527	4.7	0.43	61	0.029	12.2	0.975	1.195	0.795	1.536	0.650	21	12.8	0.681	0.565	0.923	17	10.0	3198	57.17%	42.83%	30.14%
528	4.7	0.43	61	0.029	12.2	0.948	1.171	0.775	1.517	0.625	22	13.2	0.681	0.555	0.899	17	10.8	3037	56.21%	43.79%	30.18%
531	5.2	0.47	67	0.029	12.2	1	1.201	0.742	1.636	0.579	26	15.8	0.666	0.511	0.912	16	9.8	2896	63.14%	36.86%	34.41%
532	5.2	0.47	67	0.029	12.2	0.984	1.234	0.817	1.591	0.529	22	13.4	0.677	0.560	0.945	18	10.7	3029	58.91%	41.09%	31.89%
533	5.2	0.47	67	0.029	12.2	0.975	1.19	0.803	1.652	0.634	20	12.2	0.684	0.560	0.933	16	9.8	3525	58.72%	41.28%	28.65%
536	5.7	0.52	74	0.029	12.2	1.052	1.234	0.864	1.659	0.591	27	16.0	0.677	0.521	0.939	18	9.8	2827	63.17%	36.83%	34.40%
537	5.7	0.52	74	0.029	12.2	1.039	1.252	0.857	1.599	0.707	22	13.1	0.724	0.603	0.990	16	9.9	3177	58.39%	41.61%	30.26%
538	5.7	0.52	74	0.029	12.2	1.039	1.252	0.857	1.599	0.707	22	13.1	0.724	0.603	0.990	16	9.9	3177	58.39%	41.61%	30.26%
541	6.6	0.60	86	0.029	12.2	1.157	1.403	0.867	1.786	0.724	27	16.5	0.789	0.529	1.092	19	11.6	2597	68.67%	31.33%	31.77%
542	6.6	0.60	86	0.029	12.2	1.08	1.349	0.897	1.659	0.716	21	12.9	0.769	0.618	1.043	19	11.4	3016	54.43%	45.57%	29.73%
543	6.6	0.60	86	0.029	12.2	1.19	1.503	1.010	1.758	0.841	21	12.9	0.854	0.719	1.157	20	12.3	2958	51.79%	48.21%	28.24%
801	1.7	0.15	22	0.036	14.7	0.988	0.68	0.402	1.201	0.307	21	12.4	0.391	0.296	0.518	14	8.2	3517	61.09%	38.91%	31.08%
802	1.7	0.15	22	0.036	14.7	0.834	0.762	0.505	1.142	0.423	16	9.8	0.478	0.388	0.607	14	8.5	4008	55.20%	44.80%	24.90%
803	1.7	0.15	22	0.036	14.7	0.63	0.753	0.517	1.130	0.419	17	10.0	0.478	0.379	0.619	15	9.0	3831	53.46%	46.54%	24.18%
806	2.1	0.19	27	0.036	14.7	0.67	0.777	0.463	1.300	0.362	23	13.6	0.452	0.350	0.603	12	7.2	3505	66.84%	33.16%	32.42%
807	2.1	0.19	27	0.036	14.7	0.688	0.826	0.559	1.208	0.457	17	10.4	0.52	0.422	0.668	13	7.8	4003	58.05%	41.95%	25.45%
808	2.1	0.19	27	0.036	14.7	0.686	0.818	0.571	1.199	0.457	17	10.0	0.524	0.422	0.673	13	7.6	4161	58.54%	41.46%	24.73%
811	3	0.27	39	0.036	14.7	0.78	0.896	0.560	1.425	0.449	23	14.1	0.536	0.419	0.712	12	7.3	3449	67.88%	32.12%	31.33%
812	3	0.27	39	0.036	14.7	0.798	0.924	0.634	1.327	0.517	17	10.5	0.584	0.461	0.752	12	6.9	4207	61.73%	38.27%	25.63%
813	3	0.27	39	0.036	14.7	0.789	0.923	0.631	1.373	0.503	18	10.8	0.574	0.466	0.738	12	7.2	4054	61.74%	38.26%	27.31%
816	3.6	0.33	47	0.036	14.7	0.8	0.918	0.572	1.419	0.439	23	14.0	0.544	0.420	0.722	12	7.0	3496	66.45%	33.55%	32.00%
817	3.6	0.33	47	0.036	14.7	0.919	0.959	0.649	1.346	0.516	18	10.9	0.591	0.473	0.771	12	7.2	4056	61.77%	38.23%	27.79%
819	3.6	0.33	47	0.036	14.7	0.939	0.974	0.699	1.345	0.574	17	10.2	0.536	0.525	0.809	12	7.3	4171	58.77%	41.23%	24.11%
821	4.2	0.38	54	0.036	14.7	0.924	0.956	0.595	1.452	0.481	24	14.5	0.559	0.433	0.744	13	7.7	3279	66.67%	33.33%	32.12%
822	4.2	0.38	54	0.036	14.7	1.059	0.736	0.424	1.424	0.595	18	11.1	0.563	0.535	0.650	13	7.8	3656	59.90%	40.10%	26.26%
823	4.2	0.38	54	0.036	14.7	0.904	1.076	0.595	1.405	0.595	19	10.9	0.56	0.528	0.670	13	8.1	3823	58.59%	41.41%	26.96%
826	4.7	0.43	61	0.036	14.7	0.93	1.089	0.680	1.582	0.532	24	14.4	0.633	0.495	0.845	12	7.4	3376	67.97%	32.03%	31.87%
827	4.7	0.43	61	0.036	14.7	0.945	1.116	0.749	1.485	0.598	20	12.0	0.684	0.538	0.888	13	7.7	3690	62.22%	37.78%	29.76%
828	4.7	0.43	61	0.036	14.7	0.951	1.106	0.776	1.499	0.657	19	11.2	0.711	0.588	0.912	13	7.6	3871	60.74%	39.26%	25.23%
831	5.2	0.47	67	0.036	14.7	1.01	1.195	0.748	1.616	0.597	25	15.0	0.678	0.529	0.933	14	8.5	3128	65.61%	34.39%	32.94%
832	5.2	0.47	67	0.036	14.7	1.003	1.178	0.816	1.537	0.677	19	11.8	0.73	0.684	0.958	13	8.0	3754	61.00%	39.00%	27.25%
833	5.2	0.47	67	0.036	14.7	0.984	1.176	0.786	1.552	0.632	20	11.7	0.7	0.680	0.938	13	7.7	3777	61.91%	38.09%	29.65%
836	5.7	0.52	74	0.036	14.7	1.089	1.267	0.810	1.695	0.668	24	14.4	0.755	0.601	1.006	14	8.4	3216	65.06%	34.94%	30.62%
837	5.7	0.52	74	0.036	14.7	1.183	1.37	0.980	1.790	0.669	19	11.4	0.889	0.763	1.156	13	8.1	3789	60.34%	39.66%	24.08%
838	5.7	0.52	74	0.036	14.7	1.205	1.366	0.989	1.773	0.914	18	10.7	0.947	0.814	1.171	12	7.1	4117	61.92%	38.08%	21.46%

C.3.2 Disturbance Wave Celerity Data

Run Number	Liquid Flowrate (l/min)	Liquid Flowrate (kg/m s)	Film Reynolds Number	Air Mass Flowrate (kg/s)	Air Velocity (m/s)	Correlated Time Shift (ms)	Mean Wave Celerity (m/s)
1	1	0.09	13	0.000	0.0	124	0.54
2	1.7	0.16	23	0.000	0.0	104	0.64
3	2.1	0.20	28	0.000	0.0	102	0.66
4	3	0.28	40	0.000	0.0	84	0.80
5	3.6	0.34	49	0.000	0.0	84	0.80
6	4.2	0.40	57	0.000	0.0	74	0.91
7	4.7	0.44	63	0.000	0.0	70	0.96
8	5.2	0.49	70	0.000	0.0	58	1.16
9	5.7	0.54	77	0.000	0.0	62	1.08
10	6.6	0.62	89	0.000	0.0	62	1.08
11	7.4	0.70	100	0.000	0.0	58	1.16
12	8.1	0.76	109	0.000	0.0	48	1.46
13	8.8	0.83	119	0.000	0.0	48	1.40
14	10	0.94	135	0.000	0.0	38	1.76

29	1	0.09	13	0.012	5.2	134	0.50
30	1.7	0.16	23	0.012	5.2	122	0.55
31	2.1	0.20	28	0.012	5.2	88	0.76
32	3	0.28	40	0.012	5.2	74	0.91
33	3.6	0.34	49	0.012	5.2	68	0.99
34	4.2	0.40	57	0.012	5.2	64	1.05
35	4.7	0.44	63	0.012	5.2	72	0.93
36	5.2	0.49	70	0.012	5.2	72	0.93
37	5.7	0.54	77	0.012	5.2	62	1.08
38	6.6	0.62	89	0.012	5.2	56	1.20
39	7.4	0.70	100	0.012	5.2	62	1.08
40	8.1	0.76	109	0.012	5.2	52	1.29
41	8.8	0.83	119	0.012	5.2	52	1.29
42	10	0.94	135	0.012	5.2	46	1.46

57	1.7	0.16	23	0.023	9.7	116	0.58
58	2.1	0.20	28	0.023	9.7	110	0.61
59	3	0.28	40	0.023	9.7	104	0.64
60	3.6	0.34	49	0.023	9.7	86	0.78
61	4.2	0.40	57	0.023	9.7	84	0.80
62	4.7	0.44	63	0.023	9.7	72	0.93
63	5.2	0.49	70	0.023	9.7	72	0.93
64	5.7	0.54	77	0.023	9.7	72	0.93
65	6.6	0.62	89	0.023	9.7	64	1.05
66	7.4	0.70	100	0.023	9.7	62	1.08
67	8.1	0.76	109	0.023	9.7	60	1.12
68	8.8	0.83	119	0.023	9.7	54	1.24

Run Number	Liquid Flowrate (l/min)	Liquid Flowrate (kg/m s)	Film Reynolds Number	Air Mass Flowrate (kg/s)	Air Velocity (m/s)	Correlated Time Shift (ms)	Mean Wave Celerity (m/s)
15	1	0.09	13	0.006	2.6	130	0.52
16	1.7	0.16	23	0.006	2.6	102	0.66
17	2.1	0.20	28	0.006	2.6	104	0.64
18	3	0.28	40	0.006	2.6	84	0.80
19	3.6	0.34	49	0.006	2.6	72	0.93
20	4.2	0.40	57	0.006	2.6	74	0.91
21	4.7	0.44	63	0.006	2.6	62	1.08
22	5.2	0.49	70	0.006	2.6	56	1.20
23	5.7	0.54	77	0.006	2.6	62	1.08
24	6.6	0.62	89	0.006	2.6	68	0.99
25	7.4	0.70	100	0.006	2.6	48	1.40
26	8.1	0.76	109	0.006	2.6	46	1.46
27	8.8	0.83	119	0.006	2.6	50	1.34
28	10	0.94	135	0.006	2.6	44	1.52

43	1	0.09	13	0.018	7.3	140	0.48
44	1.7	0.16	23	0.018	7.3	126	0.53
45	2.1	0.20	28	0.018	7.3	108	0.62
46	3	0.28	40	0.018	7.3	82	0.82
47	3.6	0.34	49	0.018	7.3	94	0.71
48	4.2	0.40	57	0.018	7.3	80	0.84
49	4.7	0.44	63	0.018	7.3	74	0.91
50	5.2	0.49	70	0.018	7.3	72	0.93
51	5.7	0.54	77	0.018	7.3	70	0.96
52	6.6	0.62	89	0.018	7.3	56	1.20
53	7.4	0.70	100	0.018	7.3	64	1.05
54	8.1	0.76	109	0.018	7.3	48	1.40
55	8.8	0.83	119	0.018	7.3	50	1.34
56	10	0.94	135	0.018	7.3	54	1.24

Run Number	Liquid Flowrate (l/min)	Liquid Flowrate (kg/m s)	Film Reynolds Number	Air Mass Flowrate (kg/s)	Air Velocity (m/s)	Correlated Time Shift (ms)	Mean Wave Celerity (m/s)
69	1.25	0.12	17	0.029	12.2	124	0.54
70	1.7	0.16	23	0.029	12.2	120	0.56
71	2.1	0.20	28	0.029	12.2	116	0.58
72	3	0.28	40	0.029	12.2	102	0.66
73	3.6	0.34	49	0.029	12.2	90	0.74
74	4.2	0.40	57	0.029	12.2	80	0.84
75	4.7	0.44	63	0.029	12.2	96	0.70
76	5.2	0.49	70	0.029	12.2	82	0.82
77	5.7	0.54	77	0.029	12.2	64	1.05
78	6.6	0.62	89	0.029	12.2	58	1.16

Run Number	Liquid Flowrate (l/min)	Liquid Flowrate (kg/m s)	Film Reynolds Number	Air Mass Flowrate (kg/s)	Air Velocity (m/s)	Correlated Time Shift (ms)	Mean Wave Celerity (m/s)
79	1.25	0.12	17	0.035	14.7	116	0.58
80	1.7	0.16	23	0.035	14.7	116	0.58
81	2.1	0.20	28	0.035	14.7	110	0.61
82	3	0.28	40	0.035	14.7	100	0.67
83	3.6	0.34	49	0.035	14.7	86	0.78
84	4.2	0.40	57	0.035	14.7	70	0.96
85	4.7	0.44	63	0.035	14.7	56	1.20

C.4 ETHOXYLATED ALCOHOL

C.4.1 Data from Spatial Film Thickness Measurements

Run No.	Liquid Flowrate (l/min)	Liquid Flowrate (kg/m s)	Liquid Film Reynolds Number	Air Mass Flowrate (kg/s)	Air Velocity (m/s)	Mean Film Thickness (mm)	Mean Disturbance Height (mm)	Mean Disturbance Wave Min Start (mm)	Mean Disturbance Wave Max Finish (mm)	Mean Disturbance Wave Cell Number	Mean Disturbance Wave Length (mm)	Mean Substrate Height (mm)	Mean Substrate Min Value (mm)	Mean Substrate Max Value (mm)	Mean Substrate Cell Number	Mean Substrate Length (mm)	Number of Disturbance Wavelets	% Area Covered By Disturbance Waves	% Area Covered By Substrate	% Volume Contained in Disturbance Waves	
1	1	0.09	5	0.000	0.0	0.968	1.232	0.931	1.539	0.879	56	33.4	0.679	0.702	0.984	59	95.4	1110	51.89%	48.11%	29.71%
2	1	0.09	5	0.000	0.0	0.989	1.258	0.917	1.451	0.822	45	26.7	0.676	0.681	0.989	48	28.5	1345	50.34%	49.66%	30.23%
3	1	0.09	5	0.000	0.0	0.962	1.171	0.908	1.366	0.853	19	11.4	0.810	0.777	1.019	29	17.4	2633	42.14%	57.86%	15.81%
4	1.7	0.16	8	0.000	0.0	1.194	1.625	1.154	2.032	0.993	29	17.6	0.946	0.904	1.244	53	32.1	1476	36.49%	63.52%	20.74%
5	1.7	0.16	8	0.000	0.0	1.177	1.692	1.127	2.042	0.950	33	20.0	0.919	0.959	1.234	52	31.4	1370	36.34%	61.66%	21.92%
6	1.7	0.16	8	0.000	0.0	1.181	1.630	1.117	1.951	0.991	23	13.9	0.972	0.986	1.250	51	30.3	1626	31.75%	68.25%	17.69%
7	2.1	0.20	10	0.000	0.0	1.255	1.718	1.181	2.107	1.036	29	17.4	1.007	0.930	1.310	51	30.8	1490	36.29%	63.71%	20.40%
8	2.1	0.20	10	0.000	0.0	1.271	1.696	1.211	2.076	1.095	25	15.1	0.996	0.962	1.315	45	27.1	1756	37.10%	62.90%	21.60%
9	2.1	0.20	10	0.000	0.0	1.279	1.696	1.211	2.076	1.078	23	13.9	1.025	0.979	1.328	41	24.5	1840	37.67%	62.33%	19.84%
10	3	0.28	15	0.000	0.0	1.352	1.510	1.379	2.450	1.095	30	23.0	1.045	1.002	1.424	60	35.3	1207	38.57%	61.13%	24.30%
11	3	0.28	15	0.000	0.0	1.422	2.050	1.344	2.550	1.150	33	19.9	1.135	1.009	1.498	69	40.6	1121	31.31%	66.69%	20.15%
12	3	0.28	15	0.000	0.0	1.444	2.052	1.405	2.790	1.189	33	20.0	1.105	1.009	1.493	63	37.8	1275	35.73%	64.27%	23.41%
13	4.2	0.40	20	0.000	0.0	1.655	2.343	1.720	3.066	1.298	42	25.1	1.315	1.180	1.731	70	41.9	1022	35.95%	64.05%	21.93%
14	4.2	0.40	20	0.000	0.0	1.579	2.434	1.699	3.284	1.265	47	28.2	1.261	1.127	1.712	79	47.5	902	35.61%	64.39%	24.89%
15	4.2	0.40	20	0.000	0.0	1.745	2.432	1.717	3.109	1.352	37	22.2	1.302	1.204	1.813	58	34.9	1259	39.19%	60.81%	25.39%
16	5.2	0.49	25	0.000	0.0	1.770	2.483	1.799	3.237	1.429	41	24.7	1.345	1.255	1.834	69	41.1	1081	37.33%	62.67%	24.00%
17	5.2	0.49	25	0.000	0.0	1.805	2.698	1.940	3.316	1.445	46	27.4	1.381	1.235	1.891	86	51.4	907	34.77%	65.23%	23.46%
18	5.2	0.49	25	0.000	0.0	1.771	2.554	1.816	3.408	1.389	45	27.0	1.393	1.224	1.829	89	53.8	876	33.11%	66.89%	21.89%
19	6.6	0.62	32	0.000	0.0	1.980	3.012	2.041	4.177	1.570	58	36.0	1.531	1.388	2.018	117	70.1	619	30.34%	69.66%	22.69%
20	6.6	0.62	32	0.000	0.0	1.938	2.751	1.941	3.273	1.775	38	22.9	1.498	1.419	2.039	80	48.2	1096	35.13%	64.87%	22.71%
21	6.6	0.62	32	0.000	0.0	1.989	2.777	2.107	3.426	1.715	50	29.8	1.561	1.400	2.065	88	53.1	845	35.23%	64.77%	21.54%
22	8.1	0.76	39	0.000	0.0	2.266	3.193	2.329	4.110	1.729	62	37.4	1.628	1.519	2.311	76	45.5	803	47.06%	57.94%	28.80%
23	8.1	0.76	39	0.000	0.0	2.178	2.968	2.248	3.549	2.061	48	28.6	1.661	1.649	2.293	81	48.6	986	39.55%	60.45%	23.75%
24	8.1	0.76	39	0.000	0.0	1.968	2.787	2.075	3.320	1.755	46	27.7	1.521	1.478	2.093	93	55.8	913	35.37%	64.63%	22.75%

Run No.	Liquid Flowrate (l/min)	Liquid Flowrate (kg/ms)	Liquid Film Reynolds Number	Air Mass Flowrate (kg/s)	Air Velocity (m/s)	Mean Film Thickness (mm)	Mean Disturbance Height (mm)	Mean Wave Min Start (mm)	Mean Disturbance Wave Max (mm)	Mean Wave Min Finish (mm)	Mean Disturbance Wave Cell Number	Mean Wave Length (mm)	Mean Substrate Height (mm)	Mean Substrate Min Value (mm)	Mean Substrate Max Value (mm)	Mean Substrate Cell Number	Mean Substrate Length (mm)	Number of Disturbance Wavelets	% Area Covered By Disturbance Waves	% Area Covered By Substrate	% Volume Contained in Disturbance Waves
25	1	0.09	5	0.006	2.6	0.968	1.288	0.980	1.655	0.793	44	26.5	0.688	0.667	0.979	48	26.7	1309	48.65%	61.35%	31.26%
26	1	0.09	5	0.006	2.6	0.974	1.270	0.973	1.674	0.825	46	27.3	0.702	0.700	1.006	52	31.2	1263	47.88%	52.12%	27.92%
27	1	0.09	5	0.006	2.6	0.971	1.234	0.963	1.528	0.824	37	22.2	0.715	0.724	0.993	41	24.8	1687	49.34%	50.66%	26.37%
28	1.7	0.16	8	0.006	2.6	1.211	1.646	1.175	2.150	0.982	32	19.2	0.937	0.899	1.244	52	31.3	1436	36.62%	61.38%	22.61%
29	1.7	0.16	8	0.006	2.6	1.107	1.406	1.044	1.706	0.988	24	14.2	0.686	0.863	1.157	38	22.6	2074	41.27%	58.73%	19.02%
30	1.7	0.16	8	0.006	2.6	1.156	1.690	1.133	1.943	0.949	29	17.1	0.667	0.854	1.204	43	25.6	1689	40.66%	59.44%	23.26%
31	2.1	0.20	10	0.006	2.6	1.294	1.772	1.276	2.280	1.078	31	18.7	1.013	0.953	1.336	58	34.6	1419	37.13%	62.87%	21.78%
32	2.1	0.20	10	0.006	2.6	1.249	1.716	1.224	2.142	1.017	28	17.1	0.983	0.938	1.304	51	30.5	1614	36.17%	63.83%	21.28%
33	2.1	0.20	10	0.006	2.6	1.292	1.796	1.247	2.338	1.050	28	16.8	1.007	0.942	1.337	52	30.9	1632	36.05%	63.94%	22.07%
34	3	0.28	15	0.006	2.6	1.418	2.068	1.441	2.768	1.077	38	23.0	1.066	0.955	1.456	73	43.7	1091	35.15%	64.84%	24.84%
35	3	0.28	15	0.006	2.6	1.398	1.978	1.361	2.610	1.107	34	20.1	1.077	1.026	1.450	61	36.5	1265	35.66%	64.34%	22.98%
36	3	0.28	15	0.006	2.6	1.402	2.090	1.405	2.684	1.123	33	20.1	1.092	1.009	1.470	73	43.9	1105	31.04%	68.96%	22.99%
37	4.2	0.40	20	0.006	2.6	1.644	2.296	1.683	3.010	1.391	42	25.4	1.260	1.167	1.709	70	42.3	1051	37.41%	62.59%	23.35%
38	4.2	0.40	20	0.006	2.6	1.680	2.345	1.681	3.054	1.323	37	22.4	1.226	1.160	1.736	56	33.7	1291	49.43%	50.57%	27.03%
39	4.2	0.40	20	0.006	2.6	1.662	2.370	1.637	2.941	1.456	43	25.9	1.286	1.220	1.744	76	45.6	954	34.63%	65.37%	22.69%
40	5.2	0.48	25	0.006	2.6	1.730	2.536	1.772	3.533	1.191	61	36.8	1.269	1.101	1.745	93	55.8	706	36.38%	63.62%	26.65%
41	5.2	0.48	25	0.006	2.6	1.751	2.474	1.772	3.198	1.541	40	24.2	1.310	1.205	1.815	72	43.1	1117	37.88%	62.12%	25.18%
42	5.2	0.48	25	0.006	2.6	1.794	2.611	1.794	3.315	1.475	46	27.3	1.332	1.193	1.859	78	45.4	944	36.13%	63.87%	25.75%
43	6.6	0.62	32	0.006	2.6	1.931	2.779	2.110	3.802	1.567	54	32.6	1.431	1.255	2.021	100	59.9	814	37.11%	62.89%	25.81%
44	6.6	0.62	32	0.006	2.6	1.939	2.768	2.093	3.696	1.426	48	28.5	1.412	1.198	1.968	78	47.0	973	36.67%	61.33%	27.18%
45	6.6	0.62	32	0.006	2.6	1.947	2.574	1.954	3.151	1.644	48	28.5	1.420	1.357	1.943	82	48.9	926	36.98%	63.02%	23.11%
46	8.1	0.76	39	0.006	2.6	2.166	2.972	2.218	3.601	1.938	42	25.2	1.687	1.625	2.269	75	45.0	1055	37.26%	62.74%	22.10%
47	8.1	0.76	39	0.006	2.6	2.144	3.140	2.283	4.263	1.729	62	37.1	1.690	1.378	2.198	115	69.0	668	35.77%	64.23%	26.66%
48	8.1	0.76	39	0.006	2.6	2.063	2.947	2.109	3.751	1.603	49	29.1	1.688	1.603	2.145	95	57.0	638	34.26%	65.74%	22.67%
49	1	0.09	5	0.012	4.9	0.954	1.212	0.926	1.548	0.810	27	16.3	0.731	0.732	0.992	33	19.9	2033	48.30%	53.70%	23.34%
50	1	0.09	5	0.012	4.9	0.918	1.153	0.875	1.491	0.747	33	20.0	0.677	0.854	0.924	35	20.8	1808	50.72%	49.28%	26.30%
51	1	0.09	5	0.012	4.9	0.966	1.261	0.916	1.615	0.833	21	12.4	0.802	0.751	1.025	33	20.0	2302	40.07%	59.93%	18.65%
52	1.7	0.16	8	0.012	4.9	1.132	1.539	1.090	2.015	0.920	26	15.4	0.867	0.803	1.171	44	26.7	1742	37.59%	62.41%	21.65%
53	1.7	0.16	8	0.012	4.9	1.140	1.570	1.076	2.131	0.853	26	15.0	0.868	0.801	1.176	43	25.7	1764	37.00%	63.00%	22.13%
54	1.7	0.16	8	0.012	4.9	1.145	1.526	1.067	2.006	0.904	23	13.8	0.902	0.813	1.164	38	22.6	2019	38.99%	61.01%	21.25%
65	2.1	0.20	10	0.012	4.9	1.202	1.666	1.190	2.191	1.015	27	16.4	0.968	0.864	1.261	55	33.0	1606	34.52%	65.48%	20.33%
66	2.1	0.20	10	0.012	4.9	1.212	1.670	1.190	2.241	0.937	24	14.5	0.941	0.834	1.230	43	25.9	1630	37.16%	62.84%	22.35%
67	2.1	0.20	10	0.012	4.9	1.177	1.641	1.135	1.921	1.010	24	14.2	0.937	0.888	1.214	40	23.9	2000	39.66%	60.34%	20.35%
68	3	0.28	15	0.012	4.9	1.390	1.940	1.352	2.679	0.957	35	21.1	1.059	0.897	1.397	55	32.9	1272	37.60%	62.40%	23.63%
69	3	0.28	15	0.012	4.9	1.363	1.979	1.337	2.615	1.044	31	18.9	1.084	0.948	1.436	59	35.6	1262	30.39%	69.61%	21.61%
70	3	0.28	15	0.012	4.9	1.421	2.071	1.352	2.912	0.937	32	19.4	1.061	0.898	1.446	55	32.8	1314	36.63%	63.37%	25.33%
71	4.2	0.40	20	0.012	4.9	1.636	2.327	1.635	3.103	1.227	42	25.0	1.234	1.062	1.676	74	44.6	1052	36.70%	63.30%	24.69%
72	4.2	0.40	20	0.012	4.9	1.601	2.331	1.550	3.146	1.165	38	22.6	1.195	1.034	1.634	66	39.6	1121	35.74%	64.26%	25.36%
73	4.2	0.40	20	0.012	4.9	1.591	2.319	1.595	3.155	1.171	40	23.7	1.211	1.012	1.630	73	43.6	1032	34.30%	65.70%	23.69%
74	5.2	0.48	25	0.012	4.9	1.681	2.498	1.742	3.200	1.371	45	27.1	1.270	1.152	1.742	91	54.8	882	33.46%	66.54%	24.44%
75	5.2	0.48	25	0.012	4.9	1.686	2.374	1.718	3.257	1.212	46	27.7	1.264	1.127	1.700	71	42.5	950	36.91%	63.09%	23.86%
76	5.2	0.48	25	0.012	4.9	1.703	2.498	1.708	3.195	1.381	37	21.9	1.304	1.200	1.785	75	45.1	1053	32.35%	67.65%	22.27%
77	6.6	0.62	32	0.012	4.9	1.864	2.800	1.945	3.475	1.480	47	28.3	1.387	1.248	1.923	77	46.0	995	39.38%	60.62%	25.63%
78	6.6	0.62	32	0.012	4.9	1.936	2.833	1.975	3.738	1.512	49	29.8	1.476	1.273	1.990	92	55.3	817	33.89%	66.11%	23.75%
79	6.6	0.62	32	0.012	4.9	1.913	2.808	1.882	3.510	1.626	44	26.7	1.411	1.325	1.994	84	50.1	962	35.93%	64.07%	26.24%
80	8.1	0.76	39	0.012	4.9	2.154	3.130	2.314	3.972	1.837	57	34.5	1.547	1.474	2.264	103	61.7	794	36.31%	61.69%	28.16%
81	8.1	0.76	39	0.012	4.9	2.165	3.266	2.302	4.323	1.609	64	38.5	1.549	1.365	2.215	106	63.9	666	36.93%	64.07%	28.48%
82	8.1	0.76	39	0.012	4.9	2.013	2.757	2.043	3.324	1.827	40	24.2	1.578	1.519	2.116	70	42.1	1091	36.91%	63.09%	21.62%

Run No.	Liquid Flowrate (l/min)	Liquid Flowrate (kg/ms)	Liquid Film Reynolds Number	Air Mass Flowrate (kg/s)	Air Velocity (m/s)	Mean Film Thickness (mm)	Mean Disturbance Height (mm)	Mean Wave Min Start (mm)	Mean Disturbance Wave Max (mm)	Mean Wave Min Finish (mm)	Mean Disturbance Wave Cell Number	Mean Wave Length (mm)	Mean Substrate Height (mm)	Mean Substrate Min Value (mm)	Mean Substrate Max Value (mm)	Mean Substrate Cell Number	Mean Substrate Length (mm)	Number of Disturbance Wavelets	% Area Covered By Disturbance Waves	% Area Covered By Substrate	% Volume Contained in Disturbance Waves
73	1	0.09	5	0.018	7.4	0.883	0.922	0.529	1.198	0.396	81	36.7	0.325	0.265	0.581	42	25.1	1186	59.82%	40.18%	52.28%
74	1	0.09	5	0.018	7.4	0.823	0.813	0.458	1.068	0.394	43	26.0	0.342	0.317	0.587	31	18.8	1641	59.72%	40.28%	45.15%
75	1	0.09	5	0.018	7.4	0.865	0.824	0.582	1.109	0.501	28	16.9	0.467	0.444	0.682	24	14.3	2383	56.53%	43.47%	31.20%
76	1.7	0.16	8	0.018	7.4	1.021	1.436	0.924	2.174	0.733	22	13.1	0.782	0.696	1.035	40	24.3	1905	36.45%	63.55%	23.35%
77	1.7	0.16	8	0.018	7.4	1.028	1.466	0.937	2.290	0.702	20	12.2	0.789	0.682	1.040	39	23.6	2092	35.63%	64.37%	23.44%
78	1.7	0.16	8	0.018	7.4	0.967	1.349	0.900	1.983	0.740	19	11.4	0.786	0.717	1.004	37	22.0	2240	35.90%	64.20%	20.42%
79	2.1	0.20	10	0.018	7.4	1.110	1.609	1.034	2.657	0.715	21	12.3	0.867	0.726	1.104	42	25.4	1896	32.69%	67.31%	21.85%
80	2.1	0.20	10	0.018	7.4	1.121	1.669	1.061	2.694	0.690	21	12.6	0.867	0.717	1.128	45	27.0	1783	31.65%	68.35%	22.64%
81	2.1	0.20	10	0.018	7.4	1.069	1.616	0.965	2.337	0.711	24	14.6	0.801	0.722	1.062	44	26.3	1759	36.03%	63.97%	24.40%
82	3	0.28	15	0.018	7.4	1.253	1.940	1.259	3.125	0.760	24	14.6	0.953	0.773	1.292	52	31.0	1631	33.45%	66.55%	25.73%
83	3	0.28	15	0.018	7.4	1.322	1.953	1.298	3.153	0.908	25	14.8	0.952	0.769	1.315	45	27.9	1649	34.27%	65.73%	24.52%
84	3	0.28	15	0.018	7.4	1.332	1.978	1.269	3.208	0.722	25	15.0	0.970	0.779	1.312	43	25.8	1712	35.98%	64.04%	27.21%
85	4.2	0.40	20	0.018	7.4	1.498	2.158	1.403	3.283	0.766	29	17.3	1.095	0.842	1.436	44	25.3	1694	38.52%	61.48%	27.69%
86	4.2	0.40	20	0.018	7.4	1.488	2.149	1.375	3.267	0.798	31	18.6	1.015	0.792	1.379	43	26.0	1600	41.77%	58.23%	31.63%
87	4.2	0.40	20	0.018	7.4	1.493	2.125	1.360	3.327	0.657	27	16.0	1.063	0.870	1.452	39	22.7	1611	40.49%	59.51%	28.80%
88	5.2	0.49	25	0.018	7.4	1.855	2.382	1.512	3.557	0.957	31	18.3	1.151	0.912	1.587	43	25.8	1622	41.85%	58.15%	30.48%
89	5.2	0.49	25	0.018	7.4	1.830	2.351	1.465	3.363	0.972	30	18.2	1.136	0.923	1.563	41	24.9	1698	40.75%	59.25%	30.49%
90	5.2	0.49	25	0.018	7.4	1.882	2.398	1.522	3.446	1.037	28	17.0	1.176	0.937	1.602	41	24.5	1738	41.43%	58.57%	30.13%
91	6.8	0.62	32	0.018	7.4	1.833	2.620	1.666	3.624	0.983	33	19.8	1.248	0.942	1.732	38	23.0	1680	46.09%	53.91%	32.03%
92	6.8	0.62	32	0.018	7.4	1.854	2.634	1.622	3.563	1.150	28	16.9	1.264	1.001	1.754	33	19.8	1995	46.47%	53.53%	31.83%
93	6.8	0.62	32	0.018	7.4	1.896	2.692	1.713	3.510	1.113	30	18.2	1.337	1.054	1.806	37	22.5	1744	44.50%	55.50%	29.46%
94	8.1	0.76	39	0.018	7.4	1.978	2.671	1.770	3.606	1.222	33	19.9	1.331	1.105	1.850	36	21.6	1734	46.28%	51.72%	32.71%
95	8.1	0.76	39	0.018	7.4	2.113	2.861	1.880	3.714	1.363	32	18.9	1.465	1.188	2.026	37	21.9	1766	46.80%	53.20%	31.14%
96	8.1	0.76	39	0.018	7.4	2.125	2.840	1.801	3.683	1.288	31	18.7	1.436	1.100	1.967	39	23.6	1748	46.79%	54.21%	32.41%
97	1	0.09	5	0.024	10.0	0.919	1.272	0.796	2.172	0.586	17	9.9	0.726	0.813	0.915	30	18.1	2528	95.21%	4.79%	20.92%
98	1	0.09	5	0.024	10.0	0.846	1.128	0.722	1.908	0.559	17	10.1	0.669	0.654	0.848	27	16.3	2611	99.78%	0.22%	22.05%
99	1	0.09	5	0.024	10.0	0.890	1.221	0.771	1.971	0.630	14	8.6	0.726	0.628	0.910	30	18.0	2761	93.15%	6.85%	18.44%
101	1.7	0.16	8	0.024	10.0	1.227	1.698	1.103	2.736	0.834	18	10.6	0.994	0.860	1.229	35	20.9	2280	93.46%	6.54%	18.95%
102	1.7	0.16	8	0.024	10.0	1.271	1.754	1.160	2.819	0.830	17	10.4	1.039	0.893	1.275	34	20.6	2239	92.49%	7.51%	18.28%
103	1.7	0.16	8	0.024	10.0	1.258	1.778	1.137	2.877	0.820	17	10.1	1.024	0.865	1.266	38	22.6	2201	91.07%	8.93%	18.62%
104	2.1	0.20	10	0.024	10.0	1.403	1.902	1.262	3.082	0.883	19	11.3	1.105	0.939	1.375	31	18.7	2256	97.36%	2.64%	21.22%
105	2.1	0.20	10	0.024	10.0	1.399	1.938	1.213	3.129	0.895	17	10.2	1.071	0.891	1.351	29	17.3	2567	96.76%	3.24%	22.95%
106	2.1	0.20	10	0.024	10.0	1.389	1.954	1.266	3.042	0.936	17	10.3	1.110	0.922	1.420	32	19.1	2343	93.85%	6.15%	20.66%
107	3	0.28	15	0.024	10.0	1.658	2.079	1.362	3.380	0.862	19	11.4	1.170	0.932	1.450	26	15.5	2656	42.88%	57.12%	24.90%
108	3	0.28	15	0.024	10.0	1.662	2.116	1.411	3.374	0.976	19	11.7	1.192	0.961	1.505	31	18.4	2454	40.12%	59.88%	23.71%
109	3	0.28	15	0.024	10.0	1.668	2.136	1.384	3.363	0.907	19	11.2	1.196	0.956	1.623	28	17.0	2448	38.56%	61.44%	23.24%

C.4.2 Disturbance Wave Celerity Data

Run Number	Liquid Flowrate (l/min)	Liquid Flowrate (kg/m s)	Liquid Film Reynolds Number	Air Mass Flowrate (kg/s)	Air Velocity (m/s)	Correlated Time Shift (ms)	Mean Wave Celerity (m/s)
1	1	0.09	5	0.000	0.0	146	0.48
2	1.7	0.16	8	0.000	0.0	116	0.60
3	2.1	0.20	10	0.000	0.0	104	0.67
4	3	0.28	15	0.000	0.0	86	0.81
5	4.2	0.40	20	0.000	0.0	92	0.76
6	5.2	0.49	25	0.000	0.0	72	0.97
7	6.6	0.62	32	0.000	0.0	58	1.21
8	8.1	0.76	39	0.000	0.0	48	1.46
17	1	0.09	5	0.012	4.9	160	0.44
18	1.7	0.16	8	0.012	4.9	106	0.66
19	2.1	0.20	10	0.012	4.9	104	0.67
20	3	0.28	15	0.012	4.9	88	0.80
21	4.2	0.40	20	0.012	4.9	70	1.00
22	5.2	0.49	25	0.012	4.9	60	1.17
23	6.6	0.62	32	0.012	4.9	50	1.40
24	8.1	0.76	39	0.012	4.9	48	1.46
33	1	0.09	5	0.024	10.0	126	0.55
34	1.7	0.16	8	0.024	10.0	106	0.66
35	2.1	0.20	10	0.024	10.0	102	0.69
36	3	0.28	15	0.024	10.0	96	0.73
37	4.2	0.40	20	0.024	10.0	86	0.81
38	5.2	0.49	25	0.024	10.0	84	0.83

Run Number	Liquid Flowrate (l/min)	Liquid Flowrate (kg/m s)	Liquid Film Reynolds Number	Air Mass Flowrate (kg/s)	Air Velocity (m/s)	Correlated Time Shift (ms)	Mean Wave Celerity (m/s)
9	1	0.09	5	0.006	2.6	146	0.48
10	1.7	0.16	8	0.006	2.6	108	0.65
11	2.1	0.20	10	0.006	2.6	102	0.69
12	3	0.28	15	0.006	2.6	90	0.78
13	4.2	0.40	20	0.006	2.6	92	0.76
14	5.2	0.49	25	0.006	2.6	72	0.97
15	6.6	0.62	32	0.006	2.6	72	0.97
16	8.1	0.76	39	0.006	2.6	66	1.06
25	1	0.09	5	0.018	7.4	160	0.44
26	1.7	0.16	8	0.018	7.4	110	0.64
27	2.1	0.20	10	0.018	7.4	112	0.63
28	3	0.28	15	0.018	7.4	102	0.69
29	4.2	0.40	20	0.018	7.4	74	0.95
30	5.2	0.49	25	0.018	7.4	70	1.00
31	6.6	0.62	32	0.018	7.4	74	0.95
32	8.1	0.76	39	0.018	7.4	66	1.06
39	1	0.09	5	0.030	12.5	108	0.65
40	1.7	0.16	8	0.030	12.5	96	0.73
41	2.1	0.20	10	0.030	12.5	94	0.74
42	3	0.28	15	0.030	12.5	80	0.88